INVESTIGATION OF NONLINEAR OPTICAL PROPERTIES OF LARGE AREA MONOLAYER MOLYBDENUM DISULFIDE (MoS_2) AND ITS APPLICATION AS PLANAR WAVEGUIDE SATURABLE ABSORBER

CHEW JING WEN

FACULTY OF SCIENCE
UNIVERSITI MALAYA
KUALA LUMPUR

2023

INVESTIGATION OF NONLINEAR OPTICAL PROPERTIES OF LARGE AREA MONOLAYER MOLYBDENUM DISULFIDE (MoS_2) AND ITS APPLICATION AS PLANAR WAVEGUIDE SATURABLE ABSORBER

CHEW JING WEN

THESIS SUBMITTED IN FULFILMENT OF THE REQUIREMENTS FOR THE DEGREE OF DOCTOR OF PHILOSOPHY

DEPARTMENT OF PHYSICS
FACULTY OF SCIENCE
UNIVERSITI MALAYA
KUALA LUMPUR

2023

UNIVERSITI MALAYA

ORIGINAL LITERARY WORK DECLARATION

Name of Candidate: **CHEW JING WEN**

Matric No: **17029040/2**

Name of Degree: **DOCTOR OF PHILOSOPHY**

Title of Thesis ("this Work"):

INVESTIGATION OF NONLINEAR OPTICAL PROPERTIES OF LARGE AREA MONOLAYER MOLYBDENUM DISULFIDE (MoS_2) AND ITS APPLICATION AS PLANAR WAVEGUIDE SATURABLE ABSORBER Field of Study:

EXPERIMENTAL PHYSICS

I do solemnly and sincerely declare that:

(1) I am the sole author/writer of this Work;
(2) This Work is original;
(3) Any use of any work in which copyright exists was done by way of fair dealing and for permitted purposes and any excerpt or extract from, or reference to or reproduction of any copyright work has been disclosed expressly and sufficiently and the title of the Work and its authorship have been acknowledged in this Work;
(4) I do not have any actual knowledge nor do I ought reasonably to know that the making of this work constitutes an infringement of any copyright work;
(5) I hereby assign all and every rights in the copyright to this Work to the University of Malaya ("UM"), who henceforth shall be owner of the copyright in this Work and that any reproduction or use in any form or by any means whatsoever is prohibited without the written consent of UM having been first had and obtained;
(6) I am fully aware that if in the course of making this Work I have infringed any copyright whether intentionally or otherwise, I may be subject to legal action or any other action as may be determined by UM.

Candidate's Signature Date:

Subscribed and solemnly declared before,

Witness's Signature Date:

Name:

Designation:

INVESTIGATION OF NONLINEAR OPTICAL PROPERTIES OF LARGE AREA MONOLAYER MOLYBDENUM DISULFIDE (MoS_2) AND ITS APPLICATION AS PLANAR WAVEGUIDE SATURABLE ABSORBER

ABSTRACT

Transition metal dichalcogenides are a type of two-dimensional (2D) material that has been widely studied in the last decade. Among the transition metal dichalcogenides, 2D molybdenum disulfide (MoS_2) has attracted much attention among the scientific community due to its unique electrical and optical properties. To obtain MoS_2 in its 2D form, top-down exfoliation technique from its bulk material or bottom-up synthesis method can be used. One of the common methods to obtain 2D MoS_2 that have been used in photonics studies is chemical vapor deposition (CVD), which is a bottom-up synthesis approach. It relies on the chemical reaction between molybdenum oxide and sulfur precursors at high temperature to produce 2D MoS_2. This method provides advantages such as better control in MoS_2 thin film thickness uniformity, which allows one to control the properties of 2D MoS_2 with higher confidence level. In this work, the nonlinear optical (NLO) properties, particularly the nonlinear refractive index, of a CVD-grown large area monolayer MoS_2 is investigated at the telecommunication wavelength band (or C-band) using time-resolved Z-scan technique. The result shows that it exhibits a nonlinear refractive index of 1.40×10^{-13} m^2 W^{-1}, which is a few orders of magnitude larger than that of common bulk dielectric materials. It shows that monolayer MoS_2 is a good 2D material candidate for NLO application in C-band wavelength range. To utilize the NLO properties of the monolayer MoS_2, different coating lengths of the MoS_2 film is transferred onto a planarized optical waveguide using a polymer-assisted transfer method. These MoS_2-coated waveguides show saturable absorption properties measured using I-scan technique. Q-switched pulse lasers are produced when they are integrated into an erbium-doped fiber laser cavity. It is found that performance of the Q-switched fiber laser

(in terms of the repetition rate, pulse duration, average output power, pulse energy and wavelength tunability range) does not only scale monotonically with the coating length but also depends on the coating quality of the coated MoS_2 thin film as well. Among the saturable absorbers (SAs), the waveguide with MoS_2 coating length of 7.2 mm shows the widest wavelength tunability. This observation can be attributed to the concentration of vacancy-defect in the thin film. This is verified upon inspections using X-ray photoelectron spectroscopy and optical transmission spectroscopy. Therefore, it can be concluded that a long coating length of MoS_2 thin film with minimum exposed edge sites enhances the performance of Q-switching and its wavelength tunability. This work is valuable such that it paves a way for the development of a compact laser source using MoS_2 as the SA, which in turn will bring benefits for the development in all-planar waveguide laser technology.

Keywords: monolayer molybdenum disulfide, nonlinear refractive index, planarized optical waveguide, saturable absorber, interaction length

KAJIAN SIFAT OPTIK BUKAN LINEAR MOLIBDENUM DISULFIDA (MoS_2) BERLAPISAN TUNGGAL BERKAWASAN LUAS DAN APLIKASINYA SEBAGAI PENYERAP TEPU PEMANDU GELOMBANG RATA

ABSTRAK

Dikalkogenida logam peralihan ialah sejenis bahan dua dimensi (2D) yang telah banyak dikaji dalam dekad terakhir. Antara dikalkogenida logam peralihan, molibdenum disulfida (MoS_2) 2D telah menarik perhatian yang besar dalam kalangan komuniti saintifik kerana menpunyai sifat elektrik dan optik yang unik. Untuk mendapatkan MoS_2 dalam bentuk 2D, teknik pengelupasan dari bahan pukalnya atau kaedah sintesis bawah ke atas boleh digunakan. Salah satu kaedah yang biasa digunakan dalam kajian fotonik untuk mendapatkan MoS_2 2D adalah pemendapan wap kimia (PWK), iaitu pendekatan sintesis bawah ke atas. Ia bergantung pada tindak balas kimia antara molibdenum oksida dan pendahulu sulfur dalam keadaan suhu tinggi untuk menghasilkan MoS_2 2D. Pendekatan ini menyediakan kelebihan seperti pengawalan baik dalam pembuatan filem nipis MoS_2 yang berketebalan seragam, dengan ini membolehkan seseorang meramalkan sifat-sifat MoS_2 2D dengan tahap keyakinan yang lebih tinggi. Dalam kajian ini, sifat optik bukan linear (OBL), terutamanya indeks biasan bukan linear, bagi MoS_2 berlapisan tunggal berkawasan luas yang disintesis melalui PWK disiasat pada jalur panjang gelombang telekomunikasi (atau dikenali sebagai C-band) dengan menggunakan teknik Z-scan beresolusi masa. Hasil eksperimen menunjukkan bahawa MoS_2 memiliki indeks biasan bukan linear bernilai 1.40×10^{-13} m^2 W^{-1}, dan nilai ini adalah beberapa kali ganda lebih besar daripada bahan dielektrik bahan pukal biasa. Hasil ini menunjukkan bahawa MoS_2 berlapisan tunggal merupakan calon bahan 2D yang baik bagi aplikasi OBL dalam jalur panjang gelombang C-band. Untuk menggunakan sifat OBL MoS_2 berlapisan tunggal, salutan filem nipis MoS_2 yang berpanjangan beza dipindahkan ke atas pemandu gelombang rata dengan menggunakan kaedah pemindahan berbantukan polimer.

Pemandu-pemandu gelombang bersalut MoS_2 ini menunjukkan sifat penyerapan tepu yang diukur dengan teknik I-scan. Laser denyutan Q-switched dihasilkan apabila pemandu-pemandu gelombang tersebut disalurkan ke dalam rongga laser gentian dop erbium. Hasil kajian menunjukan bahawa prestasi laser gentian Q-switched (dari segi kadar ulangan, tempoh denyutan, kuasa keluaran purata, tenaga denyutan dan julat kebolehlarasan panjang gelombang) bukan sajaha tidak meningkat secara monotonik dengan panjang salutan tetapi juga bergantung juga pada kualiti salutan filem nipis MoS_2. Antara penyerap-penyerap tepu (PT), pemandu gelombang yang mempunyai panjang salutan MoS_2 sebanyak 7.2 mm menunjukkan kobolehlarasan panjang gelombang terluas. Pemerhatian ini boleh dikaitkan dengan kepekatan kecacatan kekosongan dalam filem nipis tersebut. Ini telah disahkan dengan menggunakan pemeriksaan spektroskopi fotoelektron sinar-X, serta spektroskopi transmisi optik. Oleh itu, kesimpulan boleh dibuat bahawa panjang salutan yang panjang bagi filem nipis MoS_2 dengan tapak tepi terdedah minimum dapat meningkatkan prestasi pensuisan Q dan kebolehlarasannya terhadap panjang gelombang. Kajian ini adalah berharga kerana ia membuka jalan bagi pembangunan sumber laser padat dengan menggunakan MoS_2 sebagai PT, dan seterusnya akan membawa manfaat dalam pembangunan teknologi laser pemandu gelombang rata seluruh.

Kata kunci: molibdenum disulfida berlapisan tunggal, indeks biasan bukan linear, pemandu gelombang rata, penyerap tepu, panjang interaksi

ACKNOWLEDGEMENTS

First and foremost, I would like to express my sincere gratitude to my supervisors Datuk Professor Ulung Dr. Harith Ahmad, Associate Professor Dr. Chong Wu Yi and Professor Dr. Sithi Vinakayam Muniandy. Datuk Professor Ulung Dr. Harith Ahmad provides me the opportunity to conduct research in the field of photonics in Photonics Research Centre, University of Malaya (PRCUM). With his support, I can utilize the facilities in PRCUM to conduct research in the fulfilment of my PhD program.

I would like to express my deepest appreciation to Associate Professor Dr Chong Wu Yi who is a diligent and knowledgeable supervisor and scientist. He gave me insight in the field of photonics research and my PhD study. He always allocates his time for discussion and gives advices to me in every stage of my study. Besides, he is also a high achiever, and his advices always lead to a positive research outcome. His dedication and timely reminder always motivate me to meet the deadlines of each milestones.

I owe a gratitude to Professor Dr. Sithi Vinayakam Muniandy for the guidance in theoretical knowledge for my research. His expertise guides me well to deal with noisy data in my research analysis. He also taught me the way to generate scientific idea and skills in writing manuscripts. Without his help, this thesis would not have been possible.

I thank profusely to Dr. Yap Yuen Kiat, the collaborator from Heriot-Watt University Malaysia for providing assistance in supplying the raw material for my PhD research. His help is truly valuable for my thesis completion. Besides, I would like to thank Professor Dr. Tan Chee Leong, Ng Kok Bin, Gan Soon Xin, Tey Lian Seng and Chong Wen Sin for their precious discussion and kind assistance during my study. I would like to thank Malaysia's Ministry of Education for supporting me through MyBrainSc scholarship. Lastly, I am very thankful to my parents, siblings and friends for giving me understanding and mental support during my hard time in the research period.

TABLE OF CONTENTS

LIST OF FIGURES

LIST OF TABLES

LIST OF SYMBOLS AND ABBREVIATIONS

α	:	absorption coefficient
P_{out}	:	average output power
ω	:	beam radius
ω_0	:	beam waist radius
J_0	:	Bessel function
$\tilde{n}$	:	complex refractive index
ρ	:	density of material
N	:	density of absorbing atoms
L_{eff}	:	effective length of sample
δE	:	energy difference between ground state and virtual state
hv	:	energy of photon
$Ei(x)$	:	exponential-integral function
k	:	extinction coefficient
ω	:	frequency of laser
F	:	focal length of lens
GL(x)	:	Gaussian-Lorentzian product
G_i	:	Gaussian beam amplitude at the entrance plane
G_0	:	Gaussian beam amplitude at the exit plane

$T(I)$	:	intensity dependent transmission
I	:	intensity of the optical field
$\chi^{(1)}$	:	linear susceptibility
L_{Max}	:	maximum flake length
<L>	:	mean flake size
<w>	:	mean flake width
σ	:	multiphoton absorption cross section
α_{ns} or α_{NL}	:	non-saturable loss
n_2	:	nonlinear refractive index
n_{2,MoS_2}	:	nonlinear refractive index of MoS_2
$n_{2,PDMS}$	:	nonlinear refractive index of PDMS
Δx_{p-v}	:	normalized peak-to-valley distance
$T(z)$	:	normalized transmittance
$I_0(t)$	:	on-axis intensity
$\Delta\phi_0(z,t)$	:	on-axis phase shift
$\Delta\Phi_0(t)$	:	on-axis phase shift at the focus
$\tilde{E}(t)$	:	optical field
q	:	order of photon absorption
ΔT_{p-v}	:	peak-to-valley transmittance changes
ϵ_0	:	permittivity of free space

$I(z,r,t)$	:	photon flux
h	:	Planck's constant
$\tilde{P}(t)$	:	polarization, or dipole moment per unit volume
$P(t)$	:	power of pulse
τ_p	:	pulse duration
E_p	:	pulse energy
Δ	:	Raman modes separation
z_0	:	Rayleigh length
n	:	refractive index of material
n_0	:	refractive index under weak light
f	:	repetition rate of laser
β	:	reverse saturable absorption (or TPA) coefficient
I_s	:	saturation intensity
α_s or α_0	:	saturable loss
$\tilde{P}^2(t)$	:	second order nonlinear polarization
$\chi^{(2)}$	:	second order nonlinear susceptibility
c_p	:	specific heat
c	:	speed of light
t_c	:	thermal characteristic time
κ	:	thermal conductivity

D	:	thermal diffusion coefficient
ϑ	:	thermal lens strength
dn/dT	:	thermo-optical coefficient
L_{MoS_2}	:	thickness of MoS_2 thin film
L_{PDMS}	:	thickness of PDMS substrate
L	:	thickness of sample
$\tilde{P}^3(t)$	:	third order nonlinear polarization
$\chi^{(3)}$	:	third order nonlinear susceptibility
λ	:	wavelength of laser
k	:	wave vector

AdC	:	adventitious carbon
NH_3	:	ammonia gas
$(NH_4)_2MoS_4$	:	ammonium thiomolybdate
AFM	:	atomic force microscopy
BS	:	beamsplitter
BSCCO	:	bismuth strontium calcium copper oxide
BP	:	black phosphorus
C	:	carbon
CO_2	:	carbon dioxide

CS_2	:	carbon disulfide
CCD	:	charge-coupled device
CVD	:	chemical vapor deposition
CA Z-scan	:	closed aperture Z-scan
CW	:	continuous wave
Cu	:	copper
CHP	:	cyclohexylpyrrolidonone
EDFL	:	erbium-doped fiber laser
FHD	:	flame hydrolysis deposition
FA	:	fluorinated antimonene
FWM	:	four-wave mixing
FWHM	:	full width at half maximum
Au	:	gold
GVD	:	group velocity dispersion
h-BN	:	hexagonal boron nitride
HRTEM	:	high resolution transmission electron microscopy
HOPG	:	highly oriented pyrolytic graphite
H_2S	:	hydrogen sulfide
H_2	:	hydrogen
LPE	:	liquid phase exfoliation
MOCVD	:	metal-organic chemical vapor deposition

MBE	:	molecular beam epitaxy
Mo	:	molybdenum
MoS_2	:	molybdenum disulfide
V_{MoS_2}	:	molybdenum disulfide vacancy
$MoTe_2$	:	molybdenum ditelluride
MoO_3	:	molybdenum trioxide
MoS_3	:	molybdenum trisulfide
V_{Mo}	:	molybdenum vacancy
NMP	:	n-methyl-pyrrolidone
Nd:YAG	:	neodymium-doped yttrium aluminium garnet
NLA	:	nonlinear absorption
NLO	:	nonlinear optical
NLR	:	nonlinear refraction
O	:	oxygen atom
OA Z-scan	:	open aperture Z-scan
OC	:	optical coupler
ISO	:	optical isolator
OPM	:	optical power meter
OSA	:	optical spectrum analyser
OSC	:	oscilloscope
PD	:	photodiode

PL	:	photoluminescence
PIC	:	photonics integrated circuit
PC	:	polarization controller
PDMS	:	polydimethylsiloxane
PMMA	:	polymethyl methacrylate
PVA	:	polyvinyl alcohol
PS	:	polystyrene
Q factor	:	quality factor
RF	:	radio-frequency
SA	:	saturable absorber
SEM	:	scanning electron microscopy
SPM	:	self-phase modulation
SNR	:	signal-to-noise
Si	:	silicon
SiO_2	:	silicon dioxide
STD	:	standard deviation
S	:	sulfur
V_S	:	sulfur vacancy
TRT	:	thermal release tape
THG	:	third harmonic generation
Ti:sapphire	:	titanium-sapphire

TEM	:	transmission electron microscopy
TI	:	topological insulator
TBF	:	tunable bandpass filter
TMD	:	transition metal dichalcogenide
WS_2	:	tungsten disulfide
2D	:	two-dimensional
TPA	:	two photon absorption
V_{2S}	:	two-sulfur vacancy
UV-vis	:	ultraviolet-visible
UV-vis-NIR	:	ultraviolet-visible-near-infrared
VOA	:	variable optical attenuator
V_2O_5	:	vanadium pentoxide
SA1	:	waveguide with 2.5 mm MoS_2 coating length
SA2	:	waveguide with 4.4 mm MoS_2 coating length
SA3	:	waveguide with 7.2 mm MoS_2 coating length
SA4	:	waveguide with 9.2 mm MoS_2 coating length
WDM	:	wavelength division multiplexer
XPS	:	X-ray photoelectron spectroscopy

LIST OF APPENDICES

CHAPTER 1: INTRODUCTION

Two-dimensional (2D) materials received a vivid interest from scientific community after the successful exfoliation of graphene from its bulk graphite crystal (Novoselov et al., 2004; Wang et al., 2012; Xia et al., 2014a). In general, 2D materials refer to crystalline materials that consist of single- or few-layer structures of atoms (Xiong et al., 2021). Sometimes, these atomically thin 2D materials are referred to as layered materials or 2D nanosheets or nanoflakes (Li & Zhu, 2015). The nanosheets are formed due to the strong in-plane interatomic interactions, which is much stronger than the out-of-plane stacking direction. Consider graphene as an example, it comprises carbon atoms bonded hexagonally by strong sp^2 hybridization, forming a nanosheet with large physical strength. Each nanosheet can stack on each other by the weak van der Waals forces, forming a multilayer graphene or graphite. Due to the strong in-plane and weak out-of-plane atomic interaction characteristics, it is thus possible to obtain monolayer graphene from graphite using a simple "scotch tape" mechanical exfoliation method, as demonstrated by Novoselov and his co-workers (Novoselov et al., 2004). Such 2D materials received much attention in the research field due to their outstanding physical, electrical and optical properties, despite their atomically thin size (Li & Zhu, 2015; Wang et al., 2012). For example, the monolayer graphene has extraordinary physical strength (Lee et al., 2008), high thermal conductivity (Balandin et al., 2008), high carrier mobility (Bolotin et al., 2008), excellent optical properties (Nair et al., 2008; Xiong et al., 2021), etc. Particularly, in the field of photonics, it exhibits excellent nonlinear optical (NLO) properties as well. The NLO properties are essential in making laser, optical switchers, optical modulators, which are essential in developing telecommunication network, fundamental research, all-optical devices, etc (Guo et al., 2019). These excellent properties lead to the application of graphene in electronics, optoelectronics, sensors, and, of course, NLO devices (Xiong

et al., 2021). Due to the practical demand in the nonlinear photonics field, searching for suitable optical materials, like 2D materials, has become an important and on-going process (Guo et al., 2019).

1.1 2D Materials

Since then, a variety of 2D materials analogues to graphene such as hexagonal boron nitride (h-BN), transition metal dichalcogenides (TMDs), black phosphorus (BP), MXenes, topological insulators (TIs), etc have been discovered (Guo et al., 2019). Although some families like h-BN, TMDs, MXene and TIs are made up of more than one element, they still share the same interatomic interaction characteristic as graphene, i.e. strong in-plane and weak out-of-plane bonding forces, allowing them to turn into 2D materials using certain exfoliation technique. Figure 1.1 demonstrates some of the schematic structure of 2D materials, namely graphene, BP, TMDs and h-BN. Graphene and BP are made up from single element (carbon and phosphorus, respectively), whereas TMDs and h-BN are not. h-BN consists of boron and nitrogen (red and blue atom in Figure 1.1 respectively) atoms held by strong interatomic force. Similarly, TMDs are a class of compounds with the formula MX_2, where M is a transition metal element (such as Mo or W) and X is a chalcogen (such as S, Se or Te), indicated as black and yellow atoms in Figure 1.1 respectively. Among the TMDs, molybdenum disulfide (MoS_2) attracted our attention due to its unique properties which will be described in detail in Chapter 2 (Manzeli et al., 2017). Generally, these 2D materials can be obtained using either top-down exfoliation from bulk materials or bottom-up synthesis. Each of the techniques has their own advantages and disadvantages, as well as produces different forms of 2D material.

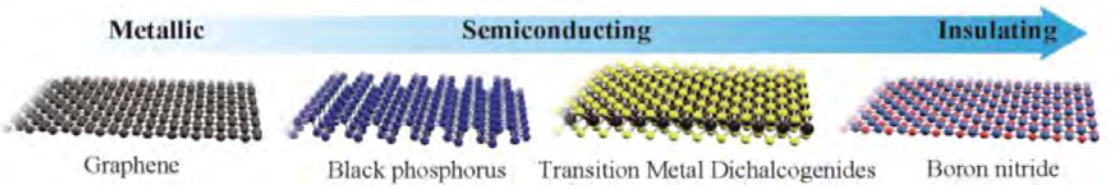

Figure 1.1: Schematic diagram of the atomic structure of graphene, BP, TMDs and h-BN, from left to right. Figure adapted from (Long et al., 2019).

1.2 Preparation Methods of 2D Material

Top-down exfoliation involves the separation of atomically thin 2D materials from its pristine, bulk counterpart. Since the 2D materials are held together by weak van der Waals force, they can be easily exfoliated using methods such as the aforementioned mechanical exfoliation (Novoselov et al., 2004); lithium intercalation (Zeng et al., 2011); and liquid phase exfoliation (LPE) (Coleman et al., 2011). The mechanical exfoliation is very popular in the laboratory for fundamental research or rapid prototyping of 2D material devices due to its simplicity, cost effectiveness and the ability to obtain high quality monolayer sheets. However, the disadvantages of this technique include its low yield and inability to control the size of the sheet and number of layers (Li & Zhu, 2015). Another way to obtain 2D materials is by lithium intercalation method. The small alkali metal atoms, like lithium, are able to enter the interlayer gap of the host material due to their small size. When this alkali metal-intercalated layer materials are added to water, hydrogen bubbles, produced from the chemical reaction between alkali metal and water, expand the interlayer gap and eventually exfoliate them into 2D materials in the solvent (Cai et al., 2018). This method increases the yield of 2D materials greatly compared to the mechanical exfoliation method. However, it should be noted that this method may induce phase distortion of the crystal lattice due to the intercalation of lithium atoms. Benavente et al. showed that the lithium intercalation method changes the crystal lattice of pristine 2H-MoS_2 into 1T-MoS_2 (Benavente et al., 2002). This will change the quality

of the sample since a 2H-MoS_2 is semiconducting whereas 1T-MoS_2 has metallic property (Manzeli et al., 2017; Wang et al., 2012). In 2011 as well, Coleman et al. demonstrated the exfoliation of suspended bulk layered material into its 2D counterpart in organic solvent through ultrasonication without changing the crystal lattice of the material (Coleman et al., 2011). In the ultrasonic bath, bubbles are created in the solvent and the collapse of bubbles generates a mechanical force that exfoliate the bulk layered material. The yield of obtaining 2D material can be further increased by increasing the amount of pristine bulk material as well as the ultrasonication time (O'Neill et al., 2012). This LPE technique provides an easy 2D material production route, but it is difficult to control the thickness and lateral size of the produced 2D material.

On the other hand, bottom-up synthesis method refers to the assembly of atoms or precursors into useful structures on a substrate (Gerberich et al., 2003). It allows the development of large area 2D material on a substrate. Chemical vapor deposition (CVD) (Li et al., 2009a; Zhan et al., 2012); metal-organic chemical vapor deposition (MOCVD) (Eichfeld et al., 2015); and molecular beam epitaxy (MBE) (Dumcenco et al., 2015; Rollings et al., 2006) are common techniques in the deposition of large area 2D materials. CVD method involves the direct chemical reaction between different precursor materials, whereas MOCVD method uses metal-organic precursors. For example, in CVD, large-area monolayer MoS_2 can be synthesized onto a silicon dioxide (SiO_2) substrate by sulfurization of molybdenum trioxide powder (Lee et al., 2012). Typically, CVD can produce a high quality, large area film on the substrate with desired thickness. Besides, it does not require ultrahigh vacuum environment and is easier to be integrated into existing industrial processes (Manzeli et al., 2017). However, CVD can only produce 2D material with an area of few cm^2 at a time, limiting the production scale (Bhuyan et al., 2016). Another direct growth method of 2D materials is MBE. This technique is widely used in semiconductor device manufacturing. High-purity elemental source materials (e.g.

molybdenum and tellurium in making 2D $MoTe_2$) are put into an ultrahigh vacuum chamber to form a molecular beam. The sample will be deposited on a preheated substrate with a typical growth rate of ~ 0.1 nm/min (Roy et al., 2016). This technique allows greater control on the thickness of the deposited film and the ability to grow heterostructure with high quality with abrupt interfaces (Roy et al., 2016). Yet, it has a limiting factor in terms of small production scale, which is similar to the CVD method (Bhuyan et al., 2016).

1.3 Issues Encountered by Top-Down Exfoliation and Possible Solution

From the above discussion, it is obvious that the top-down exfoliation and bottom-up synthesis method have their own benefits and downsides. One of the differences between these methods is that the top-down exfoliation typically produces 2D materials in the form of flakes with micrometer or sub-micrometer flake size, whereas the bottom-up synthesis produces a large-area 2D material in sub-centimeter to centimeter area. Therefore, it is essential to choose fabrication technique wisely to suit a specific study or application. The condition and quality of the 2D material may affect the characteristic of the sample. Consider using a top-down exfoliation approach such as LPE, it produces 2D material in the flakes form, suspended in solvent, with a distribution of flakes thickness and lateral size. For example, 2D MoS_2 in n-methyl-pyrrolidone (NMP) solvent produced using LPE technique has mean flake size <L> of ~ 2 μm (approximately 1.6 μm to 2.7 μm) with different flake thickness (O'Neill et al., 2012). In this case, nonlinear absorption (NLA) measurement (one of the NLO properties) upon the MoS_2:NMP dispersion will give the effective NLA of the group of flakes. If one were to make a 2D material-based device, the LPE method may impose problems that include the inability in (1) producing a uniform, fixed thickness 2D material on the device; (2) predicting the properties of the

2D material with a particular thickness (rather than a group of flakes with random size distribution and thickness); and (3) producing a device with the same performance using the same process steps. The popular methods to assemble 2D material dispersion onto a device include spin coating (Yamaguchi et al., 2010; Zhang et al., 2014a), spray coating (Kelly et al., 2016) and inkjet printing (McManus et al., 2017). It is difficult to produce a uniform, monolayer thin film using these integration methods. More often, many parameters need to be optimized to deposit a film with good quality (Cai et al., 2018; Yamaguchi et al., 2010). Otherwise, the coated film may contain staked flakes, thereby producing a multilayer 2D material in random orientation and low coverage area, which may induce problem as discussed previously.

To solve this problem, the bottom-up synthesis approach may be a better choice. It offers benefits in terms of better control of thickness and uniformity of 2D material thin film compared to the top-down approaches (Bhuyan et al., 2016). With the help of various transfer techniques, the CVD-grown large area 2D material can be transferred from the original substrate to the target. The transfer technique can generally be categorized into two ways, namely wet transfer and dry transfer (Watson et al., 2021). As the name suggests, wet transfer involves water or liquid chemicals to delaminate the 2D films from the original substrate before transferring to the target; whereas dry transfer does not. In both transfer techniques, a supporting layer is needed. Usually, polymers are used as the supporting layer as they are flexible, mechanically strong and able to form a uniform contact with the 2D material, allowing one to integrate 2D material with the desired platform. Care must be taken for wet transfer process as contaminants or residues may still exist after transferring 2D material to the target. On the other hand, dry transfer process does not produce contaminants, but air bubble trapped between 2D material and the target substrate may happen (Watson et al., 2021). Nevertheless, these methods are able to transfer the large area 2D material thin film to the target surface while maintaining

its physical size and thickness. This indicates that the 2D material grown by bottom-up synthesis approach provides an advantage in terms of better accuracy in predicting the characteristic of the film and the performance of the device. For instance, CVD method has been utilized in making 2D material-based NLO devices like optical modulator (Kravets et al., 2019; Phare et al., 2015), optical limiter (Ouyang et al., 2016), pulse laser (Bao et al., 2009; Khazaeizhad et al., 2014) and frequency converter (Wu et al., 2015). Hence, the bottom-up approach will be more favourable in making wafer-scale 2D material-based photonics device (Wang et al., 2012).

1.4 Application of 2D Material in NLO Devices

One of the 2D material-based NLO devices that is widely studied is the generation of a pulse laser source. The generation of pulse laser relies on a NLO effect called saturable absorption. After the successful demonstration of ultrafast pulse laser sources using graphene (Bao et al., 2009; Sun et al., 2010), the exploration of other 2D materials to achieve the same objective has been actively pursued by the research community. Guo et al. reported that 2D materials show saturable absorption property across a wide wavelength band, ranging from visible light to infrared region (Guo et al., 2019). One of interesting findings are that the generation of pulse laser from 2D materials can be done on optical waveguide platforms. This suggests that the top-down exfoliation and bottom-up synthesis methods of a 2D material can be used to realize a pulse laser source. In general, LPE and CVD processes are the most common methods used to obtain 2D material in this field of study. If LPE is used, the 2D materials usually exist in two forms, (1) 2D nanoflakes encapsulated by a polymer to become a thin film structure (Liu et al., 2014c; Sun et al., 2010; Woodward et al., 2014); or (2) nanoflakes coated onto a waveguide to become the element in producing pulses (Mao et al., 2016a; Song et al., 2010; Zhu et al., 2013). On the other hand, if CVD is used, the 2D materials are usually

transferred onto the waveguide (Bao et al., 2009; He et al., 2012; Khazaeizhad et al., 2014). However, as discussed in the previous section, optical devices based on liquid phase exfoliated 2D material may impose problems such as reproducibility. While CVD-grown 2D material may solve the problem, there is still a lack of study involving integration of a monolayer 2D material on an optical waveguide, which will be discussed in detail in Chapter 2.4.5.3.

1.5 Motivation of the Study

As mentioned previously, MoS_2 is the most studied 2D optical material among the TMD family. Various studies show that MoS_2 has excellent optical and NLO properties at the telecommunication wavelength band (or commonly known as C-band) of 1550 nm (Guo et al., 2019; Säynätjoki et al., 2017; You et al., 2019). However, many studies were done using few-layer MoS_2 nanoflakes or multilayer films. They include fundamental study of nonlinear refractive index of multilayer MoS_2 through self-phase modulation method (Zhang et al., 2018); and pulse laser generation using MoS_2 nanoflakes through saturable absorption process (Chen et al., 2015a; Huang et al., 2014; Liu et al., 2014b). The former could not provide information on the nonlinear refractive index of a monolayer MoS_2; whereas the latter may lead to the problems such as film uniformity and repeatability as discussed above. There is a need to investigate the optical properties of MoS_2 at a fixed thickness. In this thesis, the NLO properties of a CVD-grown large area monolayer MoS_2 thin film were studied using Z-scan technique. The MoS_2 was integrated with an optical planarized waveguide with different coating length using an all-dry transfer technique. The optical planarized waveguide was used as the integrating platform due to (1) its capability in providing evanescent field interaction between MoS_2 and the laser; and (2) its mechanical robustness that is compatible with the all-dry transfer technique. The NLA properties of MoS_2-coated waveguides were studied using I-scan

technique. Besides that, they were coupled into a fiber ring laser cavity for pulse laser generation. The studies showed that the coating length of MoS_2 on the waveguide affects the performance of pulse laser generation. The effect can be described by the amount of defect of the MoS_2 film produced from the fabrication technique.

1.6 Thesis Objectives

The objectives of this work are:

1. To measure the nonlinear refractive index of large area monolayer MoS_2 at the 1550 nm wavelength band using Z-scan technique.
2. To integrate the large area monolayer MoS_2 on optical planarized waveguides using an all-dry transfer technique.
3. To characterize the MoS_2-coated waveguide using I-scan technique.
4. To study the performance of pulse laser generation with different coating length of MoS_2 on the waveguide.

1.7 Thesis Outline

The achievement of these objectives is outlined as follows.

The fundamental properties and fabrication methods of MoS_2 will be discussed in the next chapter. The linear and nonlinear optical properties of MoS_2 will be discussed as well. Moreover, methods to characterize the NLO properties of MoS_2 will be discussed as well. Next, the characterization of large area monolayer MoS_2 will be discussed in Chapter 3. The characterization includes, Raman spectroscopy, atomic force microscopy (AFM), X-ray photoelectron spectroscopy (XPS) and Z-scan measurement. Subsequently, the techniques for preparation of sample will be discussed in the same chapter. These

include the fabrication method of planarized optical waveguide, preparation of MoS_2 sample and integration method of the sample (using an all-dry transfer technique) on the waveguide. In chapter 4, the characterization of the MoS_2-coated waveguide will be discussed. Moreover, the application of MoS_2-coated waveguide as a Q-switched pulse laser at 1550 nm wavelength band will be presented. The preparation and performance of Q-switched pulse laser will be discussed as well. Furthermore, the interaction-length-dependent wavelength tunability of the Q-switched pulse laser will be discussed in the same chapter. Finally, a thesis conclusion and future potential work will be discussed in Chapter 5. The supplementary information on the XPS measurement on MoS_2 sample will be provided in Appendix A.

CHAPTER 2: LITERATURE REVIEW: GENERAL PROPERTIES OF MOLYBDENUM DISULFIDE (MoS_2), ITS PREPARATION AND CHARACTERIZATION TECHNIQUES

MoS_2 is one of the most studied material among other TMD material, as mentioned in the previous chapter. Before it is exfoliated into a 2D material, MoS_2 exists in crystal form naturally as shown in Figure 2.1(a). The crystal is formed by multiple MoS_2 layers, stacking on top of each other by van der Waals forces. As depicted in Figure 1.1, each layer of MoS_2 can be viewed as a three-atomic-planes (sulfur-molybdenum-sulfur or simply S-Mo-S), held strongly by covalent bonds (Li & Zhu, 2015). A monolayer MoS_2 has a interlayer spacing of ~ 0.65 nm, illustrated in Figure 2.1(b) (Radisavljevic et al., 2011). MoS_2 is found to be interesting due to its unique properties such as possessing a direct bandgap and lack of inversion symmetry. The former is essential for developing a photoluminescence device (Mak et al., 2010; Splendiani et al., 2010); while the latter can be used in spintronic device (Mak et al., 2012; Wang et al., 2012).

In the field of photonics, MoS_2 exhibits strong linear and nonlinear optical (NLO) properties which can be used in producing pulsed laser source (Guo et al., 2019), wavelength converter (Säynätjoki et al., 2017) and single photon emitter (Barthelmi et al., 2020; Klein et al., 2021). Thus, it is important to study the linear and NLO properties of MoS_2 at a specific wavelength band of interest for the development of MoS_2 as an optical material in photonics devices. One such wavelength band is the 1550 nm optical fiber telecommunication wavelength band (or C-band).

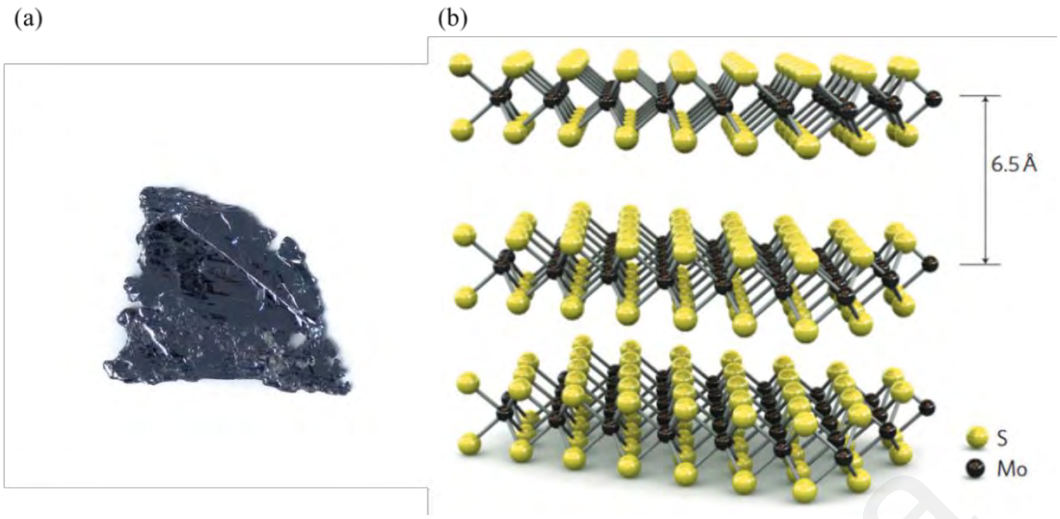

Figure 2.1: (a) A natural bulk MoS_2 crystal before it is exfoliated into its 2D form, photo adapted from (*SPI Supplies Molybdenum Disulfide (MoS_2) Crystal*, 2022); (b) Schematic diagram of a three-layer MoS_2, with its interlayer spacing of ~ 0.65 nm. Figure adapted from (Radisavljevic et al., 2011).

2.1 Physical Properties of MoS_2 and Its Nature

The stoichiometry of 2D MoS_2 and its electronic band structure will be discussed in this section.

2.1.1 Stoichiometry of MoS_2

A thermodynamically stable MoS_2 has a S:Mo stoichiometry of 2:0 (Baker et al., 1999). However, in some cases, the MoS_2 stoichiometry may change and does not remain strictly to the value of 2:0. A few methods are found to cause alteration of the stoichiometry, such as preferential sputtering process (Baker et al., 1999), annealing process (Choi et al., 2021; Iacovella et al., 2020) and bottom-up synthesis method of MoS_2 using CVD (Kim et al., 2014; Syari'ati et al., 2019). Baker et al. performs a preferential sputtering process on pristine MoS_2 to purposely reduce the ratio of sulfur for his study (Baker et al., 1999). In most case, the change in MoS_2 stoichiometry comes from the bottom-up CVD synthesis method and post-annealing process. A brief introduction of CVD of MoS_2 technique will be discussed in Section 2.2.3. Kim et al. demonstrated that the exposure time of sulfur

vapor in the CVD chamber can affect the stoichiometry of CVD-grown MoS_2 (Kim et al., 2014). Besides that, Choi et al. shows that MoS_2 stoichiometry can be affected significantly by the annealing temperature (Choi et al., 2021). The MoS_2 stoichiometry can influence its electrical and optical properties, which have been predicted theoretically (Kunstmann et al., 2017; Saha & Yoshiya, 2018; Zhou et al., 2013) and verified experimentally (Iacovella et al., 2020; Kim et al., 2014; Syari'ati et al., 2019). Therefore, it is important to determine the MoS_2 stoichiometry in any study that will exploit the optical properties of the MoS_2 material itself.

There are a few technique that can be employed to examine the ratio of S:Mo of the 2D MoS_2 sample, including high resolution transmission electron microscopy (HRTEM) and X-ray photoelectron spectroscopy (XPS) (Baker et al., 1999; Choi et al., 2021; Kondekar et al., 2017; Syari'ati et al., 2019; Wu et al., 2018; Xiong et al., 2021). The utilization of HRTEM is relatively expensive with tedious sample preparation. On the other hand, XPS provides a few benefits in terms of cheaper cost and simple sample preparation, which encourages its utilization in stoichiometry study of 2D MoS_2. Besides that, most of the samples can be analysed by XPS technique in a non-destructive manner. Baker et al. reports a systematic study to determine the stoichiometry of 2D MoS_2 using XPS to a high degree of accuracy based on the binding energy difference between Mo $3d_{5/2}$ and S $2p_{3/2}$. Figure 2.2 illustrates a linear relationship between MoS_2 stoichiometry and (Mo $3d_{5/2}$ – S $2p_{3/2}$) binding energy (Baker et al., 1999). The author claims that the accuracy that was achieved is as high as $x \pm 0.1$ from the plot in Figure 2.2. Their results give a promising guidance to estimate the stoichiometry of 2D MoS_2 based on a relative simpler method. This technique will be used to examine the CVD-grown MoS_2 samples used in this thesis.

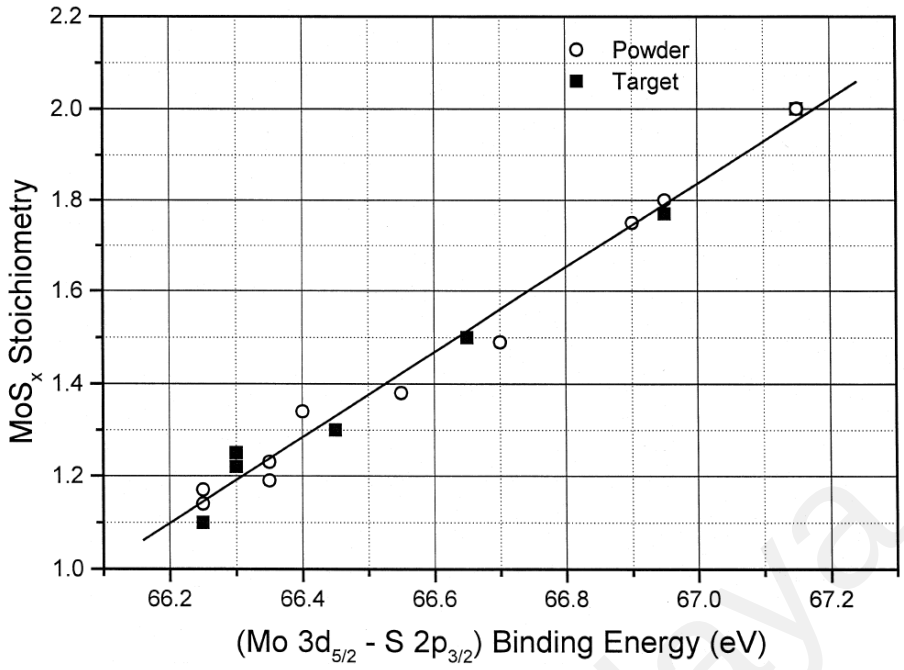

Figure 2.2: Graph of the MoS_2 stoichiometry against (Mo $3d_{5/2}$ – S $2p_{3/2}$) binding energy. Figure adapted from (Baker et al., 1999).

2.1.2 Electronic Band Structure

The pristine, monolayer MoS_2 is found to be semiconducting. This is evidence by the emergence of bandgap photoluminescence (PL) of a monolayer MoS_2. In the year of 2010, Splendiani et al. showed that as the number of layers of MoS_2 decreases from bulk to monolayer, PL signal increases and becomes strongest when it is monolayer, as depicted in Figure 2.3(a). This indicates that a monolayer MoS_2 is a semiconductor with a direct bandgap, whereas bulk MoS_2 has an indirect bandgap (Splendiani et al., 2010). The study shows that two PL peaks are observed at 677 nm and 627 nm, which correspond to the direct excitonic transitions of A- and B-excitons of MoS_2 at the Brillouin zone K point. To prove this, theoretical analysis to study the electronic structure of bulk and monolayer MoS_2 has been carried out (Li & Galli, 2007). Using density functional theory, the evolution of the band structure of MoS_2 with different number of layers is illustrated in Figure 2.3(b) (Splendiani et al., 2010). The bulk MoS_2 has an indirect bandgap of 1.23 eV while the monolayer MoS_2 has a direct bandgap of 1.88 eV (Gusakova et al., 2017).

This direct bandgap property makes monolayer MoS_2 useful in making semiconductor and optoelectronic devices.

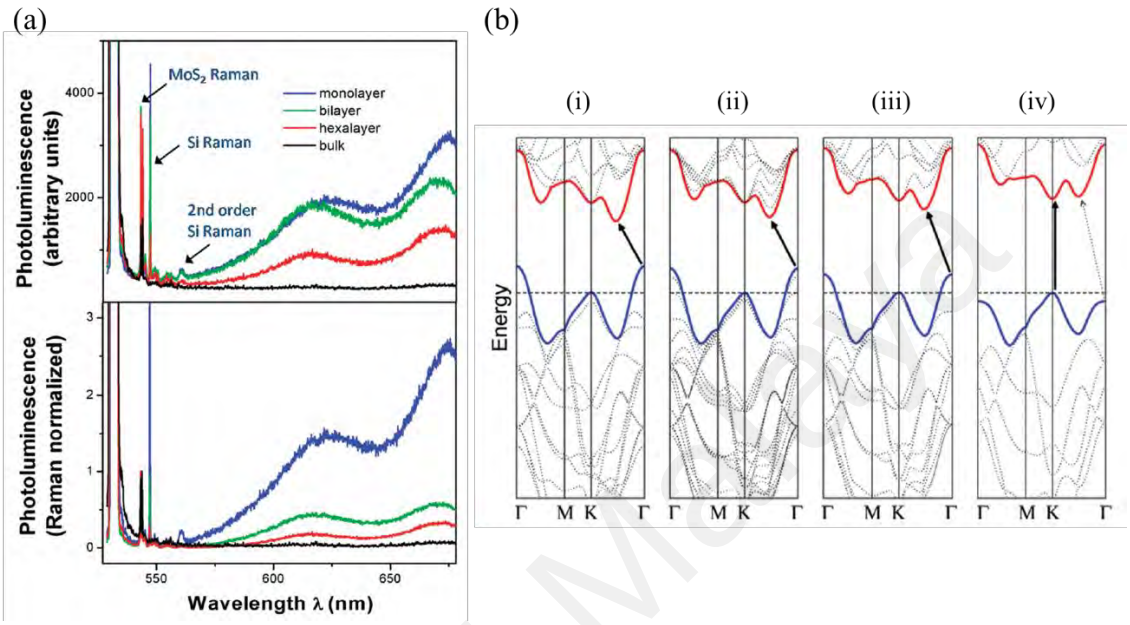

Figure 2.3: (a) Effect of number of layers of MoS_2 to the PL spectra. The PL spectrum is the strongest in monolayer MoS_2; (b) Band structures calculated using density functional theory for (i) bulk MoS_2, (ii) quadrilayer MoS_2, (iii) bilayer MoS_2, and (iv) monolayer MoS_2. As the thickness decreases, the indirect bandgap becomes larger. For monolayer MoS_2, it becomes a direct bandgap. Figures adapted from (Splendiani et al., 2010).

2.1.3 Forms of MoS_2

2D MoS_2 exists in different forms, depending on the fabrication technique as described briefly in Chapter 1. The type of form of MoS_2 can be discussed from two perspectives, that is, its number of layers and lateral size.

2.1.3.1 Number of Layers of MoS_2

The number of layers relates to the thickness of MoS_2. In this thesis, the number of layers will be used to describe the form of MoS_2. Besides that, the convention reported

by Bhuyan et al. to categorize the form of MoS_2 by its number of layers will be considered, discussed as follow (Bhuyan et al., 2016). One, two and three MoS_2 layers are known as monolayer, bilayer and trilayer MoS_2, respectively. For number of layers between 5 to 20, the term "few-layer" MoS_2 will be used. When the number of layers is more than 20 layers, the sample will be considered as multilayer MoS_2. While few- and multilayer MoS_2 can be produced using any top-down exfoliation or bottom-up synthesis method, the fabrication methods to obtain monolayer MoS_2 will be discussed in detail. There are a few methods to obtain monolayer MoS_2, such as mechanical exfoliation (Säynätjoki et al., 2017), CVD (Zhan et al., 2012), and possibly LPE (Bang et al., 2014). Among the three techniques, CVD can control the number of layers of MoS_2 with better accuracy than the mechanical exfoliation and LPE. The fabrication techniques will be discussed in more detail in Chapter 2.2 later. As-deposited monolayer MoS_2 using the three techniques above are shown in Figure 2.4. As can be seen in Figure 2.4(b), CVD process allows the growth of large area, monolayer MoS_2 on a substrate. Compared to this, the individual MoS_2 flakes obtained using mechanical exfoliation (Figure 2.4(a)) and LPE (Figure 2.4(c)) contains a mixture of different number of layers of MoS_2.

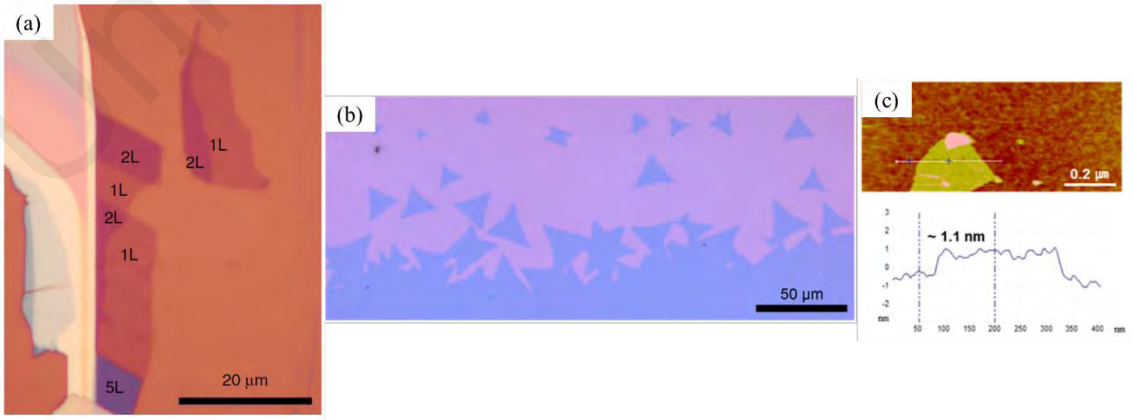

Figure 2.4: Monolayer MoS_2 obtained by (a) mechanical exfoliation, figure adapted from (Säynätjoki et al., 2017); (b) CVD, figure adapted from (Zhan et al., 2012); and (c) LPE technique, figure adapted from (Bang et al., 2014).

2.1.3.2 Lateral Size of MoS_2

The lateral size will determine whether the 2D MoS_2 is in the form of flake or thin film. A flake is an isolated piece of material with a finite size. For example, a large number of MoS_2 flakes, suspended in a solvent, can be obtained by LPE. Those flakes typically have lateral size ranging from sub-micrometer to micrometer (Coleman et al., 2011; Jawaid et al., 2016; O'Neill et al., 2012). Due to the small size, they named their sample as MoS_2 nanosheets or nanoflakes. Larger size can be obtained by controlling the centrifugation rate. O'Neill et al. showed that larger MoS_2 flake size can be selected when the centrifugation rate is smaller. At 300 rpm centrifugation rate, MoS_2 flakes, suspended in NMP solvent, with mean flake size <L> of ~ 2 μm (approximately 1.6 μm to 2.7 μm) can be obtained as shown in Figure 2.5 (O'Neill et al., 2012).

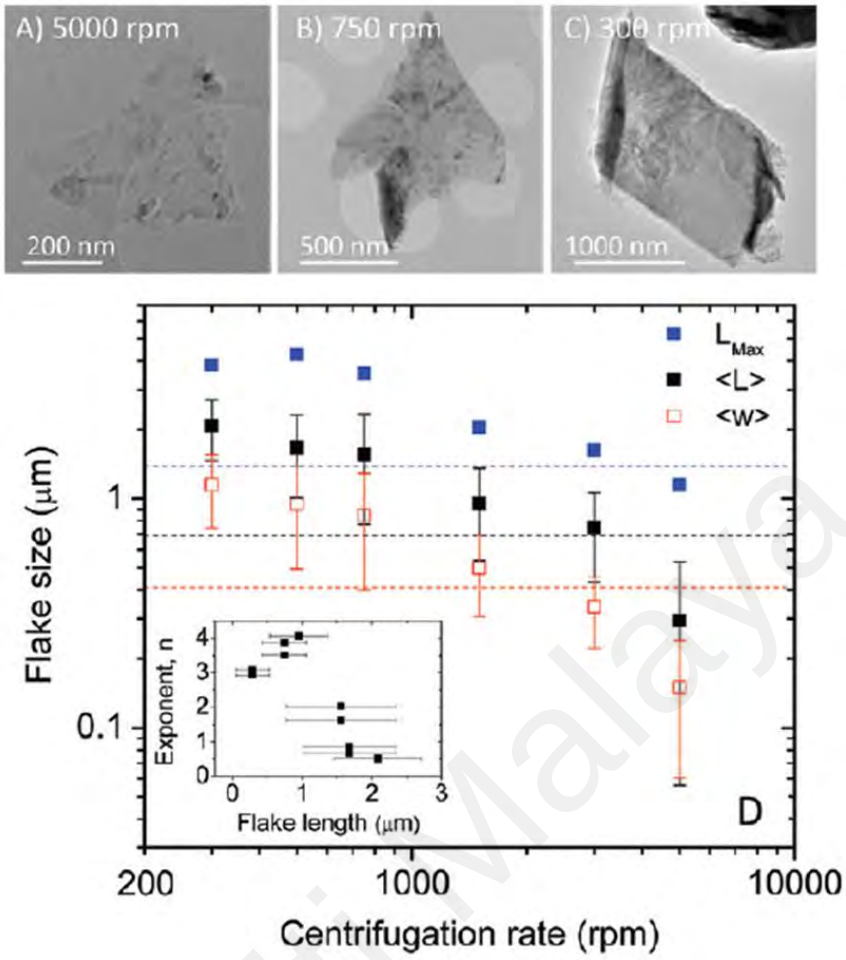

Figure 2.5: (A, B, and C) MoS_2 flakes images taken by transmission electron microscopy (TEM) with different centrifugation rates; (D) MoS_2 flake size as a function of centrifugation rate. L_{Max}, <L>, and <w> are maximum flake length, mean flake length and width respectively. Figures adapted from (O'Neill et al., 2012).

On the other hand, a thin film refers to a layer of material with a continuous, large area coverage. A large area MoS_2 thin film can be produced using CVD process (Lee et al., 2012; Zhan et al., 2012). Zhan et al. grew a MoS_2 thin film using CVD process with a size as large as 0.8 cm × 0.8 cm as shown in Figure 2.6(b) (Zhan et al., 2012). In 2019, He et al. synthesized monolayer MoS_2 thin film with an even larger area, i.e. 4.7 cm × 0.6 cm (He et al., 2019).

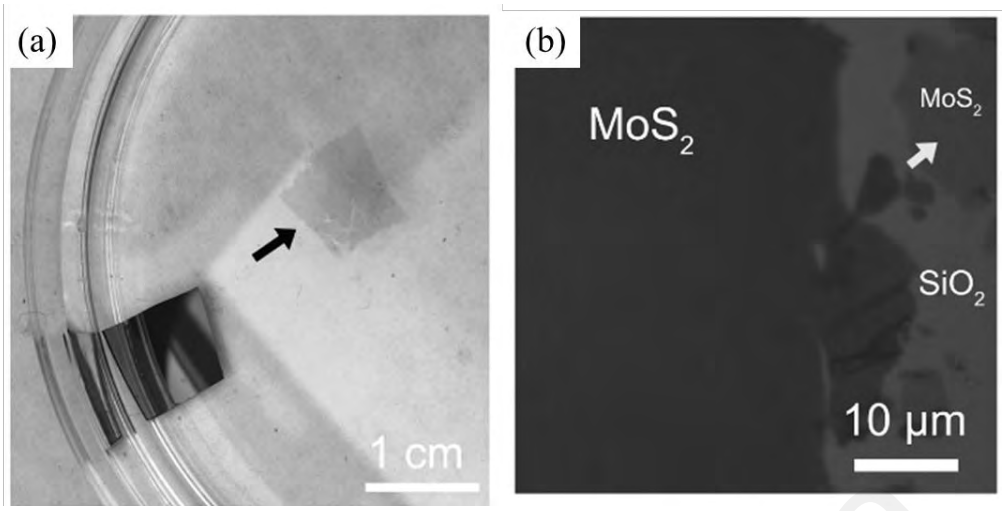

Figure 2.6: Micrographs of CVD-grown MoS_2. (a) Few-layer MoS_2 (indicated by the arrow) after peeled off from the substrate; (b) Optical micrograph of the grown MoS_2 on the SiO_2 substrate. Large, dark grey area is the few-layered MoS_2. The light grey area marked by arrow is mono- or bilayer MoS_2; The micrographs show that the MoS_2 thin film are grown is continuous, uniform and in a large area. Figures adapted from (Zhan et al., 2012).

In short, MoS_2 exists as mono- or few-layer, as well as flake or thin film form. Each form possesses different properties and can be applied for different purposes. It is important to choose the fabrication method to obtain the desired form of MoS_2. In the following section, various fabrication techniques will be discussed, alongside with their advantages and disadvantages, as well as their potential applications.

2.2 Synthesis Methods of 2D MoS_2

In the previous discussion, two preparation approaches to obtain 2D MoS_2 were introduced, i.e. the top-down exfoliation and bottom-up synthesis techniques. In this section, examples of these techniques will be discussed in detail, starting from its precursors until its final products. For top-down exfoliation technique, two common methods shall be discussed. They are the mechanical exfoliation and LPE methods. On the other hand, the bottom-up synthesis technique that will be discussed is CVD.

2.2.1 Mechanical Exfoliation

2D MoS_2 flakes can be obtained using the mechanical exfoliation or more commonly known as the "Scotch tape" technique. Mechanical exfoliation is also called micromechanical cleavage and the exfoliation processes are illustrated in Figure 2.7. The raw material required is bulk MoS_2. Using adhesive tape, part of the bulk MoS_2 will be separated out. Afterwards, a new tape can be applied on the separated MoS_2, which further separating the bulk MoS_2 into thinner MoS_2. The bulk MoS_2 can be exfoliated or tore into its thinner form in this way due to the fact that the MoS_2 layers are held together by weak van der Waals force. By repeating the tearing process, 2D monolayer or few-layer MoS_2 flakes can be obtained. The obtained 2D MoS_2 flakes can be directly transferred to a target substrate, such as a SiO_2/Si substrate, from the tape. As illustrated in Figure 2.7(c), the flakes are attached on the substrate. By slowly removing the tape from the substrate, the flakes can be transferred onto the substrate due to the van der Waals force exerted between MoS_2 and the substrate (Gupta et al., 2020).

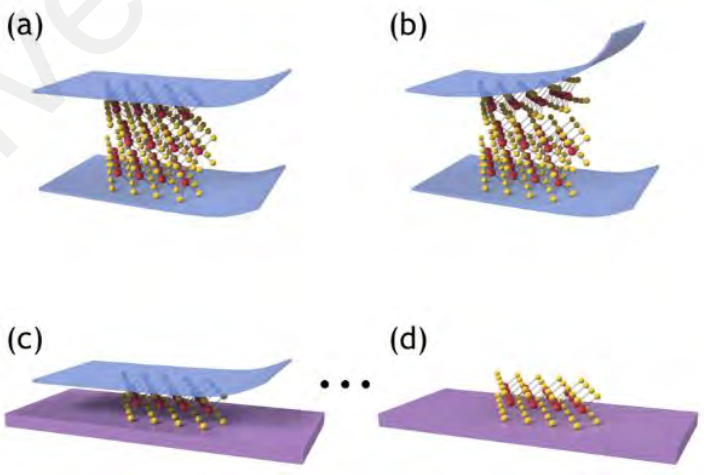

Figure 2.7: Schematic diagram of the mechanical exfoliation process: (a) bulk MoS_2 is place between two blue adhesive tapes, (b) exfoliating MoS_2 into its thinner form by tearing apart the adhesive tapes, (c) transferring the exfoliated 2D MoS_2 on the substrate, and (d) transferred 2D MoS_2 on a substrate. Figures adapted from (Tamulewicz-Szwajkowska et al., 2022).

This method is useful in obtaining pristine 2D MoS_2 with high structural quality for fundamental studies and device prototyping. However, most of the exfoliated flakes have lateral sizes of less than 10 μm. The process yield is also relatively small yield due to difficulty in term of obtaining the desired flake thickness (Magda et al., 2015; Samy et al., 2021). Besides that, the type of tape used will affect the quality of the transferred MoS_2. The common types of adhesive tape used for mechanical exfoliation of MoS_2 are Nitto SPV 224 tape (Hsu et al., 2019), Nitto 21379CR-7.50 Clear Low Tack SPV214R dicing tape, Scotch magic removable (8112PK) tape (Tamulewicz-Szwajkowska et al., 2022) and 3M Scotch transparent film tape (Rusdi et al., 2016). Among them, tape with large adhesive strength such as Scotch magic tape will cause undesired contamination and fragmentation to the 2D material. Tamulewicz-Szwajkowska et al. showed that a very sticky Scotch magic tape leaves glue contamination after transferring the sample to a substrate (Tamulewicz-Szwajkowska et al., 2022). Moreover, Budania et al. demonstrates that Scotch tape can cause fragmentation of 2D MoS_2 during the transferring process as shown in Figure 2.8, thus reducing the lateral size of the transferred flake (Budania et al., 2017). One way to avoid these two problems is by using an additional stamping process. Instead of transferring the material directly from the adhesive tape to the target substrate, the material can be transferred to a viscoelastic stamp, namely polydimethylsiloxane or PDMS stamp, first. The PDMS stamp has ~ 100 times less adhesive strength than the Scotch tape, allowing the transfer of larger surface area MoS_2 flakes to the substrate (Budania et al., 2017; Yan et al., 2016). Nevertheless, the small exfoliated flake size may limit the use of mechanically exfoliation MoS_2 layers in real life applications.

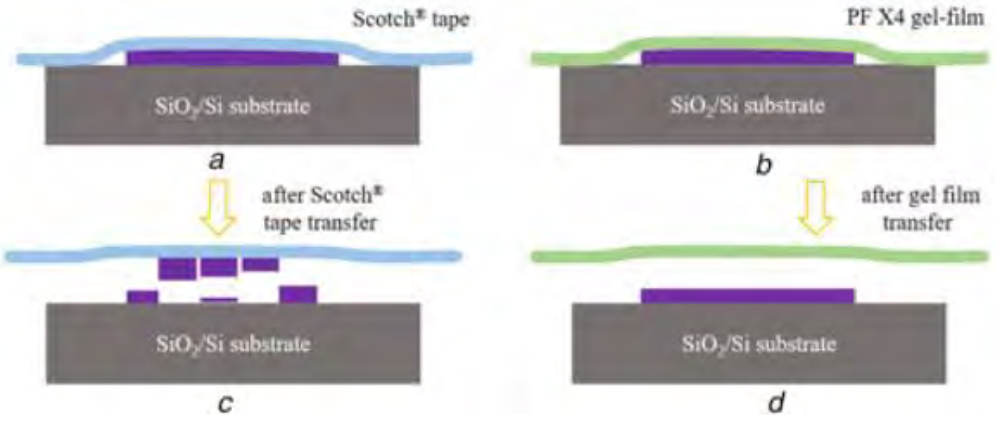

Figure 2.8: Schematic illustration of the Scotch tape and viscoelastic stamp transfer technique: (a, b) mechanical exfoliated 2D materials are brought into contact with the silicon dioxide substrate; (c) 2D material is fragmented into a few smaller flakes during the transfer process; (d) viscoelastic stamp with lower adhesive strength transfers 2D material without fragmentation. Figures adapted from (Budania et al., 2017).

2.2.2 LPE Method

LPE involves the exfoliation of bulk MoS_2 by mechanical means in the presence of solvent. The mechanical means include sonication, shearing, stirring and bubbling, as shown in Figure 2.9 (Cai et al., 2018; Coleman et al., 2011; Forsberg et al., 2016; Paton et al., 2014; Varrla et al., 2015). Although the exfoliation process is done by physical mean, LPE still involves some chemistry (Backes et al., 2017; Bodík et al., 2019; Coleman et al., 2011; Jawaid et al., 2016). Coleman et al. are considered the pioneers for this method due to their systematic studies on the LPE of 2D materials in a variety of solvents. They utilized an ultrasonic bath to realize a sonication-assisted LPE. The ultrasonic waves generate bubbles (called cavitation effect) in the solvent, and the collapse of bubbles create forces (or microjet effect) that exfoliate the bulk layered material. To achieve efficient exfoliation, it is found that the surface energy between the layered material and the solvent must be closely matched. The matching of surface energy between solute and solvent is described by the Hansen solubility parameter theory (Coleman et al., 2011). It is found that for efficient exfoliation of MoS_2, organic solvent

like NMP can be used (Coleman et al., 2011; O'Neill et al., 2012). To further increase the amount of exfoliated MoS_2, the sonication time and initial concentration of the MoS_2 dispersion can be increased as demonstrated by O'Neill et al (O'Neill et al., 2012). For example, when the initial concentration of MoS_2 is increased from 5 to 100 mg ml^{-1}, the final concentration of 2D MoS_2 is increased by a factor of 20. In addition, prolonged sonication does not cause damage or disruption in the hexagonal structure of MoS_2 (O'Neill et al., 2012). In short, this technique can be used to exfoliate MoS_2 into its 2D forms at a low-cost way compared to bottom-up synthesis technique because the former does not require sophisticated machineries to produce 2D MoS_2. It can produce relatively high quality MoS_2 nanosheets in the sense that the pristine MoS_2 structure does not change during the exfoliation process. At the same time, compared to mechanical exfoliation technique, LPE improves the yield of 2D MoS_2 greatly (Sun et al., 2017).

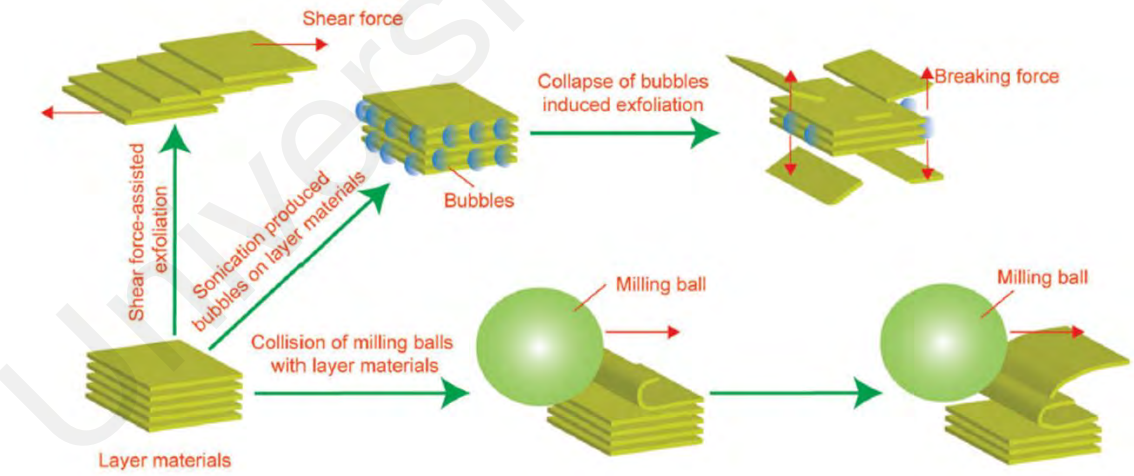

Figure 2.9: A schematic diagram of different means of LPE process, such as shear force-assisted LPE, sonication-assisted LPE and ball milling-assisted LPE. Figure adapted from (Cai et al., 2018).

However, there are disadvantages of this technique as well, i.e. (a) non user-friendly organic solutions are required as the solvent; (b) unable to produce a large amount of

monolayer MoS_2; (c) MoS_2 produced have relatively wide thickness and size distribution; (d) low reproducibility; and (e) difficulty in depositing a uniform, monolayer MoS_2 film on a substrate (Backes et al., 2017). Good solvents used in LPE usually suffer from issues such as high boiling point and toxicity. For example, NMP has a boiling point of 202 °C, which is usually undesirable for many practical applications. Nonetheless, low boiling point and easy-to-handle solvents such as water has a large surface energy which cannot disperse and exfoliate MoS_2 well. To solve this problem, additives (such as surfactants, polymers and organic molecules) can be added into water or organic solvents during LPE process (Cai et al., 2018). The additives are adsorbed by the basal planes of MoS_2 via physisorption which improve the efficiency of the exfoliation and the stability of the dispersion. The common additives used are sodium cholate, cetyltrimethylammonium bromide, protein, etc (Backes et al., 2017; Cai et al., 2018). However, the adsorbed additives are difficult to be removed completely, which have potential to affect the properties of 2D MoS_2 and the performance of MoS_2-based device. As mentioned above, LPE will produces 2D MoS_2 nanosheet dispersion with a relative wide size and thickness distribution, although there are methods to select nanosheets by size and enrich the monolayer population (Backes et al., 2014; Backes et al., 2016). Besides, the popular assembly method of MoS_2 nanosheets onto a device such as spin coating, spray coating and inkjet printing (as discussed in Chapter 1 briefly) are not able to produce a uniform, monolayer thin film. For example, spray coating often suffers from lack of precision and material wastage, as pointed out by Backes et al. (Backes et al., 2017). On the other hand, inkjet printing provides a more precise way to deposit MoS_2 on a substrate, but faces the challenge in producing a suitable ink with high concentration of 2D MoS_2. Overall, optimization of many parameters is needed to deposit 2D MoS_2 produced by LPE to obtain a high quality, large coverage area film.

2.2.3 CVD Method

CVD is one of the bottom-up synthesis methods to grow 2D MoS_2. It is attractive because it allows synthesis of 2D materials on a wafer-scale, which aids in applications like large-scale integrated electronics and photonics. Besides that, this technique can manage the defects, crystallinity and morphology of the product by controlling several synthesis parameters. Briefly, CVD involves the chemical reaction of precursors in vapour form on the substrate to produce a large-area thin film.

To prepare 2D MoS_2 using this method, several common precursors are used, namely molybdenum trioxide (MoO_3) powder (Lee et al., 2012; Pondick et al., 2018), ammonium thiomolybdate ($(NH_4)_2MoS_4$) solution (Liu et al., 2012; Shi et al., 2012) and elemental molybdenum (Laskar et al., 2013). In 2012, Lee et al. used MoO_3 and S powders as precursors to make a large-area, monolayer MoS_2 film on amorphous SiO_2 substrate. Figure 2.10(a) illustrates the experimental setup, in which MoO_3 and S powders are placed in two separate ceramic boats, side by side, in a reaction chamber. A pre-treated substrate is placed in the chamber as well. The chamber is heated in a nitrogen environment. The precursors sublime, and through chemical reaction, MoO_3 is reduced to MoS_2, forming a film on the substrate (Lee et al., 2012). Tristar-shaped MoS_2 sheets are grown on SiO_2/Si substrate as in Figure 2.10(b). Lee et al. also found that these MoS_2 sheets can be merged to become a continuous MoS_2 film with a lateral size up to 2 mm. The second common precursor used is $(NH_4)_2MoS_4$. To form MoS_2, thermolysis of $(NH_4)_2MoS_4$ in a heated reaction chamber filled with nitrogen gas can be carried out. The transformation of $(NH_4)_2MoS_4$ to MoS_2 requires a few steps by changing the thermolysis temperature. In addition, it is also suggested that the thermolysis temperature can be lowered down to ~ 425°C in the presence of H_2 gas (Liu et al., 2012). The typical reactions of this CVD process can be summarized below:

$$(NH_4)_2MoS_4 \rightarrow 2NH_3 + H_2S + MoS_3 \quad (2.1)$$

$$MoS_3 \rightarrow MoS_2 + S \quad (2.2)$$

$$(NH_4)_2MoS_4 + H_2 \rightarrow 2NH_3 + 2H_2S + MoS_2 \quad (2.3)$$

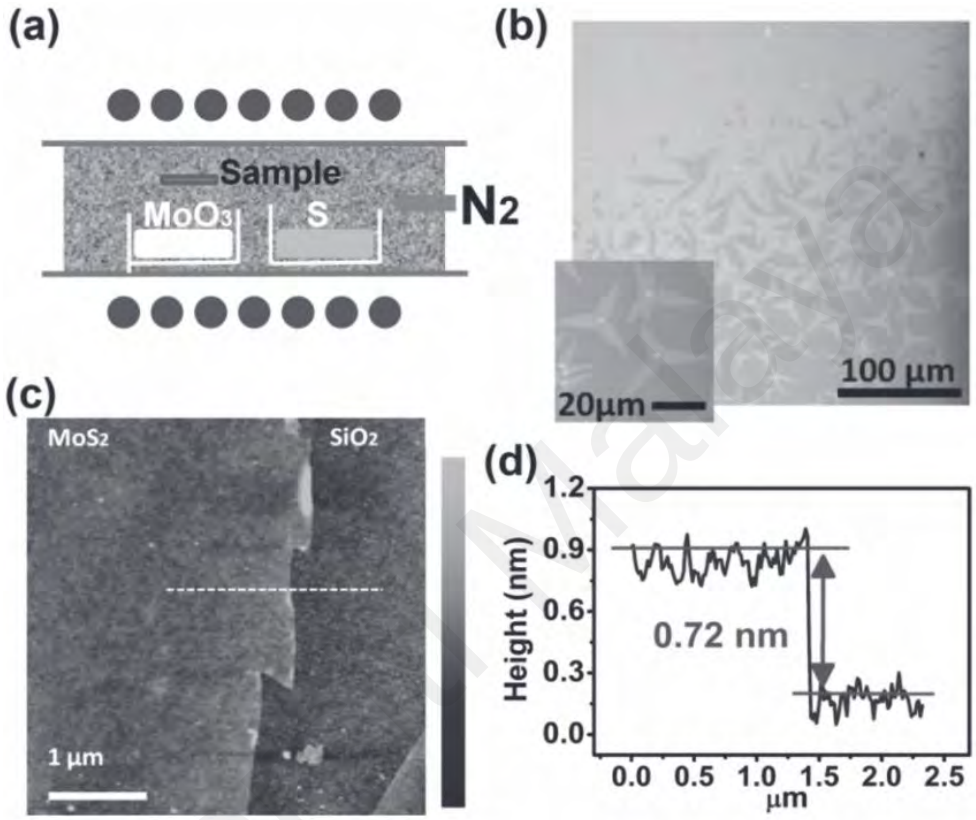

Figure 2.10: (a) Schematic illustration of the CVD experiment set up; (b) optical micrograph of the MoS_2 layer grown on the pre-treated substrate. Inset: magnified optical micrograph of the film; (c) AFM image of a monolayer MoS_2 film; (d) thickness of MoS_2 monolayer measured by AFM along the line indicated in (c). Figures adapted from (Lee et al., 2012).

Apart from fabricating a large-area, high quality continuous thin film with controlled thickness, it also allows a direct grow of 2D MoS_2 based heterostructures. In 2012, Shi et al. demonstrated the direct growth of MoS_2/graphene heterostructures using CVD (Shi et al., 2012). MoS_2 nanoflakes are grown on a graphene surface with crystal size ranging from sub-micrometers to micrometers. This is followed by the production of relatively continuous MoS_2 monolayer films on other 2D materials (McCreary et al., 2014; Samad

et al., 2016; Zhang et al., 2017). As the deposition process is carried out in an inert environment, it ensures that interfacial contamination introduced during layer-by-layer transfer process can be avoided to a large extend.

However, some drawbacks can be pointed out. If one would like to tailor atomic level properties, or control the stoichiometry and defects in MoS_2 while preserving the crystalline feature of the entire MoS_2, further optimizations are required (Krishnan et al., 2019; Wu et al., 2018). More often, the growth of large-area MoS_2 using CVD method may come from many isolated grains from different nucleation sites joint or arranged side-by-side to form uniform structures, leading to the presence of grain boundaries with different grain orientation (Yin et al., 2014). Furthermore, CVD process may produce sulphur vacancies defect in the MoS_2 thin film (Pandey et al., 2016). This may affect the quality of the produced MoS_2 film. Yet, CVD is still a widely use method in producing large area MoS_2 thin films.

To sum up this section, pristine, high crystal quality 2D MoS_2 can be obtained using the mechanical exfoliation and LPE methods. However, these techniques have disadvantages such as low controllability in terms of lateral size and thickness of the 2D MoS_2, as well as low reproducibility. Moreover, the method to assemble 2D MoS_2 on a device still remain a challenge when a uniform MoS_2 film with a desired thickness is required. These problems may be solved by using a bottom-up synthesis approach. CVD method can produce a uniform, large-area, high quality 2D MoS_2 on a wafer. It also exhibits relatively high precision in thickness control. This would allow a more predictable optical and NLO properties of MoS_2 when it comes to practical applications. Furthermore, CVD is more favourable as it is an established fabrication technique commonly used in laboratory and industry. There are a few companies which fabricate 2D MoS_2 (and other 2D material as well) using CVD method for commercial purposes. Therefore, in our studies, a CVD-grown monolayer MoS_2 thin film will be utilized. It

should be noted that the MoS_2 is usually grown on a substrate such as a Si wafer, sapphire, etc. To utilize MoS_2, transfer of the grown MoS_2 film from the growth substrate to the target substrate (or platform) such as a planarized optical waveguide is required. In the next section, various transfer techniques will be discussed, alongside with their advantages and disadvantages.

2.3 Transfer Technique

Transfer of 2D MoS_2 to a target substrate allows one to study the characteristic of the material as well as to utilize its properties in making functional devices. Transfer techniques can be classified into wet and dry transfer. Wet transfer involves water or liquid chemicals to delaminate the 2D film from the original substrate to the target, whereas dry transfer does not. There are many ways that have been suggested to transfer a 2D film, each of them having their own advantages and drawbacks as reviewed by Watson et al. (Watson et al., 2021). In addition, transfer techniques that rely on a combination of wet and dry transfer techniques have also been reported. These examples will be discussed in the following sub-section.

Most of the time, a temporary substrate or support layer is needed to transfer the 2D film from growth substrate to the target. The support layer must possess characteristics such as high mechanical strength, flexible and able to form a uniform contact with the 2D film (Watson et al., 2021). Polymers are suitable to be used as support layer as they meet these requirements. The types of polymers that have been used include polymethyl methacrylate (PMMA) (Amani et al., 2014; Lin et al., 2012), polydimethylsiloxane (PDMS) (Castellanos-Gomez et al., 2014; Choi et al., 2013; Liu et al., 2014d) and polystyrene (PS) (Gurarslan et al., 2014; Xu et al., 2015). Support layer other than polymers (such as thin metallic film) is reported as well (Lin et al., 2015).

The polymer-assisted transfer method relies on the surface energies of the polymer, the growth substrate and the target substrate. Low surface energy is akin to low adhesion force (Johnson et al., 1971). Typically, polymer has a lower surface energy than that of the target substrate. During the transfer process, the 2D film can adhere on the target substrate firmly as the surface energy of the substrate is larger. At the same time, the polymer can be removed more easily due to its lower surface energy characteristic, hence minimizing the chance of damaging the 2D film or leaving residues on the film (Watson et al., 2021). From this point of view, the choice of polymer support must be considered according to the target substrate used. A number of common transfer techniques and their issues related to film quality and uniformity will be discussed below.

2.3.1 PMMA-Assisted Transfer

The PMMA-assisted transfer is initially used to transfer mechanically exfoliated graphene flakes and CVD-grown graphene film (Dean et al., 2010; Li et al., 2009b; Liang et al., 2011). It is then been utilized to transfer CVD-grown 2D MoS_2 (Lin et al., 2012). Briefly, the process involves spin-coating a layer of PMMA polymer on the CVD-grown 2D MoS_2. After that, strong etchant such as potassium hydroxide is used to etch the SiO_2 layer, causing the detachment of PMMA/MoS_2 layer from the etched substrate (Amani et al., 2014). The PMMA/MoS_2 is then selectively transferred on the target substrate. Lastly, the PMMA is dissolved by acetone, leaving only the 2D MoS_2 on the target substrate. Such process is considered relatively expensive because the substrate is etched away and cannot be reused. To solve this problem, bubbling method can be employed, where the substrate can be reused. This method uses bubble to intercalate between the 2D film and the substrate, achieving detachment of the PMMA/2D-film (Yun et al., 2015). Yun et al. grew WS_2 film on a gold (Au) foil. The PMMA/WS_2/Au acts as a negatively charged cathode when it is immersed in sodium chloride solution. By chemical reaction, hydrogen

bubbles are generated between WS_2 film and the Au surface. The bubbles weaken the adhesion between WS_2 and Au. Eventually, the PMMA/WS_2 is detached from the Au foil and the transfer process can be carried out. Both of these transfer processes (using wet chemical etching or bubbling methods) are illustrated in Figure 2.11 below.

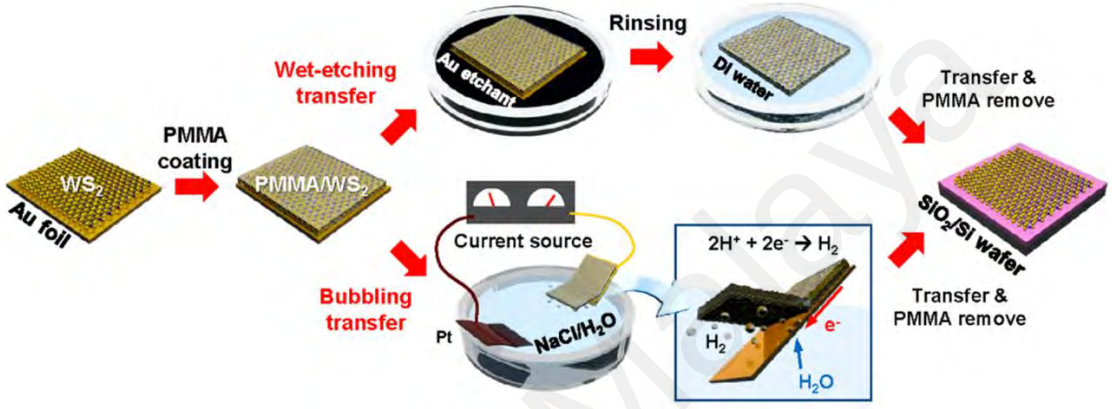

Figure 2.11: Schematic diagram of both wet chemical etching and bubbling transfer methods, assisted by PMMA polymer support, from Au foil to SiO_2/Si wafer. Figure adapted from (Yun et al., 2015).

PMMA-assisted transfer method brings about the ability to transfer large area monolayer 2D MoS_2 film between substrates. However, it should be noted that the dissolution of PMMA may leave residues on the sample surface, which is difficult if not impossible, to be completely removed (Watson et al., 2021). The etching process may degrade the quality of the 2D film. This is exemplified in the carrier mobility of CVD-grown monolayer MoS_2, in which the as-grown film shows a carrier mobility of approximately 4 $cm^2\ V^{-1}\ s^{-1}$ (Van Der Zande et al., 2013) while the transferred film gives a value of 0.8 $cm^2\ V^{-1}\ s^{-1}$ (Lin et al., 2012).

2.3.2 PDMS-Assisted Transfer

PDMS is a widely used viscoelastic polymer in transferring a 2D film. It is transparent, highly flexible, hydrophobic and has low surface energy (Vudayagiri et al., 2013), making it a very suitable polymer support. For instance, its surface energy of (~ 19 – 21 mJ m^{-2}) (Kuo, 1999) is about 3 times lower than that of the common SiO_2/Si substrate (57 mJ m^{-2}) (Zhou et al., 2018). Such low surface energy is favourable in the sense that the 2D film can be delaminated easily from PDMS. Therefore, wet chemical for etching purpose is not necessary, which could provide a cleaner transfer. However, if one wish to transfer a 2D MoS_2 film grown on SiO_2/Si substrate to another target, additional steps are needed as the low-surface-energy PDMS stamp may not be able to delaminate the film from the growth substrate. Various studies have utilized this method to transfer 2D MoS_2, but with slightly different steps (Castellanos-Gomez et al., 2014; Kang et al., 2017; Liu et al., 2014d; Paradisanos et al., 2020; Yu et al., 2017a). For example, Liu et al. used wet chemical to etch away the growth substrate, similar to PMMA-assisted transfer method (Liu et al., 2014d). On the other hand, Paradisanos et al. used deionized water droplet to lift the PDMS/MoS_2 layer from SiO_2/Si substrate before they transfer it to their target substrate. Due to the hydrophobicity of PDMS and hydrophilicity of SiO_2 surface, water can intercalate between MoS_2 and SiO_2 surface, causing delamination of PDMS/MoS_2 layer. After this layer is dried using nitrogen gun, it is then transferred to the target (Paradisanos et al., 2020). Similar work (water-assisted pick up method and PDMS-assisted transfer) is found in the work by Yu et al., as shown in Figure 2.12 (Yu et al., 2017a). This is an example of using a combination of wet and dry transfer methods, i.e. wet transfer refers to the pick-up step of 2D MoS_2 using PDMS from the growth substrate; and dry transfer refers to the transfer step of PDMS/MoS_2 to the target. In addition, the PDMS stamp can be pre-patterned first to make a patterned 2D MoS_2 on the target for the intended applications (Kang et al., 2017).

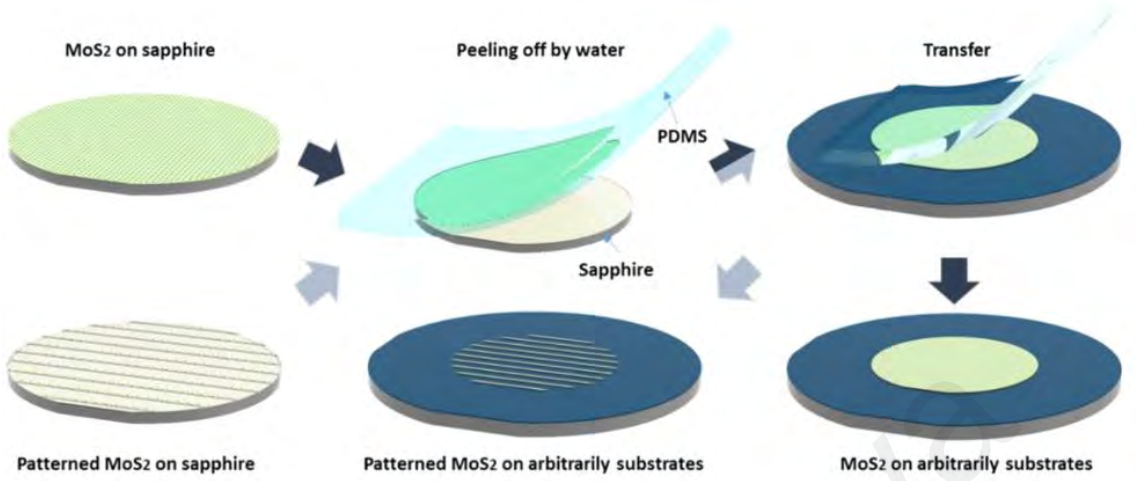

Figure 2.12: Schematic illustration of wafer-scale transfer of monolayer MoS_2 using a PDMS stamp. Figure adapted from (Yu et al., 2017a). Water is introduced to assist the picking up process of MoS_2 from the growth substrate.

This transfer method provides benefit such that wet chemical etching process to dissolve or remove the PDMS stamp is not needed. Indirectly, the transfer process becomes relatively faster compared to the PMMA-assisted transfer. Despite this advantages, it has been reported that the PDMS may contain un-crosslinked oligomers, which can be left on the surface of 2D film and causing contamination (Glasmästar et al., 2003). Additional treatment shall be done to remove such residues (Watson et al., 2021).

2.3.3 Metal-Assisted Transfer

Metal can also be used as an alternative support layer due to its large surface energy and does not leave polymer residues. An example of metal support is copper (Cu). Cu has a surface energy of 1650 mJ m^{-2} (Udin, 1951), which is about 80 times larger than that of PDMS. Lin et al. utilized a Cu and thermal release tape (TRT) assembly to transfer CVD-grown MoS_2 from a SiO_2/Si substrate to a target substrate, as shown in Figure 2.13 (Lin et al., 2015). Cu is deposited on top of the MoS_2 film. With the help of TRT, the

TRT/Cu/MoS_2 can be lifted and transferred to the target. After peeling off the TRT using thermal treatment, Cu is etched away chemically, leaving the transferred MoS_2 film on the target. Compared to PMMA which is made up of long and heavy molecular chains, the simpler structure of Cu can be more readily etched away which is confirmed by energy dispersive X-ray spectroscopy and XPS analysis (Lin et al., 2015). Although no Cu residues are left on the MoS_2 film, this transfer method will lead to cracks in the transferred film, which is due to the mechanical strain induced during the peeling process. Another drawback of this technique is that wet chemical etching is required, which could affect the MoS_2 film as discussed previously in the polymer-assisted support. The process is relatively expensive as well as metal is deposited and then removed for each transfer process.

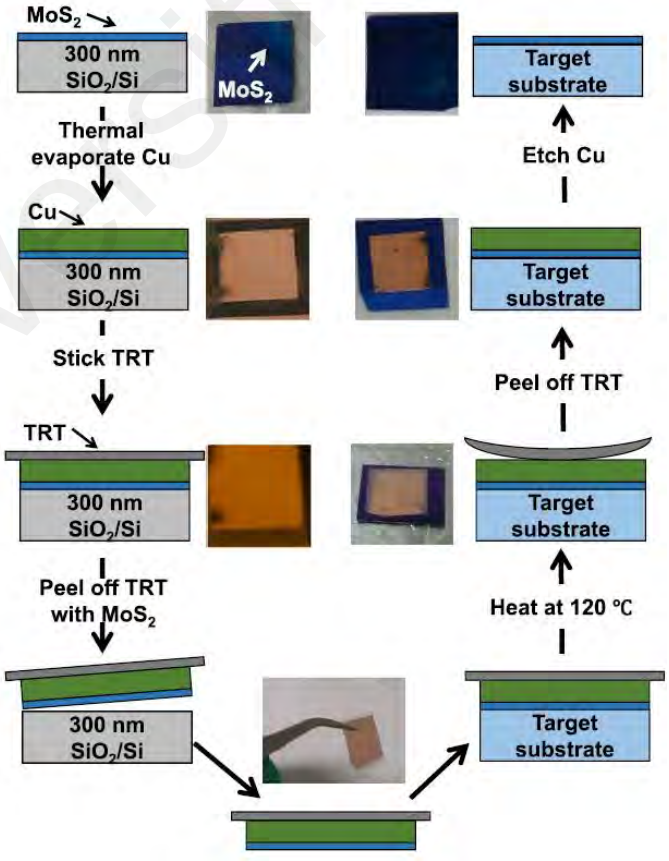

Figure 2.13: Outline of the Cu-assisted transfer process. Figure adapted from (Lin et al., 2015).

2.3.4 Possible Issues Encountered During the Transfer Process

To make use of 2D material for technological applications, it is crucial that the transferred film is of high quality to preserve its properties. One of the issues encountered that affect the film quality is polymer residues, as discussed previously. Apart from that, wrinkles, cracks and trapped bubbles that appear on the transferred film will give implications to the device performance. Depending on the application, different issues impact the device performance in different ways. For instance, the electron mobility of the 2D material can be affected by wrinkles, cracks or polymer residue (Lin et al., 2012; Liu et al., 2019). In optical application, polymer residue has less influence on the PL signal of monolayer WS_2, but adsorbed etchant molecules (such as potassium hydroxide) reduce the PL signal greatly (Wang et al., 2019b). Therefore, polymer contamination can be ignored for optical application (Watson et al., 2021). Nevertheless, these issues or defects should be minimized to ensure a more predictable device performance. The cause of these defects and possible solutions will be discussed briefly as below.

2.3.4.1 Wrinkles

The presence of wrinkles in 2D films are common and unavoidable to some extent (Watson et al., 2021). They are formed during the fabrication and transfer process. For example, etchant may cause new wrinkles via capillary forces. Yun et al. showed that the bubbling method to detach PMMA/WS_2 from Au foil could lead to wrinkles formation, as shown in Figure 2.14(a) (Yun et al., 2015). Besides that, in Figure 2.14(b), wrinkles are observed as well when transferring PMMA/MoS_2 to SiO_2/Si through wet-etching method (Shi et al., 2015). The wrinkles reduce the direct contact area of the 2D film with the surface of the substrate, and their removal could be challenging.

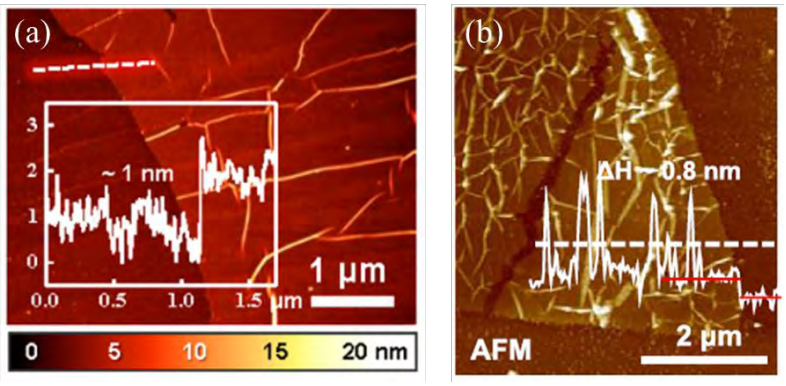

Figure 2.14: AFM image of (a) the transferred WS_2 thin film by bubbling method, figure adapted from (Yun et al., 2015); (b) the transferred MoS_2 thin film by PMMA-assisted wet etching method, figure adapted from (Shi et al., 2015).

2.3.4.2 Bubbles

Aside from wrinkles, the occurrence of bubbles is another issue during the transferring process. When the 2D film is placed onto the target substrate, contaminants and bubbles are prone to be trapped at the interface between the film and the substrate. Bubbles can be observed as trapped solvent and trapped air pockets during wet transferring and dry transferring, respectively. It is believed that if the adhesion energy between the 2D film and the target substrate is large, the contact between two materials will be stronger. This can cause a "pushing effect", in which the contaminants tend to aggregate into bigger bubbles, which is exemplified in Figure 2.15 (Watson et al., 2021). In Figure 2.15, the AFM images of graphene coated on different substrates are shown. For substrates such as h-BN, MoS_2 and WS_2 that have good adhesion with graphene layer, the contaminants are observed to clump into bigger bubbles. On the other hand, substrates such as mica, bismuth strontium calcium copper oxide (BSCCO) and vanadium pentoxide (V_2O_5) that have poor adhesion to graphene show bubble contaminations spreading across the entire interface (Kretinin et al., 2014).

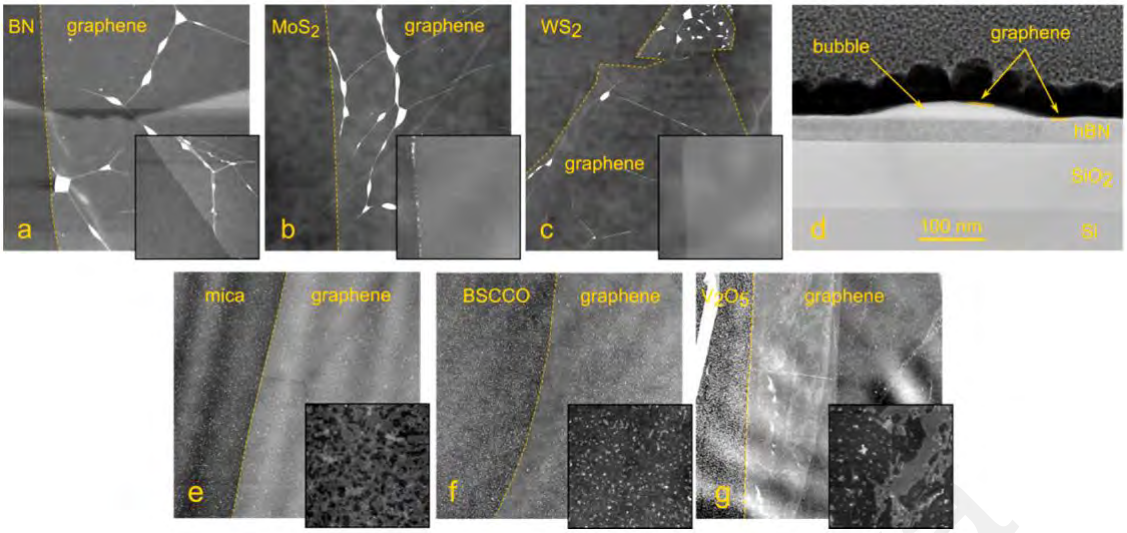

Figure 2.15: AFM topology of graphene on various substrates: (a) hBN; (b) MoS_2; (c) WS_2; (e) mica; (f) BSCCO; (g) V_2O_5. (d) TEM cross sectional image of the graphene/hBN structure, depicting the presence of bubble between the interface. Figures adapted from (Kretinin et al., 2014).

Similar to graphene, bubbles can be introduced during the transfer of MoS_2 film to the target substrate. Hong et al. showed the difference between transferred monolayer MoS_2 onto highly oriented pyrolytic graphite (HOPG) by water-assisted method and by all-dry method using a TRT (Hong et al., 2018). From the scanning electron microscopy (SEM) images in Figure 2.16, it is clear that large bubbles appear on the MoS_2–HOPG interface. The author claimed that the bubbles originate from trapped air pocket and water during the all-dry TRT-assisted and water-assisted transferring process, respectively. The frequency of trapped air pocket is lesser than the trapped water for each employed method. This shows that bubbles are unavoidable in both wet and dry transfer method. Fortunately, the trapped water can be reduced by subjecting the sample to ultrahigh vacuum annealing (Hong et al., 2018). Moreover, the trapped air can be removed, theoretically, by controlling the angle and merging time of the 2D material film and target substrate. With angle other than normal incidence and a longer merging time, bubbles have a higher possibility to escape from between the interface, forming a better contact between 2D material and the substrate (Watson et al., 2021).

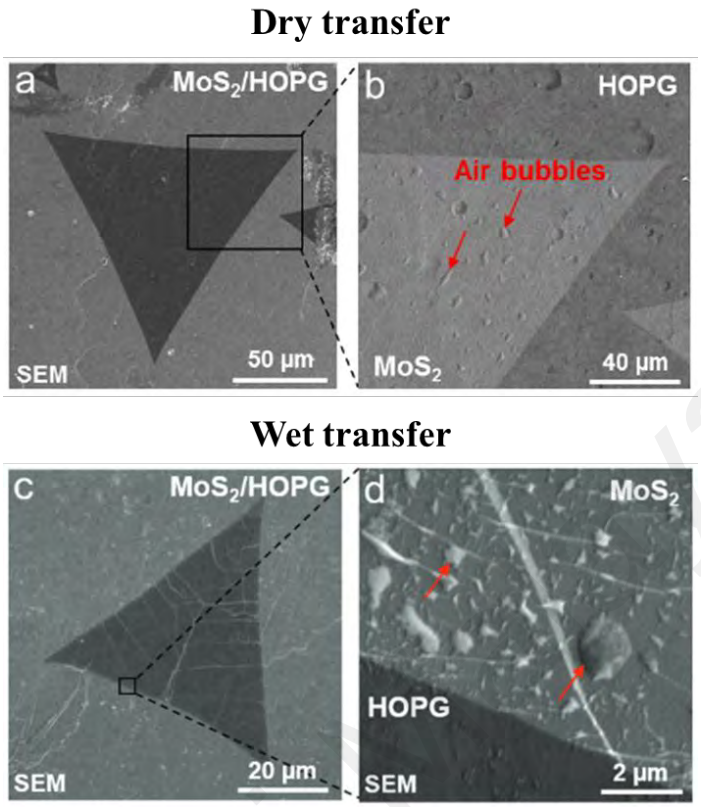

Figure 2.16: SEM images of transferred MoS_2 flake on HOPG using (a, b) all-dry TRT-assisted method; and (c, d) water-assisted wet transfer method. Figures adapted from (Hong et al., 2018).

To sum up this section, the widely use method to transfer 2D film between growth and target substrates is the polymer-assisted transfer method, using either PMMA or PDMS as intermediate support layer. PMMA-assisted transfer usually involves wet etching process to remove the growth substrate as well as the PMMA support layer. These steps may impose issues such as wrinkling, bubbling, contaminants or residues and substrate wastage. On the other hand, PDMS-assisted transfer avoids wet etching process, thereby eliminating most of the issues such as contaminants and substrate wastage, although wrinkling and bubbling may still exist. Apart from that, this method is more straight-forward and time-saving for the whole transfer process. Considering these advantages, PDMS-assisted transfer stands out among other polymer candidates, and is a suitable

approach for prototyping and experimental research purposes. In our applications, selective area transfer of 2D MoS_2 film on a planarized optical waveguide can be made as well using this method, without damaging or contaminating the planarized optical waveguide as in PMMA-assisted transfer. Therefore, the PDMS-assisted transfer technique will be employed in this study.

2.4 Optical Properties of 2D MoS_2

It is important to study the optical properties of 2D MoS_2 before transferring it to a target either for scientific study or device fabrication. In Chapter 2.1.2, it has been discussed that the PL of 2D MoS_2 is layer dependent. This is a direct indication that the optical properties of 2D MoS_2 is layer dependent. Various techniques (besides PL) have been used to study its optical properties, for instance, optical contrast (Li et al., 2012a; Li et al., 2014a; Li et al., 2016b), UV-vis spectroscopy (Castellanos-Gomez et al., 2016; Eda et al., 2011; Islam et al., 2021), Raman spectroscopy (Li et al., 2012b; Li et al., 2012c; Zhang et al., 2015), and harmonic generation (Balla et al., 2018; Säynätjoki et al., 2017; Woodward et al., 2016). These studies provide fundamental information on the optical properties of 2D MoS_2, which can be used to determine the layer-number and for the development of optoelectronic and photonic devices (Li et al., 2017b). Here, the optical properties of 2D MoS_2 will be discussed. The effect of number of layers on its optical properties determined based on different techniques will also be discussed.

2.4.1 Optical Absorption of 2D MoS_2

The optical absorption of 2D MoS_2 is usually measured using a UV-vis or UV-vis-NIR spectroscopy. This spectroscopy technique is able to measure the optical absorption of 2D MoS_2 from ultraviolet (UV) to near-infrared (NIR) wavelength range. The

appearance of bulk MoS_2 (dark grey) and 2D MoS_2 (green) indicates that there is a number of layer (or thickness) dependency on the optical absorption of MoS_2 (O'Neill et al., 2012). In 2011, Eda et al. studies the UV-vis absorption of chemically exfoliated 2D MoS_2 film with different thickness (Eda et al., 2011). Figure 2.17(a) shows a typical absorption spectrum of 2D MoS_2 in the visible wavelength range. Two absorption peaks can be observed at ~ 605 nm and ~ 660 nm, which correspond to absorption due to the B and A excitons of 2D MoS_2, respectively. Besides that, from Figure 2.17(a), it is found that the A exciton peak experiences red-shifts as the thickness of 2D MoS_2 increases. In 2016, a spatially resolved optical absorption spectroscopy of 2D MoS_2 was carried out to better show the red-shift of A exciton peaks with the number of layers (Castellanos-Gomez et al., 2016). On top of the discovery by Eda et al., Andres Castellanos-Gomez et al. observed that the C exciton peak (~ 440 nm) also experience red-shifts as the number of layer increases from 1 to 6, as illustrated in Figure 2.17(b). The shifting in A and C excitons absorption peaks provide a way for us to estimate the number of layers of 2D MoS_2 using a relatively quick, non-destructive optical method compared to atomic force microscopy (AFM). Similar results have been obtained from the UV-vis-NIR spectroscopy studies of CVD-grown 2D MoS_2 (Islam et al., 2021). Apart from obtaining the optical absorption spectra of 2D MoS_2, they also calculate the percentage of light absorption of MoS_2 with different thickness (monolayer: 0.61 nm; few-layer: 2.15 nm; and bulk: 33.5 nm). The monolayer, few-layer and bulk MoS_2 absorb 7.4%, 12.6% and 32.4% of incident light, respectively, between the wavelength range of 300 to 700 nm. After normalization of the absorption with thickness, the monolayer, few-layer and bulk MoS_2 absorbs 12.1% nm^{-1}, 5.9% nm^{-1} and 1.1% nm^{-1}, respectively. This shows that the absorption of monolayer MoS_2 is relatively high (12.1% nm^{-1}) even though it has only one-atomic layer thickness of less than 1 nm. The information of optical absorption spectrum is essential for designing a device utilizing 2D MoS_2 coating. For example, if

MoS_2 layer is used to limit the absorption within a specific spectral bandwidth, it will be useful in developing photodetectors. On the other hand, if MoS_2 layer is used to enhance broadband absorption, then it will be useful in making photovoltaic solar cells (Islam et al., 2021).

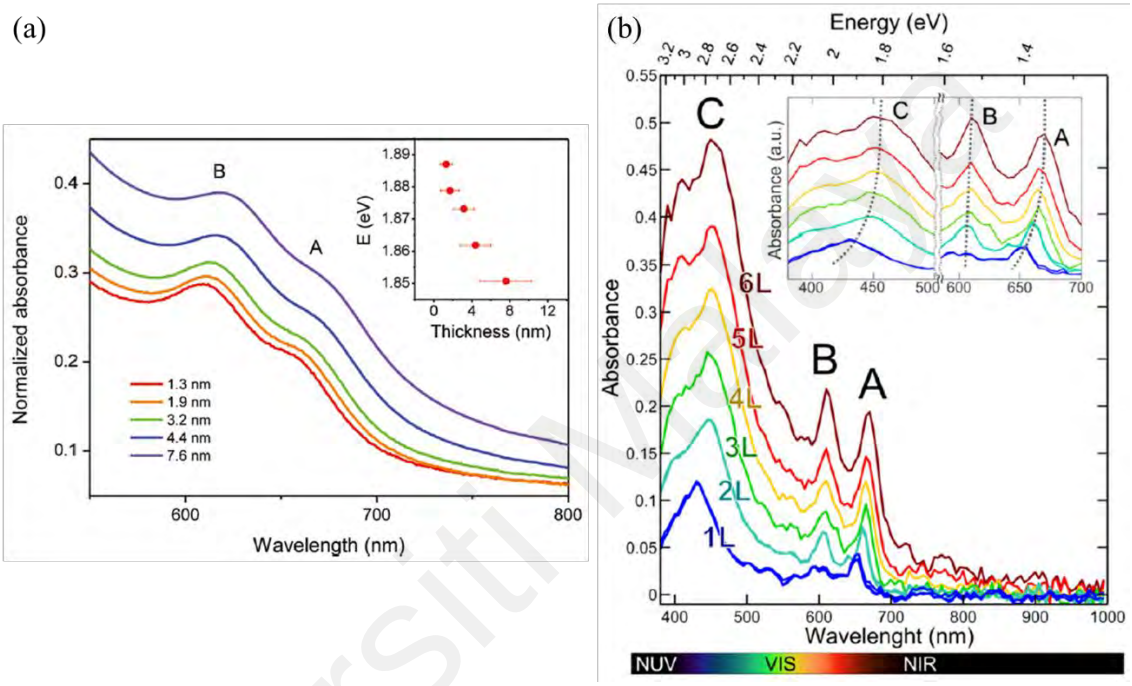

Figure 2.17: Optical absorption of (a) chemically exfoliated MoS_2 at different thickness, figure adapted from (Eda et al., 2011); and (b) pristine mechanical exfoliated MoS_2 at different number of layers, figure adapted from (Castellanos-Gomez et al., 2016). Both of the studies show that the increasing number of layers of MoS_2 cause the red-shifts of A exciton peak, which is useful for the estimation of number of layers of MoS_2 using this technique.

2.4.2 Refractive Index of 2D MoS_2

The complex refractive index, $\tilde{n}$, of a material is the most fundamental property that describe the interaction between light and the material. It is defined as follow:

$$\tilde{n} = n + ik \tag{2.4}$$

where n and k are the refractive index and extinction coefficient of the material, respectively. The real part in Equation (2.4) is responsible in modifying the optical phase

of light passing through the medium; while the imaginary part affects the amplitude of optical excitation in a medium (Yu et al., 2017b). Many studies have been reported measuring the $\tilde{n}$ of 2D and bulk MoS_2 (Ermolaev et al., 2020; Hsu et al., 2019; Islam et al., 2021; Li et al., 2017a; Li et al., 2014d; Liu et al., 2014a; Shen et al., 2013). Li et al. determines the $\tilde{n}$ of monolayer MoS_2 from reflection spectra using Kramers-Kronig analysis (Li et al., 2014d). In the same year, Liu et al. measures the $\tilde{n}$ of monolayer MoS_2 using spectroscopic ellipsometry at a single angle of incidence (Liu et al., 2014a). In the later year, it is found that the value of $\tilde{n}$ is different for different thickness of 2D MoS_2 (Hsu et al., 2019; Li et al., 2017a). These studies show, again, that the optical properties of 2D MoS_2 are layer-dependent. Therefore, the value $\tilde{n}$ of 2D MoS_2 with certain thickness at specific wavelength must be identified carefully. Li et al. reports the $\tilde{n}$ value of few-layer and multilayer MoS_2 over a broadband of wavelength range, from 1.2 eV to 6 eV (Li et al., 2017a). However, the $\tilde{n}$ of monolayer MoS_2 is not reported in their study. Hsu et al. reports the $\tilde{n}$ of mono-, bi- and tri-layer of MoS_2, but with a relatively limited wavelength range, i.e. from 400 nm to 800 nm (Hsu et al., 2019).

In recent years, the $\tilde{n}$ of monolayer, few-layer and bulk MoS_2 over the UV to NIR wavelength range have been determined using variable angle spectroscopic ellipsometry technique (Ermolaev et al., 2020; Islam et al., 2021). This method is said to have a great potential in the study of the refractive index of 2D films due to its higher sensitivity to small thickness change (Islam et al., 2021). Figure 2.18 illustrates the n and k of monolayer, few-layer and bulk MoS_2 over the wavelength range from 190 nm to 1700 nm. It is obvious that the change of n and k of MoS_2 at UV and visible wavelength range are large compared to that in the NIR wavelength range. In Figure 2.18(b), two peaks with large k at 604 nm and 650 nm can be found, which correspond to the B and A excitons of MoS_2. Furthermore, the absolute value of n and k of the three thicknesses of MoS_2 differ from each other as well. For example, at the common visible light wavelength

of 532 nm, the $\tilde{n}$ of monolayer and bulk MoS_2 are $(3.521 + 0.621i)$ and $(3.689 + 0.607i)$, respectively. At the wavelength of interest (1550 nm), the monolayer and bulk MoS_2 exhibit $\tilde{n}$ of $(2.932 + 0i)$ and $(3.029 + 0.036i)$, respectively (Islam et al., 2021). It can be seen that monolayer MoS_2 has negligible absorption and a relatively large refractive index at 1550 nm. This makes it an ideal material in developing low loss photonics devices that operate in the NIR wavelength range, especially in the telecommunication wavelength range of 1550 nm (Ermolaev et al., 2020).

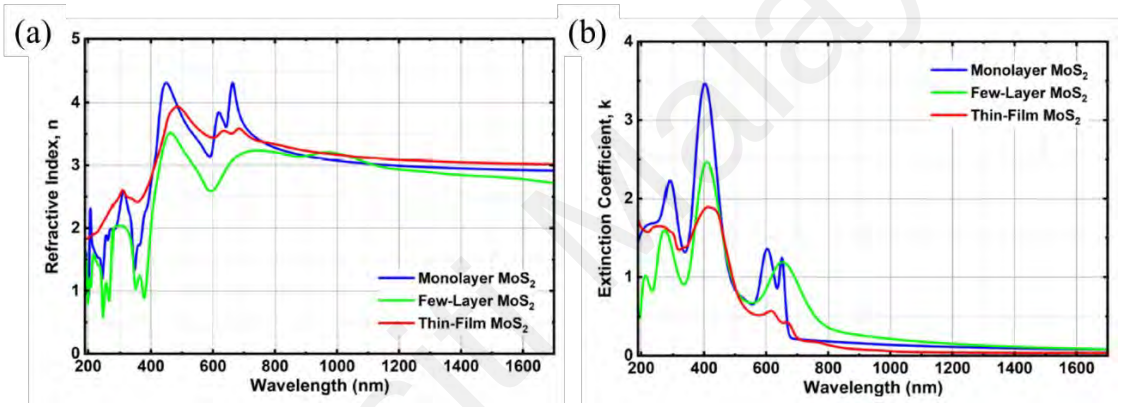

Figure 2.18: Values of (a) n and (b) k for monolayer, few-layer and thin-film (bulk) MoS_2 from 190 nm to 1700 nm. Figures adapted from (Islam et al., 2021).

2.4.3 Raman Spectroscopy of 2D MoS_2

Raman spectroscopy is a non-destructive technique that relies on the inelastic (or Raman) scattering of photons from a material when it is illuminated with a high intensity laser source. It has been used to study the quality and crystalline structures of MoS_2 (Li et al., 2012b). In bulk MoS_2, the Raman active modes are assigned as E_{1g} (286 cm^{-1}), E_{2g} (383 cm^{-1}) and A_{1g} (408 cm^{-1}). The E_{1g} mode is said to be forbidden in back-scattering experiment on a basal plane. The E_{2g} mode is an in-plane mode that arises from opposing vibration of two S atoms with respect to the Mo atom. The A_{1g} mode involves the out-of-plane vibration mode of S atoms in opposite directions. A good illustration regarding

these modes can be found in the reports by Lee et al. and Zhang et al. (Lee et al., 2010; Zhang et al., 2015).

2.4.3.1 Effect of Number of Layers on Raman Modes

Among the Raman active modes, the E_{2g} and A_{1g} modes are found useful in determining the number of layers of 2D MoS_2 on a substrate. In early 2010, Lee et al. found that these Raman modes experience shifts when the number of layers increases from monolayer to bulk (Lee et al., 2010). Particularly, the in-plane E_{2g} and the out-of-plane A_{1g} modes experience red and blue shifts, respectively, with increasing number of layers (Figure 2.19). Their work demonstrated the possibility to determine the number of layers of 2D MoS_2 based on the peak frequencies of E_{2g} and A_{1g}. It is easier to identify the number of layers using their difference in frequencies, that is, the frequency spacing between the A_{1g} and E_{2g} modes. From Figure 2.19, it can be seen that the peak difference is more significant for number of layers that is less than four. When the number of layers is more than five, these modes converge to values similar to bulk MoS_2. As the number of layers increases, the atomic vibration is suppressed due to the increasing interlayer Van der Waals force of MoS_2, causing A_{1g} mode to stiffen and experiences blue shift. On the other hand, it is believed that the red shift in E_{2g} mode arises from induced structural changes or long-range Coulombic interlayer interactions in bulk MoS_2 (Li et al., 2012b; Li et al., 2012c).

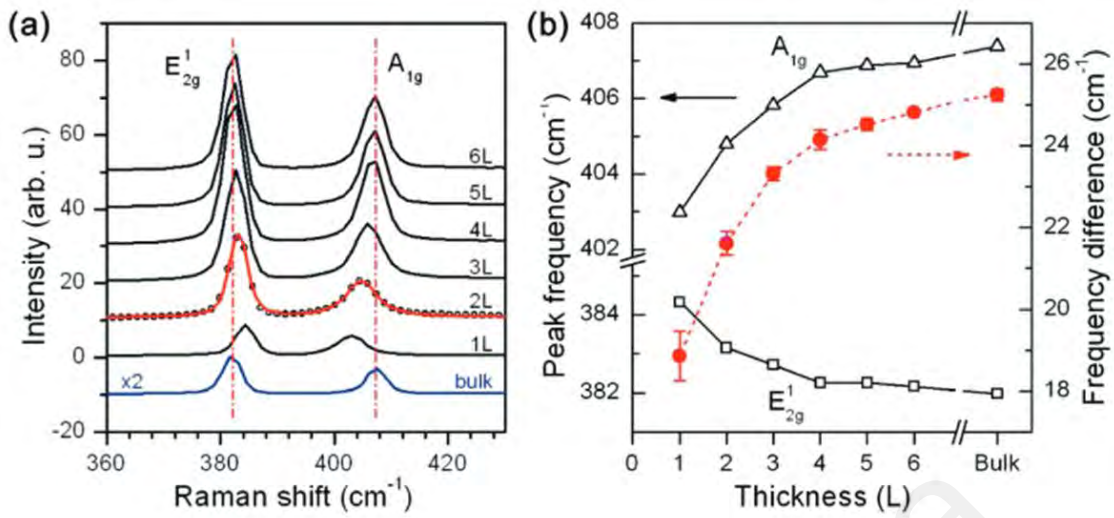

Figure 2.19: (a) Raman spectra of MoS_2 with different number of layers; (b) Frequencies of E_{2g} and A_{1g} modes (left y-axis) and their difference (right y-axis) as a function of number of layers of MoS_2. Figures adapted from (Lee et al., 2010).

2.4.3.2 Effect of Wavelength of Excitation Source on Raman Modes

Years later, more quantitative studies have been carried out on the evolution of Raman scattering of MoS_2 from monolayer to its bulk forms. Conditions such as excitation wavelength of the laser, fabrication technique and deposition substrate may affect the frequency of Raman modes. Li et al. shows that the frequency of Raman modes varies with the wavelength of excitation laser used (Li et al., 2012b). In other word, the peaks of E_{2g} and A_{1g} will have different values depending on the wavelength of the excitation laser. For example, when 532 nm (632.8 nm) laser is used, the values of E_{2g} and A_{1g} of monolayer MoS_2 are 384.7 cm^{-1} (385 cm^{-1}) and 402.7 cm^{-1} (403.8 cm^{-1}), respectively (Li et al., 2012b). Therefore, attention must be given to the analysis of Raman shifts based on the excitation wavelength. Li et al. also reported that five common laser wavelengths can be used, namely 325 nm, 488 nm, 514.5 nm, 532 nm and 632.8 nm, thus providing more flexibility in studying the Raman shifts of 2D MoS_2.

2.4.3.3 Effect of Fabrication Technique on Raman Modes

Besides that, the fabrication technique will affect the frequency of Raman modes as well. In the discussion above, the 2D MoS_2 studied comes from the mechanical exfoliated pristine MoS_2. Consider mechanical exfoliated monolayer MoS_2 as an example, the difference in E_{2g} and A_{1g} modes gives a frequency of ~ 18 cm^{-1} (Lee et al., 2010; Li et al., 2012b; Li et al., 2012c). However, for a CVD-grown monolayer MoS_2, the peak difference yields a value of ~ 20 cm^{-1} (Kumar et al., 2018; Mohapatra et al., 2016; Park et al., 2014a). It should be noted that the peak difference of the Raman modes of a CVD-grown bilayer MoS_2 is ~ 22 cm^{-1}, so the number of layers determination using Raman spectroscopy is still useful for CVD-grown 2D MoS_2.

2.4.3.4 Effect of Substrate on Raman Modes

In addition, the deposition substrate affects the Raman modes as well. Castellanos-Gomez and his co-workers found that the choice of substrate changes the frequency of Raman modes, especially the E_{2g} modes of monolayer MoS_2 (Buscema et al., 2014). Different common dielectric substrates such as SiO_2, PDMS-derivative film, h-BN and mica, as well as conducting substrates like Au and few-layer graphene have been chosen as their substrate candidates. With different substrate, the shift in A_{1g} and E_{2g} modes are more pronounce for monolayer MoS_2, as shown in Figure 2.20. Despite that, determination of number of layers less than four is still possible due to the significant change in peak difference between E_{2g} and A_{1g}.

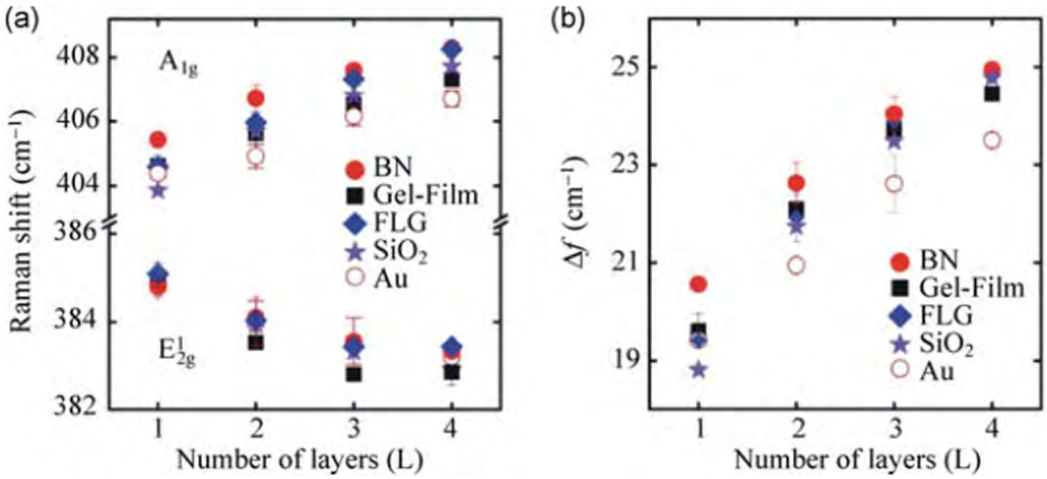

Figure 2.20: (a) Frequency of A_{1g} and E_{2g} Raman modes, and (b) frequency difference between A_{1g} and E_{2g} modes of 2D MoS_2 at different number of layers for different substrates. Figures adapted from (Buscema et al., 2014).

In short, 2D MoS_2 shows Raman scattering under high intensity laser irradiation. The presence of Raman modes such as A_{1g} and E_{2g} modes act as a fingerprint for itself and, most interestingly, it is number of layer dependent. The information of frequency of both A_{1g} and E_{2g} modes allow us to determine the number of layers of MoS_2 in a relatively easy and non-destructive way. However, care must be taken as several factors may affect the shifts in those Raman modes, namely the excitation laser wavelength, fabrication technique as well as the substrate choice. With careful consideration, the number of layers of MoS_2 can be determined without the characterization using AFM. This technique will be used as well in this works in determining the number of layers of MoS_2.

2.4.4 Nonlinear Refractive Index of 2D MoS_2

2.4.4.1 Nonlinear Refractive Index: A Brief Introduction

The nonlinear refractive index, often represented with the symbol n_2, of a material is present when the material interacts with an intense laser source. In this sense, the refractive index of a material, n, is expressed in this form of:

$$n = n_0 + n_2 I \tag{2.5}$$

where n_0 is the refractive index of a material under weak light, and I is the intensity of the optical field (or laser). This makes the refractive index of a material dependent to the intensity of the laser. As the intensity of the laser increases, the n changes due to the contribution of the $n_2 I$ term. The n_2 is related to the third order nonlinear susceptibility, $\chi^{(3)}$, of a material. $\chi^{(3)}$ is one of the parameters used to describe the dipole moment per unit volume, or polarization $\tilde{P}(t)$, of a material that depends on the strength of applied optical field, $\tilde{E}(t)$ (Boyd, 2008). In conventional (or linear) optics, the induced polarization depends linearly on the $\tilde{E}(t)$ by:

$$\tilde{P}(t) = \epsilon_0 \chi^{(1)} \tilde{E}(t) \tag{2.6}$$

where ϵ_0 is the permittivity of free space and $\chi^{(1)}$ is the linear susceptibility of a material. In NLO, the $\tilde{P}(t)$ is expressed in the form of:

$$\tilde{P}(t) = \epsilon_0 \left[\chi^{(1)} \tilde{E}(t) + \chi^{(2)} \tilde{E}^2(t) + \chi^{(3)} \tilde{E}^3(t) + \cdots \right] \tag{2.7}$$

$$\tilde{P}(t) \equiv \tilde{P}^1(t) + \tilde{P}^2(t) + \tilde{P}^3(t) + \cdots \tag{2.8}$$

where $\chi^{(2)}$ and $\chi^{(3)}$ are the second and third order susceptibilities, respectively. $\tilde{P}^2(t) = \epsilon_0 \chi^{(2)} \tilde{E}^2(t)$ is the second order nonlinear polarization and $\tilde{P}^3(t) = \epsilon_0 \chi^{(3)} \tilde{E}^3(t)$ is the third order nonlinear polarization. In Equation 2.6 and 2.7, $\tilde{P}(t)$ and $\tilde{E}(t)$ are considered to be scalar quantities for simplicity. The polarization plays an important role to describe the NLO process. The conditions to excite the effect of $\tilde{P}^2(t)$ and $\tilde{P}^3(t)$ are different. The second order NLO interaction can only occur in non-centrosymmetric crystals, whereas the third order NLO interaction can occur in both centrosymmetric and non-centrosymmetric media. Common materials such as amorphous solids, liquids, gases, and some crystals are centrosymmetric, so the effect of $\chi^{(2)}$ vanishes and second order NLO interactions will not occur. On the other hand, 2D MoS_2 shows a unique characteristic in such a way that its number of layers affects its centrosymmetric property. MoS_2 with odd

number of layers is non-centrosymmetric, while its even number of layers is centrosymmetric (Kumar et al., 2013; Li et al., 2013; Säynätjoki et al., 2017).

The n_2 is related to the third order NLO process contributed by the $\tilde{P}^3(t)$. In the simplest case, when a monochromatic laser, $\tilde{E}(t) = \mathcal{E}\cos\omega t$, is incident upon a material, and using the identity $\cos^3\omega t = \frac{1}{4}\cos 3\omega t + \frac{3}{4}\cos\omega t$, the nonlinear polarization $\tilde{P}^3(t)$ can be expressed as

$$\tilde{P}^3(t) = \frac{1}{4}\epsilon_0\chi^{(3)}\mathcal{E}^3\cos 3\omega t + \frac{3}{4}\epsilon_0\chi^{(3)}\mathcal{E}^3\cos\omega t \tag{2.9}$$

The first term in Equation (2.9) describes a third order response in which a photon at frequency 3ω is created by a laser operating at frequency ω. This process is called third-harmonic generation (THG), see Figure 2.21. This process allows conversion of long wavelength to a shorter wavelength, which is essential in producing laser source in the UV wavelength range. On the other hand, the second term in Equation (2.9) describes the nonlinear change of polarization at frequency ω of the applied laser. This term leads to the nonlinear change of refractive index which can be represented as in Equation (2.5). The n_2 in Equation (2.5) can be written, in term of $\chi^{(3)}$, as

$$n_2 = \frac{3}{2n_0^2\epsilon_0 c}\chi^{(3)} \tag{2.10}$$

where c is the speed of light in free space. The n_2 can be considered as an optical parameter that characterizes the strength of the optical nonlinearity (Boyd, 2008).

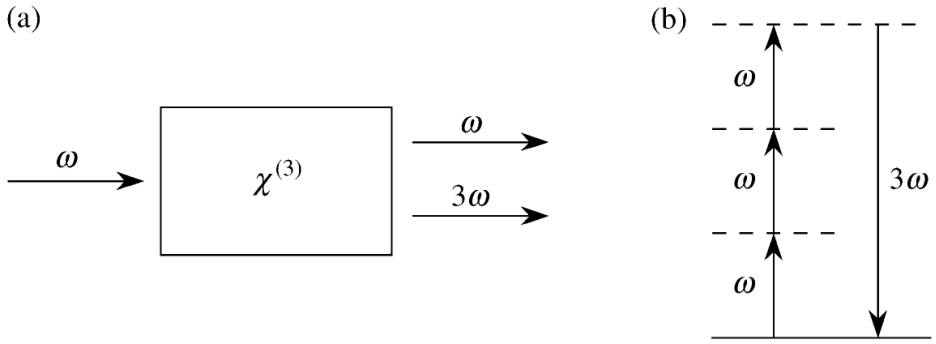

Figure 2.21: (a) Illustration of a THG process involving the interaction of a $\chi^{(3)}$ medium and an applied field at frequency ω; (b) Energy-level description of a THG process. Figures adapted from (Boyd, 2008).

2.4.4.2 Methods Used to Measure Nonlinear Refractive Index of a Material

Since n_2 and $\chi^{(3)}$ are related, the value of n_2 can be determined by several methods, either based on the effect of new frequency (or wavelength) generation, or based on the change of refractive index, as per the first and second term in Equation (2.9), respectively. The former involves the processes such as THG and four-wave mixing (FWM). Through these processes, new wavelength(s) of light is generated from the material. By measuring the output power of the new wavelength, the $\chi^{(3)}$ or n_2 of the material can be determined. On the other hand, the latter involves the processes such as self-phase modulation (SPM) and nonlinear refraction (NLR). In general, these processes originate from the change of refractive index of the material as a result of its interaction with the high intensity of the applied laser. The $\chi^{(3)}$ or n_2 can be evaluated from the magnitude of change of the transmitted beam profile. These processes are considered as a parametric process, which means that the initial and final quantum-mechanical states of the system do not change and remain the same. The transition of electron between the ground state and virtual state occurs only for a short interval of time (Figure 2.21). Electron can occupy the virtual level for a period of $\hbar/\delta E$ based on the uncertainty principle, where $\hbar = h/2\pi$, h is the Planck's constant and δE is the energy difference between the ground state and virtual

state (Boyd, 2008). Among these four processes mentioned above, the evaluation of n_2 based on SPM and NLR processes are much more popular than that of THG and FWM due to a simpler experimental setup to excite the former processes.

2.4.4.3 Nonlinear Refractive Index of 2D MoS_2 Based on Wavelength Conversion Techniques

Several reports have been found to investigate the $\chi^{(3)}$ or n_2 of 2D MoS_2 using the THG (Säynätjoki et al., 2017; Wang et al., 2014b; Woodward et al., 2016) and FWM (Zhang et al., 2020) processes. For example, Säynätjoki et al. reports the $\chi^{(3)}$ of pristine 2D MoS_2 (mechnical exfoliated, 1 – 5 layers) is $10^{-17} - 10^{-19} m^2 V^{-2}$ based on THG process at the excitation wavelength of 1560 nm (Säynätjoki et al., 2017). To convert their $\chi^{(3)}$ to n_2, Equation (2.10) can be used. Consider the n_0 of MoS_2 to be 2.93 at 1560 nm (Figure 2.17), the converted n_2 of MoS_2 based on Säynätjoki et al. work is in the range of $10^{-16} - 10^{-18} m^2 W^{-1}$. In 2020, Zhang et al. evaluated the n_2 of CVD-grown few-layer MoS_2 to be $2.70 \times 10^{-16} m^2 W^{-1}$ based on FWM process at the wavelength of 1550 nm (Zhang et al., 2020). Based on their work, it can be seen that the pristine and CVD-grown MoS_2 have the same magnitude of n_2 ($10^{-16} m^2 W^{-1}$) at the C-band wavelength.

2.4.4.4 Nonlinear Refractive Index of 2D MoS_2 Based on Self-Phase Modulation and Nonlinear Refraction Techniques

Besides that, studies to investigate the $\chi^{(3)}$ or n_2 of 2D MoS_2 by SPM (Liu et al., 2015b; Zhang et al., 2018) and NLR (Bikorimana et al., 2016; Li et al., 2016a; Neupane et al., 2020; Pan et al., 2020; Wang et al., 2014a; Wei et al., 2015) processes have also

been reported. For instance, through SPM process, Liu et al. found that the n_2 of CVD-grown few-layer MoS_2 is $1.1 \times 10^{-16} m^2 W^{-1}$ (Liu et al., 2015b) at 1554.5 nm wavelength. On the other hand, the measurement of n_2 of 2D MoS_2 via the NLR process is widely studied since the last decade. The technique particularly used to do such measurement is called the Z-scan technique. Most of the studies were carried out with exfoliated 2D MoS_2 flakes in a dispersion at relatively shorter wavelengths, namely at 532 nm (Neupane et al., 2020; Wang et al., 2014a), 700 nm (Li et al., 2016a), 800 nm (Wei et al., 2015) and 1064 nm (Wang et al., 2014a). Only a few n_2 measurement is done with thin film MoS_2 at 1064 nm (Bikorimana et al., 2016) and 2000 nm (Pan et al., 2020). In this work, 2D MoS_2 in the form of dry thin film rather than suspended MoS_2 flakes is of interest, as the former provides more predictable NLO properties as mentioned in Section 2.2. For this reason, the n_2 of CVD-grown MoS_2 thin film reported by Bikorimana et al. and Pan et al. work are compared. The former measured the n_2 of bulk MoS_2 (25 μm thickness) at 1064 nm, while the latter studied the properties of monolayer MoS_2 (0.8 nm thickness) at 2000 nm. Both of the works do not measure the n_2 of MoS_2 at C-band using this technique. The lack of information of n_2 of MoS_2 at C-band may limit the development of 2D MoS_2 technology in the research or telecommunication field. This becomes the motivation to study the n_2 of large area monolayer MoS_2 at the 1550 nm wavelength range using Z-scan technique. The concept of Z-scan technique, its advantages and disadvantages will be discussed in brief in Section 2.5.1. Table 2.1 summarizes the measurement of n_2 of MoS_2 in different forms based on NLR process using the Z-scan technique.

Table 2.1: Comparison of n_2 of 2D MoS_2 obtained based on NLR process using Z-scan technique.

Laser (wavelength, pulse width, repetition rate)	Form	n_2 (m^2W^{-1})	Ref
532 nm, 6 ns, 10 Hz	Suspended flakes	-9.2×10^{-14}	(Neupane et al., 2020)
532 nm, 100 ps, 10 kHz	Suspended flakes	-2.5×10^{-16}	(Wang et al., 2014a)
700 nm, not given, 2 kHz	Suspended flakes	2.6×10^{-13}	(Li et al., 2016a)
800 nm, 130 fs, 1 kHz	Suspended flakes	9.07×10^{-20}	(Wei et al., 2015)
1064 nm, 100 ps, 10 kHz	Suspended flakes	-2.07×10^{-17}	(Wang et al., 2014a)
1064 nm, 25 ps, 20 Hz	Thin film	1.88×10^{-16}	(Bikorimana et al., 2016)
2000 nm, 50 ns, 3 kHz	Thin film	2.5×10^{-13}	(Pan et al., 2020)

2.4.5 Saturable Absorption in 2D MoS_2

2.4.5.1 Saturable Absorption: A Brief Introduction

Saturable absorption is a non-parametric NLO process. A non-parametric process involves the transition of electron from a real level to another, which is usually described by the complex susceptibility. In addition, unlike a parametric process in which photon energy is always conserved, photon energy need not be conserved in a non-parametric process (Boyd, 2008). For a material that exhibits saturable absorption, its absorption coefficient, α, reduced when measured at high intensity of laser source. The relationship between α of a material and laser intensity I can be represented by the following equations:

$$\alpha = \frac{\alpha_s}{1 + I/I_s} + \alpha_{ns} + \beta I \tag{2.11}$$

where α_s and α_{ns} are the saturable and non-saturable loss, respectively. Sometimes, α_s and α_{ns} are written as α_0 and α_{NL}. β is the reverse saturable absorption coefficient of a material. Reverse saturable absorption happens when the absorption increases at high

laser intensity, and it may or may not happen depending on the property of the material. Here, I_s is defined as the saturation intensity, i.e. the intensity that decreases the absorption by half of the maximum α_s, considering α_{ns} and β to be zero (Woodward et al., 2015). If $\beta = 0$, reverse saturable absorption is absence.

The saturable absorption of a material, typically, can be measured by Z-scan or I-scan technique (also known as the balanced twin-detector technique, which will be discussed in Section 2.5.2) (Woodward et al., 2015). The measurement of saturable absorption of 2D MoS_2 using Z-scan and I-scan will be discussed separately.

2.4.5.2 Saturable Absorption of 2D MoS_2 Measured Using Z-scan Technique

In 2013, Wang et al. measures the saturable absorption of exfoliated MoS_2 dispersion at 800 nm wavelength using Z-scan technique (Wang et al., 2013). After a year, they extended the measurement using different laser wavelengths, i.e. 515 nm, 532 nm, 800 nm, 1030 nm and 1064 nm (Wang et al., 2014a). Their studies show that the α_{NL} is greatly affected by the wavelength of incident laser. However, the sample contains suspended flakes, so the measurement of α_{NL} is carried out on a group of flakes, with different thickness, lateral size and orientation, which may not reflect the α_{NL} of 2D MoS_2 at a particular thickness. An evident can be obtained based on their Z-scan studies that involve 800 nm laser in 2013 and 2014, as presented in the first and forth row in Table 2.2, respectively. The MoS_2 samples are both exfoliated in cyclohexylpyrrolidonone (CHP) solvent by LPE technique. Although the LPE process (during ultrasonication until centrifugation steps) is the same, the MoS_2 dispersion products show different α_0 and α_{NL}. The comparison demonstrates that the experimental results reflects on different group of MoS_2 dispersion. The measured I_s, α_0, and α_{NL} may not be comparable to each other.

Few years later in 2019, Wang et al. carried out Z-scan measurement on CVD-grown monolayer MoS_2 at 400 nm and finds that the α_{NL} is as large as $-2.79 \times 10^4 cmGW^{-1}$ (Wang et al., 2019c). Then, Pan et al. shows that the α_{NL} of monolayer MoS_2, fabricated by physical vapor deposition, is in the same order of magnitude as reported by Wang et al. but at the wavelength of 2000 nm (Pan et al., 2020). In other word, the obtained α_{NL} of MoS_2 based on bottom-up synthesis method does not show large variation as compared to the MoS_2 dispersion prepared by LPE technique. This means that the former studies are more reliable as the saturable absorption of 2D MoS_2 are determined on samples with known thickness and size. Table 2.2 summarizes the saturable absorption of 2D MoS_2 measured using Z-scan technique.

Table 2.2: Saturable absorption of 2D MoS_2 measured using Z-scan technique

Laser	Form	I_s $(GWcm^{-2})$	α_0 (cm^{-1})	α_{NL} $(cmGW^{-1})$	Ref
800 nm, 100 fs, 1 kHz	Suspended flakes	405	2.85	-5.80×10^{-3}	(Wang et al., 2013)
515 nm, 340 fs, 1 kHz	Suspended flakes	58	25.34	-0.357	(Wang et al., 2014a)
532 nm, 100 ps, 10 kHz	Suspended flakes	1.13	25.7	-26.2	(Wang et al., 2014a)
800 nm, 100 fs, 1 kHz	Suspended flakes	381	11.2	-2.42×10^{-2}	(Wang et al., 2014a)
1030 nm, 340 fs, 1 kHz	Suspended flakes	114	11.8	-9.17×10^{-2}	(Wang et al., 2014a)
1064 nm, 100 ps, 10 kHz	Suspended flakes	2.1	11.6	-5.5	(Wang et al., 2014a)
400 nm, 65 fs, not given	Monolayer thin film	-	-	-2.79×10^4	(Wang et al., 2019c)
800 nm, 65 fs, not given	Few-layer thin film	-	-	-0.8×10^3	(Wang et al., 2019c)
2000 μm, 50 ns, 3 kHz	Monolayer thin film	2.71×10^{-4}	-	-1.6×10^4	(Pan et al., 2020)

2.4.5.3 Saturable Absorption of 2D MoS_2 Measured Using I-Scan Technique

I-scan is another measurement method commonly used to determine the saturable absorption of 2D MoS_2. Table 2.3 shows the comparison of saturable absorption of 2D MoS_2 measured using I-scan technique. A large number of saturable absorption studies are done using 2D MoS_2-PVA composite, i.e. PVA polymer encapsulated MoS_2 flakes (Huang et al., 2014; Luo et al., 2014; Wei et al., 2016; Woodward et al., 2014). For example, in the C-band wavelengths, the values of I_s and α_s are quite similar to each other as reported by Huang et al. and Luo et al. (Huang et al., 2014; Luo et al., 2014). However, large discrepancies are found when they are compared with CVD-grown few layer (5 layer) MoS_2. Consider the value of α_s, the reported α_s are ~ 17 times larger based on Xia et al. and Li et al. works (Li et al., 2014b; Xia et al., 2014b). This discrepancy may be explained by the fact that the measurement done on MoS_2-PVA composite reflect the effective saturable absorption of a group of MoS_2 flakes, similar to suspended MoS_2 flakes in a dispersion. This does not reflect the saturable absorption of 2D MoS_2 with a particular thickness. On the other hand, the works carried out on the CVD-grown few-layer MoS_2 on either fiber facet or side-polished fiber at C-band wavelength are considered to be more reliable as the thickness is known (Khazaeizhad et al., 2014; Li et al., 2014b; Xia et al., 2014b).

Table 2.3: Saturable absorption of 2D MoS_2 measured using I-scan technique

Laser	Form / platform	I_s ($MWcm^{-2}$)	α_s (%)	α_{ns} (%)	Ref
1560 nm, 250 fs, 22.2 MHz	Exfoliated flakes-PVA composite	10	2	48.5	(Huang et al., 2014)
1566 nm, 212 fs, 22.0 MHz	Exfoliated flakes-PVA composite	13	1.6	54.8	(Luo et al., 2014)
1550 nm, 250 fs, 20.0 MHz	CVD-grown few-layer MoS_2 on fiber facet	0.34	35.4	34.1	(Xia et al., 2014b)
1563 nm, 800 fs, not given	CVD-grown few-layer MoS_2 on side-polished fiber	> 100	> 2.5	< 70	(Khazaeizhad et al., 2014)
1550 nm, 250 fs, 20.0 MHz	CVD-grown few-layer MoS_2 on fiber facet	0.43	33.2	35	(Li et al., 2014b)
1064 nm, 0.8 ns, 7 MHz	Exfoliated flakes on quartz plate	8.7×10^{-4}	4.6	-	(Zhang et al., 2014a)
1065 nm, 500 fs, 26.4 MHz	Exfoliated flakes-PVA composite	1.6	6.3	18	(Woodward et al., 2014)
800 nm, 130 fs, 1 kHz	Exfoliated flakes-PVA composite	1.17×10^5	42.8	-	(Wei et al., 2016)
1031 nm, 30 ps, 10.3 MHz	Exfoliated MoS_2-doped glass	18.8	14.7	27.5	(Lv et al., 2019)

Based on the discussion above, together with Table 2.2 and Table 2.3, the saturable absorption of 2D MoS_2 can be measured using Z-scan and I-scan techniques. However, most of the investigations were carried out on the 2D MoS_2 dispersion (in Z-scan) as well as MoS_2-PVA composite (in I-scan). The results may not truly reflect the saturable absorption of a 2D MoS_2 layer. Rather, they show their effective saturable absorption as a group of MoS_2 flakes within a volume as these flakes have a distribution of thickness, lateral size and orientation across the volume. Therefore, the saturable absorption study should be carried out on CVD-grown 2D MoS_2 which is more controllable and reproducible. In addition, from Table 2.2 and Table 2.3, there is a lack of information on the saturable absorption of CVD-grown monolayer MoS_2 at C-band wavelength. It is

believed that the investigation will contribute to the development of 2D MoS_2 photonics application.

2.4.6 Application of NLO Properties of 2D MoS_2

In the previous sections, we discussed the NLO properties of MoS_2 in terms of n_2 and α_{NL} (or α_s). They contribute to different photonics applications. The n_2 of 2D MoS_2 is responsible for the third order NLO processes such as THG and FWM, which convert wavelength from the commercially available laser pump source into new wavelength that is not commercially available. For example, a commercial Nd:YAG laser which operates at 1064 nm can produce 355 nm laser via THG, producing an alternative UV laser source. The same THG process can be used on another commercial Ti:sapphire laser to realize a tunable laser for wavelength range between 250 – 300 nm, enabling applications that require deep UV and mid UV lasers (Weber, 2018). Besides, through FWM process, a special laser source called frequency comb that contains a wavelength spectrum with a series of discrete, equally spaced wavelength lines can be generated (Supradeepa & Weiner, 2012). Furthermore, a material with large n_2 can produce a quantum light source through spontaneous FWM process which is essential for quantum information processing applications (Garay-Palmett et al., 2007). From these examples, the NLO properties of a material that involves n_2 is very useful in fundamental studies, photonics and quantum applications. Therefore, this has driven me to investigate the n_2 of a large area monolayer MoS_2 using Z-scan technique at C-band wavelength.

Besides n_2, the saturable absorption of a material is also essential in fundamental studies and photonics applications. This process allows the generation of pulsed laser from a continuous wave laser. Typically, a material that exhibits saturable absorption property is named as a saturable absorber (SA). Using SA in a laser cavity, pulsed laser

can be generated in two ways, that is, through Q-switching or mode-locking process. By definition, Q-switching is a technique to generate energetic short laser pulses (typically ns and μs pulses) by modulating the intracavity losses, leading to a modulation of Q factor (or quality factor) of the laser cavity (Rüdiger, 2004). These high energy Q-switched pulses are essential in material processing and machining (Woodward & Kelleher, 2015). On the other hand, mode-locking refers to a method to generate ultrashort pulses (even shorter than Q-switching pulses, typically ps and fs pulses) using SA by "locking modes" in the laser cavity. Mode-locked lasers are attractive as they produce pulsed laser with high output peak power and ultrashort pulse duration, making them suitable for material processing, metrology, telecommunication technologies and biophotonic imaging (Menzel, 2007; Woodward & Kelleher, 2015). Due to the versatility of a SA, it will be useful to determine the saturable absorption properties of large area monolayer MoS_2 and its ability to generate pulse laser either via Q-switching or mode-locking. In this work, monolayer MoS_2 thin film will be integrated onto a planarized waveguide and the saturable absorption of the MoS_2-coated waveguide will be measured using I-scan technique. To study its ability in generating pulse laser, the device will be coupled into an erbium-doped fiber laser cavity, and its output will be observed using detectors such as an oscilloscope (OSC), optical power meter (OPM) and optical spectrum analyser (OSA), which will be discussed in Chapter 4.1 and 4.2 later.

2.4.6.1 Saturable Absorber Based on Chip-Based Waveguide

Waveguide-based pulse laser source refers to a chip-based waveguide laser as compared to fiber-based laser source. One of the advantages of waveguide-based pulse laser source is its potential in miniaturization as compared to the conventional solid-state pulse laser source which requires bulk optics alignment (Li et al., 2020), as well as fiber-

based pulse laser source that consists of multiple individual optical fiber components. In fact, the waveguide-based pulse laser source can solve some of the issues that are commonly found in the conventional bulk laser. For example, to efficiently obtain a stable pulse laser output, the laser with pure fundamental mode and constant spot size is preferred in the laser cavity. Yet, the bulk optics system faced the issues in maintaining a fundamental mode with a stable size due to accumulated thermal effects. Such issues can be resolved readily when a waveguide structure is used, because the higher-order modes can be well-suppressed in the finite waveguide core size (Jia & Chen, 2019). This advantage allows the continuous growth in the development of the compact waveguide-based pulse laser source over the last two decades.

In general, the waveguide-based pulse laser source can be arranged in a few different ways, in which the SA can either interact directly or evanescently with the laser mode as shown in Figure 2.22. Figure 2.22(a) shows the most common waveguide-based laser cavity arrangement, in which SA is coated on a sapphire substrate and placed at the output of the Nd:YVO_4 waveguide (Li et al., 2018). The SA provides two functions, that are, it acts as a partial reflector and a saturable absorption element, hence realizing a laser cavity that can generate Q-switched mode-locked laser. This arrangement is beneficial in terms of simplicity in preparation process, full optical field interaction and efficient dispersion management (Jia & Chen, 2019). However, such experimental arrangement has a few disadvantages. For instance, the SA is prone to physical damage due to the arrangement between the waveguide and the SA. It is also prone to optical damage due to the interaction between the high intensity laser and the SA. The use of bulk optics may also limit the development of compact, monolithic laser device (Jeong et al., 2013; Jia & Chen, 2019). To avoid physical and optical damage, the SA can be deposited on the waveguide, as exemplified in Figure 2.22(b). In this way, the SA interacts with the laser field evanescently, which can increase the damage threshold of the device (Kim et al., 2013).

Moreover, it has the flexibility to control the interaction length between the SA and laser, which is useful in enhancing the overall nonlinear interaction in generating pulses. Furthermore, the bulk optics can be replaced by an all-optical fiber laser setup, as shown in Figure 2.22(c). Jeong et al. designed the SA-coated waveguide in such a way that the waveguide is butt-coupled in a fiber laser cavity to achieve pulse laser generation (Jeong et al., 2013). This design allows a more monolithic solution towards a more compact waveguide-based pulse laser source. It paves a way in the development of the planar photonics integrated circuit technology.

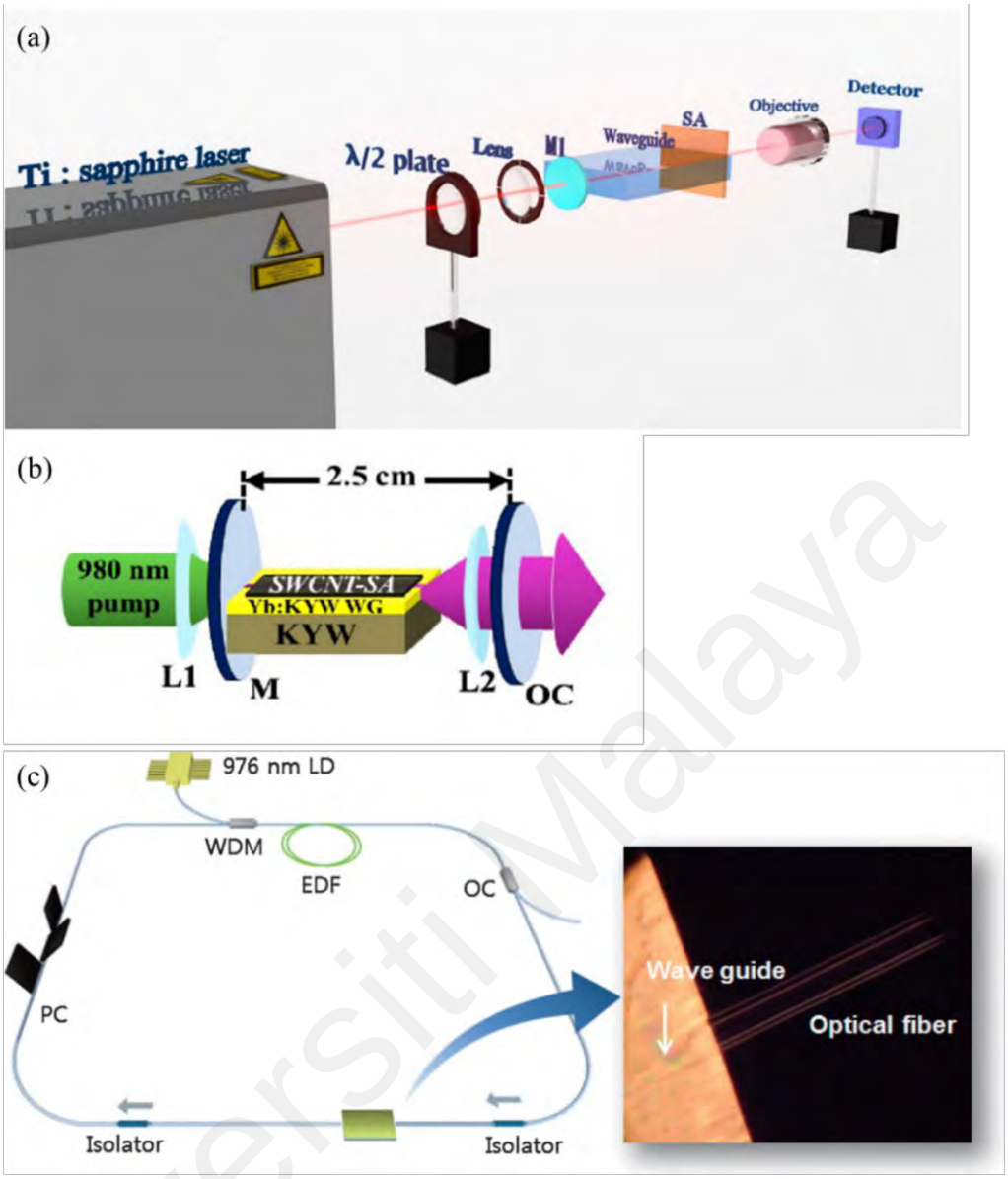

Figure 2.22: Different arrangement of laser cavity: (a) Direct field interaction scheme in which SA is placed at the output interface of the waveguide, yet some bulk optics are used in the laser cavity. Figure adapted from (Li et al., 2018). (b) Similar setup as in (a) except that SA is deposited on the surface of waveguide core to realize an evanescent field interaction scheme. Figure adapted from (Kim et al., 2013). (c) Evanescent field interaction scheme in which SA is coated on a waveguide. The waveguide is coupled in a fiber laser cavity. Figure adapted from (Jeong et al., 2013).

Li et al. revealed that 2D materials have great potential in the development of compact waveguide-based pulse laser source due to their excellent saturable absorption properties (Li et al., 2020). However, the pulse laser sources that utilize 2D materials typically operate at the wavelength band of ~ 1.0 μm and ~ 2.0 μm, with only a few reports on the

operation in the C-band wavelength range (Choudhary et al., 2015; Wang et al., 2019a). The C-band wavelength is important as it is the wavelength band for standard telecommunication network. The lack of study in utilizing 2D material, especially a monolayer MoS_2, in producing a waveguide-based pulse laser source serves as the motivation to take initiative in filling up this research gap.

2.5 Technique to Characterize NLO Properties of Large Area Monolayer MoS_2

The n_2 of monolayer MoS_2 can be characterized by Z-scan technique, whereas its saturable absorption can be measured using Z-scan and I-scan technique. In this section, the fundamental concepts of Z-scan and its modification to overcome thermal lensing effect during measurement will be discussed. Afterwards, the I-scan technique and its advantages will be described briefly.

2.5.1 Z-Scan Technique

2.5.1.1 Conventional Z-Scan Technique

Z-scan technique is developed by Sheik-Bahae et al. in 1990 (Sheik-Bahae et al., 1990). This technique offers the advantages of sensitive measurement on both the NLR and NLA using a single laser beam. Since then, Z-scan technique becomes the common measurement technique to characterize the third order NLO properties of a material (De Araújo et al., 2016; De Nalda et al., 2002). Though Z-scan technique is initially proposed to measure the NLO properties of a crystal (Sheik-Bahae et al., 1989), it can be used on samples in other form as well, such as in liquid (Sheik-Bahae et al., 1990; Wang et al., 2014a) and 2D material deposited on a substrate (Pan et al., 2020; Zhang et al., 2012; Zheng et al., 2015).

In practical, the Z-scan technique has the experimental arrangement as shown in Figure 2.23. A thin sample is translated along the propagating path of a focused laser beam. The transmittance of the sample as a function of the sample position, z with respect to the focal plane is measured by two detectors, namely Detector 1 without an aperture and Detector 2 with an aperture placed in the far field. The measurements with and without an aperture are called closed aperture Z-scan (CA Z-scan) and open aperture Z-scan (OA Z-scan), respectively. The OA Z-scan measure the NLA of the sample, while the NLR is measured by the CA Z-scan. Take the CA Z-scan measurement as an example. Consider a material with a $-n_2$, with its thickness L smaller than Rayleigh length z_0 of the focused beam ($L < z_0$). As it is translated towards the focus, the intensity of laser increases, leading to self-lensing that alter the transmittance of the sample. A $-n_2$ material that exhibit negative self-lensing. At $-z$ near to the focus (prefocal position), the beam will tend to be narrowed at the aperture, leading to an increase in the recorded transmittance. After this material passed through the focus ($+z$ or postfocal position), the same negative self-lensing effect continues to diverge the beam, causing the beam to be broaden at the aperture which leads to a decrease in transmittance. This peak-to-valley configuration manifests a negative NLR, i.e. a self-defocusing characteristic. On contrary, a valley-to-peak configuration shows a positive NLR, i.e. a self-focusing characteristic. The typical transmittance curve obtained from a CA Z-scan measurement is illustrated in Figure 2.23. The transmittance-position curve provides a quick and useful method to determine the n_2 of a material, including our monolayer MoS_2, provided no NLA such as multiphoton or saturable absorption is present. A multiphoton (saturable) absorption will manifest a decrease (increase) in transmittance at the focal point in OA Z-scan measurement. If NLA occurs, saturable absorption will suppress the valley and enhance the peak, while multiphoton absorption gives the opposite effect. Anyway, the effect given by NLA can

be separated from NLR by simply dividing the normalized transmittance of CA Z-scan by the one with OA Z-scan (Sheik-Bahae et al., 1990).

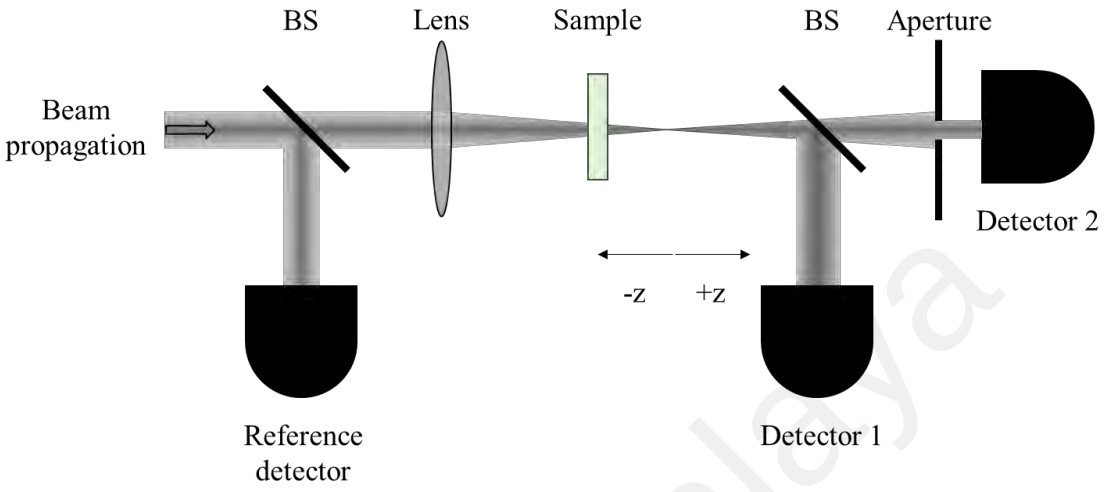

Figure 2.23: Arrangement of Z-scan technique. BS: beamsplitter.

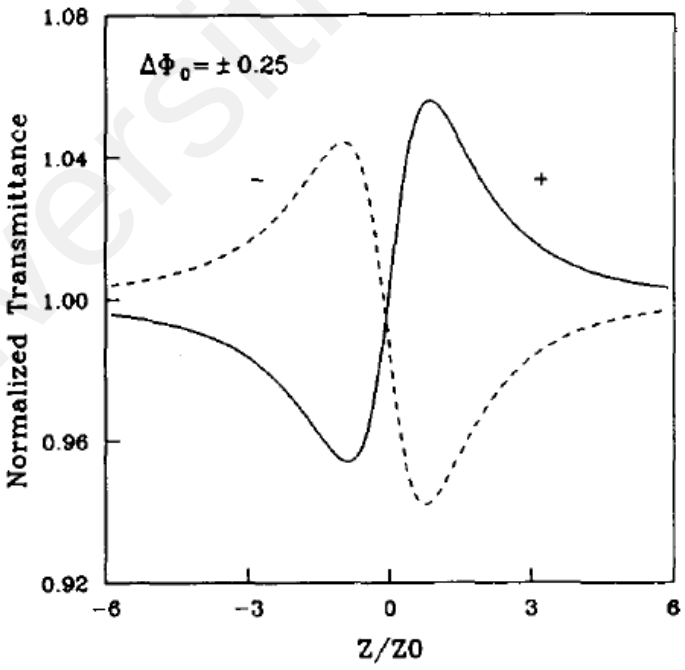

Figure 2.24: Illustration of NLR with different polarity, i.e. negative (self-defocusing) and positive NLR (self-focusing), using a small aperture size. Figure adapted from (Sheik-Bahae et al., 1990).

The analysis of NLR is based on the phase distortion of the wavefront of the beam when propagating through a nonlinear thin sample ($L < z_0$). Thin sample approximation is important in the Z-scan formalism. A detail analysis can be found in the Sheik-Bahae's work (Sheik-Bahae et al., 1990). Essentially, the n_2 of a material can be determined from the normalized transmittance, $T(z)$ curve of the NLR process as in Figure 2.24. The curve can be fitted using the following equation

$$T(z, \Delta\Phi_0) \simeq 1 - \frac{4\Delta\Phi_0 x}{(x^2+9)(x^2+1)} \tag{2.12}$$

where $x = z/z_0$, $z_0 = \pi\omega_0^2/\lambda$ is the Rayleigh length of the beam, ω_0 is the beam waist radius, and λ is the wavelength of laser, all in free space. The curve-fitting term $\Delta\Phi_0$ is the on-axis phase shift at the focus, which can be defined as

$$\Delta\Phi_0(t) = k\Delta n_0(t) L_{eff} \tag{2.13}$$

where $k = 2\pi/\lambda$ is the wave vector, $L_{eff} = (1 - e^{-\alpha L})/\alpha$, with α the linear absorption coefficient and L the sample length. $\Delta n_0 = n_2 I_0(t)$ with $I_0(t)$ is the on-axis intensity at the focus. Substituting these parameters into Equation (2.13), the $\Delta\Phi_0(t)$ becomes:

$$\Delta\Phi_0(t) = \frac{2\pi}{\lambda} n_2 I_0(t) \frac{(1 - e^{-\alpha L})}{\alpha} \tag{2.14}$$

Note that once the fitting term $\Delta\Phi_0$ is known, the n_2 of a material can be determined.

For OA Z-scan case, a trace will show a minimum (maximum) transmittance at the focus if multiphoton (saturable) absorption happens in the nonlinear medium. Consider a medium which exhibit two photon absorption (TPA). The $T(z)$ can be expressed as

$$T(z) \simeq 1 - \frac{1}{2\sqrt{2}} \frac{\beta I_0(t) L_{eff}}{(1+x^2)} \tag{2.15}$$

where β is the TPA coefficient. If saturable absorption is present, the normalized transmittance can be expressed in term of I_s. Following the work by H Zhang et al. (Zhang et al., 2014a), the normalized transmittance can be derived in term of I_s as:

$$T(z) = \frac{T_{nonlinear}}{T_{linear}} = \frac{1 - \frac{\alpha_0 L}{1 + I/I_s} - \beta I L}{1 - \alpha_0 L} \tag{2.16}$$

where $I = I_0/(1 + x^2)$. The third term in the numerator of Equation (2.16) vanishes when there is no TPA occurs from the sample. Using this equation, the saturation intensity I_s and modulation depth $\alpha_0 L$ can be determined.

There are several parameters that can affect the sign and strength of the NLR and NLA. For example, the concentration of the liquid / suspension sample (Couris et al., 1995), the wavelength of the excitation laser (Couris et al., 1995; Wang et al., 2014a), and the crystalline phase effect of a particular 2D material (Stavrou et al., 2022), to name a few. Moreover, the fabrication method of a material will affect its nonlinearities as well, as shown in Table 2.1 to 2.3 in this chapter. These examples provide useful information for one to study NLO properties of a material with different parameters using Z-scan technique. The detail for each parameter can be obtained from the references given in this paragraph.

However, due to the simplicity of the Z-scan technique, it is not suitable to apply on studies that involves high repetition rate of laser (De Nalda et al., 2002). The high repetition rate of laser will induce thermal lensing effect, which can mask the NLR response of the material (De Nalda et al., 2002; Sheik-Bahae et al., 1990). This could give a misleading observation on the Z-scan trace (as well as its analysis), even though the shape of NLR and thermal lensing effect looks similar. To encounter the problem, a variation named time-resolved Z-scan (or sometimes called as time-dependent Z-scan or thermally managed Z-scan) can be employed to separate the effect between NLR and thermal lensing effect of the sample (Falconieri, 1999; Gnoli et al., 2005; Stavrou et al., 2020). In the next section, the conditions that trigger the thermal lensing effect, modification in experimental arrangement of time-resolved Z-scan technique, and its analysis method will be discussed.

2.5.1.2 Time-Resolved Z-Scan Technique

Asides from NLR induced by third order nonlinearity, the CA Z-scan is also sensitive to refractive index changes from density variation induced by thermal lensing effect. This thermal lensing effect (a thermo-optical effect) originates from either linear or nonlinear absorption of light in the thin sample. It is found that even a very small linear absorption coefficients can lead to strong thermal lensing effect which can be observed from the experiment. In Falconieri's work, thermal effects build up when the sample is illuminated by a pulse train with pulse spacing shorter than the thermal characteristic time, t_c of the sample, irrespective of the pulse duration (Falconieri, 1999). The thermal characteristic time is defined by $t_c = \omega^2/4D$, where D is the thermal diffusion coefficient of the sample in the unit of cm^2s^{-1} and ω is the beam radius. This relationship tells us that t_c is ω-dependent, which makes it to be z-position dependent in the Z-scan setup. Typically, liquids and optical glasses have D values ranging from 10^{-3} to $6 \times 10^{-3} cm^2s^{-1}$, which results in t_c to be larger than 40 μs in a typical Z-scan setups. Based on this condition, laser with repetition rate greater than just a few kHz can induce cumulative heating in the sample (Falconieri, 1999; Gnoli et al., 2005). This shows that thermal lensing effect will take place in most of the common mode-locked lasers that operate at high repetition rate (MHz). Hence, to effectively distinguish between instantaneous optical nonlinearities (that comes from $\chi^{(3)}$ process) and thermal lensing effect, time-resolved Z-scan must be used.

In 1999, Falconieri develops a model to determine CA Z-scan trace due to thermal lensing effect caused by arbitrary order of absorption process (Falconieri, 1999). In his model, he follows the thin sample approximation ($L < z_0$) as well. The model starts with modelling temperature profile of the sample due to absorption of light in arbitrary order, with the assumption that all the absorbed energy is thermalized. Consider an average

heating of the sample, the rate of energy density absorbed that involves q photon absorption is:

$$E(z,r) = qh\nu N\sigma f \int I^q(z,r,t)\, dt \tag{2.17}$$

where $h\nu$ is the energy of photon (J), N denotes the density of absorbing atoms (cm^{-3}), σ is the multiphoton absorption cross section ($cm^{2q}s^{q-1}$), f is the repetition rate of laser (s^{-1}), $I(z,r,t)$ represents the photon flux (cm^2s^{-1}) of a laser pulse and the integral is over the pulse duration. For a laser that operates in TEM_{00} mode, $I(z,r,t) = \left[\frac{2P(t)}{\pi\omega^2(z)}\right] e^{\left(\frac{-2r^2}{\omega^2(z)}\right)}$, where $P(t)$ is the power of the pulse. Using these equations, the heat generated per unit length is derived as:

$$Q(z,r)2\pi r\, dr = E(z,r)2\pi r\, dr \tag{2.18}$$

$$= qh\nu N\sigma f \left[\frac{2}{\pi\omega^2(z)}\right]^q e^{\left[\frac{-2qr^2}{\omega^2(z)}\right]} H(q)2\pi r\, dr$$

where $H(q) = \int P^q(t)\ dt$.

The temperature profile caused by the absorption can be solved using the Green function for heat conduction equation. After integrating Equation (2.18), the temperature profile can be written as:

$$\Delta T(z,r,t) = qh\nu N\sigma f \left[\frac{2}{\pi\omega^2(z)}\right]^{q-1} \frac{H(q)}{4\pi\kappa q} \tag{2.19}$$

$$\times \left\{ Ei\left[\frac{-2qr^2}{\omega^2(z)}\right] - Ei\left[\frac{-2qr^2}{\omega^2(z)}\frac{1}{1+2qt/t_c}\right]\right\}$$

where κ denotes the thermal conductivity of the sample ($Wcm^{-1}K^{-1}$), $Ei(x)$ is the exponential-integral function defined in elsewhere (Gradshteyn & Ryzhik, 2014). Note that Equation (2.19) is expressed in terms of t_c, which is, again, z-position dependent through the changing of laser spot size in the Z-scan technique.

The change in temperature will affect the refractive index profile through the thermo-optical coefficient known as dn/dT (K^{-1}) of the sample. To include this effect in the optically thin sample, the propagation of the beam in the sample can be treated as the multiplication of the Gaussian beam by the thermo-optical phase factor induced by the change in refractive index. Let the Gaussian beam amplitude at the entrance plane of the sample as G_i, the beam amplitude at the exit plane G_0 can be written as:

$$G_0(z,r,t) = G_i(z,r)e^{\left[-ik\frac{dn}{dT}\Delta T(z,r,t)L\right]} \tag{2.20}$$

where k is the wavevector of light (cm^{-1}) and L denotes the sample length (cm).

Next, the thermal lens signal is defined by the on-axis $(r = 0)$ intensity of the field resulting from the propagation of the field from the exit plane of the sample to the detector plane $z = d$, normalized to the intensity at $t = 0$. This signal, as given by Falconieri (Falconieri, 1999), can be solved numerically as follow:

$$E(r = 0, z, t) = \frac{2\pi}{i\lambda(d-z)}J_0(0)\int_0^\infty r' G_0(z,r',t) \times e^{\left[\frac{i\pi r'^2}{\lambda(d-z)}\right]}\, dr' \tag{2.21}$$

where J_0 is a Bessel function, G_0 is the field defined in Equation (2.20) and λ is the wavelength of laser. This equation allows us to predict the nonlinearity caused by thermal lensing effect.

Although such numerical equation can provide the solution, an analytical form for the signal is always preferable. To obtain an analytical equation, approximation is needed. Sheldon et al. uses the Fraunhofer region approximation, linearizes the thermo-optical phase factor and considers the aberrated nature of the thermal lens to create an analytical solution (Sheldon et al., 1982). They define a parameter called thermal lens strength ϑ that account for multiphoton absorption of arbitrary order q as follow:

$$\vartheta(q) = kL\frac{qh\nu H(q)N\sigma f}{2\pi\kappa}\frac{dn}{dT}\left(\frac{2}{\pi\omega_0^2}\right)^{q-1} \tag{2.22}$$

where ω_0 is the beam waist radius of the laser at the focus. Using this parameter, the on-axis electric field at the detector plane can be written as

$$E(0,x,t) = const \times \left[1 - i\frac{\vartheta(q)}{2q(1+x^2)^{q-1}} \ln\frac{(1+ix)(1+2qt/t_c)+2q}{1+2q+ix}\right] \tag{2.23}$$

Ultimately, the normalized intensity, neglecting higher order terms of ϑ^2, is

$$\frac{I(x,t)}{I(x,0)} = 1 + \frac{\vartheta(q)}{q}\frac{1}{(1+x^2)^{q-1}} \times \tan^{-1}\left(\frac{2qx}{[(2q+1)^2+x^2]\frac{t_c(x)}{2qt}+2q+1+x^2}\right) \tag{2.24}$$

Equation (2.24) expresses the time-resolved Z-scan curves generated by thermal lensing effects. In addition, due to the linearity of the model, it is possible to add higher order absorption processes. This analytical model is in good agreement with the numerical calculation, therefore it is useful in shorten the analysis process of a study (Falconieri, 1999). This approach have been used in several Z-scan studies that involves high repetition rate of laser (Gnoli et al., 2005; Lin et al., 2005; Stavrou et al., 2020).

To further discuss this model, Falconieri shows the Z-scan trace due to thermal lensing effect for $\vartheta(q) = 1$ and for $q = 1$ to 3, for different values of normalized time τ, where $\tau = t/t_c(x = 0)$, as shown in Figure 2.25(a). From this figure, it is found that peak-to-valley transmittance changes ΔT_{p-v} is always proportional to $\vartheta(q)/q$, and the cumulative heating process is also proportional to the laser repetition rate and power. Besides that, another important parameter that can be used to characterize the time-resolved Z-scan trace, which is the normalized peak-to-valley distance Δx_{p-v}. Falconieri reports the Δx_{p-v} against τ, as shown in Figure 2.25(b), and found that Δx_{p-v} is proportional to τ, and remain steady at large τ. This information is essential and provide

an alternative mean to determine the order of absorption q that results in thermal lensing effect. Table 2.4 shows the time limits of the time-dependent Δx_{p-v} for $q = 1$, 2 and 3 (Falconieri, 1999).

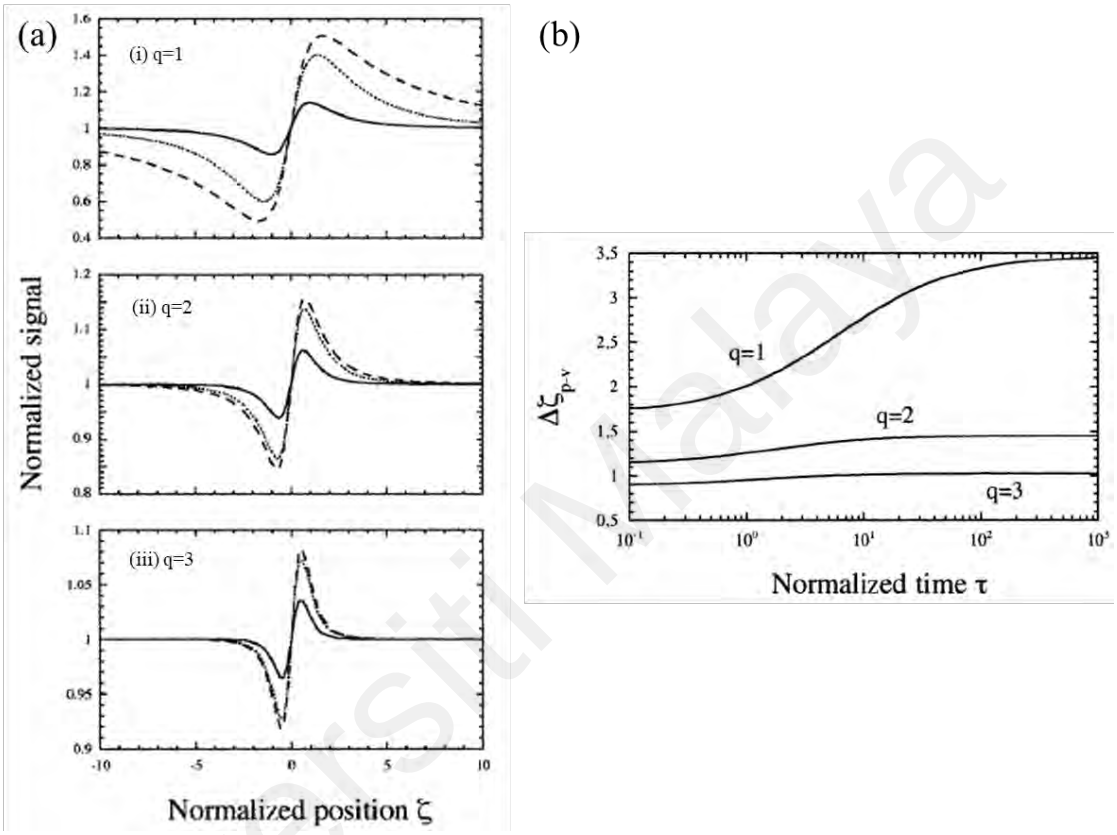

Figure 2.25: (a) Illustration of Z-scan trace due to thermal lensing effect, calculated for $\vartheta(q) = 1$ and for (i) $q = 1$, (ii) $q = 2$, (iii) $q = 3$, for $\tau = 1$ (continuous curve), $\tau = 10$ (dotted curve), and $\tau = 100$ (dashed curve); (b) Graph of Δx_{p-v} against τ for $q = 1$, 2 and 3. Figures adapted from (Falconieri, 1999).

Table 2.4: Time limits of the time-dependent Δx_{p-v} for $q = 1$, 2 and 3

Order of absorption q	Limit $t \to 0$	Limit $t \gg t_c$
	Normalized peak-to-valley distance Δx_{p-v}	Normalized peak-to-valley distance Δx_{p-v}
1	1.717	3.46
2	1.13	1.45
3	0.89	1.02

If the material possesses both electronic (NLR) and thermo-optical (thermal lensing) nonlinearities, they can be predicted and separated using Equation (2.24). This convenient comes from the fact that Equation (2.24) is linearized and both the nonlinearities can be sum simply together for calculation (Falconieri, 1999). Gnoli et al. demonstrates this process to obtain the electronic nonlinearity from the large thermal lensing effect introduced by their laser, which works in high repetition rate of 76 MHz (Gnoli et al., 2005). Their experimental setup is as illustrated in Figure 2.26, based on the suggestion by M Falconieri et al. (Falconieri & Salvetti, 1999; Gnoli et al., 2005). The main difference of time-resolved Z-scan setup compared to the conventional one is the use of a chopper to modulate the laser beam; and photodiodes as the photodetectors to measure the optical signal in time base. The chopper is essential in the setup as it allows a small interval of opening window for laser beam to pass through for measurement, and a long interval of closed window (or dark time) to allow the sample to dissipate heat and recover its initial temperature before the next illumination. In this way, at a particular z-position and opening window of the chopper, the time evolution of optical signal passed through the sample can be recorded by the photodiode. Then, the normalized transmittance of the sample can be analysed using Equation (2.24). Furthermore, Gnoli et al. propose an approach to obtain the electronic nonlinearity with a better accuracy. They suggest the need of extrapolate the Z-scan trace at $t = 0$, and uses the values of normalized transmittance at $t = 0$ as the representative of the electronic nonlinearity, see Figure 2.27 (Gnoli et al., 2005). From Figure 2.27(a), the time-resolved Z-scan curves at prefocal and postfocal positions are extrapolated to $t = 0$. These extrapolated values are employed to reconstruct a Z-scan trace to represent the NLR of the material, which can be seen in Figure 2.27(b). With this, the value of n_2 can be evaluated using Equation (2.12) and (2.14). This method gives a significant improvement to the work suggested by Falconieri et al (Falconieri & Salvetti, 1999), where they consider the first measured values of

normalized transmittance at tens of μs as the representative of the instantaneous electronic nonlinearity. The suggestion by Gnoli et al. is found to be reasonable and will be used in the time-resolved Z-scan measurement on the large area monolayer MoS_2 in this work. In fact, there is a recent paper that uses this technique to measure the n_2 of 2D graphene dispersion as well (Stavrou et al., 2020), indicating the versatility of this technique for different type of sample.

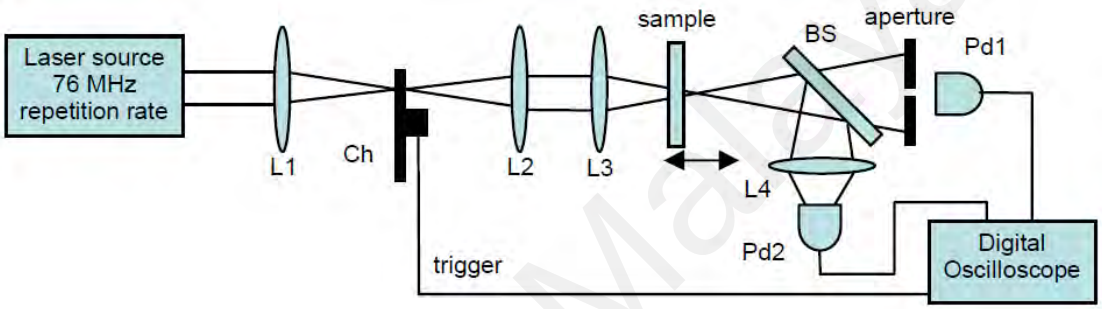

Figure 2.26: Experimental arrangement of the time-resolved Z-scan technique. L1, L2, L3 and L4 are focusing lenses; Ch represents a chopper; BS denotes a beam splitter; Pd1 and Pd2 are Si photodiodes for the CA and OA Z-scan, respectively. Figure adapted from (Gnoli et al., 2005).

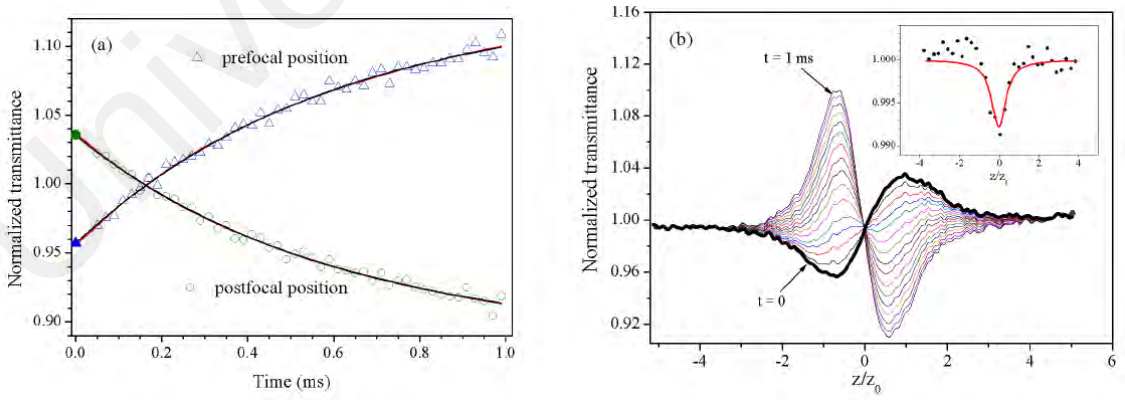

Figure 2.27: (a) Illustration of normalized time-resolved Z-scan traces at prefocal and postfocal positions for a CS_2 sample. Open symbols are the experimental data. The black curves are fitting curves acquired using Equation (2.24). Solid symbols are extrapolated values obtained from Equation (2.24) as the representative of the NLR caused by electronic nonlinearity; (b) Reconstructed Z-scan traces at different time *t*. The inset shows the OA Z-scan profile. Solid dots are the experimental data and red curve is its fits. Figures adapted from (Gnoli et al., 2005).

2.5.2 I-Scan Technique

Often known as balanced twin detectors technique, I-scan technique is widely used to measure the NLA, particularly saturable absorption of a material. Its popularity comes from the simple experimental arrangement as well as analysis method. Figure 2.28 shows the common I-scan technique for free space arrangement and the typical acquired result (Zhang et al., 2019). The fundamental idea of I-scan is similar with the conventional OA Z-scan technique. As discussed earlier, the Z-scan technique measures the transmittance of the sample that experiences different laser intensity while it is translating along a focused beam propagation axis. Instead of translating the sample, the sample is kept in a fixed position and the power (and hence the intensity) of the laser beam intensity is varied, and the transmittance of the sample is measured using a photodetector, as shown in Figure 2.28(a). Figure 2.28(b) depicts the normalized transmittance of the sample as a function of peak intensity of the incident laser beam. The normalized transmittance increases nonlinearly as the peak intensity of the laser increases and saturate at larger peak intensity ($> 0.2 MW cm^{-2}$ in the work by G. Zhang et al.). This represents a saturable absorption phenomenon. The raw data in Figure 2.28(b) can be fitted using Equation (2.11) by setting $\beta = 0$ if TPA is absent or negligible.

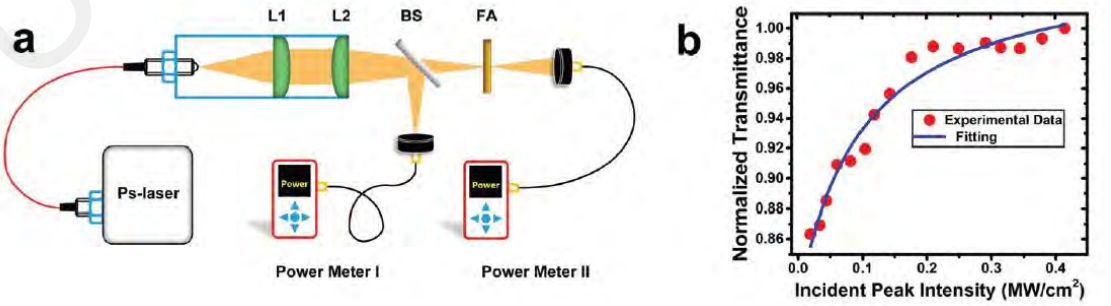

Figure 2.28: (a) Schematic diagram of the I-scan technique in free space arrangement. L1 and L2 are lenses; BS is a beamsplitter; and FA is the fluorinated antimonene sample; (b) Plot of the normalized transmission of the sample against the input peak intensity. Figures adapted from (Zhang et al., 2019).

This method can be modified into optical fiber-based arrangement as well as shown in Figure 2.29 (Mao et al., 2016a). The type of experimental arrangement is mainly dependent on the type of laser source used. For instance, it is commonly used together with a mode-locked fiber laser source, while the I-scan in free space arrangement is usually used with a free-space bulk mode-locked laser source. In fact, most recent I-scan measurements are based on optical fiber setup (Ahmad et al., 2019; Du et al., 2017; Lin et al., 2021; Siddiq et al., 2019). One of the advantages of using fiber-based I-scan technique is that the setup is more flexible and compact as free space laser beam alignment is not necessary (Ahmad et al., 2020; Luo et al., 2014; Mao et al., 2016a; Mao et al., 2016b; Woodward et al., 2015). Due to these benefits, a fiber-based I-scan technique will be used to study the NLA of the large area monolayer MoS_2 in this thesis.

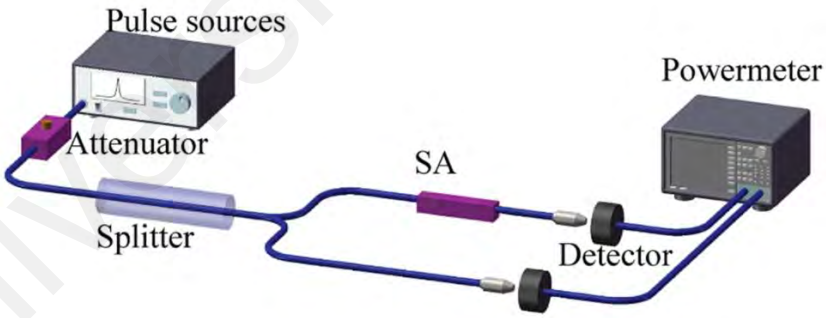

Figure 2.29: Illustration of the I-scan technique using optical fibers arrangement. SA denotes the saturable absorber sample. Figure adapted from (Mao et al., 2016a).

To sum up this section, a few types of measurement technique are described in order to determine the NLA coefficient and the n_2 of a material. To measure NLA effect of a material, both Z-scan and I-scan technique can be used. On the other hand, the value of n_2 of a material can only be determined using Z-scan technique.

The Z-scan technique shows its versatility in measuring both the interested coefficients using the OA and CA Z-scan method. The experimental setup is relatively simple, and it allows high sensitivity detection of NLR effect that comes from the studied material. However, the NLR measurement using CA Z-scan technique is only feasible when a low repetition rate of laser is used. If one would like to use a laser with high repetition rate, other nonlinearities (like thermo-optical nonlinearity) would present, which will alter the obtained normalized transmittance graph, hence hindering the effectiveness of measuring n_2 accurately. A possible way to overcome this issue is using an improvised version of Z-scan, namely the time-resolved Z-scan technique. This technique allows one to separate the nonlinear refraction that comes from the electronic (NLR) and thermo-optical (thermal lensing) nonlinearities. By extracting the value of time-dependent normalized transmittance curve at $t = 0$ for each z-position, the Z-scan trace can be reconstructed to represent the NLR resulted from the electronic nonlinearity of the material.

To determine the NLA coefficients, an OA Z-scan and I-scan techniques can be performed. Both methods utilize the same concept, that is, by measuring the transmittance of the material at increasing intensity of the incident laser beam. The difference between them are the way to change the intensity of the incident laser beam. OA Z-scan relies on the translation of sample across the propagation path of the focused laser beam, so that the material can experience different intensity due to the change of laser beam size. On the other hand, translation of the sample is not necessary in the I-scan technique. The change in intensity of the laser beam comes from the change in optical power of the source. Furthermore, I-scan technique can be arranged in free space or fiber form depending on the type of laser source used, hence providing flexibility to the user in designing the study.

Above all the advantages of these technique, it has been shown that both Z-scan and I-scan technique can be used to measure the NLO properties of 2D MoS_2. Reports are found to use both techniques to study the NLO properties of 2D MoS_2 flakes and CVD-

grown large area 2D MoS_2 thin film at various wavelengths. However, the investigation of NLO properties of large area 2D MoS_2, particularly in its monolayer form, in the C-band wavelength range using Z-scan technique is not yet found, to the best of author's knowledge. Driven by this motivation, the NLA and NLR of our large area monolayer MoS_2 will be measured using a time-resolved Z-scan method at 1560 nm wavelength, since our mode-locked laser operates in high repetition rate (1 MHz). It is believed that the results will provide useful information that pave the development of 2D MoS_2-based nanophotonics application in the future at this wavelength range.

CHAPTER 3: CHARACTERIZATION OF LARGE AREA MONOLAYER MoS_2 THIN FILM AND PDMS-ASSISTED MoS_2 TRANSFER TECHNIQUE

In this chapter, the characterization of large area monolayer MoS_2 thin film by various techniques will be discussed in detail. First, the morphology of the MoS_2-PDMS sample will be examined using an optical microscope. Next, Raman spectroscopy will be carried out to study its vibrational modes and estimate the number of layers of the MoS_2 thin film. The number of layers of MoS_2 thin film will then be verified using AFM. The quality of the sample is characterized using XPS. The NLO properties of the thin film characterized using time-resolved Z-scan will be described. Afterwards, the preparation technique to obtain the experimental platform will be described. One of the objectives of this thesis is to integrate the large area monolayer MoS_2 on a planarized optical waveguide. Therefore, in this chapter as well, the fabrication technique of the planarized optical waveguide as well as the integration method involved to transfer the 2D MoS_2 using PDMS-assisted transfer technique will be discussed.

3.1 Optical Micrograph of the MoS_2-PDMS Sample

A CVD-grown large area monolayer MoS_2 on a PDMS substrate was purchased from 6Carbon Technology, as depicted in Figure 3.1(a). It has a monolayer MoS_2 with a large coating area of 10 mm × 10 mm. The yellowish-green hue represents the monolayer MoS_2 film, and it appears homogeneous upon visual inspection (Figure 3.1(b)). The MoS_2-PDMS sample was observed using an optical microscope with 10x magnification in reflection mode. Figure 3.1(c) shows the optical micrograph of the MoS_2 thin film boundary on the PDMS substrate. Despite its atomically thin thickness, there is a distinguishable optical contrast between MoS_2 film and PDMS substrate. The existence

of this contrast aids in the identification of the thin film during the transfer process, which will be described in Section 3.8 later. Besides that, a small number of flakes that appear brighter compared to the thin film were observed as well. It is believed that these flakes are few-layer MoS_2 due to the fabrication tolerance of CVD, which can be observed as well in other reports (Islam et al., 2021; Lee et al., 2012; Liu et al., 2015a; Yin et al., 2014; Zhu et al., 2017). For instance, Zhu et al. described the size of Mo-based precursor can lead to the growth of few-layer MoS_2 in CVD process (Zhu et al., 2017). Nonetheless, the occurrence of these flakes is low across the MoS_2 thin film. This is evident in Figure 3.1(d), where the thin film appears uniform with only a low count of few-layer MoS_2 flakes over a large area. No micro-cracks and grain-like structure are observed at the center of the thin film, showing that the CVD-grown MoS_2 thin film is relatively high quality morphologically.

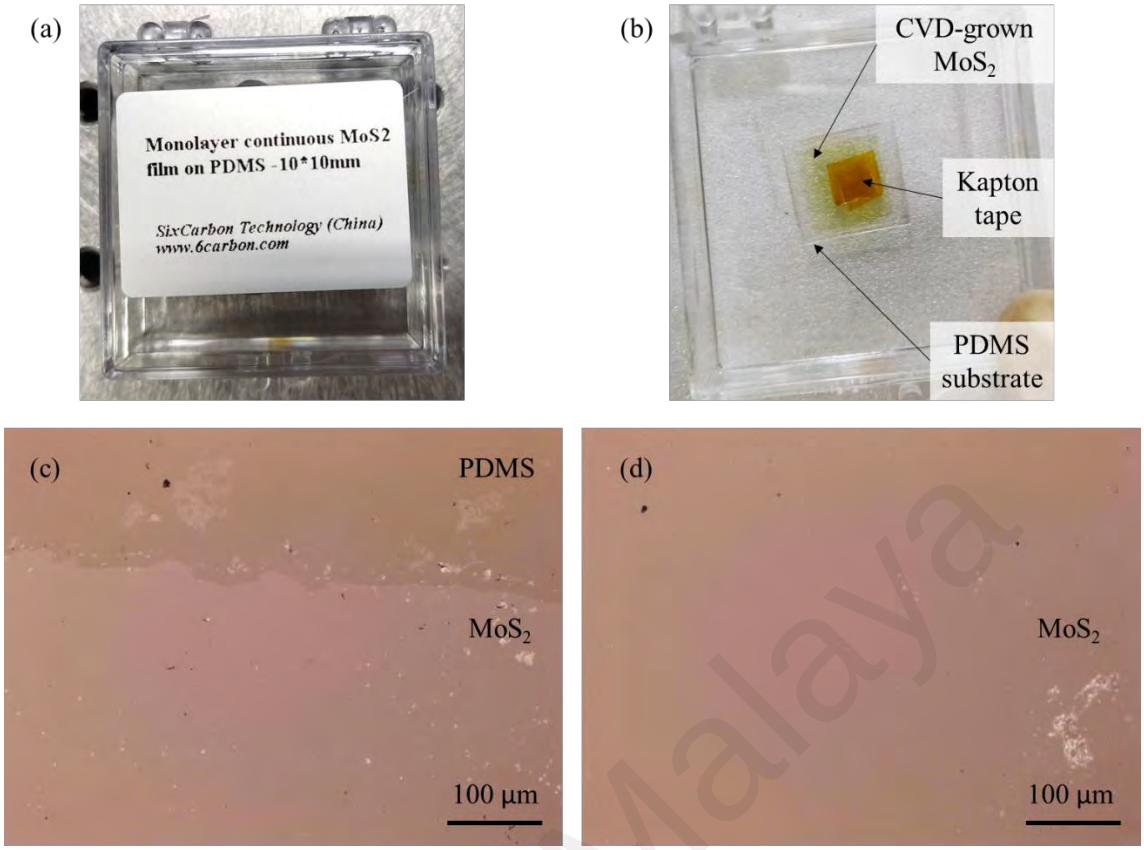

Figure 3.1: (a, b) Photographs of the purchased CVD-grown large area monolayer MoS_2 film on PDMS substrate. Optical micrograph of MoS_2-PDMS sample: (c) at the boundary of the MoS_2 thin film, figure adapted from (Chew et al., 2023); (d) at the center of the thin film, figure adapted from (Chew et al., 2023).

3.2 Raman Spectroscopy of the MoS_2 Thin Film

MoS_2 thin film on two different substrates, namely on PDMS and SiO_2/Si substrates, were studied using Raman spectroscopy (*Renishaw* InVia micro-Raman spectrometer), with an excitation wavelength of 532 nm. Raman spectroscopy on MoS_2-PDMS sample was carried out first. The power of laser source was kept as low as 0.25 mW to avoid optical damage to the sample. Figure 3.2 shows the Raman spectra of MoS_2-PDMS sample. Scans were carried out on three regions of the sample with different morphologies. Figure 3.2(a) and (b) are the optical micrograph and Raman spectrum of MoS_2 thin film, respectively. Two peaks at 384.6 cm^{-1} and 405.2 cm^{-1}, that correspond to the E_{2g} and A_{1g} Raman modes of MoS_2, were observed (Lee et al., 2010; Zhang et al., 2015). The modes

separation, Δ, is 20.6 cm^{-1}, which is consistent with the Raman modes of monolayer MoS_2 as discussed in Section 2.4.3 (Buscema et al., 2014). Besides, the measurement was performed as well on flakes with brighter contrast, as illustrated in Figure 3.2(c) and (e). Their corresponding Raman spectra are shown in Figure 3.2(d) and (f), respectively. Based on Figure 3.2(d) and (f), two modes appear at ~ 382 cm^{-1} and ~ 406 cm^{-1}, which clearly indicate that the flakes are indeed MoS_2 flakes. However, they do not share the same values of Δ, indicating that they consist of more than one layer of MoS_2. For instance, a flake with a faint contrast as shown in Figure 3.2(c) has Δ = 23.6 cm^{-1}, which correspond to a trilayer MoS_2. On the other hand, in Figure 4.2(e), a flake with brighter contrast and larger Δ of 24.7 cm^{-1} shows a possible number of layer > 5 (Buscema et al., 2014). Aside from material identification, Raman spectroscopy provides a relatively cost effective, fast and non-destructive method to determine the number of layers of 2D MoS_2.

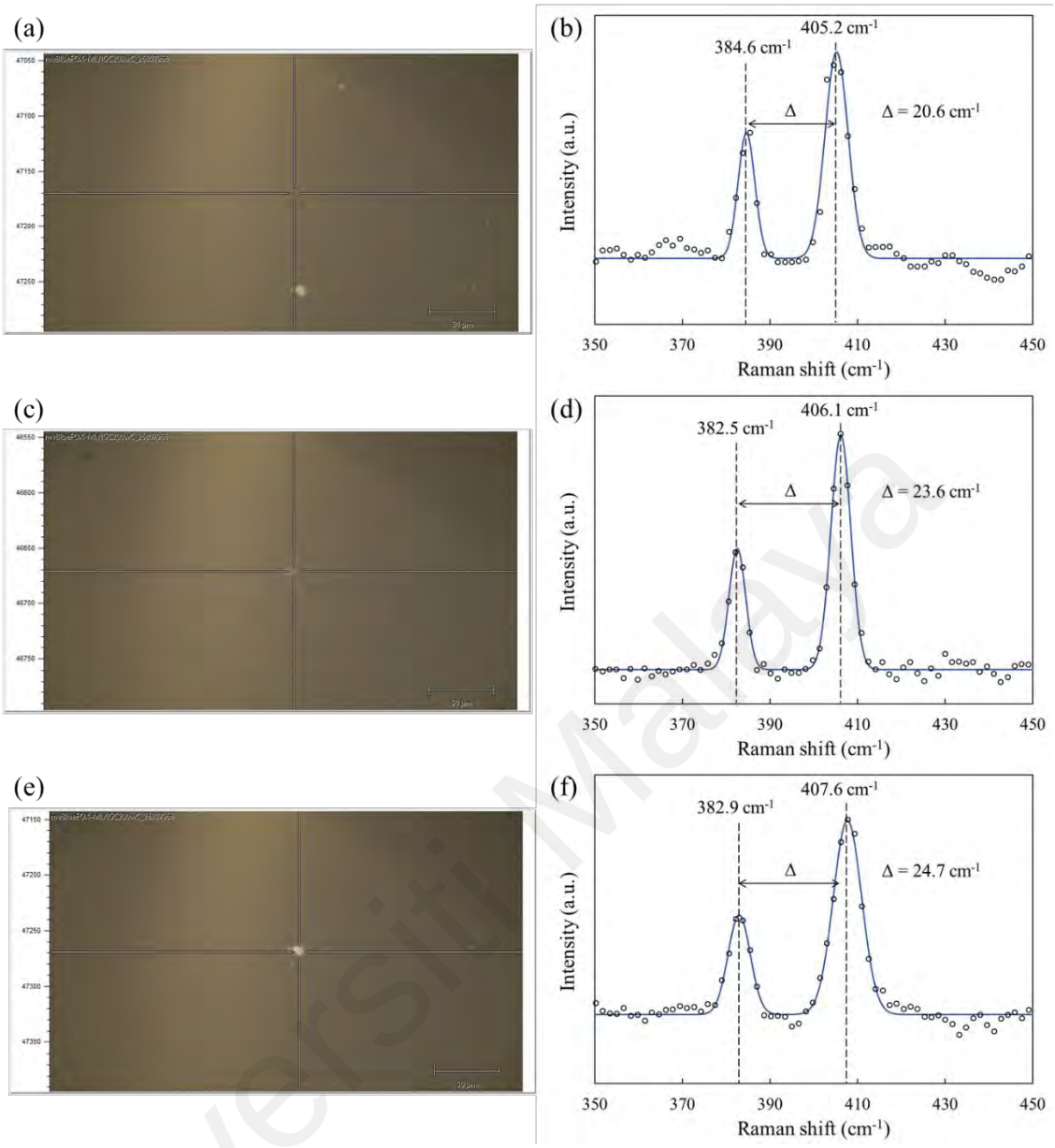

Figure 3.2: Optical micrographs (a, c, e) and the respective Raman spectroscopies (b, d, f) of MoS_2-PDMS sample at different regions with different morphology: (a) uniform thin film; (c) MoS_2 flake with faint contrast; (e) MoS_2 flake with relatively bright contrast. Figure (b) adapted from (Chew et al., 2022b).

Besides that, Raman mapping was carried out on MoS_2 thin film transferred on SiO_2/Si wafer. Raman mapping study allows one to determine the distribution of the number of layers of MoS_2 over a larger area. Figure 3.3(b) shows a 32 × 35 grid area that covers both MoS_2 thin film and the substrate. Raman spectroscopy was performed in each grid to create the mapping. The mapping was operating in raster scanning mode, with 4 μm

per step. Figure 3.3(c) and (d) show the mapping results analysed in terms of the peak position of E_{2g} and A_{1g} modes of 2D MoS_2, respectively. It is found that the thin film mainly consists of monolayer MoS_2, based on the calculation of Δ. For example, across the MoS_2 thin film, the E_{2g} and A_{1g} modes mostly have the values of ~ 385 cm^{-1} and ~ 405 cm^{-1}, respectively. This would give a Δ ~ 20 cm^{-1}, which correspond to monolayer MoS_2. Therefore, a conclusion can be drawn based on Raman spectroscopy analysis such that the CVD-grown MoS_2 thin film mainly consists of monolayer.

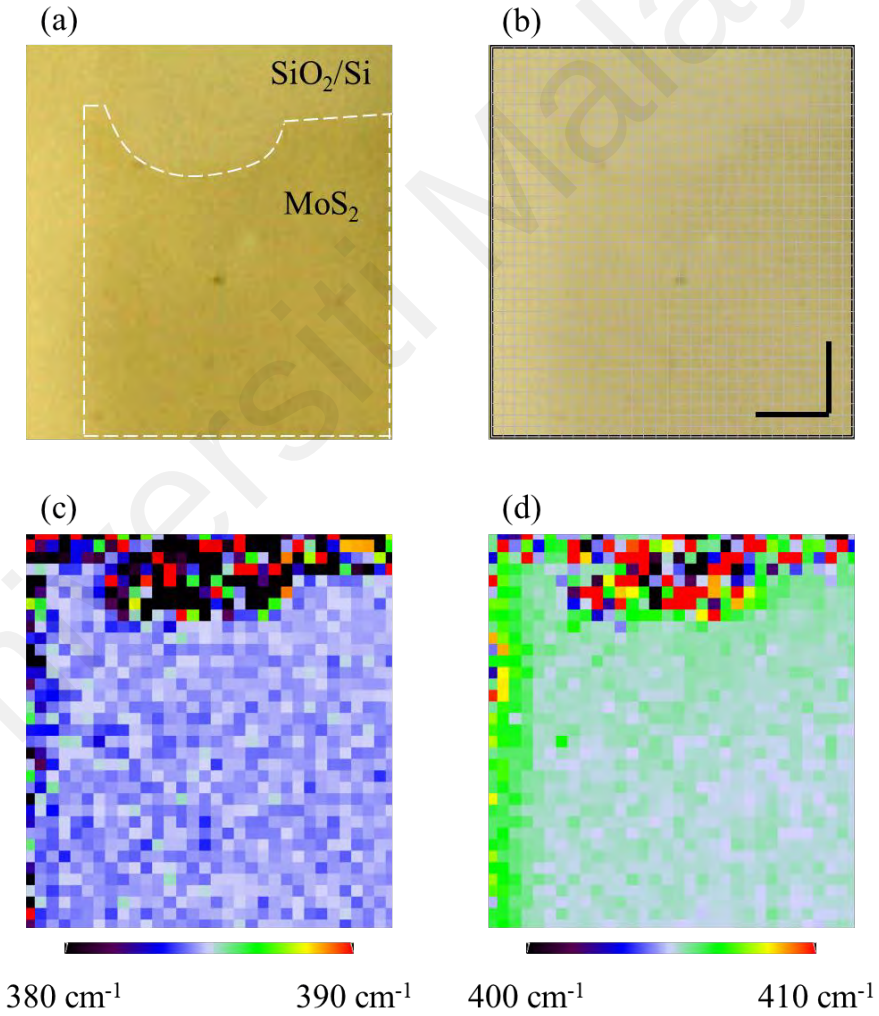

Figure 3.3: (a) Optical micrograph of transferred MoS_2 on SiO_2/Si substrate with 20x magnification, operating in reflection mode; (b) Illustration of desired area of Raman mapping with a total amount of 32 × 35 collection; (c) Raman mapping of peak position of E_{2g} mode; (d) Raman mapping of peak position of A_{1g} mode. The scale bar is 25 µm.

3.3 AFM of the MoS_2 Thin Film

AFM is one of the precise methods to physically study the thickness and morphology of a thin film. AFM study is performed on the MoS_2-PDMS sample as well as transferred MoS_2 thin film using NT-MDT with semi-contact mode. Figure 3.4 depicts the AFM result of MoS_2-PDMS sample, in which MoS_2 thin film is on the right-hand side while PDMS is on the left-hand side of the figure. It is found that the thickness of MoS_2 thin film is ~ 0.8 nm. However, the average surface roughness of PDMS substrate is found to be relatively large (~ 5 nm), which affects the accuracy of thickness analysis.

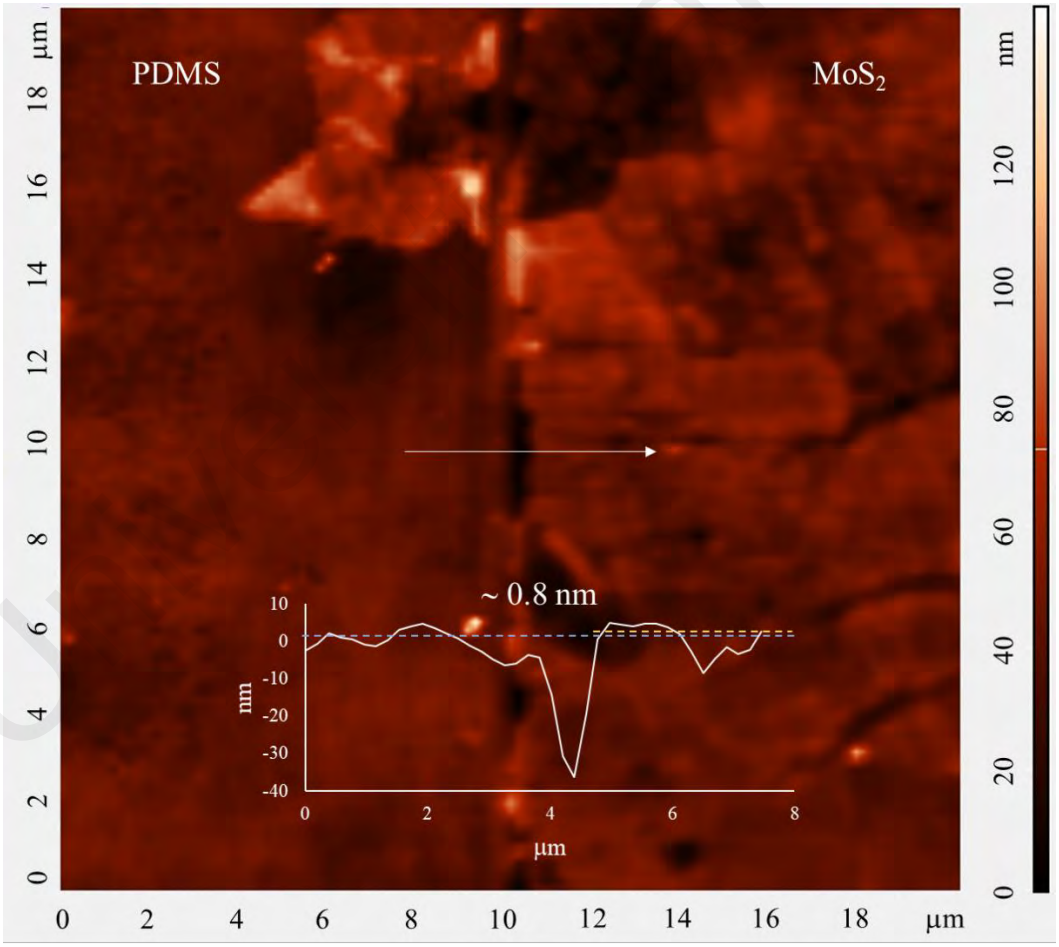

Figure 3.4: AFM of MoS_2-PDMS sample. Figure adapted from (Chew et al., 2023).

To overcome this problem, substrate with relatively low average surface roughness should be used. The average surface roughness of the SiO_2/Si substrate was found to be ~ 0.5 nm, which is approximately 10 times smaller than that of the PDMS substrate. This implies that the thickness measurement upon the transferred MoS_2 on SiO_2/Si substrate will be more reliable. Figure 3.5 shows the AFM of transferred MoS_2 on SiO_2/Si substrate. The result shows that fragmentations and contamination appear on the transferred thin film. The fragmentations may have been caused by the cutting process of MoS_2-PDMS sample using the razor blade, which will be discussed in Section 3.8 and Figure 3.20 later. On the other hand, contamination that appears as "spike" structures may be due to the trapped air bubble during the transfer process, which is similar to the example shown in Figure 2.15 (Kretinin et al., 2014). The possibility of contamination due to dust as the "spike" structures is negated because dust is not observable during optical microscope inspection, as shown in the inset in Figure 3.5. Next, the thickness of MoS_2 thin film was analysed to have a value of 0.71 nm, which is in consistence to the thickness of a monolayer MoS_2 (Luo et al., 2020; Splendiani et al., 2010). Neglecting the micro-cracks and contamination, the thickness of the transferred MoS_2 is quite uniform over a large area. This has been predicted as well using Raman mapping method as described in Section 3.2.

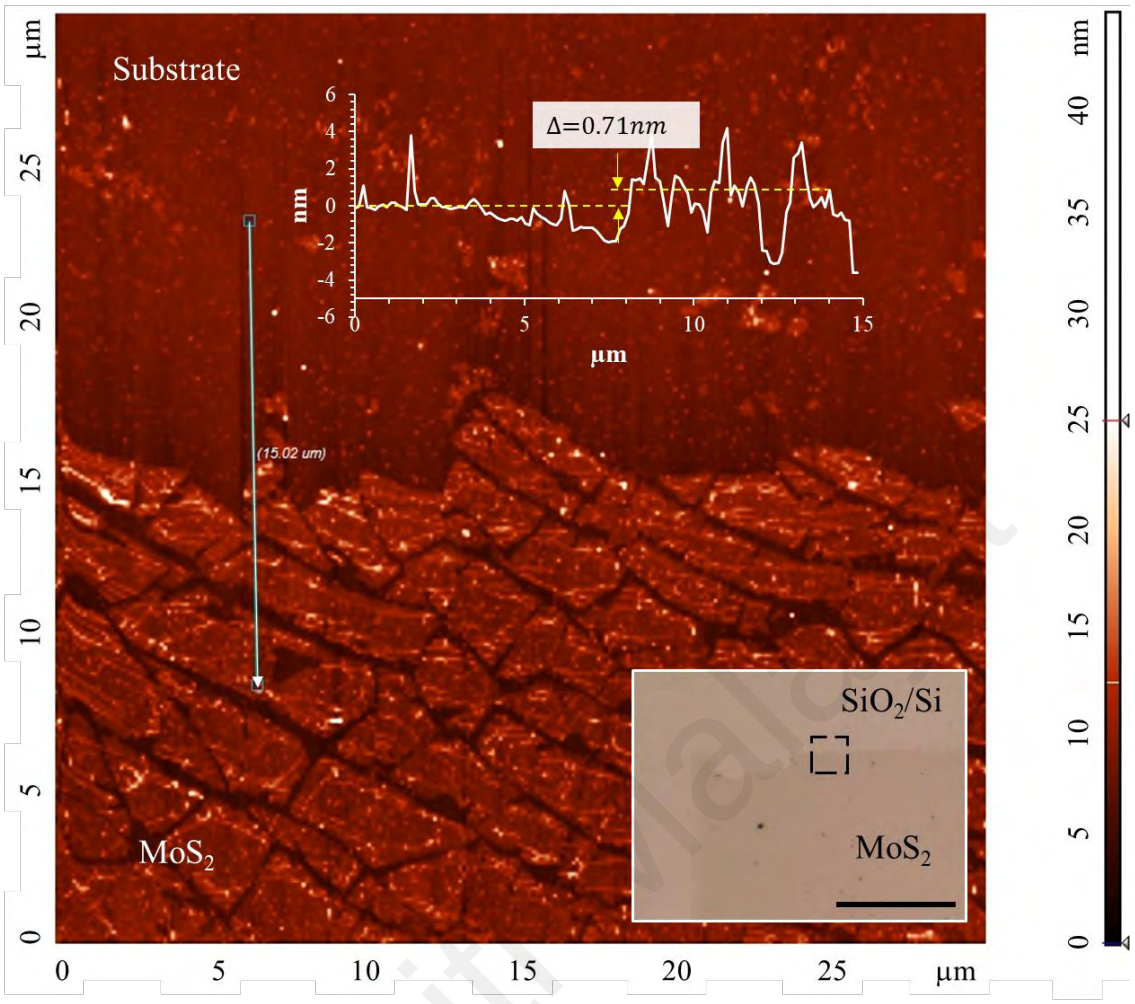

Figure 3.5: AFM of transferred MoS_2 on SiO_2/Si wafer. Inset: Optical micrograph of the area selected for AFM measurement. The scale bar in the inset is 100 µm.

3.4 XPS of MoS_2 Thin Film

XPS investigation was performed on the transferred MoS_2 thin film on a SiO_2/Si wafer. XPS is a surface elemental and composition analysis technique, which is frequently used to study the elemental composition and stoichiometry of a 2D material. Briefly, XPS involves exposing a material to an x-ray beam and analysing the energy of emitted electrons. The obtained spectrum will show the number of ejected electrons per energy interval against the kinetic energy (or binding energy). Due to the fact that the mean free path of electrons in solids is of the order of minute, the detected electrons mainly comes from the surface (within a few nanometers in depth) of the material. This makes XPS a

surface-sensitive technique for elemental analysis. More detail of XPS can be found elsewhere (Chastain & King Jr, 1992). Our XPS measurement is conducted using Kratos X-ray Photoelectron Spectrometer – Axis Ultra DLD. This spectrometer is equipped with an Al K_α monochromatic excitation source, with a source energy of 1486.6 eV. During the measurement, the operating pressure and temperature were maintained at 1×10^{-9} Torr (1.3×10^{-7} Pa) and 300 K, respectively. All spectra were analysed using CasaXPS Version 2.3.15. Figure 3.6 shows the XPS wide-scan (or survey scan) spectrum of the MoS_2 thin film on the wafer. A survey scan is crucial as it reveals the presence of expected and unexpected elements on a surface before a higher resolution narrow scan is performed (Gengenbach et al., 2021). Based on the survey scan spectrum, strong signals were obtained for elements of Si, S, Mo, C and O at their characteristic binding energies. These peaks are as expected as they correspond to the composition MoS_2 and the SiO_2/Si substrate.

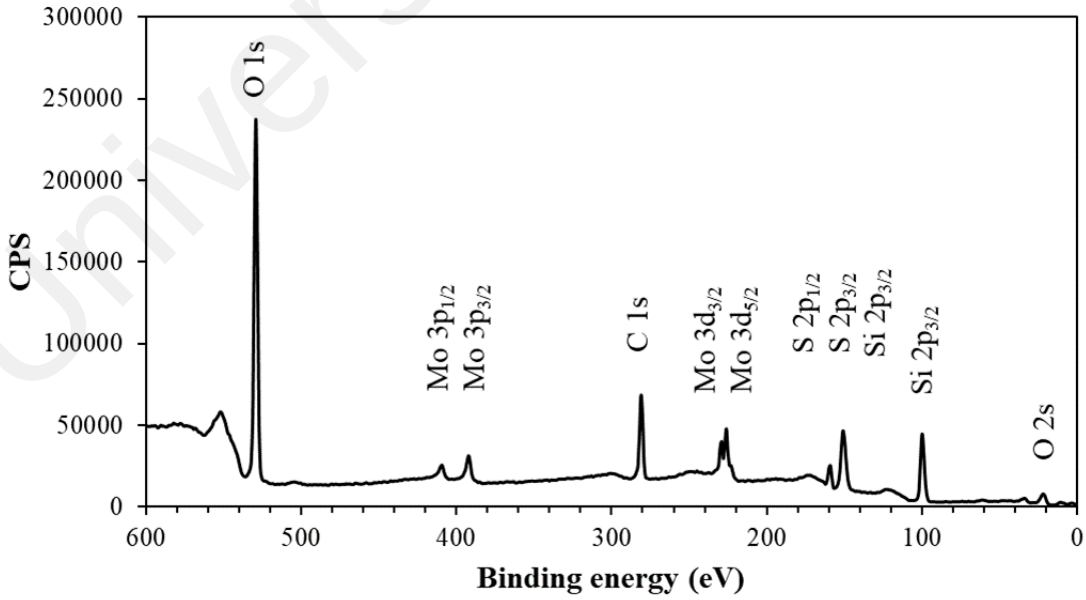

Figure 3.6: XPS wide-scan spectrum of the transferred MoS_2 thin film on a SiO_2/Si wafer.

After that, a narrow scan was performed to obtain a higher resolution spectrum for each element. Figure 3.7 shows the XPS spectra which are informative for the analysis. Again, the analysis was done using CasaXPS software based on crucial precautious and analysis steps published in (Gengenbach et al., 2021; Major et al., 2020). Curve fitting was performed using Gaussian-Lorentzian product and Shirley background. The binding energy scale of all spectra was referenced to Si $2p_{3/2}$ = 103.6 eV (Jensen et al., 2013). The Si $2p_{3/2}$ = 103.6 eV and O 1s = 532.8 eV peaks correspond to the silicon and oxygen lattices in SiO_2 layer of the wafer, respectively, as shown in Figure 3.7(a) and (b) (Jensen et al., 2013). A weak Si $2p_{3/2}$ signal at binding energy of 101.85 eV belongs to the C-Si signal from PDMS contaminant (Louette et al., 2005). The presence of PDMS contaminant can be further proven by C 1s signal with a binding energy of 284.32 eV as shown in Figure 3.7(c) (Louette et al., 2005). Besides that, a few more C 1s peaks with binding energy larger than 284.32 eV were detected which can be assigned to adventitious carbons (AdCs) contamination from the environment (Park et al., 2014b; Tanaka et al., 1993; Wiegand et al., 1989). The PDMS and AdC contamination are common on many surfaces (Gengenbach et al., 2021). More details about these peaks can be found in Table 3.1 below.

Figure 3.7(d) and (e) shows the XPS spectra of the transferred monolayer MoS_2 film. In Figure 3.7(d), three signal peaks were detected at binding energies of 229.86 eV, 233.02 eV and 227.02 eV, which correspond to Mo $3d_{5/2}$, Mo $3d_{3/2}$ and S 2s peaks, respectively. The values are consistent with previously reported values for a CVD-grown monolayer MoS_2 thin film (Park et al., 2014b). Besides, the absence of peak at ~ 236 eV indicates the absence of molybdenum oxide (MoO_3, a very common oxide contamination in CVD-grown MoS_2) on the sample (Kim et al., 2014; Park et al., 2014b; Syari'ati et al., 2019). This can be further confirmed by the absence of peaks larger than the doublet S 2p peaks (S $2p_{3/2}$ = 162.69 eV and S $2p_{1/2}$ = 163.86 eV) of MoS_2 as shown in Figure 3.7(e)

(Park et al., 2014b; Syari'ati et al., 2019). These analyses provide information that the CVD-grown MoS_2 does not oxidize easily in ambient condition. It should be noted that the XPS measurement was done 9.5 months from the purchasing date. This means that the sample is suitable for long-term MoS_2-based application.

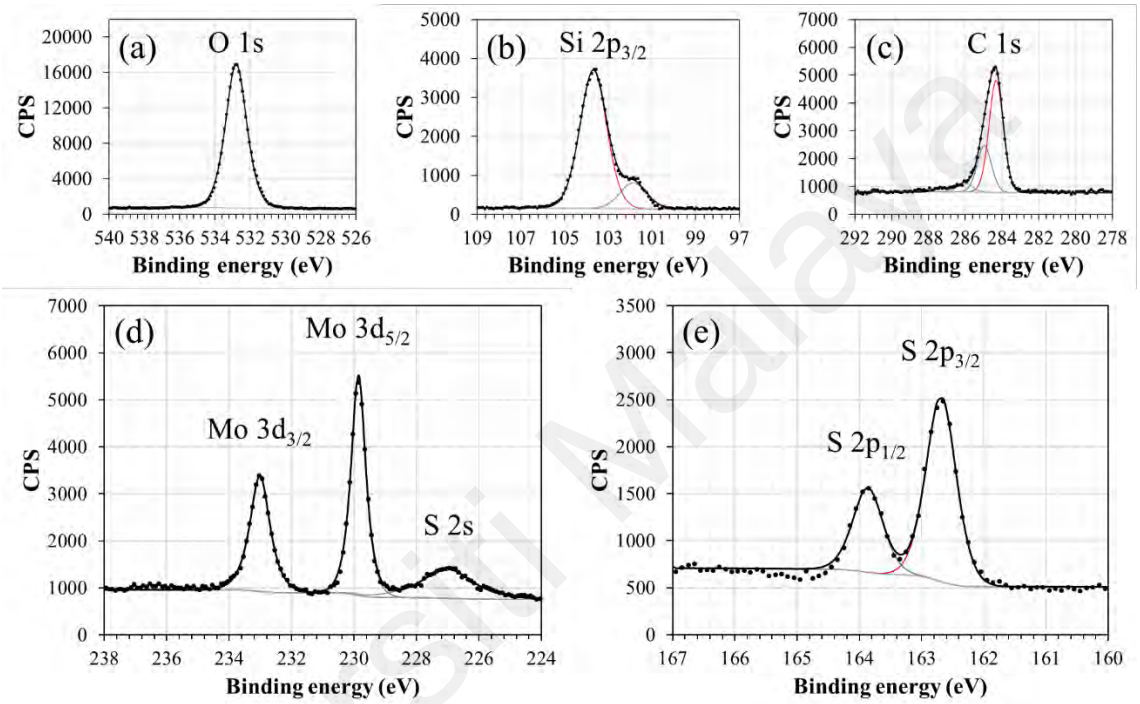

Figure 3.7: XPS narrow scan spectra of the transferred MoS_2 thin film on a SiO_2/Si wafer: (a) O 1s; (b) Si 2p; (c) C 1s; (d) Mo 3d; (e) S 2p spectrum, respectively. Black, filled markers are the measured data while black line corresponds to the fitted curve. CPS is photoelectron counts in counts/s. A Shirley background is used.

To check the stoichiometry of MoS_2, the method described in Section 2.1.1 was used by evaluating the value of (Mo $3d_{5/2}$ – S $2p_{3/2}$) binding energy (Baker et al., 1999). After calculation, it shows that the value of (Mo $3d_{5/2}$ – S $2p_{3/2}$) binding energy is 67.18 eV, which corresponds to MoS_x stoichiometry of slightly more than 2 (~ 2.01). The evaluation leads to an inference that the CVD-grown MoS_2 may contain molybdenum vacancies, which is different with other reported CVD-grown MoS_2 which possess a stoichiometry of less than 2 or sulfur vacancies (Choi et al., 2021; Kim et al., 2014; Wu et al., 2018).

Table 3.1 consists of some important spectral features from the XPS narrow scan. The fitting residuals curve for each of the spectrum in Figure 3.7 are compiled in Appendix A at the end of the thesis.

Table 3.1: Table of XPS spectral features. FWHM: full width at half maximum. Gaussian-Lorentzian product, GL(x) is a curve fitting function defined in CasaXPS, in which GL(100) means a pure Lorentzian while GL(0) means a pure Gaussian.

Element/ transition	Peak Energy (eV)	Peak Width at FWHM (eV)	Sensitivity Factor	Gaussian-Lorentzian product, GL(x)	Peak Assignment
O 1s	532.80	1.41	0.78	GL(58)	Oxygen in SiO_2
C 1s	287.30	0.91	0.278	GL(30)	AdC
C 1s	286.03	0.91	0.278	GL(30)	AdC
C 1s	284.96	0.91	0.278	GL(30)	AdC
C 1s	284.32	0.91	0.278	GL(30)	Carbon in PDMS
Mo $3d_{3/2}$	233.02	0.75	3.321	GL(80)	Molybdenum in MoS_2
Mo $3d_{5/2}$	229.86	0.55	3.321	GL(80)	Molybdenum in MoS_2
S 2s	227.02	1.90	3.321	GL(80)	Sulfur in MoS_2
S $2p_{1/2}$	163.86	0.57	0.668	GL(45)	Sulfur in MoS_2
S $2p_{3/2}$	162.69	0.57	0.668	GL(45)	Sulfur in MoS_2
Si $2p_{3/2}$	103.68	1.44	0.328	GL(32)	Lattice silicon in SiO_2
Si $2p_{3/2}$	101.85	1.44	0.328	GL(32)	Silicon in PDMS

3.5 Time-Resolved Z-Scan Measurement

Time-resolved Z-scan measurements were carried out on the MoS_2-PDMS sample to determine the nonlinear refractive index, n_2, of the large area monolayer MoS_2 thin film. One of the advantages of this sample is that the PDMS substrate is transparent over a

broad spectral range, making it a suitable substrate for optical studies. Moreover, the MoS_2 thin film is uniform over a large surface area, which favours the time-resolved Z-scan measurement because the thickness and morphology of the thin film remain the same across the z-position. Again, this technique is typically used to solve thermal lensing effect from the sample induced by a continuous wave or high repetition rate pulsed laser source in the measurement. To determine if it is necessary to apply this technique, the thermal characteristic time, $t_c = \omega^2/4D$, of the sample should always be evaluated first (Falconieri, 1999). Cumulative heating effect usually happens on the substrate or liquid medium (such as the solvent in liquid phase exfoliated MoS_2 dispersion) that holds the sample. In this reasoning, the t_c of PDMS substrate shall be determined first. A PDMS has density $\rho = 965\ kg\ m^{-3}$, specific heat $c_p = 1460\ J\ kg^{-1}K^{-1}$, and thermal conductivity $\kappa = 0.15\ W\ m^{-1}K^{-1}$, the thermal diffusion coefficient can be determined as $D = \kappa/\rho c_p = 1.06 \times 10^{-7} m^2 s^{-1}$ (Falconieri & Salvetti, 1999). If the beam waist at focus position of Z-scan has a radius, $\omega_0 = 26\mu m$, then $t_c \cong 1.6ms$. This means that thermal effect induced by a laser pulse at the focal point persists over ~ 1.6 ms in a PDMS substrate. In the laser setup, the repetition rate of the mode-locked laser is 1.0 MHz, which gives a pulse-to-pulse spacing of 1.0 μs. As t_c of PDMS at the focal spot is longer than the pulse-to-pulse spacing, cumulative heating effect will occur, which could lead to thermal effects. Therefore, time-resolved Z-scan should be carried out to separate the thermal lensing effect from the instantaneous NLR effect of the MoS_2 sample.

3.5.1 Experimental Setup of Time-Resolved Z-Scan Technique

The apparatus of time-resolved Z-scan is shown in Figure 3.8 below. A homemade mode-locked fiber laser source operating at a center wavelength of 1560 nm was used. The laser has pulse width and repetition rate of 450 fs and 1.0 MHz, respectively. The

polarization state of the laser was set and verified to be vertically polarized (polarization which is parallel to the direction of gravity) using a polarimeter (Thorlabs PAN5710IR3). An optical attenuator was placed at the output of laser source to vary the laser power. The laser beam was expanded by a factor of 10 using a pair of plano-convex lenses, namely L_1 and L_2. After the expansion, the laser beam has a diameter of ~ 4.3 mm measured using conventional knife-edge technique. Within this Keplerian beam expanding arrangement, a mechanical shutter (Minolta Dynax 7) was placed at the focal point of L_1 to create an opening window for the experiment. Although optical chopper is often used by other works (Falconieri & Salvetti, 1999; Gnoli et al., 2005), the mechanical shutter provides the similar function as well while providing a simpler control in setting the duration of the opening window. In our experiment, an opening window of 5 ms with risetime of 30 μs is employed. Next, a plano-convex lens (L_3) with a focal length f = 100 mm was used to focus the laser beam. At focus, a beam waist radius of $\omega_0 = 26\mu m$ and Rayleigh length $z_0 = 1.4mm$ can be achieved. A pair of identical photodiodes (Thorlabs PDA50B-EC), namely PD_1 and PD_2, were used to collect the OA and CA signal powers, respectively. The aperture transmission $S = 0.2$ was used for CA Z-scan. An oscilloscope (Tektronix TDS1001B) was used to record the output signals. The sample was translated along the laser axis with a linear translation stage (Thorlabs LTS300/M). It should be noted that the measurement technique of time-resolved Z-scan is different from conventional Z-scan. In a conventional Z-scan, optical power meters will be used to collect the signal while the sample is translated along the laser path. On the other hand, time-resolved Z-scan relies on the collection of temporal transmission signal from the sample at a fixed z-position using photodiodes. This means that the signal collection is performed on a step-by-step basis from negative to positive z-position. In this experiment, measurement at each z-position was repeated 3 times.

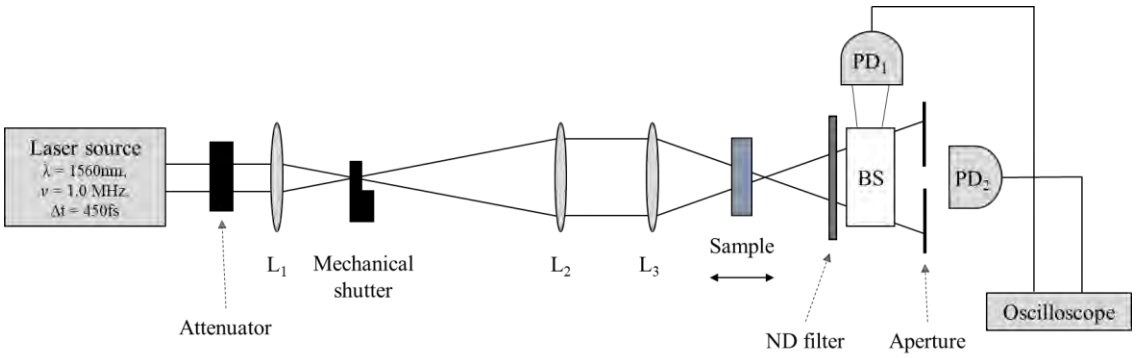

Figure 3.8: Experimental arrangement of the time-resolved Z-scan technique. Here, L_1, L_2 and L_3 are plano-convex lens; BS represents a beam splitter; PD_1 and PD_2 are photodiodes for OA and CA signal measurement, respectively. Figure adapted from (Chew et al., 2023).

3.5.2 Results and Discussion

In a time-resolved CA Z-scan measurement, the normalized signal intensity from the sample can be described using Equation 2.24. Before commencing the further analysis, one should determine the order of absorption parameter q. This is because the value of q will change the characteristic of thermal lensing effect over the z-position. To do this, conventional Z-scan measurements were first performed on the MoS_2-PDMS sample using two different laser sources - a pulsed laser and a continuous wave (CW) laser source. The experimental setup is very similar to that shown in Figure 3.8, except the replacement of PDs with OPMs (Thorlabs, S144C). The reason of using CW source is to check whether thermal lensing effect happens due to linear absorption of the laser (q = 1) by the sample. As the intensity of the CW source is very low (less than 1 kW/cm^2), NLR should be absent during the CA Z-scan measurement. If the transmittance of the sample shows a refraction-like traces (similar to Figure 2.25(a)), then thermal lensing effects are expected to occur. In fact, using both laser sources, at the same average power levels (3 mW), their output transmittance curves show a peak-to-valley configuration which correspond to self-defocusing behavior, as shown in Figure 3.9.

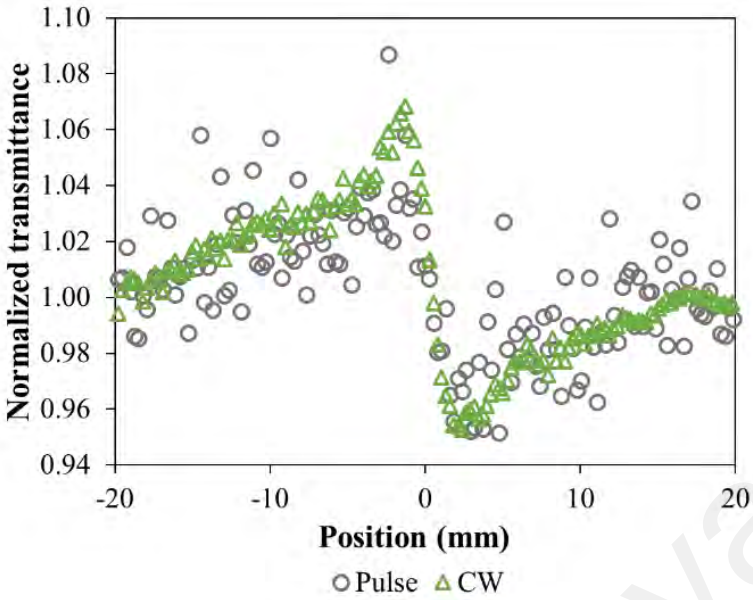

Figure 3.9: Output transmittance of conventional CA Z-scan measurements upon MoS_2-PDMS sample using pulse and CW laser sources. The average power of both lasers is set to 3 mW. A similar peak-to-valley trend between two laser sources imply that the observed lensing properties comes from thermal lensing effect. Figure adapted from (Chew et al., 2023).

The normalized peak-valley transmittance difference (ΔT_{p-v}) obtained from Z-scans using both lasers show a similar value of ~ 0.11. It should be noted that the measurement sensitivity of our current measurement setup is 1%. This implies that the self-defocusing properties arise from thermal lensing effect in MoS_2-PDMS sample. For further verification, the normalized peak-valley distance (Δx_{p-v}) was determined as suggested in Table 2.4 in Section 2.5.1.2. Both curves show $\Delta x_{p-v} = 3.7 z_0$, which is close to the predicted value of $3.46 z_0$ for one photon absorption thermal lensing effect (Falconieri, 1999). For this reason, we use q = 1 in our time-resolved Z-scan analysis. Therefore, Equation 2.24 (Falconieri, 1999) can be reduced to:

$$\frac{I(x,t)}{I(x,0)} = 1 + \vartheta(1)\tan^{-1}\left(\frac{2x}{[9+x^2]\frac{t_c(x)}{2t} + 3 + x^2}\right) \tag{3.1}$$

Figure 3.10 depicts two normalized transmittance curves of the MoS_2-PDMS sample over a period of 2 ms obtained from time-resolved CA Z-scan measurement. The blue and orange open symbols in Figure 3.10 correspond to the normalized transmittance at the prefocal and postfocal z-position, respectively. One can notice that there is an intersection at t = 0.45 ms. This indicates that there is a change in normalized transmittance before and after 0.45 ms. In other words, there is an inversion of peak and valley in the CA curve. The Z-scan signal changes from a valley-peak to a peak-valley configuration. This implies that the instantaneous electronic nonlinearity (in this case, the NLR effect) and thermal lensing effect of MoS_2-PDMS sample have opposite signs. Note that the solid symbols are extrapolated values at t = 0, which will be used to reconstruct the Z-scan curve as a representation of the NLR as discussed in the last part in Section 2.5.1.2.

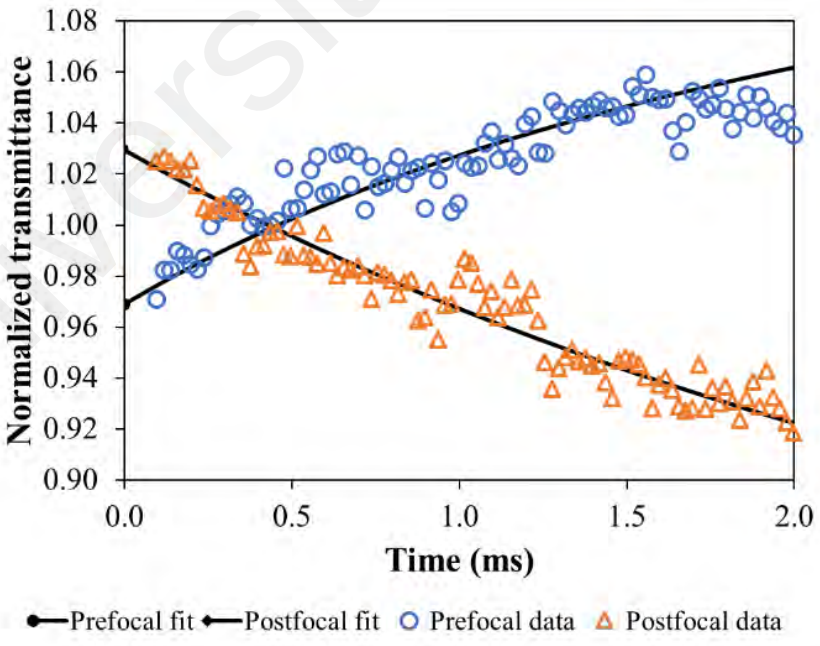

Figure 3.10: Normalized CA transmittance curve of MoS_2-PDMS sample obtained at prefocal and postfocal z-positions. The black curves are the fits evaluated from Equation 3.1. Open symbols are the experimental data, whereas the solid symbols are extrapolated values at t = 0, which will be used to reconstruct the Z-scan profile for NLR process. Figure adapted from (Chew et al., 2023).

Figure 3.11 shows the reconstructed CA Z-scan profiles of MoS_2-PDMS sample at time t = 0 and 2 ms. The reconstructed profile shows that at t = 0, the NLR resembles self-focusing characteristic (valley-to-peak configuration). The Δx_{p-v} of the NLR trace is evaluated to be $1.80z_0$, which is close to the theoretical value of $1.72z_0$ for Kerr induced self-focusing effect (refer Table 2.4). At t = 2 ms, the sample manifests self-defocusing thermal lensing characteristic, which is similar in Figure 3.9. It should be noted that at this intensity, no NLA such as saturable absorption was observed from MoS_2 from the OA Z-scan measurement, as illustrated in the inset of Figure 3.11. One of the possible reasons may be due to the fact that the linear absorption of monolayer MoS_2 is as low as 0.2%, which is less than the 1% measurement sensitivity of our current measurement setup. Nevertheless, the possibility of the presence of NLA cannot be omitted totally, as it can exist within the noise level.

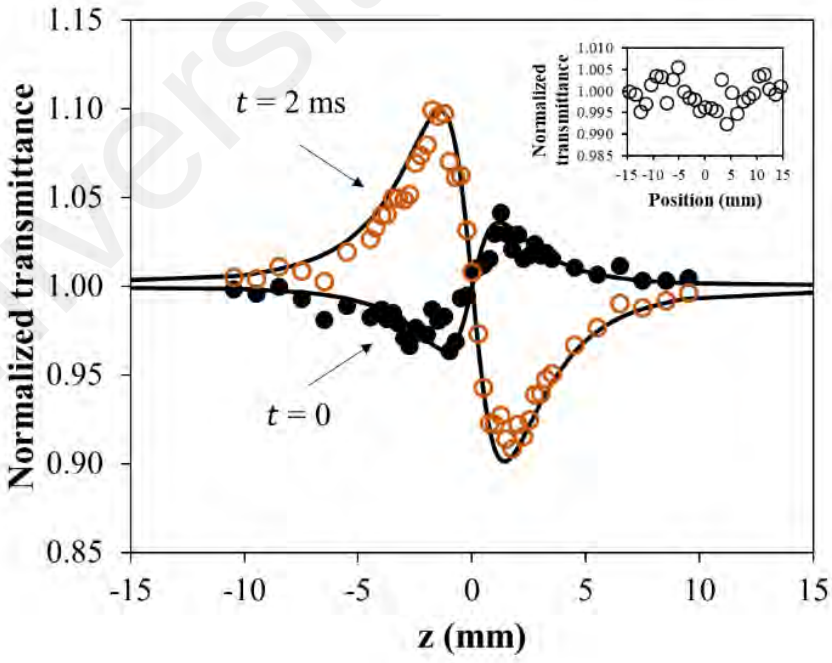

Figure 3.11: Reconstructed CA Z-scan profiles of MoS_2-PDMS sample at time t = 0 and 2 ms. The solid curves are theoretical fit. Inset: OA Z-scan trace, where no significant NLA can be observed. Figure adapted from (Chew et al., 2023).

The normalized transmittance of Z-scan trace at t = 0 and 2 ms in Figure 3.11 can be fitted using Equation 2.12 and Equation 3.1, respectively. By fitting the data at t = 0, the value of $\Delta\Phi_0$ can be determined, which allow the evaluation of n_2 of MoS_2-PDMS sample using Equation 2.13, with L the thickness of the sample, where $L = L_{MoS_2} + L_{PDMS}$. It is worth noting that the linear absorption coefficient of the sample at 1550 nm is approximately 2.0 cm^{-1}. As a result, the n_2 of MoS_2-PDMS sample was calculated to be 1.49×10^{-18} m^2 W^{-1}. However, this value refers to the effective n_2 of the sample, which consists of the monolayer MoS_2 as well as the PDMS substrate. To separate the NLR effect of PDMS substrate from the MoS_2 thin film, Equation 2.13 (Boyd, 2008) can be re-written as:

$$\Delta\Phi_0 = kI_0(n_{2,MoS_2}L_{MoS_2} + n_{2,PDMS}L_{PDMS}) \tag{3.2}$$

In this way, the n_{2,MoS_2} can be determined from Equation 3.3 below:

$$n_{2,MoS_2} = \frac{n_2 L_{eff} - n_{2,PDMS}L_{PDMS}}{L_{MoS_2}} \tag{3.3}$$

where the MoS_2 thin film thickness, L_{MoS_2} is 0.7 nm, PDMS substrate thickness, L_{PDMS} is 500 μm, and effective nonlinear refractive index of the MoS_2-PDMS sample, n_2, is 1.49×10^{-18} m^2 W^{-1}. To determine the contribution of $n_{2,PDMS}$, time-resolved Z-scan was performed on a clean PDMS substrate without the MoS_2 thin film coating. The result shows that PDMS exhibits a $n_{2,PDMS}$ = 1.22×10^{-18} m^2 W^{-1}. Hence, the value of n_{2,MoS_2} is deduced to be 1.40×10^{-13} m^2 W^{-1}. The deduced n_{2,MoS_2} shares a similar magnitude with reported value for monolayer MoS_2 measured at 2.0 μm wavelength, which is 2.5×10^{-13} m^2 W^{-1} (Pan et al., 2020). Furthermore, it is approximately 5 (Hon et al., 2011; Tsang et al., 2002; Zhang et al., 2014b) and 7 (Agrawal, 2000; Boyd, 2008) orders of magnitude larger than that of the silicon and common bulk dielectric materials, respectively. This

indicates the potential of monolayer MoS_2 in the development of optical nonlinear devices, such as an all-optical switch, operating in the C-band wavelength range.

3.6 Fabrication of Planarized Optical Waveguide

The planarized optical waveguide is fabricated through the process steps as shown in Figure 3.12. The first step involves flame hydrolysis deposition (FHD) to deposit a SiO_2 core layer on a 7 μm-SiO_2/silicon substrate. Using oxy-hydrogen flame, metal halides such as silicon tetrachloride, germanium tetrachloride and boron trichloride are hydrolized and turn into their respective oxides in the form of a soot layer. The hydrolysis between silicon tetrachloride and germanium tetrachloride can produce a germanium-doped SiO_2 layer on top of the SiO_2/silicon substrate, with a refractive index which is higher than the pure SiO_2 layer. By optimizing the process parameters, a 3 μm-thick germanium-doped SiO_2 layer is produced. The refractive index and propagation loss of this layer are examined using a prism coupler, and their values are 1.486 and < 0.2 dB/mm (at 1550 nm), respectively. To obtain straight channel waveguide structures, a chromium layer followed by a photoresist layer are deposited on the core layer. By conducting photolithography and plasma etching processes, straight channel structure is obtained. After removing the chromium mask, a polymer named ZPU13 with refractive index of 1.44 (measured at 1550 nm) is spin-coated on the patterned waveguide as the overcladding. The overcladding is then etched using oxygen plasma etching method until it reaches the top of the waveguide core. With these steps, a planarized, straight channel waveguide is fabricated and is ready for basic characterizations.

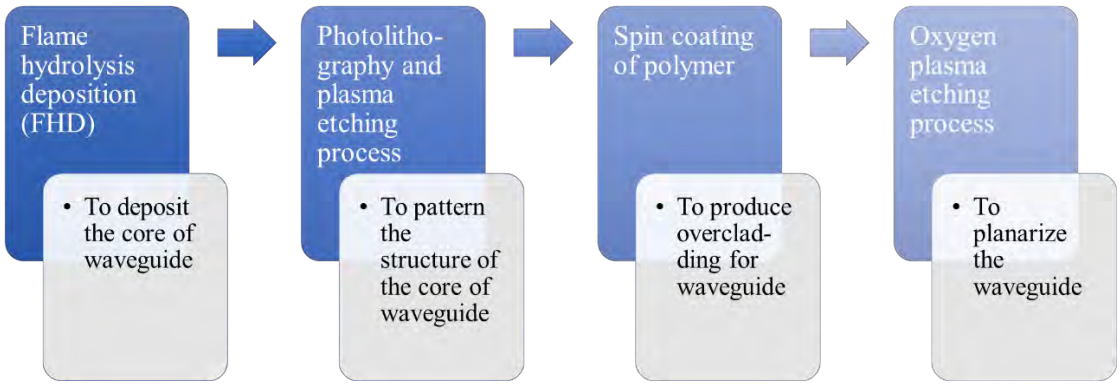

Figure 3.12: Flow chart for the fabrication process of the planarized optical waveguide.

Figure 3.13 shows the cross-sectional view of the planarized optical waveguide produced using the above fabrication processes. Its micrograph is taken using an optical microscope that operates in transmission mode, as shown in Figure 3.13(b). The core of the waveguide appears bright, which shows its capability in light guiding. The core has a dimension of 2.4 μm × 3 μm that supports fundamental mode of light propagation only at the C-band wavelength. One of the advantages of this planarized structure is that evanescent field interaction is made possible between a material that is coated on top of the waveguide core and the guided field. Besides that, this structure is considered mechanically robust compared to other fiber-based waveguides that also allow evanescent field interaction, such as side-polished optical fiber or tapered fiber. Due to its physical robustness, it will not break easily, which makes it a good prototype platform to deposit other material such as 2D MoS_2 on top of the core to functionalize the waveguide. The outcome can pave a way for the development of photonics integrated circuits (PICs).

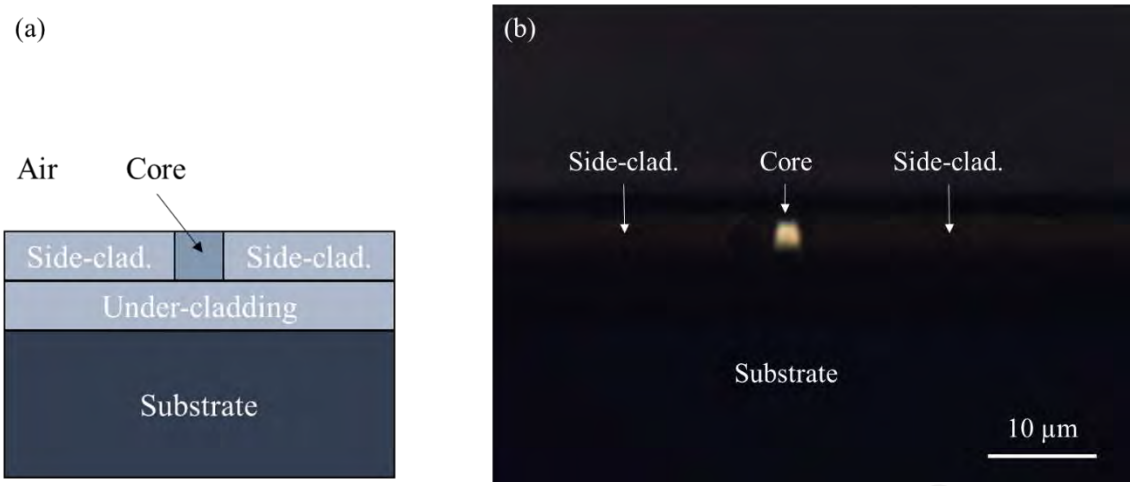

Figure 3.13: (a) Schematic diagram of the cross-sectional view of the planarized optical waveguide; (b) Optical micrograph of the planarized optical waveguide using an optical microscope operating in transmission mode. Figures adapted from (Chew et al., 2022a).

The PICs bring significant development in terms of signal transmission in telecommunications (Hunsperger, 2009). In general, the concept of a PIC is to use optical waveguides (as a basic structure) with different structures to realize compact and robust devices performing functions similar (and better than) to an electrical integrated circuit (Hunsperger, 2009; Suhara & Fujimura, 2003). The development starts from 1980s until today, and this technology provides numerous advantages to the mankind. The most direct impact to our mankind is that we can enjoy the fast data transmission speed on the Internet. Besides the increased data transmission bandwidth benefit, the PICs allow a more compact, low weight and lower power consumption advantages to realize their function. For example, various optical components such as mirrors, lenses, prism, electro-optic modulators and detectors are needed for signal processing. The equipment may occupy large spaces, typically a few or tens of meter on a laboratory bench. However, by integrating these components in a PIC, the size can be greatly reduced into a chip-size (Hunsperger, 2009; Suhara & Fujimura, 2003). So far, numerous components of PICs have been developed, which include electro-optic and acousto-optic devices, waveguide lasers, dense wavelength division multiplexers, and optical parametric amplifiers. By

integrating such components together, a PIC with a specific function can be realized, which is useful for, says, optical communications (Hunsperger, 2009; Jia & Chen, 2019; Suhara & Fujimura, 2003). The present work that integrates MoS_2 on planarized waveguide can serve as a study to provide a useful insight in developing a chip-based optical device. The aim is to utilize the nonlinear optical properties of a large area monolayer MoS_2 on a waveguide, for fundamental study as well as application. To achieve this, the monolayer MoS_2 will be transferred to a planarized waveguide using PDMS-assisted transfer technique. In the next sub-chapter, the preparation of MoS_2-PDMS stamp as well as its transferring process will be discussed.

3.7 Preparation of MoS_2-PDMS Stamp

As discussed in Section 2.3.2, 2D MoS_2 can be transferred to a target surface using a viscoelastic PDMS stamp. The CVD-grown large area monolayer MoS_2 on a PDMS substrate as shown in Figure 3.1(a) will act as the MoS_2-PDMS stamp. The focus in this section is to discuss to the details of the MoS_2-PDMS stamp preparation with a suitable size for experimental purpose, as well as some precautions taken during transferring process.

3.7.1 Cutting Method

In order to prepare MoS_2-PDMS stamp with the desirable size, a suitable cutting method must be considered so that the cut piece is not contaminated and the MoS_2 film is not damaged. To achieve these, two approaches were tested. The first is a contactless laser cutting method whereas the second, a razor blade cutting method.

3.7.2 Laser Cutting on PDMS

Laser cutting method is common in cutting polymeric materials (Caiazzo et al., 2005; Ham & Lee, 2020; Mushtaq et al., 2020; Ng et al., 2020; Ortiz et al., 2020), including PDMS (Isiksacan et al., 2016; Liu & Gong, 2009; Wu et al., 2022). It is considered as a contactless cutting method which may be beneficial to avoid damaging the MoS_2 film due to physical contact. Figure 3.14(a) illustrates a schematic diagram of the laser cutting method. A laser source (either pulsed or continuous wave) is focused by a lens onto the polymer workpiece. By translating the workpiece, a line cut, or a kerf, can be formed due to the applied laser energy that ablates the polymer, as shown in Figure 3.14(b). The kerf width is dependent on a few parameters, such as the power of incident laser, and cutting speed. Studies show that the kerf width is directly proportional to laser power (Sheng & Cai, 1996), and inversely proportional to the cutting speed (Al-Sulaiman et al., 2006; Quintero et al., 2011). Furthermore, the ablation depth is affected by number of pulses, laser power, scan speed (Caiazzo et al., 2005; Liu & Gong, 2009; Ng et al., 2020). Depending on the laser parameters, a kerf that cut and separate the polymer may not be appeared. Sometimes, the polymer is only partially ablated, and more efforts (such as multiple pass of laser on the same position) are needed to cut the polymer completely. Examples of partially ablated PDMS sample is shown in the inset of Figure 3.14(c) and (d). Figure 3.14(c) shows that the cutting (or ablated) depth of PDMS sample increases with increasing laser power. On the other hand, as the cutting speed increases, the cutting depth reduces (Liu & Gong, 2009). Based on this study, it clearly shows that to create a large cutting depth, large laser power and slow cutting speed should be used.

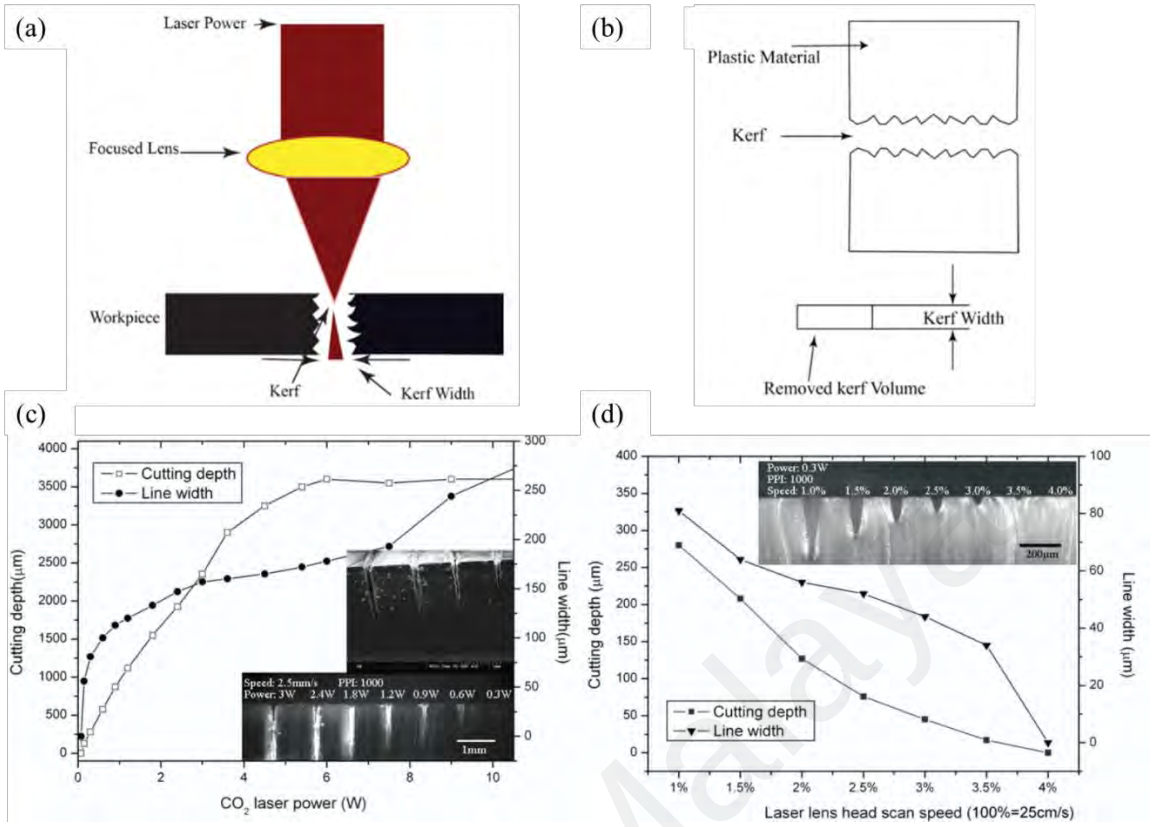

Figure 3.14: Schematic diagram of (a) laser cutting method; (b) the kerf formation due to the laser cutting process, figures adapted (Mushtaq et al., 2020); (c) relationship between the cutting depth of PDMS sample and CO_2 laser power; (d) the dependency of cutting depth of PDMS sample on the cutting speed, figures adapted from (Liu & Gong, 2009).

Before cutting the MoS_2-PDMS stamp, a plain PDMS was used as the trial workpiece to investigate the required laser parameters. The laser cutting setup is shown in Figure 3.15. A high energy pulsed laser source with center wavelength of 515 nm and variable repetition rate was used (NKT ORIGAMI 10 XP). The laser was focused by a plano-convex lens with a focal length of 62.9 mm. The PDMS sample surface that was placed on a 3-axis translation stage was brought to the focus of the laser. The laser irradiated spot of the sample was monitored using a CCD camera, as shown in the figure.

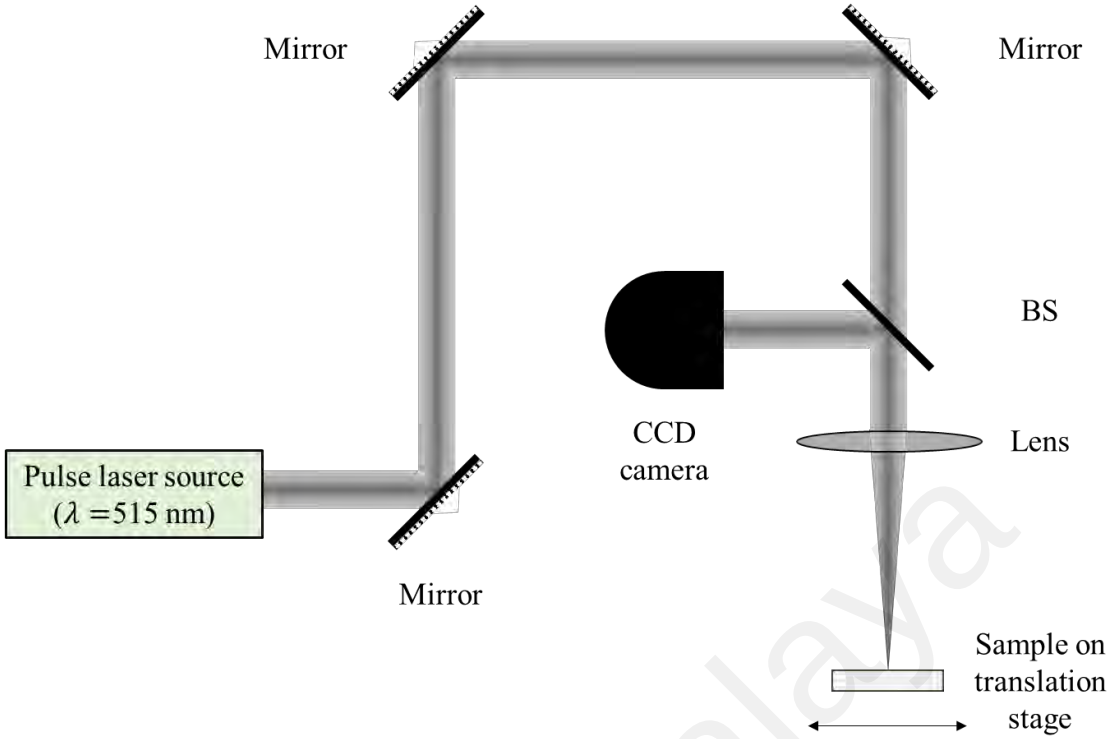

Figure 3.15: Schematic illustration of the laser cutting setup.

Initially, the laser was set to a high laser energy of 16 μJ and a repetition rate of 5 kHz. The cutting process was tested with a cutting speed of 0.5 mm/s and 0.25 mm/s. The aim of using slow cutting speed is to produce large ablated depth on the PDMS sample. Ablation on PDMS was observed at both cutting speeds, as shown in Figure 3.16. The ablation depth increases from 111.2 μm to 164.5 μm when the cutting speed decreases from 0.5 mm/s to 0.25 mm/s. However, from the top view image, it is found that there are ablated debris which appeared as tiny powder-like debris spreading around the ablation line. These debris are usually called plume. From Figure 3.16, it is obvious that the coverage area of the plume is at least 200 μm from the cutting line for both cutting speed. At lower cutting speed, it is found that the amount of plume increases, and it covers a large area on the PDMS sample. This means that higher cutting speed could reduce the presence of plume. Although the ablation depth can go as deep as 164.5 μm (~ 33%

thickness of PDMS), the plume will impose contamination to the monolayer MoS_2 film, which may introduce uncertainty to the subsequent studies.

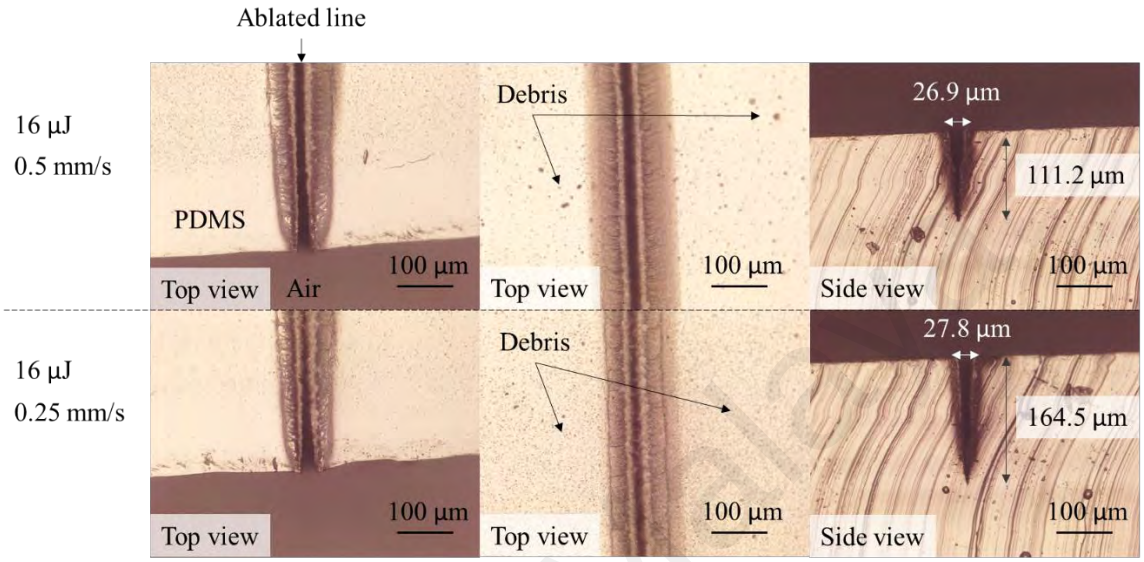

Figure 3.16: Optical micrograph of the laser ablation of PDMS substrate at a fixed pulse energy of 16 µJ and repetition rate of 5 kHz, but with different cutting speed. The image is taken with optical microscope operates in reflection mode, with 10x magnification.

The pulse energy and repetition rate were reduced to 10.6 µJ and 1 kHz, respectively, and the cutting speed was increased from 1 mm/s to 5 mm/s to see whether the plume can be reduced. The results are shown in Figure 3.17(a). It is found that by increasing the cutting speed from 1 mm/s to 5 mm/s, the plume can be reduced. However, the ablation depth of PDMS is greatly reduced. In Figure 3.17(b), it is demonstrated that the ablated depth is reduced to 6 µm at a cutting speed of 5 mm/s. This depth is approximately 1.2% of the PDMS sample thickness. Although the plume is reduced, the ablated depth becomes insignificant, making the cutting process inefficient. To increase the ablated depth, an experiment is conducted by increasing the number of laser pass on the PDMS sample at a constant cutting speed of 5 mm/s, as shown in Figure 3.17(c). As the number of pass

increases 10 times, the ablated depth is increased accordingly to a value of 51.4 μm. Despite the increase in ablated depth, the formation of plume increases as well. Therefore, a conclusion is drawn that the formation of plume is unavoidable to some extent. This is because the plume is the ablated side-products from the host material. Similar issue is found in other reports as well (Ham & Lee, 2020; Wu et al., 2022). It should be noted that there are some proposed methods that can reduce the debris deposited on the sample, for instance, by carrying out the ablation in the presence of purging gas (Chang & Molian, 1999; Ng et al., 2020) or liquid (Chang & Molian, 1999). By purging gas (such as oxygen and nitrogen gas) in the direction perpendicular to the laser beam, the plume is possible to be swept away. However, there is also case in which the plume cannot be removed in the presence of purging gas (Spiess & Strack, 1989). Their work showed that the debris is deposited on the surface in the direction of the purging gas, even though the flow rate of the purging gas is as large as 0.5 l s^{-1}. The debris has to be removed by immersed the sample with acetone in an ultrasonic bath. This shows that the gas-purging method may not be effective to completely remove the plume from the ablated region. On the other hand, if the ablation is carried out in a liquid medium, the plume could be minimized (Chang & Molian, 1999). However, due to the thermal and chemical properties of the liquid, bubbles are created during the ablation process, which affect the laser intensity and affect the ablation efficiency. If the intensity of laser is too high, chemical breakdown of the liquid may happen, producing by-products with different chemical properties. To avoid any chemical reaction between the liquid (and/ or the by-products) and MoS_2 thin film, this method is not employed. Based on the discussion, it is deduced that the contactless laser cutting method will impose contamination due to the ablation process, and therefore, not a suitable cutting method for the PDMS sample used in this work.

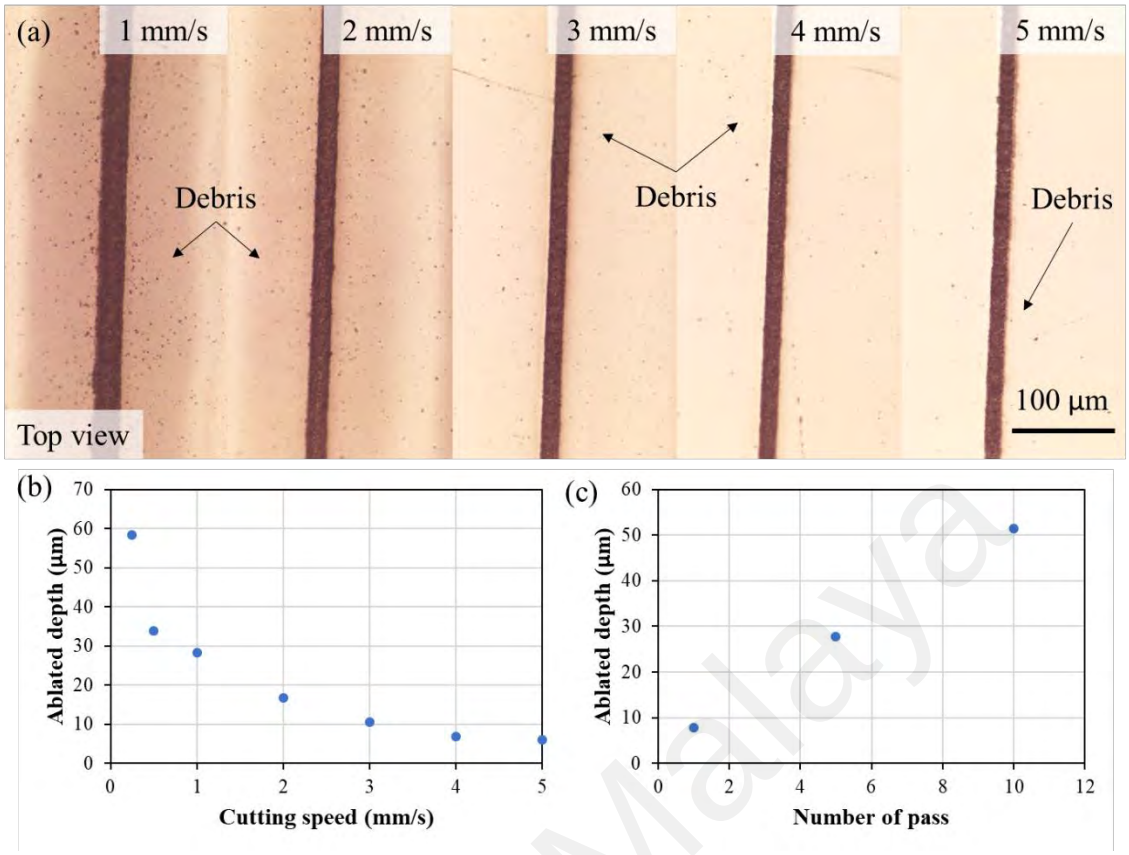

Figure 3.17: (a) Optical micrograph of the laser ablation of PDMS substrate at a fixed pulse energy of 10.6 µJ and repetition rate of 1 kHz, but with different cutting speed. The image is taken with optical microscope operates in reflection mode, with 10x magnification; (b) Graph of ablated depth of PDMS sample against laser cutting speed; (c) Graph of ablated depth of PDMS sample against number of laser pass at a fixed cutting speed of 5 mm/s.

3.7.3 Razor Blade Cutting on PDMS

Next, the investigation continues on the razor blade cutting method on MoS_2-PDMS sample. A sharp razor blade was used in the experiment. It should be noted that a razor blade, which is usually made up of metal, has a large surface energy. The MoS_2 film may adhere to the large surface energy of the sharp edge of the blade during the cutting, causing physical deformation of the film. On the other hand, a razor blade cutting is more commonly available, cheap and easier to handle compared to laser cutting. To start the cutting process, the experimental arrangement is as shown in Figure 3.18. The sample was fixed on a substrate holder. The section of the sample to be cut was observed using a

long working distance viewing system. It is found that this method can cut the MoS_2-PDMS sample into individual pieces (for example ~ 1 mm × 2 mm size) with ease. A clean, thorough cut can be done when the razor blade is lowered down perpendicularly until it reaches the bottom surface of the sample.

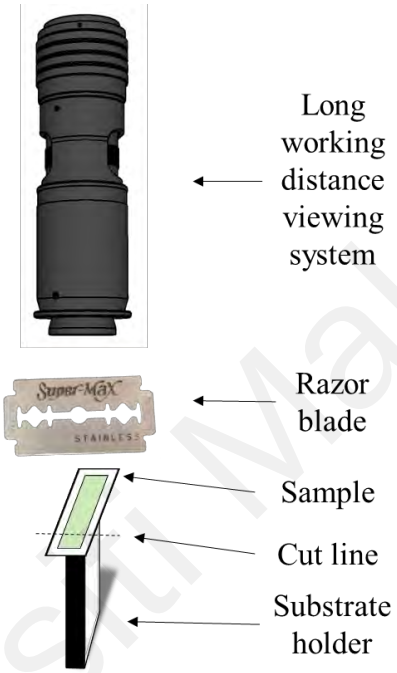

Figure 3.18: Schematic diagram of the razor blade cutting arrangement.

Figure 3.19 shows the optical micrographs of the sample cut using a razor blade at different magnifications. The sharp razor blade can produce clean cut edges which can be seen in Figure 3.19(a). It should be noted that there is an optical contrast between the atomically thin MoS_2 and the PDMS substrate, where the MoS_2 thin film appears visually brighter compared to the PDMS (Figure 3.19(c)). Besides that, a small area at the cut edges of MoS_2 thin film is delaminated from the PDMS, which can be observed in Figure 3.19(c) and (d). The delamination has a length of ~ 10 μm. This observation can be explained by the large surface energy of the metallic razor blade, in which a small portion

of MoS2 thin film (~ 10 μm) adheres on the blade and delaminated from its original PDMS substrate eventually, as illustrated in Figure 3.20(b) and (d). However, the delamination can be considered negligible (< 0.4%) compared to the MoS_2-PDMS piece which has MoS_2 thin film with few mm in length (consider 2.4 mm MoS_2 thin film, the shortest film transferred onto the waveguide which will be shown in the later chapter). This means that < 0.4% of MoS_2 thin film is lost at each cut edge.

In addition to delamination, fragmentation and micro-cracks of MoS_2 thin film can also be observed under the optical microscope with 100x magnification. The fragmentation in Figure 3.19(c) appears to be approximately 20 – 40 μm in length. These defects are absent at the area of MoS_2-PDMS away from the cutting edge, refer to Figure 3.19(b). The presence of fragmentation and micro-cracks may occur during the cutting process, as illustrated in Figure 3.20. In Figure 3.20(c), when the razor blade touches and cut through the viscoelastic PDMS, part of the PDMS will adhere to the razor blade body. The PDMS deforms as the blade moves downwards. Due to the deformation of the PDMS, the MoS_2 film coated on top of PDMS will experience stress and in-plane strain as well. If the forces are large enough to overcome the binding force of the MoS_2 particles, micro-cracks can happen, leading to film discontinuity or fragmentation near the cut edge of the sample, as shown in Figure 3.19(c), Figure 3.19(d) and Figure 3.20(d).

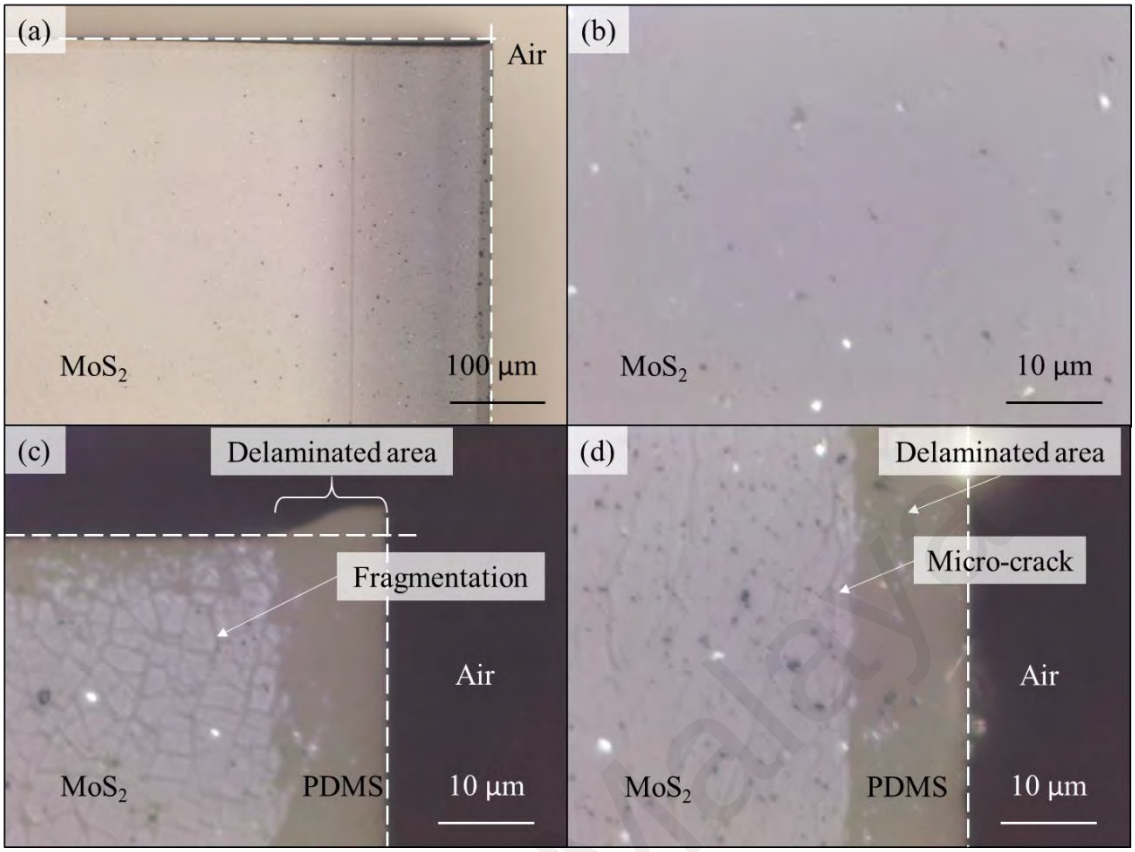

Figure 3.19: Optical micrograph of the MoS_2-PDMS sample using razor blade cutting method: (a) cutting edge (indicated by white dash line) of the sample in 10x magnification; (b) area of MoS_2-PDMS sample away from the cutting edge in 100x magnification; and (c,d) cutting edge of the sample in 100x magnification. Fragmentation and micro-cracks of MoS_2 coating can be observed in (c) and (d), respectively.

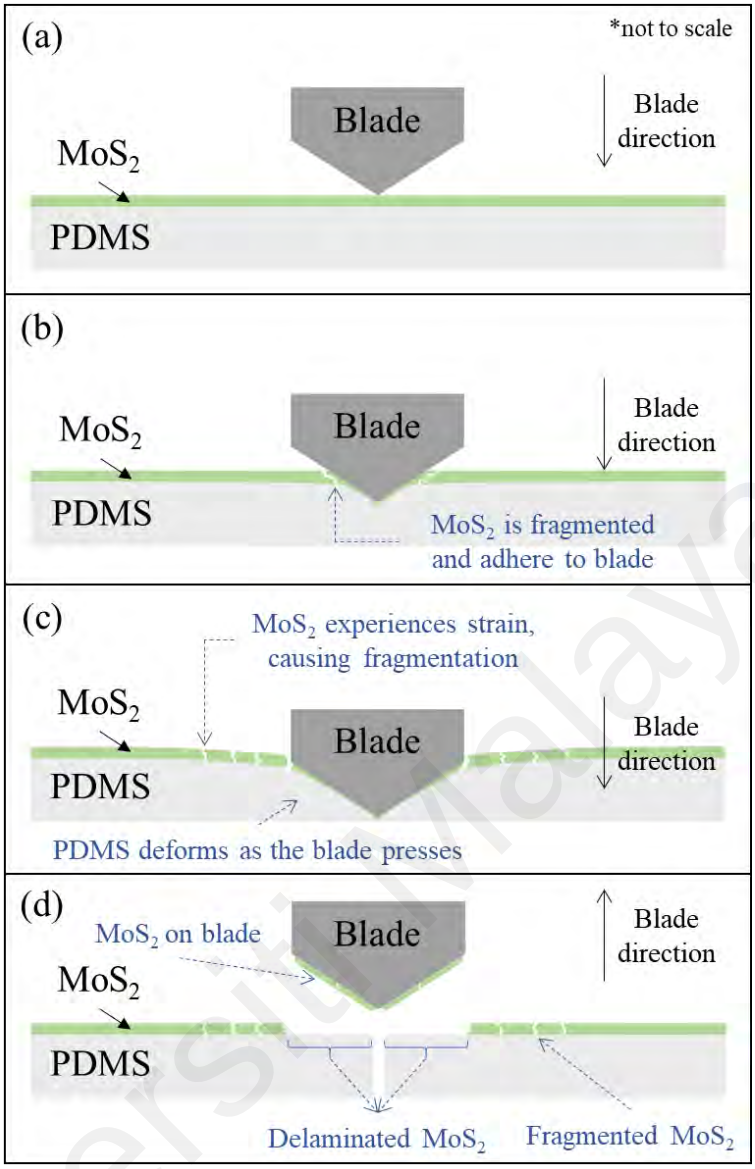

Figure 3.20: Illustration of the cutting process using a razor blade. (a) razor blade is brought downwards to start the cutting process; (b) part of the MoS_2 are fragmented and adhere to the body of blade; (c) deformation of PDMS, which leads to the fragmentation of MoS_2; (d) completed cutting process, with delaminated and fragmented MoS_2 on the PDMS substrate.

One may ask the question like will fragmentation and micro-crack of MoS_2 thin film affect the its optical properties? The fragmentation of MoS_2 creates terminated boundaries (or exposed edges) which exhibit different optical properties compared to that of the pristine or continuous film of MoS_2. For example, it is found that the edges can be examined from PL (Luo et al., 2020) and second harmonic generation imaging studies (Balla et al., 2018; Yin et al., 2014). Luo et al. showed that the emitted wavelength of PL

at the edges of MoS_2 flake is blue-shifted (Luo et al., 2020). On the other hand, the intensity of the second harmonic generated photons from the edges is slightly higher compared to the center region of MoS_2 flake (Yin et al., 2014). These observations clearly tell us that the optical property, especially the bandgap, of the exposed edge is changed. There are studies carried out to investigate the optical properties of exposed edge (Javaid et al., 2017; Tang et al., 2022; Wang et al., 2017). Based on their theoretical works, it is found that exposed edges with unsaturated Mo and S bonds generally have lower bandgap energy compared to that of continuous film of MoS_2. However, such unsaturated edges are not stable, and will be passivated by other element to form a stable structure (Javaid et al., 2017; Wang et al., 2017). The passivation of exposed edge changes the band structure of MoS_2, which leads to an increment in the bandgap energy (Javaid et al., 2017; Wang et al., 2017). For this reason, the ratio of exposed edge to MoS_2 thin film may influence the optical properties of the device when it is integrated onto the planarized waveguide. Again, if we consider a 2.4 mm MoS_2 thin film, the presence of fragmentation (20 – 40 μm in length) is considered negligible. It covers ~ 1.7% to the transferred MoS_2 film. Nevertheless, its effect will be further discussed in Chapter 4 later.

Although delamination and micro-crack occur during the razor blade cutting process, this method ensures minimum contamination to the MoS_2 film coated on top of PDMS compared to laser cutting method. Besides that, the affected length (delamination, micro-cracks and/or defragmentation length) is considered small, in which it occupies ~ 2 % of on the cut sample. In terms of cutting efficiency, razor blade cutting method stands out compared to laser cutting method as the former does not require laser alignment. This, in turn, reduces the time and financial cost for the whole cutting process. Due to these factors, razor blade cutting method will be utilized to cut the MoS_2-PDMS sample into pieces with desired size for its integration with the planarized optical waveguide.

3.8 Transfer Method of MoS_2 Using PDMS Stamp

After cutting the MoS_2-PDMS sample into the desirable size, the sample is ready for transfer process. The experimental arrangement of PDMS-assisted MoS_2 transfer process is shown in Figure 3.21 below.

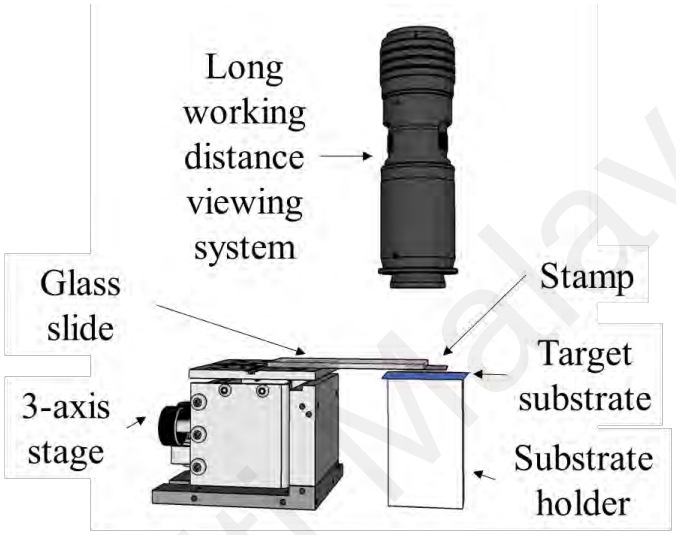

Figure 3.21: Illustration of the experimental arrangement of the PDMS-assisted MoS_2 transfer process to a target substrate. Figure adapted from (Chew et al., 2022b).

Initially, the target substrate was placed on a substrate holder and a long working distance viewing system is focused on the target surface for monitoring. To prepare the stamp, MoS_2-PDMS sample was placed on a glass slide, with MoS_2 thin film facing upwards. The glass slide was, then, fixed on a 3-axis translation stage with MoS_2 thin film facing downwards. The x- and y-axis of translation stage allowed us to select the desired stamping location of the target substrate more precisely with the help of long working distance viewing system. Note that readjustment of the focus of the viewing system is needed when the sample is moved to the desired stamping location. Up to now, the sample was ready to transfer. By adjusting the z-axis knob of the translation stage, the

sample was moved towards the target surface. As the sample touches the target surface, the optical contrast of the stamp changes, as depicted in Figure 3.22(a). The target surface, in this example, is a SiO_2/Si wafer. Figure 3.22(b) shows the image of the stamp when it was in contact with the target surface. The sample was ensured to touch fully with the surface without air bubbles. Afterwards, the PDMS stamp was lifted upwards using the z-axis knob of the stage, and the transfer process was completed as demonstrated in Figure 3.22(c) and (d). To obtain a clearer image, the transferred MoS_2 thin film on SiO_2/Si wafer is observed using an optical microscope, with 4x magnification operates in reflection mode as depicted in Figure 3.23.

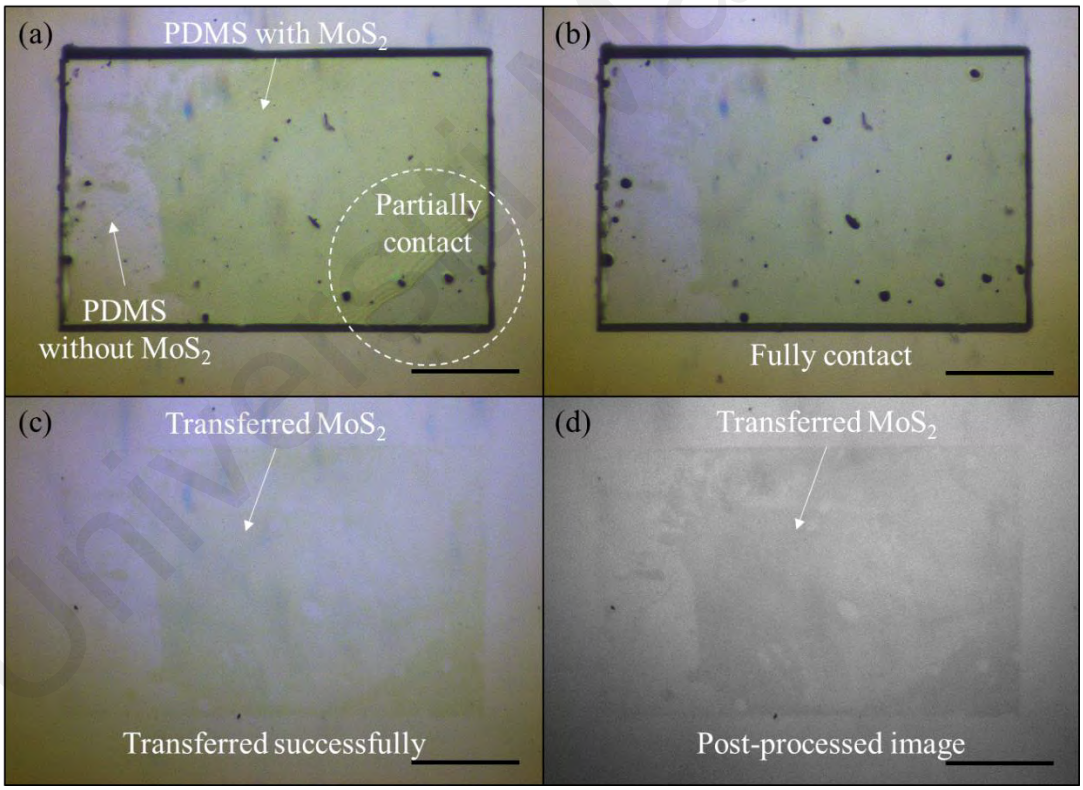

Figure 3.22: Images of the transferring process taken using the long working distance viewing system: (a) when the PDMS stamp starts to touch the target surface; (b) when the PDMS stamp is in contact with the target surface; (c) when the stamp is removed and MoS_2 thin film is transferred; (d) same image as (c) but with post-processing for better viewing purpose. The scale bar is 500 µm.

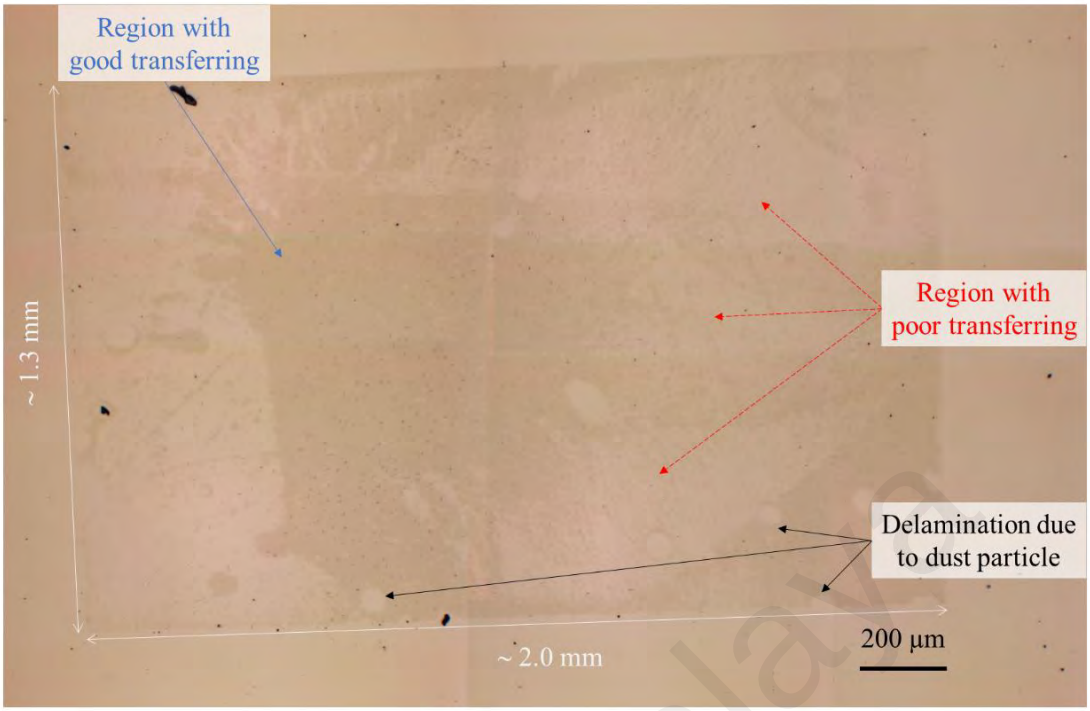

Figure 3.23: Composite photo of the transferred MoS_2 thin film on a SiO_2/Si wafer, taken using optical microscope with 4x magnification operates in reflection mode. The MoS_2 thin film appears darker visually compared to the surface of the wafer.

Figure 3.23 shows the composite photo of the transferred MoS_2 thin film. It is made by image stitching method. Multiple images were taken by an optical microscope with 4x magnification that operates in reflection mode. While translating the sample using the microscope stage, it is ensured that the image is focused. Based on Figure 3.23 also, it can be observed that the MoS_2 thin film is not fully transferred from the PDMS stamp. There are regions with good (blue arrow in the figure) and poor (red arrow) transferring, as well as delamination due to the presence of dust particle. To produce a good transfer, the first precautionary step is to ensure the surface of the stamp and target is free of dust particles. Another factor that affect the transfer quality is the peeling speed of the stamp. Lower peeling speed is preferred to ensure maximum transfer (Castellanos-Gomez et al., 2014; Ma et al., 2017; Meitl et al., 2006). In our experiment, the peeling speed of the stamp is not uniform at all time, causing the inferior transfer. The reasons that cause the uneven peeling speed are described as followed. After the stamp is in contact with the

target surface, the stamp is lifted by adjusting the z-axis knob of the translation stage manually. At this point, due to the adhesion properties between the PDMS stamp and the target surface as well as the elasticity of the stamp, the stamp tended to adhere on the target surface even after the stage was lifted for a distance which is more than its thickness. The stage was lifted upwards further until a height when the stamp began to detach from the target surface, observed using the zoom lens system. The detachment started from the left-hand-side of the stamp. At this moment, the stamp was peeled slowly by itself due to the created height difference between the stamp and target surface. Once the left-half region of the stamp was peeled, less PDMS surface was adhere on the target surface, which led to a relatively faster peeling speed. The sudden increase in peeling speed results in inferior transfer which is observable on the right-hand side of the transferred MoS_2 thin film in Figure 3.23, indicated by the red arrows. Hence, precautionary step in controlling the peeling speed is needed to transfer MoS_2 onto the surface of planarized optical waveguide. The extremely slow peeling speed are crucially needed, as shown in the video clips in these two references (Castellanos-Gomez et al., 2014; Evgeny). To minimize the sudden increase in peeling speed, the z-axis knob of the translation stage should be finely controlled until a height which is less than or equal to twice the thickness of the PDMS stamp. Alternatively, the z-axis knob of the stage can be controlled by step-motors to allow a more reliable, systematic control on the peeling speed, as demonstrated in other works (Patil et al., 2022; Yu et al., 2017a). Nevertheless, this transferred sample can still be used for basic characterizations such as Raman spectroscopy, AFM and XPS as shown previously.

3.9 Summary

The characterization of large area monolayer MoS_2 thin film on PDMS substrate and SiO_2/Si substrate has been carried out in this chapter. When examined under an optical

microscope, the MoS_2 thin film shows a very uniform morphology on the PDMS substrate, with minimum micro-crack or grain-like structures. Besides, the sample was examined with Raman spectroscopy and mapping. The results show that two Raman modes, that are E_{2g} (384.6 cm^{-1}) and A_{1g} (405.2 cm^{-1}) modes were observed. The modes separation is 20.6 cm^{-1}, which is consistent with the Raman modes of monolayer MoS_2. The Raman mapping also shows that the sample consists of a large area of monolayer MoS_2 with similar modes separation. Physical investigation of the thickness of MoS_2 was carried out using AFM. AFM was carried out on both MoS_2-PDMS sample and transferred MoS_2 on SiO_2/Si wafer. Both measurements show that the MoS_2 thin film is monolayer. Moreover, it is also found that the morphology of transferred MoS_2 on SiO_2/Si wafer has fragmentations and contamination at the edges. They may originate from the technical issues arising from handling and transferring the MoS_2-PDMS sample. Furthermore, the stoichiometry of transferred MoS_2 thin film was studied using XPS method. XPS reveals the MoS_2 has a stoichiometry of slightly more than 2.0 and no oxidation can be observed, which suggests that the CVD-grown MoS_2 might contain a small degree of molybdenum vacancies. Finally, the MoS_2-PDMS sample was studied using a time-resolved Z-scan technique. Based on the analysis, MoS_2 possesses a large n_{2,MoS_2} (1.40×10^{-13} m^2 W^{-1}) at C-band wavelength range. However, no NLA can be observed in the measurement, which may be due to the measurement sensitivity of our detectors. Nonetheless, the presence of NLA shall not be omitted due to the limitation of the detectors. All and all, the results obtained from time-resolved Z-scan measurement shows MoS_2 can be a good 2D material candidate for nonlinear optics application, operating in this wavelength range.

To integrate the monolayer MoS_2 on a planarized optical waveguide chip, a series of preparation steps shall be done. The preparation of the sample such as fabrication of planarized optical waveguide; cutting process of MoS_2-PDMS sample using a razor blade; and PDMS-assisted transfer process are also discussed in this section. Using the standard

FHD process, a germanium-doped silica-based planarized optical waveguide can be obtained. The waveguide has low propagation loss at the wavelength of interest, which suitable to be used as the study platform in this works. Before transferring MoS_2 onto the waveguide, preparation of the MoS_2-PDMS sample is needed. To cut the sample into desired size before transferring, instead of using the contactless laser cutting method that will introduce contaminants, a simple razor blade cutting method is used. The razor blade allows minimum contamination introduced to the sample during the cutting process. After that, the MoS_2-PDMS sample can be transferred to a target surface using the PDMS-assisted transfer technique. Precaution steps in ensuring the cleanliness of the sample and controlling the peeling speed are important for maximum MoS_2 transfer from PDMS stamp to the target surface. The transferred MoS_2 onto a SiO_2/Si wafer, as exemplified in Section 3.8, can be used for basic characterization such as Raman spectroscopy, AFM and XPS to characterize the properties of the MoS_2 thin film. In the next chapter, a series of basic characterization of MoS_2-coated waveguides will be discussed in detail before proceeding to its application.

CHAPTER 4: CHARACTERIZATION OF MoS_2-COATED WAVEGUIDE AND ITS APPLICATION AS SATURABLE ABSORBER

Straight channel, planarized waveguides with the dimension of 2.4 μm × 3 μm (core width × core height) were diced into smaller pieces of 15 mm length as the study platform. It is worth noting that the waveguide supports only fundamental mode light propagation at 1550 nm (Gan et al., 2020). The MoS_2-PDMS was cut into a smaller piece of 7.2 mm in length using the razor blade method. After transferring these large area monolayer MoS_2 thin film to the waveguide platform, the condition of MoS_2-coated waveguide is studied in terms of their morphology and insertion loss. Then, the saturable absorption properties of the device will be measured using I-scan technique. To utilize the saturable absorption properties, the MoS_2-coated waveguide will be integrated into an erbium-doped fiber laser (EDFL) cavity to study their capability in generating stable pulse trains. Finally, factors affecting the pulse generation performance are discussed.

4.1 MoS_2-Coated Waveguide with 7.2 mm Coating Length: Characterizations and Application

4.1.1 Optical Micrograph of MoS_2-Coated Waveguide

Figure 4.1 shows microscope image of planarized waveguides coated with 7.2 mm of MoS_2 thin film. The MoS_2 thin film is visible with a slightly different contrast, despite their atomically thin thickness. It is obvious that the thin film covers a large portion of the straight channel waveguides. The presence of dust particles is also observed which overlapped with some of the waveguides. Dust contamination can be reduced by ensuring the cleanliness of the surface of the target before commencing with the transferring process.

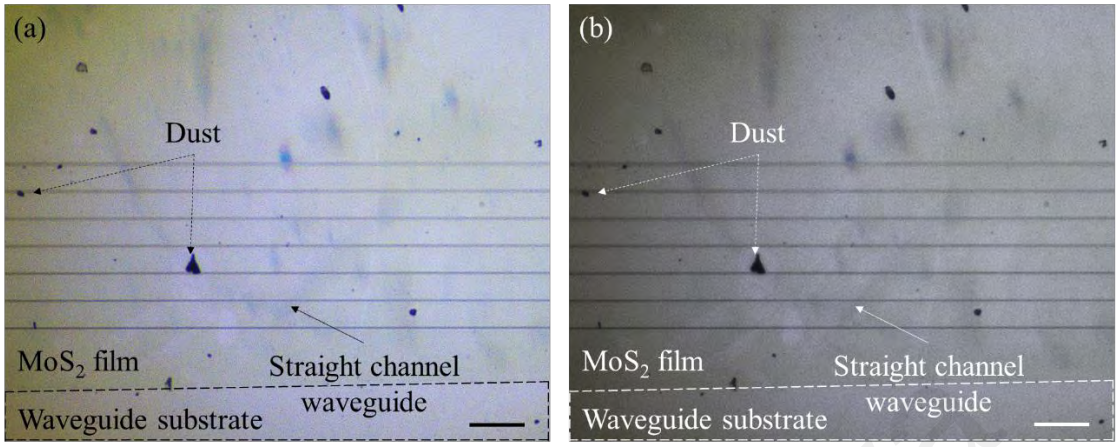

Figure 4.1: Micrograph of MoS_2 thin film coated on the planarized straight channel waveguides: (a) colour image; (b) post-processed greyscale image for better visual distinguishability between the area with and without the coating. The film covers a large area of the straight channel waveguides. The area without MoS_2 thin film coating is labelled with dash lines. The scale bar is 200 µm. Figure (a) adapted from (Chew et al., 2022b).

4.1.2 Loss Measurement

The insertion loss of the MoS_2-coated waveguide was characterized using the butt-coupling technique, as shown in Figure 4.2. A pair of single mode optical fiber pigtails with mode field diameter of 3.8 µm (Nufern, UHNA4) were used to couple light into and out of the waveguide. The mode field diameter of the fibers is close to the core dimension of the waveguide (2.4 µm × 3 µm) as shown in Figure 4.2 inset, which in turn minimize the mode field diameter mismatch loss during the coupling process. The fibers were aligned using a pair of five-axis linear translation stages (Newport, M-562) equipped with lockable differential micrometers (Newport, DM-13L). Index matching fluid was applied on both fiber tips to reduce the Fresnel reflection loss from the fiber-waveguide interfaces. This butt-coupling configuration will be used throughout the study when involving fiber-to-waveguide coupling. The total insertion loss of the MoS_2-coated waveguide is measured to be ~ 6 dB. It is found that the MoS_2 thin film coating introduces less than 0.5

dB of insertion loss and polarization dependent loss to the waveguides. This indicates that the linear absorption of MoS_2 is insignificant and the MoS_2-coated waveguide is not polarization sensitive at the C-band wavelength range, in contrast to other 2D materials such as graphene (Kim & Choi, 2012) and graphene oxide (Chong et al., 2020). The small polarization-dependency could be due to the fact that the thickness of MoS_2 overlay on the waveguide is too thin, as suggested in the work by Gan et al. (Gan et al., 2020).

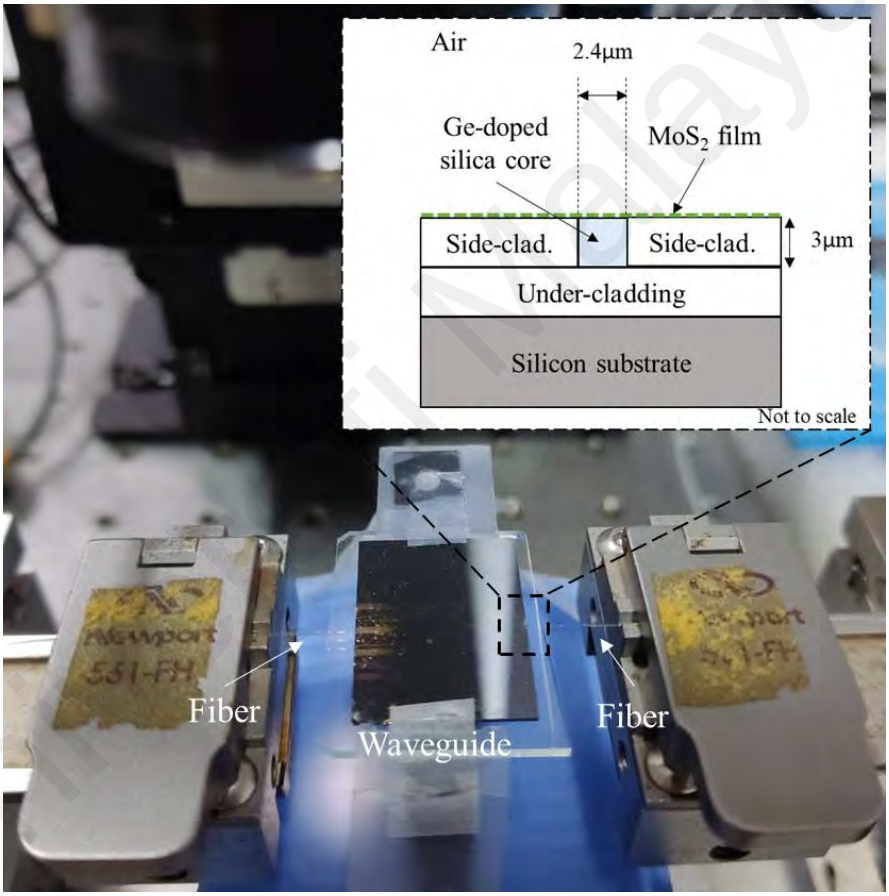

Figure 4.2: Loss measurement of MoS_2-coated waveguides using butt-coupling method. Inset: schematic diagram of the cross-section of the waveguide. Figure adapted from (Chew et al., 2022b).

4.1.3 I-scan Measurement

The nonlinear absorption property of the MoS_2-coated waveguide was measured using I-scan technique. Figure 4.3(a) schematically illustrates the arrangement of I-scan

measurement. A homemade mode-locked fiber laser with a center wavelength, pulse duration and repetition rate of 1560 nm, ~ 450 fs and 10 MHz, respectively was employed. Its optical pulse train, optical spectrum and autocorrelation trace are shown in Figure 4.3 (b), (c), and (d), respectively. By adjusting the variable optical attenuator (VOA; Anritsu, MN9610B), the intensity of the laser coupled into the waveguide can be varied. The output power was measured by two identical OPMs (Thorlabs, S144C).

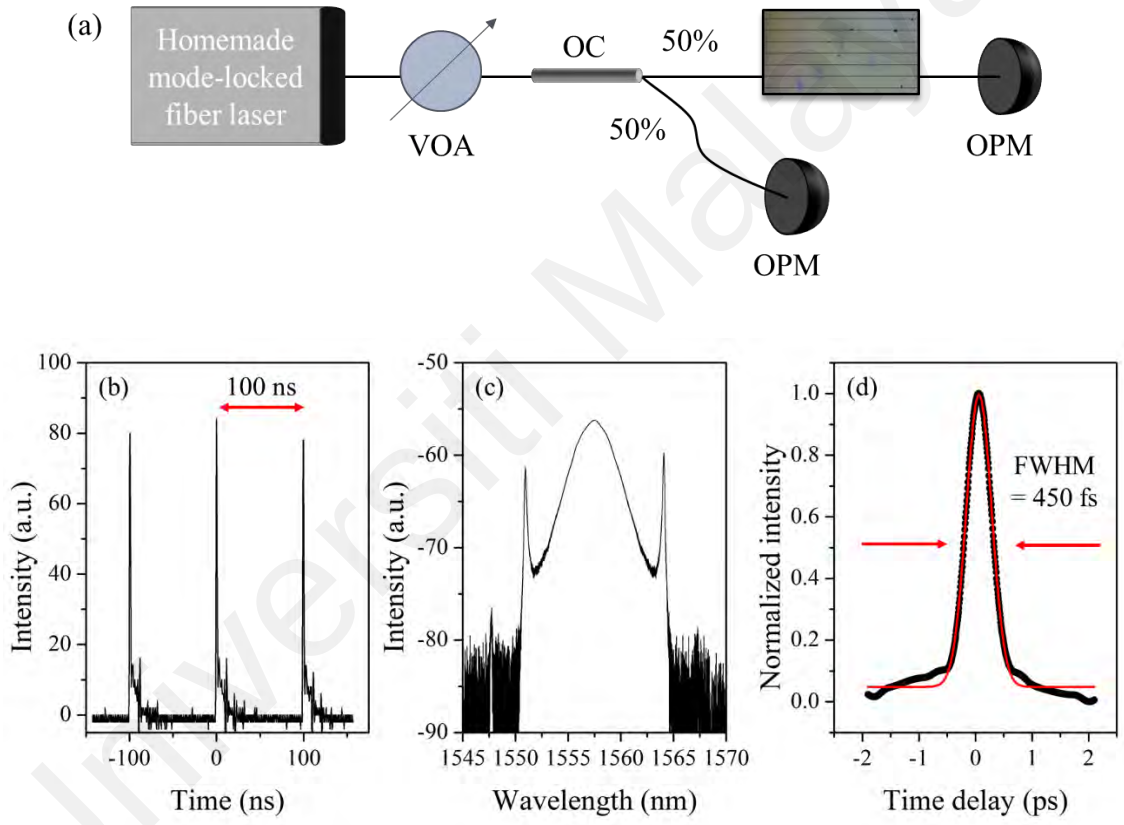

Figure 4.3: (a) Schematic diagram of the I-scan measurement of the MoS_2-coated waveguide. OC: optical coupler. (b) Optical pulse train; (c) Optical spectrum; (d) Autocorrelation trace of the homemade mode-locked laser.

Using this technique, a nonlinear transmission curve was obtained and plotted as shown in Figure 4.4. The curve resembles a typical saturable absorption profile, in which the transmission of the material increases linearly at low intensity and saturates at high intensity. Based on Figure 4.4, as the intensity of laser increases, the material absorption

decreases and saturates at ~ 2 MW cm^{-2}. This intensity dependent transmission, $T(I)$, is fitted using Equation 4.1 below (Woodward et al., 2015):

$$T(I) = 1 - \frac{\alpha_s}{1 + I/I_{sat}} + \alpha_{ns} \tag{4.1}$$

where I and I_{sat} are the intensity of the pump source and saturation intensity, respectively; α_s and α_{ns} are the modulation depth and non-saturable absorption, respectively (Guo et al., 2019). From the fitting, the α_s, I_{sat} and α_{ns} were determined to be ~ 2.7%, 0.87 MW cm^{-2} and ~ 76.8%, respectively. Based on the results, the evaluated I_{sat} value is approximately 10 (Huang et al., 2014) and 30 times (Liu et al., 2014b) larger compared to previous reports. This difference could be attributed to the difference in 2D MoS_2 fabrication techniques, which results in different size and quality of the MoS_2 flakes. This will in turn affect the performance of saturable absorption of the sample (Woodward et al., 2014). One may ask why there are absorption and saturable absorption at this wavelength band, as it is reported that a monolayer MoS_2 has negligible absorption coefficient at ~ 1550 nm (Islam et al., 2021), as discussed in Chapter 2.4.2. The reason may come from the presence of defects such as molybdenum vacancies (V_{Mo}) in the CVD-grown MoS_2 sample. In Chapter 2.1.1, it is stated that the presence of vacancies will affect the optical properties of the MoS_2. Kunstmann et al. theoretically found that the presence of V_{Mo} increase the optical absorption of MoS_2 at energies smaller than 1.9 eV (Kunstmann et al., 2017). This indicates that the V_{Mo} promotes sub-bandgap absorption in the MoS_2 thin film. Due to the presence of sub-bandgap, saturable absorption can happen in MoS_2, with its trend as shown in Figure 4.4. Consequently, it is expected that this MoS_2-coated waveguide can produce pulses when it is coupled into the EDFL cavity.

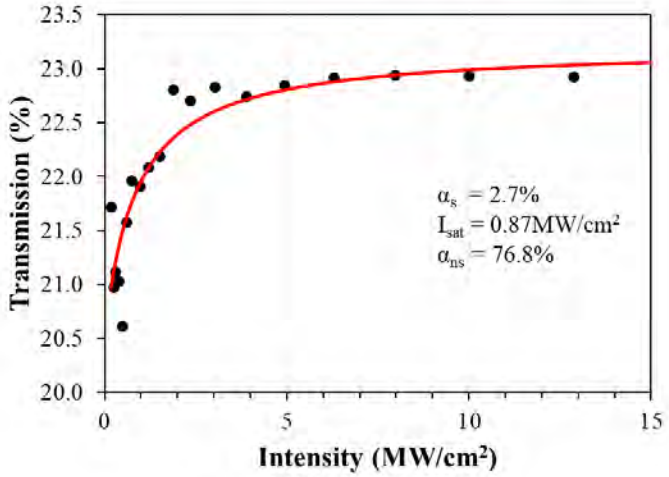

Figure 4.4: The saturable absorption characteristic of the MoS_2-coated waveguide measured using I-scan technique at 1560 nm wavelength. Black solid dots represent the experimental data; red curve represent the fitting curve.

4.1.4 Performance of Pulse Laser in an EDFL

To study the pulse laser generation performance of the 7.2mm-length MoS_2-coated waveguide, an EDFL cavity (or resonator) was built as depicted in Figure 4.5. The pump laser used is a 980 nm laser diode. It was coupled into the cavity through a 980/1550 nm wavelength division multiplexer (WDM). An EDF with a length of 0.62 m (LIEKKI Er110-4/125) is utilized as the gain medium. It has a group velocity dispersion (GVD) of 12 fs^2/mm (Li et al., 2014c). Right after the EDF, an optical isolator (ISO) was spliced to ensure single-directional laser propagation in the cavity. A polarization controller (PC) was connected to control the polarization state of the laser before the 7.2 mm-length MoS_2-coated waveguide. The MoS_2-coated waveguide was connected to the PC as the passive SA. Then, the waveguide output was coupled to an 80/20 optical coupler (OC), in which 80% of laser power is feedback into the cavity while 20% is coupled out for characterization. The generated output pulse train was measured using a photodiode (Thorlabs PDA50B-EC) connected to an oscilloscope (Tektronix TDS1001B). An optical power meter (Thorlabs, S144C) and optical spectrum analyser (OSA; Yokogawa,

AQ6370) were used to measure the optical power as well as spectrum of the output laser, respectively. The total length of the single mode fiber (without the MoS_2-coated waveguide) in the cavity is approximately 18.6 m. Consider the GVD of the single mode fiber is -22.104×10^{-3} ps^2/m (Jeon et al., 2015), the net group delay dispersion in the cavity is evaluated as -0.404 ps^2. This will make the laser cavity to operate in an anomalous dispersion regime, which is suitable for mode-locked pulse generation (Jeon et al., 2015).

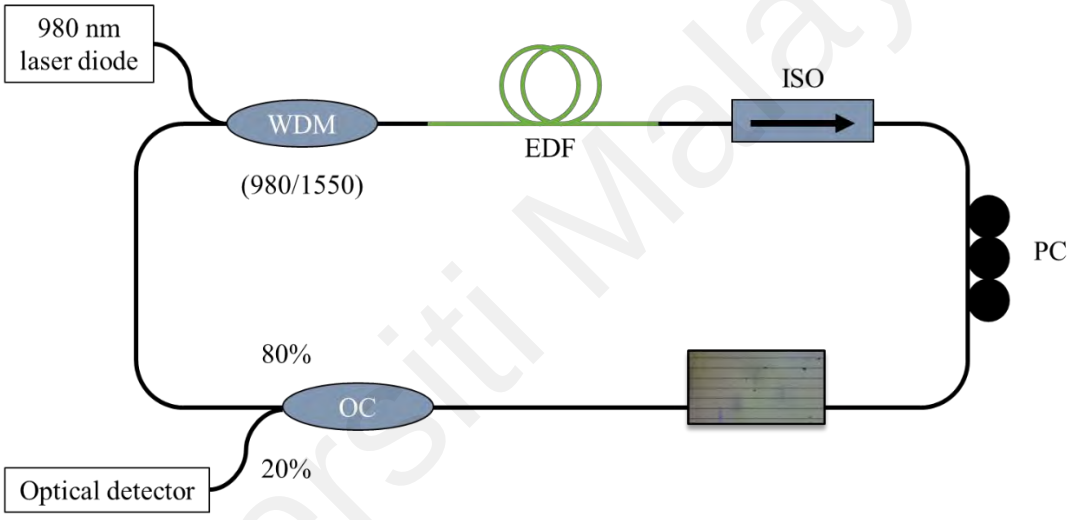

Figure 4.5: Schematic diagram of the EDFL cavity for pulse laser generation using MoS_2-coated waveguide. Figure adapted from (Chew et al., 2022a).

Initially, the laser cavity operates in continuous wave regime at low pump power. As the pump power increases to 66.0 mW, Q-switched laser operation is observed. By carefully adjusting the PC, the amplitude of the Q-switched pulses can be maximized. At pump power of 122.8 mW, a stable pulse train with a repetition rate of 22.5 kHz (pulse spacing of 44.4 μs) is observed, as illustrated in Figure 4.6(a). The produced pulses show a pulse duration of 5.24 μs as shown in Figure 4.6(b). At this pump power, the Q-switched pulse laser operates at a wavelength of 1558 nm. Furthermore, in Figure 4.6(c), the radio-

frequency (RF) spectrum of the output shows a relatively high signal-to-noise ratio of 44 dB, inferring good pulse stability. This shows that MoS_2-coated waveguide acts as a passive SA for Q-switching. The mechanism of passive Q-switching is strongly related to the loss modulation of SA. As shown in Figure 4.4, the MoS_2-coated waveguide is able to modulate the loss (or transmission) in the laser cavity, depending on the intensity in the laser cavity. Initially, as the pumping starts, the cavity loss is high due to the absorption of MoS_2. Although at this point lasing cannot be achieved, the population inversion of the gain medium that is constantly pumped can be increased to well above its threshold value. When the laser intensity in the cavity increases to a value which is higher than the saturation intensity of the MoS_2, the cavity changes from high loss to low loss. This would result in a rapid increase in photon density in the cavity, which lead to a rapid stimulated emission from the gain medium. Eventually, an intense pulse is formed and emitted (Hawkes & Latimer, 1995). Afterwards, the cavity returns to high loss condition and the processes repeat for the subsequent pulse generation. In other word, the MoS_2 changes the Q-factor of the cavity, thus producing a Q-switched pulse laser.

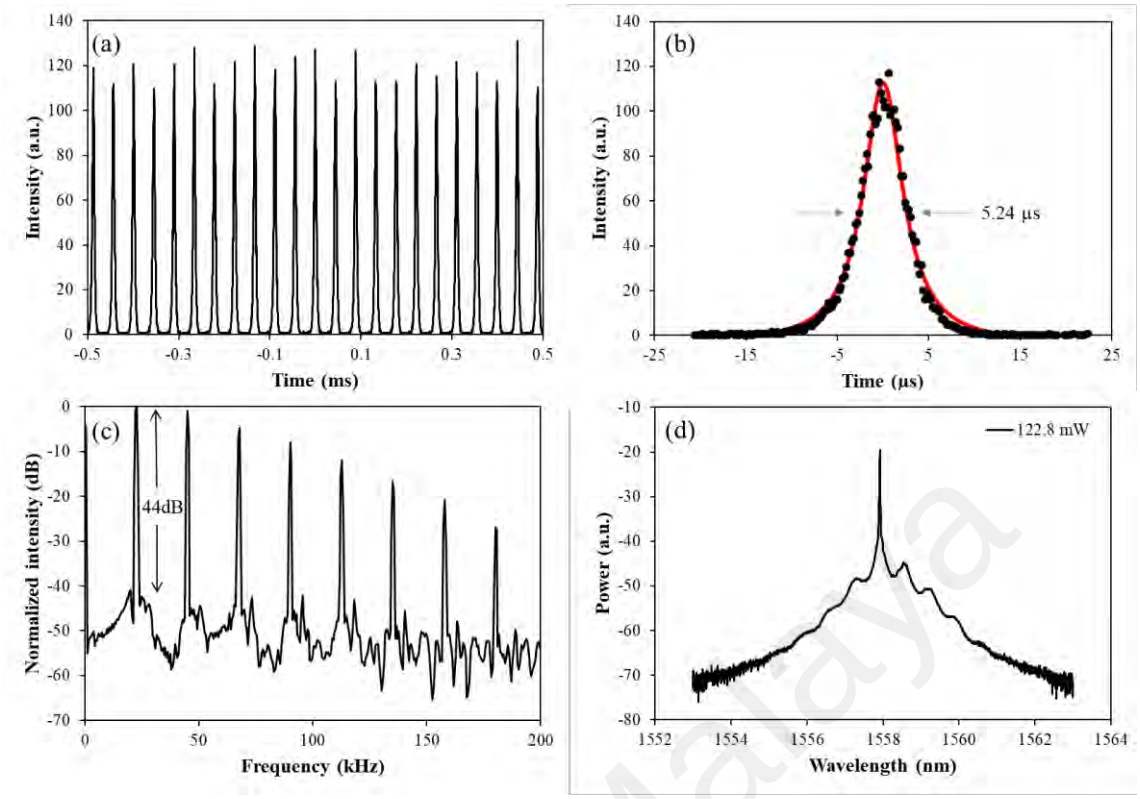

Figure 4.6: Q-switched laser characteristic produced by 7.2 mm-length MoS_2-coated waveguide: (a) pulse train at 122.8 mW; (b) its individual pulse profile; (c) its RF spectrum; (d) optical spectra of the generated pulse. Figures adapted from (Chew et al., 2022a).

The characteristic of Q-switched laser was studied with different pump power. Figure 4.7(a) shows the evolution of repetition rate and pulse width with increasing pump power. The repetition rate of Q-switched laser increases linearly with pump power. Meanwhile, the pulse duration or pulse width decreases as the pump power increases. These can be attributed to the nonlinear dynamics in the gain medium and MoS_2-coated waveguide in the laser cavity (Degnan, 1995). At high pump power, energy is extracted and decay quickly, which leads to high repetition rate and short pulse width. The nonlinear evolution of pulse duration with increasing pump power is affected by the combination effects of round-trip time of the cavity, modulation depth of the absorber, the output coupler ratio and the gain variation in the cavity (Degnan, 1995; Herda et al., 2008). For example, Herda et al. numerically and analytically shows that the nonlinear decrease in pulse

duration due to higher pump power is largely due to the modulation depth of the absorber and the gain variation in the cavity (Herda et al., 2008). The pulse duration of Q-switched laser is inversely proportional to the square root of pump power. In qualitative, at weaker pumping condition, the rapid decrease in pulse duration is caused by the fast accumulation of electrons in the upper energy level. However, at stronger pumping condition, the speed of accumulation slows down due to over-saturation in the gain medium, leading to less observable variation of pulse duration (Chen et al., 2015b). Furthermore, the average output power of the Q-switched laser increases linearly with the pump power. The maximum achievable average output power is approximately 0.14 mW at a pump power of ~ 150 mW. It is noted that the generated average output power of the Q-switched fiber laser is relatively low. The possible reason could be due to the large insertion loss from the MoS_2-coated waveguide in the current configuration. This can be improved when the MoS_2 is integrated in an all-planar waveguide laser platform, in which light couplings between fibers and MoS_2-coated waveguide are not required. Nevertheless, the present results demonstrate the potential of integration of MoS_2 thin film onto a planarized waveguide platform (with a simple straight channel structure) to produce pulse laser sources.

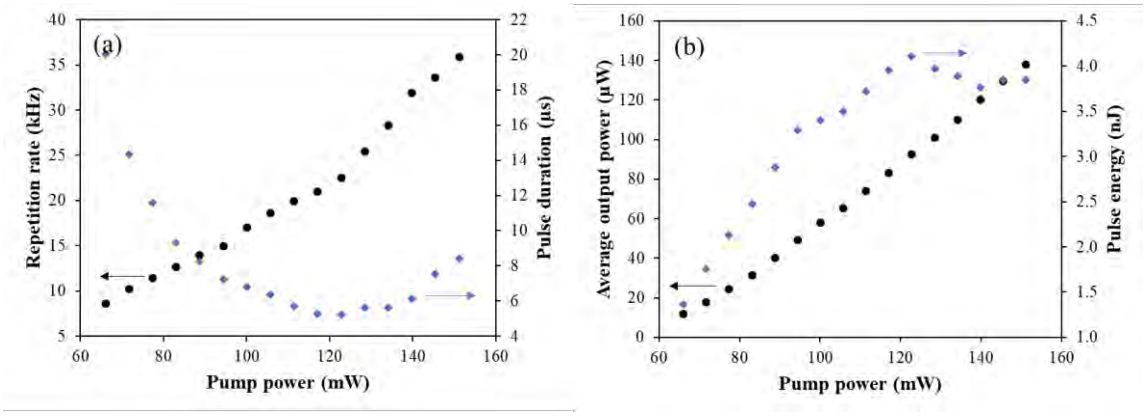

Figure 4.7: Effect of pump power towards Q-switched laser characteristic: (a) relationship between repetition rate and pulse width with pump powers; (b) variation of average output power and pulse energy with pump powers. Figures adapted from (Chew et al., 2022a).

The dependency of the pulse energy of the laser to the pump power is shown in Figure 4.7(b). The pulse energy is calculated by dividing the average output power with the repetition rate of the laser. It can be observed that the pulse energy increases from 1.4 nJ at pump power of 66.0 mW to 4.1 nJ at 122.8 mW. At larger pump power (> 122.8 mW) the pulse energy reduces slightly to ~ 3.9 nJ. This response is repeatable, which suggests that the MoS_2 is not permanently affected. In fact, the damage threshold of the MoS_2 thin film is expected to be much larger than the maximum laser power level achieved in the current work because the film interacts with the laser light evanescently. The drop in laser performance above 122.8 mW may be due to the faster rate of change of the repetition rate with pump power above the 122.8 mW level. That is, when the pump power is increased to more than 122.8 mW, the rate of change in pulse repetition rate with pump power increases, while the average output power increases linearly with the pump power throughout the pump power level studied.

In the present experimental setup, pulse laser generated via mode-locked mechanism was not observed. This is most probably due to the large insertion loss and non-saturable loss of the MoS_2-coated waveguide that prohibit the mode-locked laser operation. In

addition, Q-switched mode-locked pulse is not observed as well. Therefore, the experimental setup produces only Q-switched laser pulses using the MoS_2-coated waveguide as saturable absorber.

Table 4.1 shows the comparison for the performance of Q-switched pulsed lasers operating in the C-band wavelength using MoS_2 as SA. Most of the pulse lasers are made from the well-known fiber "sandwiching" method to integrate the SA into the laser cavity. Furthermore, their synthesis methods of 2D MoS_2 are different as well. The works in (Li et al., 2014b; Wei et al., 2016; Xia et al., 2015) achieve pulse energy of 27.2 nJ, 17.2 nJ and 8.2 nJ, respectively. It is noted that the pulse energy produced by the presented SA is 4.1 nJ, which is 2 (Xia et al., 2015) and 7 (Li et al., 2014b) times lower comparatively. These differences can be attributed to the interaction method of their SA, in which their SA interact with the entire laser mode (transmission scheme), whereas mine interact evanescently (evanescence field scheme). As the pulse energy and repetition rate are proportional to the pump power, the SA that works in transmission scheme can produce pulse laser with better performance compared to the evanescence field scheme (Degnan, 1995). Nonetheless, the obtained pulse energy from the MoS_2-coated waveguide is in the same order of magnitude to the current MoS_2-based Q-switched laser technology. Aside from that, the repetition rate of the waveguide is found to be relatively lower compared to those that operate in transmission scheme, with the reason as described previously. A lower repetition rate can be useful in application such as laser ranging (Hampf et al., 2019; Ye et al., 2005). It should be noted that the characteristic of MoS_2-based Q-switched lasers listed in Table 4.1 provides only a general reference, since other factors (such as output coupling ratio, thickness of SA, etc) that can affect the performance are not considered here.

Table 4.1: Performance of MoS_2-based Q-switched laser in C-band wavelength.

Interaction method / scheme	Wavelength (nm)	Pulse width (μs)	Frequency (kHz)	Pulse energy (nJ)	Ref.
Sandwiched / transmission	1549.91	1.66 – 6.11	10.6 – 173.1	27.2	(Li et al., 2014b)
Sandwiched / transmission	1560	3.2 – 5.1	36.8 – 91.7	17.2	(Wei et al., 2016)
Sandwiched / transmission	1560.5	1.92 – 3.7	28.6 – 114.8	8.2	(Xia et al., 2015)
Planarized waveguide / evanescence field	1558	5.2 – 20.0	8.6 – 35.9	4.1	This work

4.2 MoS_2-Coated Waveguides Characterization with Different Interaction Length

As the performance of Q-switched laser using MoS_2-coated planarized waveguide as saturable absorber relies on the evanescence field interaction with MoS_2 thin film, the investigation of MoS_2 coating length dependent Q-switched pulse generation can be further studied. This study can provide intrigue information for the development of a compact waveguide laser in all-planar waveguide laser technology.

To study the effect of coating length of MoS_2 on the generation of pulsed laser, three pieces of MoS_2-PDMS samples are cut, with length of 2.5 mm, 4.4 mm and 9.2 mm, respectively. It is observed that for the transfer of longer MoS_2 thin film, defects along the coating becomes more obvious. Figure 4.8 shows the optical micrograph of 9.2 mm-length MoS_2 thin film transferred on the waveguide surface. Delamination of the coating can be observed, which introduces discontinuities along the MoS_2-coated waveguides. Meanwhile, it is worth to note that careful inspection should be carried out on the PDMS stamp as well using an optical microscope after the transfer process. Figure 4.8(b) shows the optical micrograph of the PDMS stamp after the transfer process. It is obvious that there is MoS_2 thin film (appears in brighter colour coating) remains on the PDMS stamp.

This remaining MoS_2 thin film on the stamp comes from the unsuccessful transfer during the transfer process. Based on the Figure 4.8(b), it can be found that part of the MoS_2 thin film, which appears as straight-line structures, are missing on the stamp, as marked by the black dashed boxes in the figure. The distance between these two straight-line structures is approximately 100 μm, which corresponds to the distance between two adjacent straight channel waveguide cores. This indicates that MoS_2 thin film is transferred to the surface of the core of the waveguide (but not transferred to the side-cladding of the waveguide). However, there are discontinuities appeared on the straight-line structures. This suggests that even though MoS_2 thin film is transferred onto the surface of the core, the quality of the transferred thin film is low due to the discontinuities. The discontinuities may possibly affect the saturable absorption performance of the MoS_2-coated waveguide.

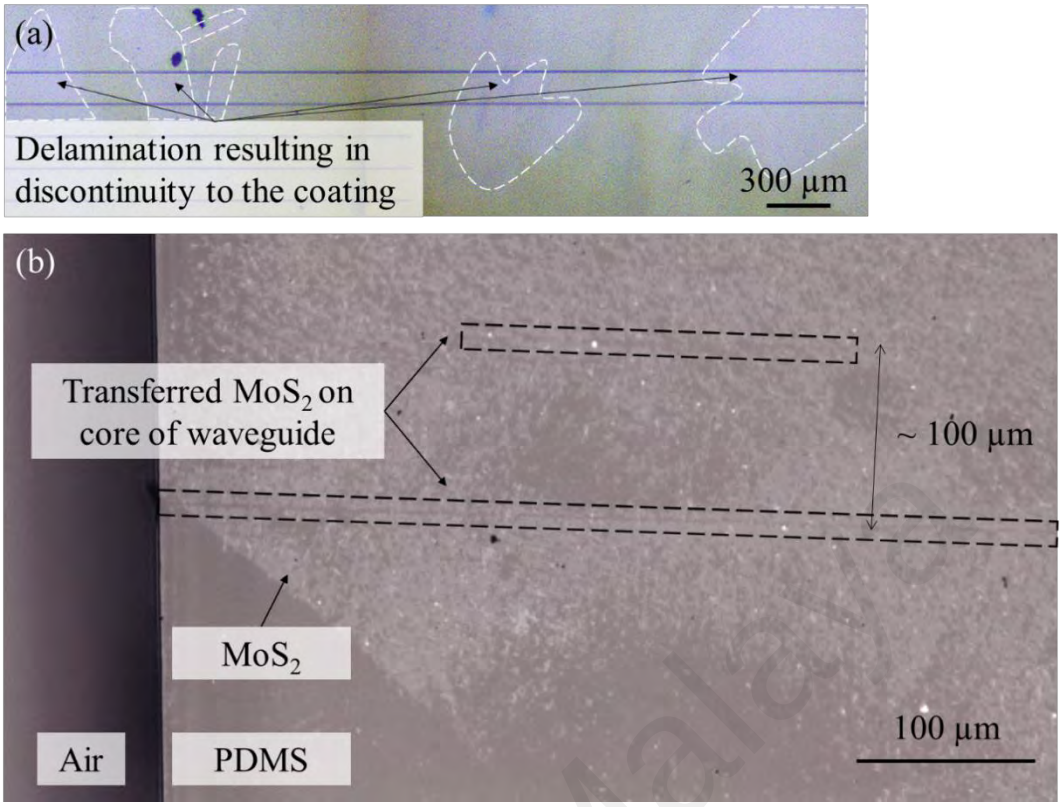

Figure 4.8: (a) Optical micrograph of 9.2 mm-length MoS_2 coating transferred on the waveguide surface. Delamination of MoS_2 thin film is observed (labelled with white dashed line), which leads to discontinuity to the coating. Figure adapted from (Chew et al., 2022b); (b) optical micrograph of PDMS stamp after transfer process. Black dashed boxed show that MoS_2 thin film is transferred to the surface of the core of the waveguide.

Similar to the 7.2 mm-length MoS_2-coated waveguide, the insertion loss of the waveguides is about 6 dB, and the MoS_2 thin films introduce insertion loss which is < 0.5 dB. To avoid confusion, in the later discussion, the MoS_2-coated waveguides with coating length of 2.5 mm, 4.4 mm, 7.2 mm and 9.2 mm are labelled as SA1, SA2, SA3 and SA4, respectively. To carefully study the characteristics of each SA, the I-scan and EDFL cavity will be slightly modified. The performance of Q-switched lasers by SAs at a fixed wavelength will be compared and discussed in the later sub-chapter.

4.2.1 Modified I-Scan Measurement

The nonlinear absorption properties of the SAs are measured using the modified I-scan measurement as shown in Figure 4.9. A homemade ns-pulse laser was used as the pump source. The pulse width and repetition rate of the laser are 30 ns and 10 kHz, respectively. The wavelength of the laser is tunable across the C-band wavelength band. Its wavelength was set to 1531 nm in this study. The reason of choosing this wavelength is that it gives the maximum gain across the gain spectrum of an EDF. The performance of a SA in generating Q-switched laser is expected to be optimized when the gain of the gain medium is maximized (Degnan, 1995). With this reason, the saturable absorption properties of the SAs at this wavelength are considered to be more valuable in C-band wavelength band. The power of the laser can be controlled by a VOA (Anritsu, MN9610B). The source was coupled into a 50/50 optical coupler (OC), with one arm connected with the SAs. The average power of both arms was recorded using two OPMs (Thorlabs, S144C).

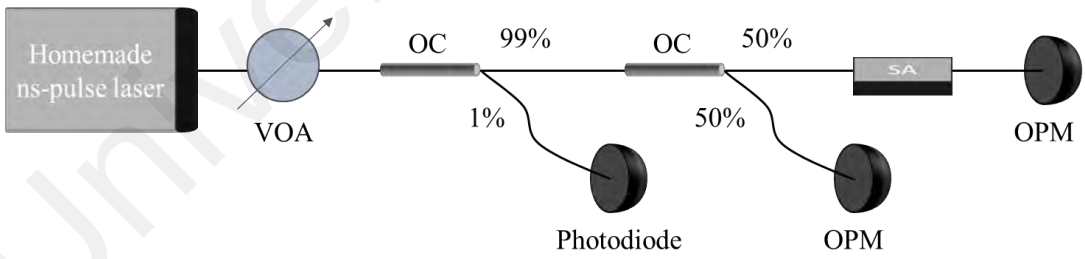

Figure 4.9: Schematic diagram of the modified I-scan measurement. Figure adapted from (Chew et al., 2022b).

Figure 4.10 depicts the nonlinear transmission curves of the SAs. Typical saturable absorption profiles were observed for all the SAs. As the peak intensity increases, the absorption of the SAs decreases and saturates after ~ 0.3 MW cm^{-2}. The profiles were

fitted using Equation 4.1. It can be seen that the α_s of SA3 is ~ 0.9%, which is more than 3 times larger compared to that of SA1, SA2 and SA4 at this wavelength. This indicates that SA3 has a higher saturable absorption, which can lead to a better pulse shaping ability (Herda et al., 2008). Apart from that, SA3 shows a lower I_{sat} (64.9 kW cm^{-2}) compared to the other SAs as well. As four SAs show saturable absorption properties, they are expected to be able to generate Q-switched pulse laser when integrated into an EDFL cavity.

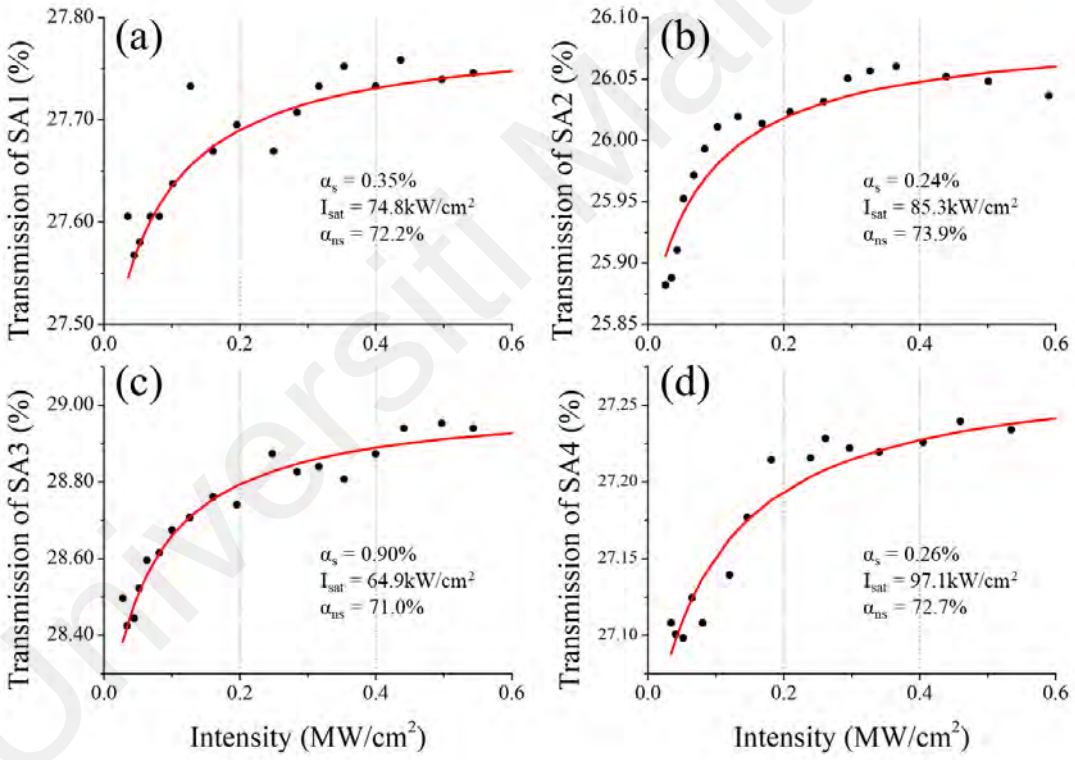

Figure 4.10: Plots of nonlinear transmission of (a) SA1; (b) SA2; (c) SA3; and (d) SA4. The black, solid dots correspond to the obtained raw data, whereas the red, solid curves represent the fitting curve. Figures adapted from (Chew et al., 2022b).

It should be noted that although the modulation depth of the SAs is small, it is still within the accepted range for pulse laser application. Several studies demonstrated that

2D materials with low modulation depth are able to produce pulse laser that operates in either mode-locking (Kivistö et al., 2009; Mao et al., 2016a; Mao et al., 2016b) or Q-switching (Huang et al., 2014) mechanism. In fact, the generation of pulse laser does not rely solely on the modulation depth of a saturable absorber. Other factors such as the cavity NLO properties, cavity group velocity dispersion and saturation gain will contribute to pulse generation (Jeon et al., 2015).

4.2.2 Performance of Q-Switched Lasers by SAs

To study the ability of SAs in producing Q-switched lasers, the SAs were coupled into a modified EDFL cavity as shown in Figure 4.11. Essentially, the experimental arrangement is similar to the one in Figure 4.4, except an etalon-based tunable bandpass filter (TBF; Agiltron, FOTF-025121332) was inserted before the SAs. This TBF is tunable from 1510 nm to 1590 nm. It is important for the study of wavelength tunability of the SAs.

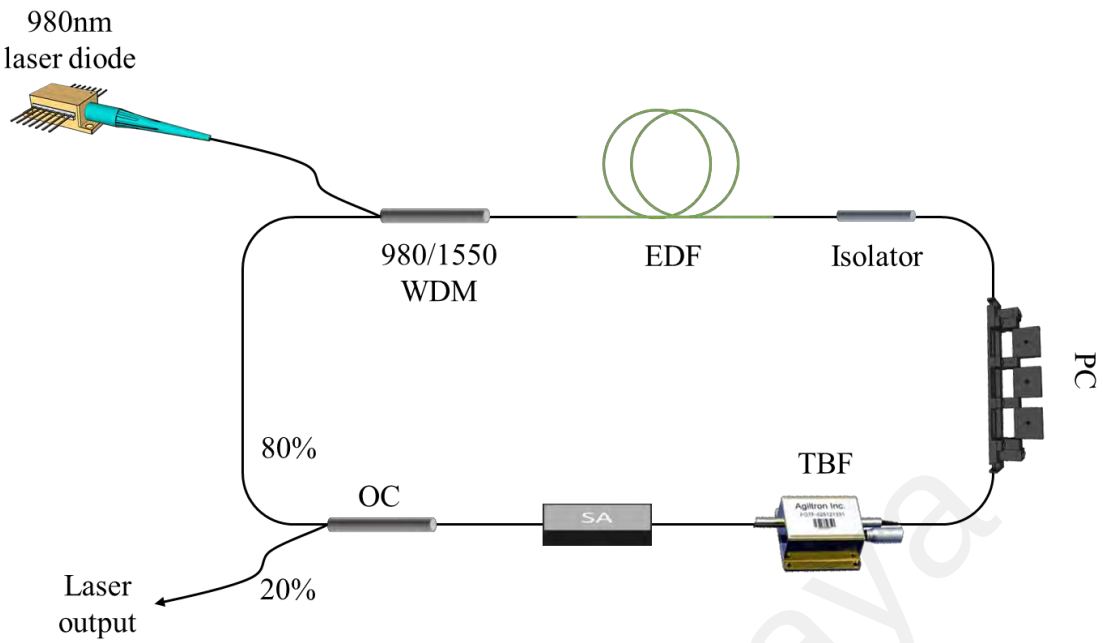

Figure 4.11: Schematic illustration of the modified EDFL cavity. Figure adapted from (Chew et al., 2022b).

Initially, the lasing wavelength was fixed at 1531 nm using the TBF. At low pump power regime, the laser operates in a continuous wave manner. As the pump power increases, stable Q-switched laser pulses can be observed. For all four SAs, similar behaviour was observed. The threshold pump power for Q-switched operation of SA1 is 88.7 mW, whereas SA2, SA3 and SA4 are 77.4 mW. It should be noted that without MoS_2 coating on the waveguide, no stable pulse can be observed for all laser pump power levels. Moreover, mode-locked pulses are not observed in the current setup, which may be due to the large insertion loss of the SAs. This issue can be resolved when the MoS_2-coated waveguides are integrated in an all-planar waveguide laser platform, in which fiber-waveguide laser coupling loss can be neglected.

Figure 4.12(a) depicts the Q-switched pulse trains generated by these SAs at pump power of 100mW. The pulse train produced by the SAs have different repetition rate, f. The f reduces from SA4 to SA1. The pulses generated by SA1 has a pulse duration, τ_p, of 10.9 μs. Meanwhile, the τ_p of pulses produced by SA2, SA3 and SA4 are 7.5 μs, 7.3

μs and 7.7 μs, respectively. These observations suggest that longer interaction length of MoS_2 improves the performance of Q-switched lasers in terms of higher f and shorter τ_p. The RF spectra of all SAs are shown in Figure 4.12(b). The RF spectrum of SAs shows an increasing trend of signal-to-noise ratio (SNR) from SA1 to SA4. This is exemplified by SA4 and SA1, in which SA4 has a SNR of 45 dB whereas SA1 has a SNR of 38 dB. Based on the results, longer interaction length could provide a better pulse stability. Furthermore, the RF spectra produced by all SAs are regular and do not show spectral modulation, suggesting that the pulse laser produced are stable for practical application.

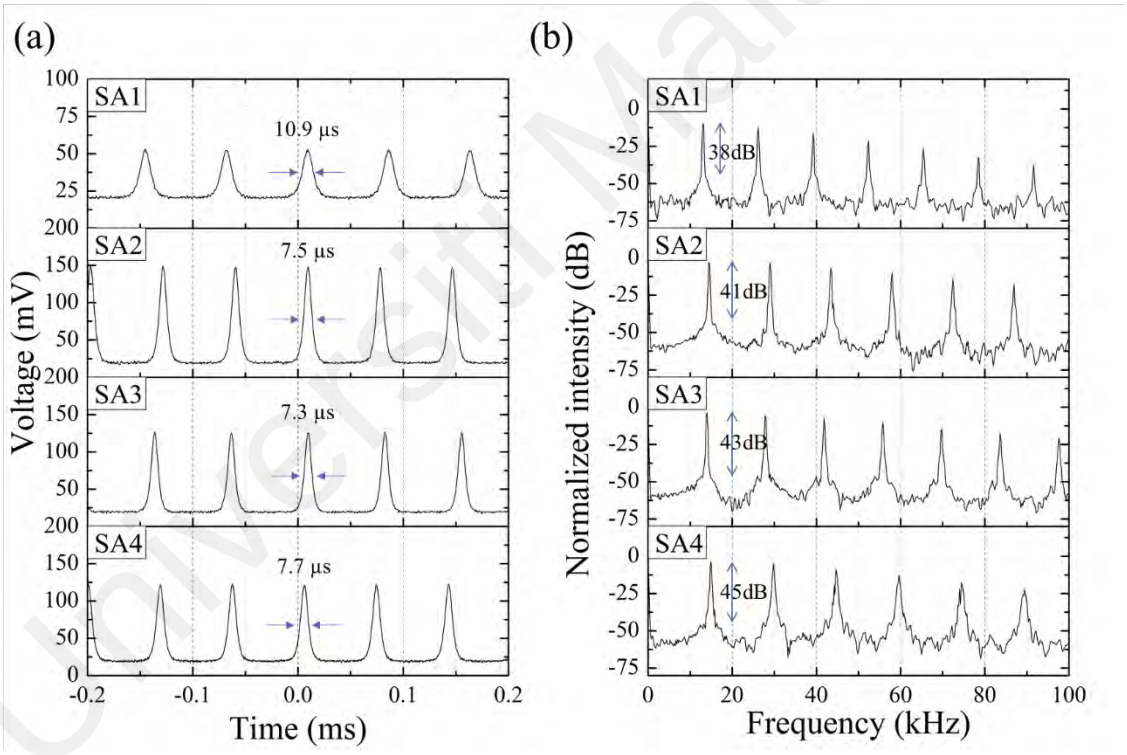

Figure 4.12: (a) Q-switched pulse train of SA1 to SA4; (b) RF spectra of the SAs at a fixed wavelength and pump power of 1531 nm and 100 mW, respectively. Figures adapted from (Chew et al., 2022b).

Next, the evolution of f and τ_p of the pulse laser as a function of pump power at a fixed wavelength of 1531 nm are studied and the results are shown in Figure 4.13. In Figure 4.13(a), it can be seen that SA3 produces pulse laser over a larger pump power

range compared to SA1, SA2 and SA4. For instance, SA3 produces stable Q-switched laser at pump power range of 77.4 mW to 190.9 mW. Above this pump power, the pulse train becomes unstable and disappear eventually. For SA1, SA2 and SA4, stable Q-switched operation occur at a smaller pump power range. Furthermore, it is found that the f of the Q-switched pulses increases monotonically with the pump power for SA3, from 6.6 kHz at 77.4 mW to 40.2 kHz at 190.9 mW. On the other hand, the variation of f of the pulse laser generated by SA1, SA2 and SA4 show similar linear proportionality trend towards the pump power. The largest attainable f of SA1, SA2 and SA4 are 24.8 kHz, 23.9. kHz and 25.8 kHz, respectively. At the same time, the τ_p of SAs show a typical Q-switching characteristic as well. It decreases as the pump power increases, as shown in Figure 4.13(b). The shortest achievable τ_p of SA3 is 2.9 μs when the pump power is set at 168.2 mW. Based on Figure 4.13(b) again, it can be seen that the overall τ_p of SA3 is shorter than that of other SAs. For instance, the shortest τ_p of SA3 (2.9 μs) is 2.9 times shorter than that of SA1 (8.3 μs).

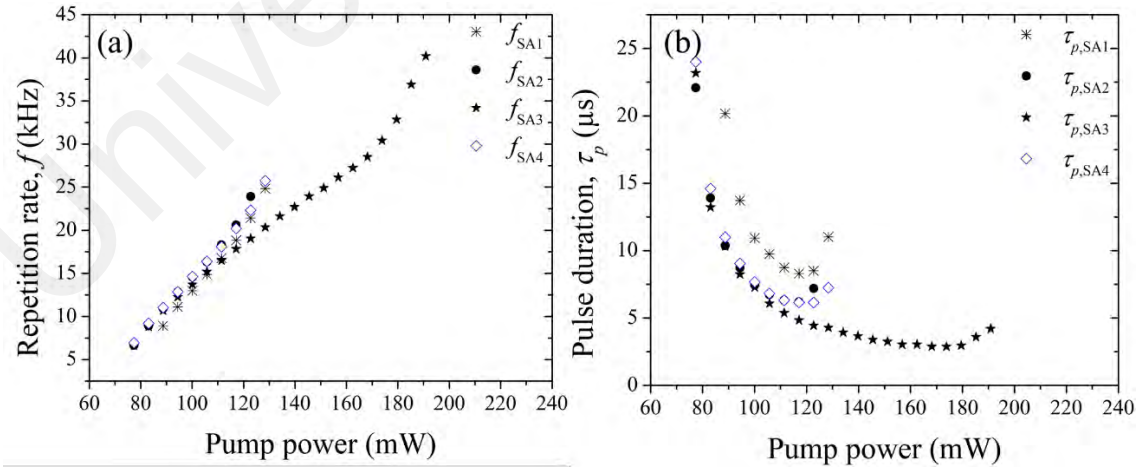

Figure 4.13: Development of (a) f and (b) τ_p of SAs against pump power. Figures adapted from (Chew et al., 2022b).

Besides, the average output power, P_{out} of the pulse laser is shown in Figure 4.14(a) and it shows a linear increment trend with pump power. In general, the P_{out} of SA3 is slightly larger than that of other SAs. The largest achievable output power, $P_{out,max}$, of SA3 is 0.22 mW at 190.9 mW pump power. Compared to SA1, its $P_{out,max}$ is 45 μW at 128.5 mW pump power. Next, the pulse energy, E_p produced using SA3 is the highest among the SAs as well. Based on Figure 4.14(b), the E_p of SA3 increases as the pump power increases until 174 mW. Above 174 mW, the E_p becomes saturated. The maximum E_p produced is 6 nJ at this pump power. This value is much larger than the largest achievable E_p of SA1, SA2 and SA4, which gives the value of 1.8 nJ, 2.5 nJ and 3.0 nJ, respectively, at lower pump power. It should be noted that the generated P_{out} and E_p of the Q-switched laser is low compared to other works (Huang et al., 2014; Li et al., 2014b). This may be due to the large insertion loss from the laser coupling between fibers and the MoS_2-coated waveguide. Furthermore, based on both Figure 4.13 and 4.14, it is interesting to find that the performance of Q-switching does not scale monotonically with the coating length of MoS_2. For example, the P_{out} and E_p of SA4 is lower than that of SA3, although the coating length is the longest. This could be attributed to the inferior coating quality (Figure 4.8), which limit the performance of the Q-switching.

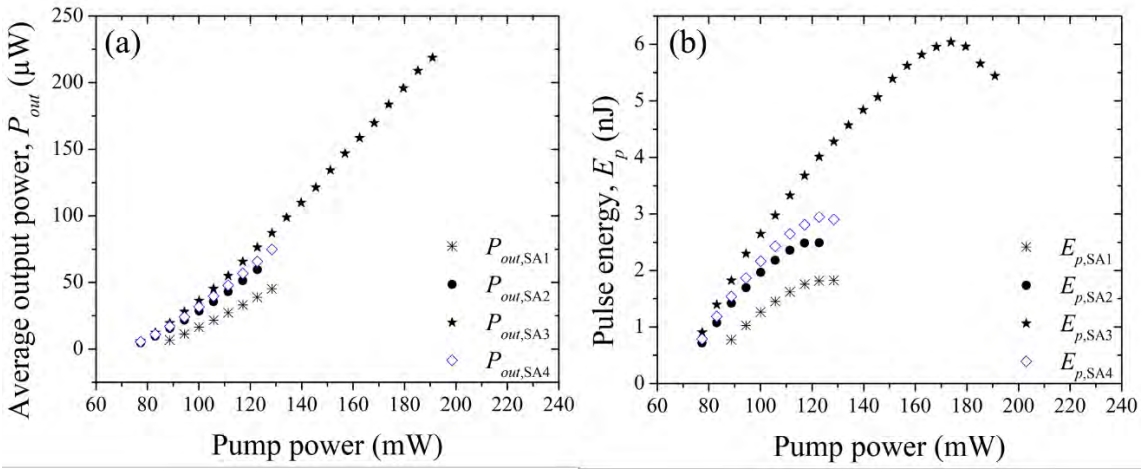

Figure 4.14: Evolution of (a) P_{out} and (b) E_p of SAs against pump power. Figures adapted from (Chew et al., 2022b).

The stability of the SA over time is also studied. Figure 4.15 shows the stability of SA3 in terms of its optical spectrum and pulse trains over an operating time of 60 min. It is obvious that over time, the optical spectrum of SA3 remains at the same power level and does not change in respect of its shape. This implies that the Q-switched laser is stable in terms of its operating wavelength as well as its average power. In addition, the pulse trains generated by SA3 remain the same as well over 60 min, as shown in Figure 4.15(b). The pulse peak power, repetition rate and pulse duration remain almost constant over time. This means that the saturable absorption properties of SA3 do not degrade over time, may withstand prolonged use and remain stable over time.

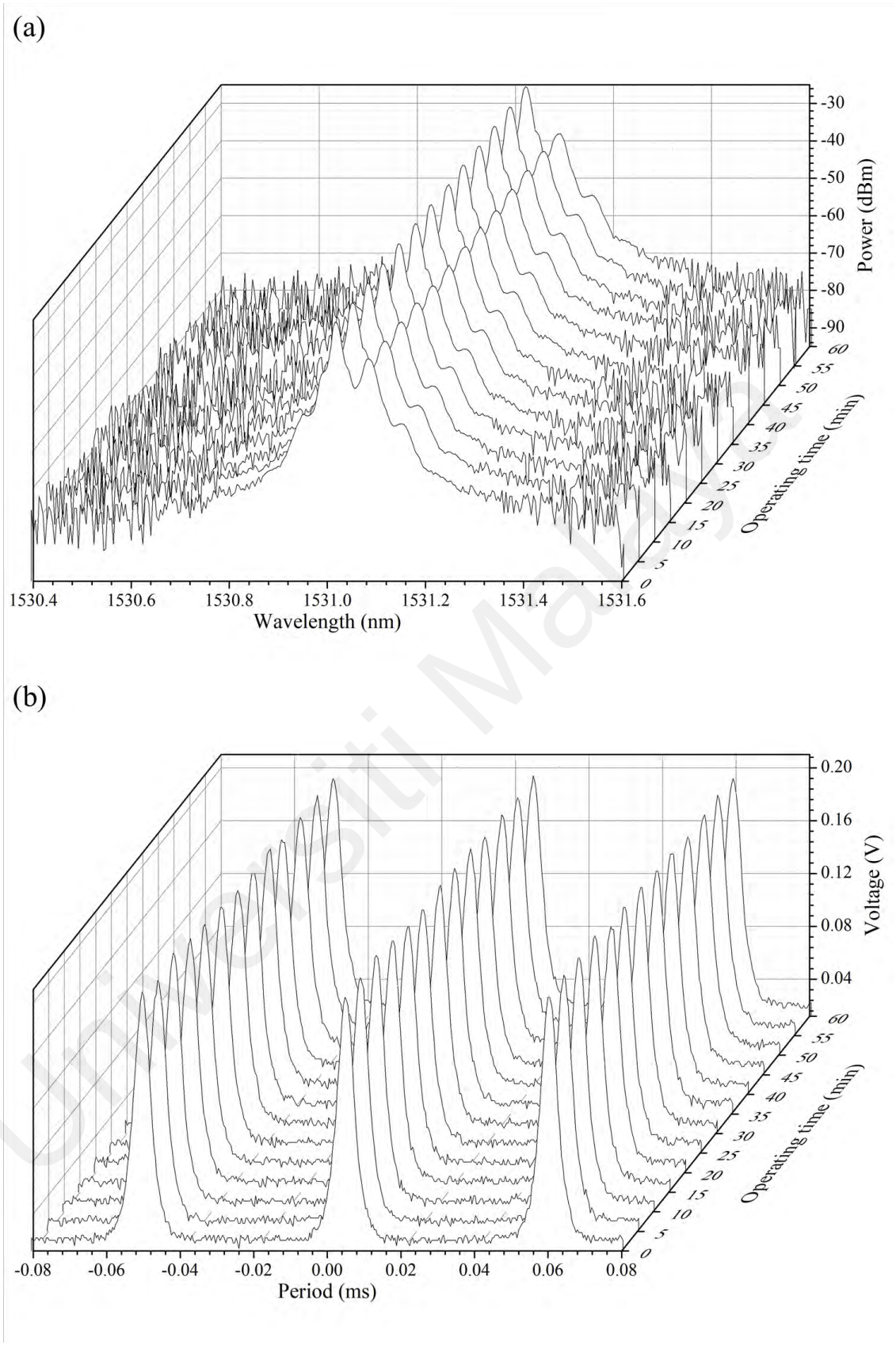

Figure 4.15: Stability of SA3 in terms of (a) optical spectrum; and (b) pulse train over an operating time of 60 min.

4.3 Interaction Length Dependent Wavelength Tunability of the Q-Switched Lasers

Wavelength tunability of a Q-switched laser based on a passive SA is essential in many applications. The study allows one to identify the operating wavelength range, which is useful in designing an application that require Q-switched laser source with specific center wavelength. Examples of application that require a pulse laser source with tunable wavelength ability include spectroscopy and biomedical diagnostics (Woodward et al., 2014). Therefore, it is important to study the operating wavelength range of the four SAs.

4.3.1 Wavelength Tunability of SAs

To investigate the wavelength tunability of SAs, the pump power of the SAs should be fixed before tuning the wavelength of laser using the TBF. In this study, the pump power was fixed at 88.7 mW for SA2, SA3 and SA4 (and 100 mW for SA1), which is approximately 10 mW above the threshold pump power when stable Q-switching are initiated. By adjusting the TBF, the optical spectra of each SA measured by OSA when Q-switched pulsed laser is produced as shown in Figure 4.16. Based on Figure 4.16(a), the lasing wavelength of the Q-switched laser by SA3 is broadly tunable, which ranges from 1527 nm to 1565.6 nm, limited only by the gain bandwidth of the EDF. At the same time, the lasing wavelength of SA1, SA2 and SA4 range from 1528 nm – 1533.9 nm, 1526 nm – 1535.6 nm and 1526.4 nm – 1536 nm, respectively. Figure 4.16(b) shows the Q-switching wavelength range of each SA. For comparison, the operating wavelength range of SA1 and SA3 are 5.9 nm and 38.6 nm, respectively. This means that SA3 can operate in a wavelength range which is 6.5 times broader than that in SA1. Moreover, the Q-switching wavelength range of SA4 is not the widest, which will be discussed in the later section.

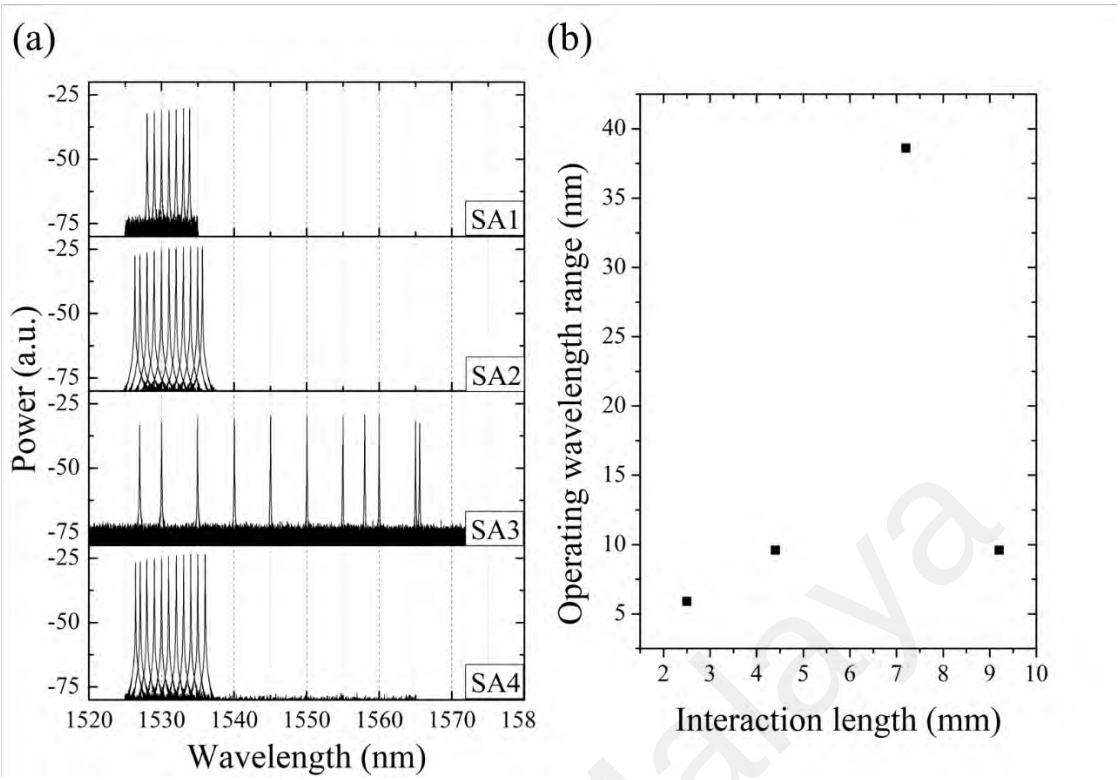

Figure 4.16: (a) The optical spectra of Q-switched laser source produced using different SAs, that indicates the respective wavelength tunability range of each SA; (b) plot of operating wavelength range and coating length of MoS_2 on the waveguide in producing Q-switched laser. Figures adapted from (Chew et al., 2022b).

4.3.2 Defect Induced Sub-Bandgap Absorption

In the previous section, SA3 produces the best Q-switching performance in terms of wavelength tunability although its MoS_2 coating length is not the longest. This can be attributed to the number of defects in the MoS_2 thin film. A longer MoS_2 coating length increases the interaction probability between the light in the waveguide with the number of defects in the MoS_2 thin film. It should be pointed out that even though a CVD-grown MoS_2 thin film may appear uniform and homogeneous during optical inspection, defects can still exist within the thin film (Yin et al., 2014). CVD process may produce sulphur (S) and molybdenum (Mo) vacancies or antisite defect in the MoS_2 thin film (Hong et al., 2015; Pandey et al., 2016). These defects, either vacancies or antisite, will modify the bandgap, which lead to the change in optical properties (especially optical absorption) of

MoS_2. It has been found that the presence of defects in monolayer MoS_2 contributes to sub-bandgap saturable absorption in the 1550 nm wavelength range (Woodward et al., 2014). Kunstmann et al. reported that the S (V_S) and 2S (V_{2S}) vacancies introduce relatively large absorption peaks at energies smaller than 1.9 eV (the bandgap energy of a perfect monolayer MoS_2 crystal is 1.9 eV). On the other hand, vacancies involve Mo and MoS_2 (V_{Mo} and V_{MoS_2}) shows relatively smaller absorption peaks at energies < 1.9 eV (Kunstmann et al., 2017). This means that the defect sites in monolayer MoS_2 introduce in-gap state(s) that promote sub-bandgap absorption. Besides that, the increase in vacancy density increases the absorption of sub-1.9 eV photons as well. Consider the numerical studies exemplified in the work of (Kunstmann et al., 2017), for monolayer MoS_2 without defect, large absorption peak can be found at ~ 1.9 eV (corresponds to ~ 652 nm wavelength), and the absorption decreases rapidly to zero at ~ 1.7 eV (~ 729 nm wavelength). However, only 6.3% of V_{Mo} will cause strong absorption peak at ~ 1.2 eV (~ 1.03 μm wavelength) that reduces in strength towards ~ 0.7 eV (~ 1.77 μm wavelength) (Kunstmann et al., 2017).

Their theoretical studies are important as they predict the ability of "defective" monolayer MoS_2 to respond to light with energies < 1.9 eV (correspond to near infrared light which includes C-band wavelength). It is anticipated that the concentration of molybdenum vacancies affects the wavelength range for Q-switching as well, since saturable absorption involves the transition of electrons between the sub-bandgaps of MoS_2. This has been predicted by XPS measurement discussed in sub-Chapter 3.4, in which the stoichiometry of MoS_2 is slightly more than 2. For further analysis, a comparison is made between SA1 and SA3. SA3 provides a longer interaction length between light in the planarized waveguide and the MoS_2 thin film. The longer interaction length increases the number of vacancies that the light "sees" along the MoS_2-coated waveguide, therefore extending the sub-bandgap absorption to the longer wavelength.

This would be a possible explanation of the extension of Q-switched lasing wavelength of SA3 to ~ 1565 nm, while SA1 can only generate Q-switching pulses over a relatively narrower wavelength range. On the other hand, the narrowing lasing wavelength range of SA4 may be due to the inferior coating quality as shown in Figure 4.8. Inferior coating quality causes the presence of exposed (or terminated) edge sites of MoS_2 coating. This certainly increases the exposed edge-to-vacancy ratio compared to others. The exposed edges will naturally be passivated by other element to form a stable structure (Javaid et al., 2017). Javaid et al. theoretically predict that the passivated MoS_2 structure has a wider bandgap compared to the unpassivated structure (Javaid et al., 2017). This may reduce the saturable absorption of SA4 at longer wavelength.

To verify the hypothesis above, the optical transmission spectra of the SAs over the wavelength range of 1500 nm – 1600 nm was measured. The experiment was carried out by coupling light from a superluminescent diode (Acterna JDSU, OBS-15) into the MoS_2-coated waveguide, and the output was measured using OSA, as shown in Figure 4.17(b). However, before commencing with the experiment, precaution has been made by checking the polarization state of light that allows Q-switching to happen using a polarimeter (Thorlabs PAN5710IR3). This is important as polarization state of light affects the performance of the SA in generating Q-switched pulses. Due to this, the optical transmission spectrum of the SAs should be taken with the similar polarization state as it is in the EDFL. Figure 4.17(a) illustrates the experimental arrangement for measuring the polarization state of the SA.

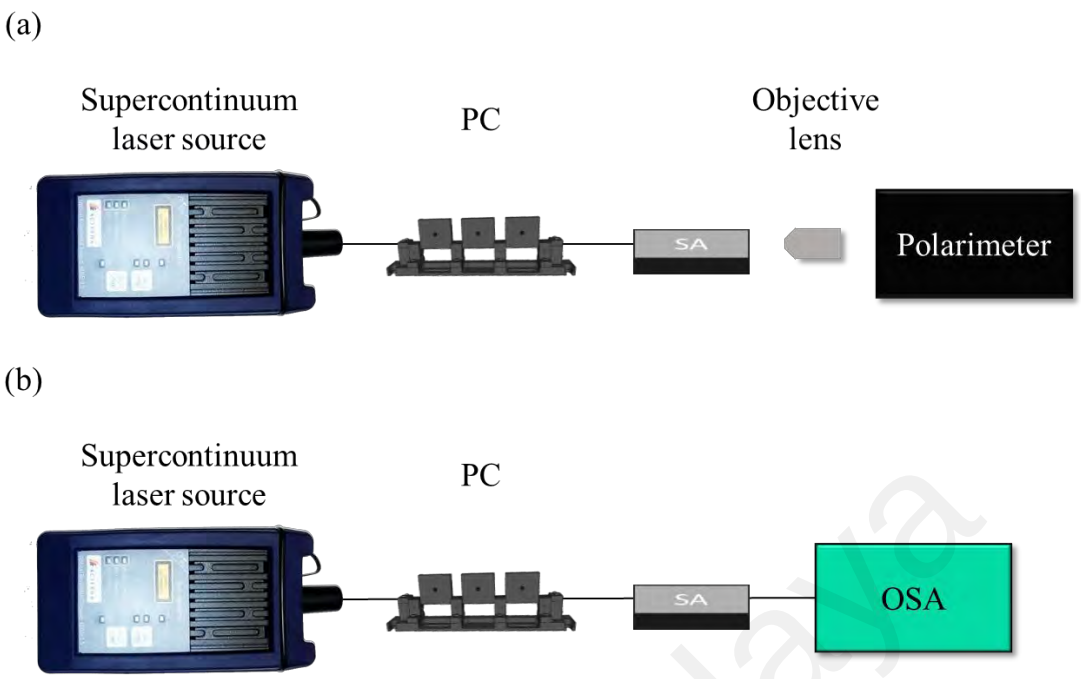

Figure 4.17: Schematic diagram of the experimental arrangement for (a) obtaining the polarization state of light before measuring the optical transmission of the SAs; (b) measuring the optical transmission spectrum of SA.

Figure 4.18 shows the optical transmission spectra of the SAs across the desired wavelength range. Based on the figure, the transmission of four SAs increase towards the longer wavelengths. This means that the absorption of the SAs at longer wavelength is relatively weaker. Furthermore, the absorption of SA3 is higher than that of other SAs. Interestingly, SA3 shows an almost constant absorption trend at shorter wavelengths between 1500 nm to 1540 nm, which then decreases at wavelengths longer than 1540 nm. This trend is quite different from that of SA2 to SA4, in which their absorption decreases monotonically from 1500 nm to 1600 nm. The lower optical absorption for SA1 and SA2 could be attributed to the lower number of V_{Mo} vacancies, which results in their inability to produce Q-switched laser pulses towards the longer wavelength range. On the other hand, it is also observed that SA4 possesses lower absorption at longer wavelength as well. This could be the reason that limits its Q-switching lasing wavelength range as shown in Figure 4.16(b). Therefore, a conclusion can be drawn such that long interaction

length of the MoS_2 coating with minimum exposed edge sites contributes to the ability of MoS2-coated planarized waveguides in producing Q-switched pulse lasers with broader operating wavelength tunability.

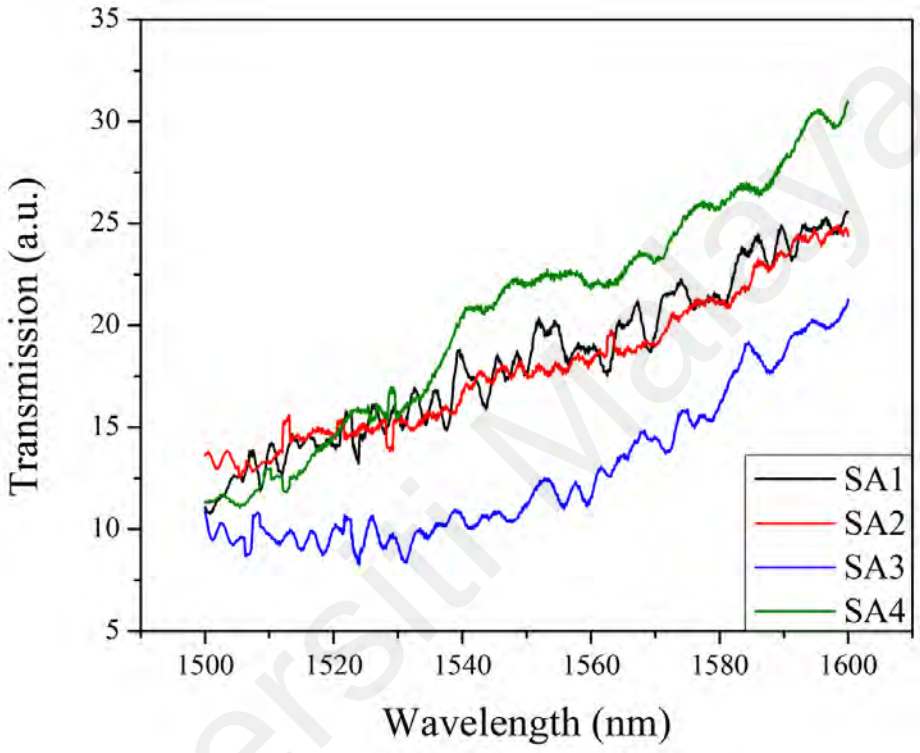

Figure 4.18: Optical transmission spectra of four SAs across a broad wavelength range of 1500 nm to 1600 nm. Figure adapted from (Chew et al., 2022b).

4.4 Summary

The characterization of a 7.2 mm-length MoS_2-coated waveguide in terms of NLA has been carried out using I-scan technique. It is found that this waveguide exhibits saturable absorption properties. The waveguide is then integrated into an EDFL cavity to study its capability in producing pulse laser source. Q-switched laser pulses are generated, although the maximum pulse energy generated is weaker compared to other MoS_2-based SA that works in transmission scheme. This finding is important in the sense that a large

area monolayer MoS_2 coated on a planarized waveguide can be used to generate waveguide-based Q-switched lasers. To the best of my knowledge, there is no MoS_2-based planarized waveguide pulse laser source at C-band wavelength region that can be found yet in the literature review (Guo et al., 2019). Therefore, this paves a new opportunity to develop a monolayer MoS_2-based planarized waveguide pulse laser source laser in this wavelength range.

Due to the advantages of the dry transfer technique and the evanescent field interaction, the investigation of the effect of MoS_2 interaction length towards the performance of Q-switched pulse lasers is made possible. To achieve this, MoS_2-coated waveguide with four coating lengths (2.5 mm, 4.4 mm, 7.2 mm and 9.2 mm; labelled as SA1, SA2, SA3 and SA4, respectively) are prepared. These four SAs show saturable absorption properties as well when measured using the I-scan technique. After coupled into a modified EDFL cavity, Q-switched pulses are observed from four SAs, with different performance. In terms of repetition rate, average output power and pulse energy, SA3 stands out among the other SAs. Yet, the longest interaction length (SA4) does not exhibit better performance compared to SA3. This could be attributed to the inferior coating quality, which affect the saturable absorption properties. Based on the observation, it indicates that longer interaction length can improve the performance of Q-switching. Apart from that, the wavelength tunability of all SAs are studied as well. The results show that SA3 has the widest wavelength tunability range, as wide as 38.6 nm (from 1527 nm to 1565.6 nm), compared to other SAs. Again, SA4 does not show a wide wavelength tunability ability, which may be due to its coating quality. The wavelength tunability could come from the defect induced sub-bandgap absorption of the CVD-grown MoS_2 thin film. In previous chapter, it is shown that the stoichiometry of MoS_2 is slightly larger than 2, which indicates that they might have molybdenum vacancies across the grown MoS_2 thin film. Defective MoS_2 thin film possesses in-gap states that allow sub-bandgap absorption,

which is studied theoretically by another group (Kunstmann et al., 2017). This would make a defective MoS_2 to become a broadband absorption, which may improve the performance of Q-switched lasers using MoS_2 SA as evident by the presented results. By relating the work from Kunstmann et al., a discussion is made to elucidate the effect of the concentration of molybdenum vacancies (related to the coating length of MoS2 on waveguide) on the wavelength range of SAs for Q-switching, since saturable absorption involves the transition of electrons from the sub-bandgaps of MoS_2. The argument is verified by carrying out the measurement of optical transmission spectra of SAs.

CHAPTER 5: CONCLUSION AND FUTURE WORKS

5.1 Conclusion

The investigation of NLO properties of CVD-grown large area monolayer MoS_2 in the C-band wavelength range has been achieved in a free space and planarized waveguide-based manners. Prior to characterizing the NLO properties, the monolayer MoS_2-PDMS sample was characterized using Raman spectroscopy, AFM and XPS techniques. The Raman spectroscopy provides the fingerprint of Raman modes of the MoS_2, which can indirectly aid in the number of layers determination using a simpler, non-contact and non-destructive manner. The physical thickness of MoS_2 sample, both on the original and target substrate, has been determined using AFM. The result obtained from Raman spectroscopy and AFM confirm that the MoS_2 has a monolayer thickness. Furthermore, the surface element and stoichiometry of MoS_2 were studied using XPS technique. The outcome of XPS shows that the sample is free from oxidation and has a S:Mo ratio of slightly more than two, which indicates that the sample might suffer from small degree molybdenum vacancies. The nonlinear refractive index, n_2 of MoS_2 was determined by carrying out a time-resolved Z-scan technique on the MoS_2-PDMS sample. This technique allows us to separate the nonlinear refraction effects that come from the thermal lensing effect as well as the instantaneous electronic nonlinearity. To the best of the author's knowledge, this would be the first determination of n_2 of monolayer MoS_2 using a Z-scan technique at this wavelength range. The n_2 of MoS_2 was determined to be as large as 1.40×10^{-13} m^2 W^{-1} at C-band wavelength range. This shows that MoS_2 can be a good 2D material candidate for nonlinear optics application.

To utilize its NLO properties, the monolayer MoS_2 was integrated on an optical planarized waveguide platform using an all-dry transfer technique. Briefly, the planarized

waveguide platform consists of a core surrounded by side-cladding and under-cladding. The refractive indices of core, side-cladding and under-cladding are 1.486, 1.44 and 1.444, respectively. It supports fundamental mode of light operation in the core, which is beneficial for investigation and implementation. A razor blade cutting method was preferably chosen (compare to laser cutting method) to cut the MoS_2-PDMS sample into desired size for application, because it minimizes surface contamination. The cut sample was transferred to the waveguide using the PDMS-assisted transfer technique. The PDMS acts as the stamp. Due to different surface energies between MoS_2-PDMS and MoS_2-SiO_2 interfaces, the large area MoS_2 thin film can be delaminated from the PDMS stamp, leaving a uniform thin film coating on the waveguide surface.

The nonlinear absorption properties of the MoS_2-coated planarized waveguide was identified during the I-scan measurement. Based on the I-scan measurement, the 7.2 mm-length MoS_2-coated waveguide exhibits saturable absorption property. The waveguide shows a modulation depth, non-saturable loss and saturation intensity of ~ 2.7%, ~ 76.8%, and 0.87 MW cm^{-2}, respectively. These values show the potential of MoS_2-coated waveguide to become a pulse laser source.

To check its capability in pulse laser generation, the MoS_2-coated waveguide was coupled into an erbium-doped fiber laser cavity. It is demonstrated that the MoS_2-coated waveguide is able to act as a saturable absorber to produce a Q-switched laser. The Q-switched laser operates at a central wavelength of 1558 nm. The maximum repetition rate and average output power achieved are 35.85 kHz and 0.14 mW, respectively, at the pump power of ~ 150 mW. The minimum pulse duration and maximum pulse energy that can be achieved are 5.24 μs and 4.1 nJ, respectively, at the pump power of 122.8 mW. Pulse laser due to mode-locked mechanism is not observed in the presented experimental setup, which could be attributed to the large insertion loss and non-saturable loss of the MoS_2-coated waveguide. The findings are considered fruitful as they will pave a route for the

development of MoS_2-based all-planar waveguide laser application, which is distinct to the current optical fiber-based application.

Apart from that, since the pulse generation is based on the evanescence field interaction with the monolayer MoS_2 thin film on the waveguide, further investigation was carried out to study the interaction length dependency on the performance of Q-switched pulse laser generation. Different lengths of MoS_2 were integrated on the waveguide and labelled as SA1, SA2, SA3 and SA4. Their coating lengths on the waveguide were measured to be 2.5 mm, 4.4 mm, 7.2 mm and 9.2 mm, respectively. The results demonstrate that the performance of Q-switching is dependent on the coating length of MoS_2 thin film. Among the SAs, the performance of SA3 (in terms of repetition rate, pulse duration, average output power, pulse energy and wavelength tunability) is more superior. In addition, SA3 shows a wide wavelength tunability range of 38.6 nm, spanning from wavelengths of 1527 nm to 1565.6 nm. The observations show that with longer interaction length, the performance of Q-switching can be increased. However, this does not reflect on SA4 which has the longest coating length in the study. The most probable reason could be due to the inferior coating of SA4, in which discontinuity of coating are observed. The large wavelength tunability of SA3 is explained by defect induced sub-bandgap absorption of the MoS_2 thin film. Defects such as molybdenum vacancies introduce in-gap states in the MoS_2, therefore permitting sub-bandgap absorption at longer wavelengths. The discussion is verified by measuring the optical transmission spectra of the SAs. Therefore, an inference can be made that with long interaction length of MoS_2 thin film and minimum exposed edge sites can enhance the performance of Q-switching and its wavelength tunability.

In short, the presented work is considered to be valuable for the development of large area monolayer MoS_2-based devices. The large n_2 of MoS_2 suggests that it can become a potential 2D material for nonlinear optical application, such as in all-optical switching

application in the C-band wavelength region. The integration of MoS_2 on a planarized waveguide is demonstrated as one of a potential method to functionalize the waveguide for linear and nonlinear optical planar waveguide application. Particularly, the successful generation of Q-switched pulse using MoS_2-coated waveguide pave a route for the development of a robust, compact waveguide laser source. This can in turn bring advantages in all-planar waveguide laser technology and lab-on-chip application.

5.2 Future Works

Based on the current investigations and achievements, a number of extension studies can be explored in the future. The current works could not achieve pulse generation based on mode-locked mechanism, which could be mainly due to the large insertion loss from the fiber-waveguide coupling interface. Efforts could be put by designing different structure of the waveguide to reduce the insertion loss. Besides that, redesigning the erbium-doped fiber laser cavity can be performed as well to manipulate the dispersion of the cavity required for mode-locked operation. This is because the condition for mode-locking in a fiber cavity is very stringent and strongly related to the modulation depth and dispersion management of the cavity. In addition, the current MoS_2-coated waveguide can be coupled into fiber laser cavity with different gain medium, such as ytterbium- or thulium-based gain medium to achieve pulse laser sources at 1 μm and 2 μm wavelength range, respectively.

Apart from that, it would be interesting to investigate the nonlinear optical properties of large area few-layer MoS_2 using the same planarized waveguide platform. In other word, large area few-layer MoS_2 can be integrated on planarized waveguide and the performance of pulse laser generation can be studied and compared with the current works. This is because the nonlinear optical properties of few-layer MoS_2 are expected to be

different from that of monolayer MoS_2. The effect of interaction length of few-layer MoS_2-coated waveguide in pulse laser generation can be compared as well. This study could provide useful information in designing waveguide-based pulse laser source. Finally, the study of enhancing the nonlinear optical properties of the MoS_2-coated waveguide can be carried out by introducing more defects on the MoS_2 thin film.

REFERENCES

Agrawal, G. P. (2000). Nonlinear fiber optics. In *Nonlinear Science at the Dawn of the 21st Century* (pp. 195-211). Springer.

Ahmad, H., Albaqawi, H. S., Yusoff, N., & Yi, C. W. (2020). 56 nm Wide-Band Tunable Q-Switched Erbium Doped Fiber Laser with Tungsten Ditelluride (WTe_2) Saturable Absorber. *Scientific Reports*, *10*(1), 1-10.

Ahmad, H., Yusoff, N., Monajemi, H., & Reduan, S. A. (2019). Nickel phosphate as a C-band optical pulse modulator. *Applied Physics B*, *125*(7), 1-9.

Al-Sulaiman, F., Yilbas, B., & Ahsan, M. (2006). CO_2 laser cutting of a carbon/carbon multi-lamelled plain-weave structure. *Journal of Materials Processing Technology*, *173*(3), 345-351.

Amani, M., Chin, M. L., Mazzoni, A. L., Burke, R. A., Najmaei, S., Ajayan, P. M., . . . Dubey, M. (2014). Growth-substrate induced performance degradation in chemically synthesized monolayer MoS_2 field effect transistors. *Applied Physics Letters*, *104*(20), Article#203506.

Backes, C., Higgins, T. M., Kelly, A., Boland, C., Harvey, A., Hanlon, D., & Coleman, J. N. (2017). Guidelines for exfoliation, characterization and processing of layered materials produced by liquid exfoliation. *Chemistry of Materials*, *29*(1), 243-255.

Backes, C., Smith, R. J., McEvoy, N., Berner, N. C., McCloskey, D., Nerl, H. C., . . . Hanlon, D. (2014). Edge and confinement effects allow in situ measurement of size and thickness of liquid-exfoliated nanosheets. *Nature Communications*, *5*(1), 1-10.

Backes, C., Szydłowska, B. M., Harvey, A., Yuan, S., Vega-Mayoral, V., Davies, B. R., . . . Katsnelson, M. I. (2016). Production of highly monolayer enriched dispersions of liquid-exfoliated nanosheets by liquid cascade centrifugation. *ACS Nano*, *10*(1), 1589-1601.

Baker, M., Gilmore, R., Lenardi, C., & Gissler, W. (1999). XPS investigation of preferential sputtering of S from MoS_2 and determination of MoS_x stoichiometry from Mo and S peak positions. *Applied Surface Science*, *150*(1-4), 255-262.

Balandin, A. A., Ghosh, S., Bao, W., Calizo, I., Teweldebrhan, D., Miao, F., & Lau, C. N. (2008). Superior thermal conductivity of single-layer graphene. *Nano Letters*, *8*(3), 902-907.

Balla, N. K., O'brien, M., McEvoy, N., Duesberg, G. S., Rigneault, H., Brasselet, S., & McCloskey, D. (2018). Effects of excitonic resonance on second and third order nonlinear scattering from few-layer MoS_2. *ACS Photonics*, *5*(4), 1235-1240.

Bang, G. S., Nam, K. W., Kim, J. Y., Shin, J., Choi, J. W., & Choi, S.-Y. (2014). Effective liquid-phase exfoliation and sodium ion battery application of MoS_2 nanosheets. *ACS Applied Materials Interfaces*, *6*(10), 7084-7089.

Bao, Q., Zhang, H., Wang, Y., Ni, Z., Yan, Y., Shen, Z. X., . . . Tang, D. Y. (2009). Atomic - layer graphene as a saturable absorber for ultrafast pulsed lasers. *Advanced Functional Materials*, *19*(19), 3077-3083.

Barthelmi, K., Klein, J., Hötger, A., Sigl, L., Sigger, F., Mitterreiter, E., . . . Florian, M. (2020). Atomistic defects as single-photon emitters in atomically thin MoS_2. *Applied Physics Letters*, *117*(7), Article#070501.

Benavente, E., Santa Ana, M., Mendizábal, F., & González, G. (2002). Intercalation chemistry of molybdenum disulfide. *Coordination Chemistry Reviews*, *224*(1-2), 87-109.

Bhuyan, M., Alam, S., Uddin, M., Islam, M., Bipasha, F. A., & Hossain, S. S. (2016). Synthesis of graphene. *International Nano Letters*, *6*(2), 65-83.

Bikorimana, S., Lama, P., Walser, A., Dorsinville, R., Anghel, S., Mitioglu, A., . . . Kulyuk, L. (2016). Nonlinear optical responses in two-dimensional transition metal dichalcogenide multilayer: WS_2, WSe_2, MoS_2 and $Mo_{0.5}W_{0.5}S_2$. *Optics Express*, *24*(18), 20685-20695.

Bodík, M., Annušová, A., Hagara, J., Mičušík, M., Omastová, M., Kotlár, M., . . . Anguš, M. (2019). An elevated concentration of MoS_2 lowers the efficacy of liquid-phase exfoliation and triggers the production of MoO_x nanoparticles. *Physical Chemistry Chemical Physics*, *21*(23), 12396-12405.

Bolotin, K. I., Sikes, K. J., Jiang, Z., Klima, M., Fudenberg, G., Hone, J., . . . Stormer, H. L. (2008). Ultrahigh electron mobility in suspended graphene. *Solid State Communications*, *146*(9-10), 351-355.

Boyd, R. W. (2008). The Nonlinear Optical Susceptibility. In *Nonlinear Optics* (3rd ed., pp. 1-17). Academic press.

Budania, P., Baine, P. T., Montgomery, J. H., McNeill, D. W., Neil Mitchell, S., Modreanu, M., & Hurley, P. K. (2017). Comparison between Scotch tape and gel-assisted mechanical exfoliation techniques for preparation of 2D transition metal dichalcogenide flakes. *Micro Nano Letters*, *12*(12), 970-973.

Buscema, M., Steele, G. A., van der Zant, H. S., & Castellanos-Gomez, A. (2014). The effect of the substrate on the Raman and photoluminescence emission of single-layer MoS_2. *Nano Research*, *7*(4), 561-571.

Cai, X., Luo, Y., Liu, B., & Cheng, H.-M. (2018). Preparation of 2D material dispersions and their applications. *Chemical Society Reviews*, *47*(16), 6224-6266.

Caiazzo, F., Curcio, F., Daurelio, G., & Minutolo, F. M. C. (2005). Laser cutting of different polymeric plastics (PE, PP and PC) by a CO_2 laser beam. *Journal of Materials Processing Technology*, *159*(3), 279-285.

Castellanos-Gomez, A., Buscema, M., Molenaar, R., Singh, V., Janssen, L., Van derZant, H. S., & Steele, G. A. (2014). Deterministic transfer of two-dimensional materials by all-dry viscoelastic stamping. *2D Materials*, *1*(011002).

Castellanos-Gomez, A., Quereda, J., van der Meulen, H. P., Agraït, N., & Rubio-Bollinger, G. (2016). Spatially resolved optical absorption spectroscopy of single- and few-layer MoS_2 by hyperspectral imaging. *Nanotechnology*, *27*(11), Article#115705.

Chang, T., & Molian, P. (1999). Excimer pulsed laser ablation of polymers in air and liquids for micromachining applications. *Journal of Manufacturing Systems*, *18*(2), 1-17.

Chastain, J., & King Jr, R. C. (1992). *Handbook of X-ray photoelectron spectroscopy* (Vol. 40). Perkin-Elmer Corporation.

Chen, B., Zhang, X., Wu, K., Wang, H., Wang, J., & Chen, J. (2015a). Q-switched fiber laser based on transition metal dichalcogenides MoS_2, $MoSe_2$, WS_2, and WSe_2. *Optics Express*, *23*(20), 26723-26737.

Chen, Y., Jiang, G., Chen, S., Guo, Z., Yu, X., Zhao, C., . . . Tang, D. (2015b). Mechanically exfoliated black phosphorus as a new saturable absorber for both Q-switching and mode-locking laser operation. *Optics Express*, *23*(10), 12823-12833.

Chew, J. W., Chong, W. Y., Muniandy, S. V., Yap, Y. K., & Ahmad, H. (2023). Determination of nonlinear refractive index of large area monolayer MoS_2 at telecommunication wavelength using time-resolved Z-scan technique. *Journal of Nonlinear Optical Physics Materials*, Article#2350052.

Chew, J. W., Chong, W. Y., Yap, Y. K., Ng, K. B., Gan, S. X., & Ahmad, H. (2022a). Saturable absorption performance of large area monolayer MoS_2 coated planarized optical waveguide. *Laser Physics Letters*, *19*(11), Article#116205.

Chew, J. W., Ng, K. B., Gan, S. X., Tey, L. S., Chong, W. Y., Yap, Y. K., & Ahmad, H. (2022b). Interaction Length-Dependent Saturable Absorption of MoS_2-Coated Planarized Waveguide and its Effect on the Performance of Q-Switched Pulse Laser Generation. *Journal of Lightwave Technology*, *41*(8), 2458-2464.

Choi, K., Lee, Y. T., Min, S. W., Lee, H. S., Nam, T., Kim, H., & Im, S. (2013). Direct imprinting of MoS_2 flakes on a patterned gate for nanosheet transistors. *Journal of Materials Chemistry C*, *1*(47), 7803-7807.

Choi, W., Kim, J., Lee, E., Mehta, G., & Prasad, V. (2021). Asymmetric 2D MoS_2 for scalable and high-performance piezoelectric sensors. *ACS Applied Materials Interfaces*, *13*(11), 13596-13603.

Chong, W., Gan, S., Lai, C., Chong, W., Choi, D., Madden, S., . . . Ahmad, H. (2020). Configurable TE-and TM-pass graphene oxide-coated waveguide polarizer. *IEEE Photonics Technology Letters*, *32*(11), 627-630.

Choudhary, A., Dhingra, S., D'Urso, B., Kannan, P., & Shepherd, D. P. (2015). Graphene Q-switched mode-locked and Q-switched ion-exchanged waveguide lasers. *IEEE Photonics Technology Letters*, *27*(6), 646-649.

Coleman, J. N., Lotya, M., O'Neill, A., Bergin, S. D., King, P. J., Khan, U., . . . Smith, R. J. (2011). Two-dimensional nanosheets produced by liquid exfoliation of layered materials. *Science*, *331*(6017), 568-571.

Couris, S., Koudoumas, E., Ruth, A., & Leach, S. (1995). Concentration and wavelength dependence of the effective third-order susceptibility and optical limiting of C_{60} in toluene solution. *Journal of Physics B: Atomic, Molecular Optical Physics*, *28*(20), Article#4537.

De Araújo, C. B., Gomes, A. S., & Boudebs, G. (2016). Techniques for nonlinear optical characterization of materials: a review. *Reports on Progress in Physics*, *79*(3), Article#036401.

De Nalda, R., Del Coso, R., Requejo-Isidro, J., Olivares, J., Suarez-Garcia, A., Solis, J., & Afonso, C. N. (2002). Limits to the determination of the nonlinear refractive index by the Z-scan method. *JOSA B*, *19*(2), 289-296.

Dean, C. R., Young, A. F., Meric, I., Lee, C., Wang, L., Sorgenfrei, S., . . . Shepard, K. L. (2010). Boron nitride substrates for high-quality graphene electronics. *Nature Nanotechnology*, *5*(10), 722-726.

Degnan, J. J. (1995). Optimization of passively Q-switched lasers. *IEEE Journal of Quantum Electronics*, *31*(11), 1890-1901.

Du, J., Zhang, M., Guo, Z., Chen, J., Zhu, X., Hu, G., . . . Zhang, H. (2017). Phosphorene quantum dot saturable absorbers for ultrafast fiber lasers. *Scientific Reports*, *7*(1), 1-10.

Dumcenco, D., Ovchinnikov, D., Marinov, K., Lazic, P., Gibertini, M., Marzari, N., . . . Chen, M.-W. (2015). Large-area epitaxial monolayer MoS_2. *ACS Nano*, *9*(4), 4611-4620.

Eda, G., Yamaguchi, H., Voiry, D., Fujita, T., Chen, M., & Chhowalla, M. (2011). Photoluminescence from chemically exfoliated MoS_2. *Nano Letters*, *11*(12), 5111-5116.

Eichfeld, S. M., Hossain, L., Lin, Y.-C., Piasecki, A. F., Kupp, B., Birdwell, A. G., . . . Li, J. (2015). Highly scalable, atomically thin WSe_2 grown via metal–organic chemical vapor deposition. *ACS Nano*, *9*(2), 2080-2087.

Ermolaev, G. A., Stebunov, Y. V., Vyshnevyy, A. A., Tatarkin, D. E., Yakubovsky, D. I., Novikov, S. M., . . . Arsenin, A. V. (2020). Broadband optical properties of monolayer and bulk MoS_2. *npj 2D Materials Applications*, *4*(1), 1-6.

Evgeny, A. *Viscoelastic Transfer of 2D Material Using PDMS*. Retrived from https://www.ossila.com/pages/viscoelastic-transfer-of-2d-material-using-pdms

Falconieri, M. (1999). Thermo-optical effects in Z-scan measurements using high-repetition-rate lasers. *Journal of Optics A: Pure Applied Optics*, *1*(6), Article#662.

Falconieri, M., & Salvetti, G. (1999). Simultaneous measurement of pure-optical and thermo-optical nonlinearities induced by high-repetition-rate, femtosecond laser pulses: application to CS_2. *J Applied Physics B*, *69*(2), 133-136.

Forsberg, V., Zhang, R., Bäckström, J., Dahlström, C., Andres, B., Norgren, M., . . . Olin, H. (2016). Exfoliated MoS_2 in water without additives. *PloS One*, *11*(4), Article#e0154522.

Gan, S. X., Lai, C. K., Chong, W. S., Chong, W. Y., Madden, S., & Ahmad, H. (2020). Large polarization response of planarized optical waveguide functionalized with 2D material overlays. *Journal of Modern Optics*, *67*(8), 730-736.

Garay-Palmett, K., McGuinness, H., Cohen, O., Lundeen, J., Rangel-Rojo, R., U'ren, A., . . . Walmsley, I. (2007). Photon pair-state preparation with tailored spectral properties by spontaneous four-wave mixing in photonic-crystal fiber. *Optics Express*, *15*(22), 14870-14886.

Gengenbach, T. R., Major, G. H., Linford, M. R., & Easton, C. D. (2021). Practical guides for x-ray photoelectron spectroscopy (XPS): Interpreting the carbon 1s spectrum. *Journal of Vacuum Science Technology A: Vacuum, Surfaces, Films*, *39*(1), Article#013204.

Gerberich, W. W., Jungk, J., & Mook, W. (2003). The bottom-up approach to materials by design. In *Nano and Microstructural Design of Advanced Materials* (pp. 211-220). Elsevier.

Glasmästar, K., Gold, J., Andersson, A.-S., Sutherland, D. S., & Kasemo, B. (2003). Silicone transfer during microcontact printing. *Langmuir*, *19*(13), 5475-5483.

Gnoli, A., Razzari, L., & Righini, M. (2005). Z-scan measurements using high repetition rate lasers: how to manage thermal effects. *Optics express*, *13*(20), 7976-7981.

Gradshteyn, I. S., & Ryzhik, I. M. (2014). *Table of integrals, series, and products*. Academic press.

Guo, B., Xiao, Q. l., Wang, S. h., & Zhang, H. (2019). 2D layered materials: synthesis, nonlinear optical properties, and device applications. *Laser Photonics Reviews*, *13*(12), Article#1800327.

Gupta, D., Chauhan, V., & Kumar, R. (2020). A comprehensive review on synthesis and applications of molybdenum disulfide (MoS_2) material: Past and recent developments. *Inorganic Chemistry Communications*, *121*, Article#108200.

Gurarslan, A., Yu, Y., Su, L., Yu, Y., Suarez, F., Yao, S., . . . Cao, L. (2014). Surface-energy-assisted perfect transfer of centimeter-scale monolayer and few-layer MoS_2 films onto arbitrary substrates. *ACS Nano*, *8*(11), 11522-11528.

Gusakova, J., Wang, X., Shiau, L. L., Krivosheeva, A., Shaposhnikov, V., Borisenko, V., . . . Tay, B. K. (2017). Electronic properties of bulk and monolayer TMDs: theoretical study within DFT framework (GVJ-2e method). *Physica Status Solidi*, *214*(12), Article#1700218.

Ham, S. S., & Lee, H. (2020). Development of method enhanced laser ablation efficiency according to fine curvature of the polymer through the preliminary preparation process using UV picosecond laser. *Polymers*, *12*(4), Article#959.

Hampf, D., Schafer, E., Sproll, F., Otsubo, T., Wagner, P., & Riede, W. (2019). Satellite laser ranging at 100 kHz pulse repetition rate. *CEAS Space Journal*, *11*(4), 363-370.

Hawkes, J., & Latimer, I. (1995). *Lasers: theory and practice*. Prentice Hall.

He, T., Li, Y., Zhou, Z., Zeng, C., Qiao, L., Lan, C., . . . Liu, Y. (2019). Synthesis of large-area uniform MoS_2 films by substrate-moving atmospheric pressure chemical vapor deposition: from monolayer to multilayer. *2D Materials*, *6*(2), Article#025030.

He, X., Liu, Z.-b., & Wang, D. (2012). Wavelength-tunable, passively mode-locked fiber laser based on graphene and chirped fiber Bragg grating. *Optics Letters*, *37*(12), 2394-2396.

Herda, R., Kivistö, S., & Okhotnikov, O. G. (2008). Dynamic gain induced pulse shortening in Q-switched lasers. *Optics letters*, *33*(9), 1011-1013.

Hon, N. K., Soref, R., & Jalali, B. (2011). The third-order nonlinear optical coefficients of Si, Ge, and $Si_{1-x}Ge_x$ in the midwave and longwave infrared. *Journal of Applied Physics*, *110*(1), Article#9.

Hong, J., Hu, Z., Probert, M., Li, K., Lv, D., Yang, X., . . . Xie, L. (2015). Exploring atomic defects in molybdenum disulphide monolayers. *Nature Communications*, *6*(1), Article#6293.

Hong, M., Yang, P., Zhou, X., Zhao, S., Xie, C., Shi, J., . . . Zhang, Y. (2018). Decoupling the Interaction between Wet-Transferred MoS_2 and Graphite Substrate by an Interfacial Water Layer. *Advanced Materials Interfaces*, *5*(21), Article#1800641.

Hsu, C., Frisenda, R., Schmidt, R., Arora, A., De Vasconcellos, S. M., Bratschitsch, R., . . . Castellanos-Gomez, A. (2019). Thickness-dependent refractive index of 1L, 2L, and 3L MoS_2, $MoSe_2$, WS_2, and WSe_2. *Advanced Optical Materials*, *7*(13), Article#1900239.

Huang, Y., Luo, Z., Li, Y., Zhong, M., Xu, B., Che, K., . . . Weng, J. (2014). Widely-tunable, passively Q-switched erbium-doped fiber laser with few-layer MoS_2 saturable absorber. *Optics express*, *22*(21), 25258-25266.

Hunsperger, R. G. (2009). Introduction. In *Integrated Optics: Theory and Technology* (6th ed., pp. 1-12). Springer. https://doi.org/10.1007/b98730

Iacovella, F., Koroleva, A., Rybkin, A. G., Fouskaki, M., Chaniotakis, N., Savvidis, P., & Deligeorgis, G. (2020). Impact of thermal annealing in forming gas on the optical and electrical properties of MoS_2 monolayer. *Journal of Physics: Condensed Matter*, *33*(3), Article#035001.

Isiksacan, Z., Guler, M. T., Aydogdu, B., Bilican, I., & Elbuken, C. (2016). Rapid fabrication of microfluidic PDMS devices from reusable PDMS molds using laser ablation. *Journal of Micromechanics Microengineering*, *26*(3), Article#035008.

Islam, K. M., Synowicki, R., Ismael, T., Oguntoye, I., Grinalds, N., & Escarra, M. D. (2021). In-plane and out-of-plane optical properties of monolayer, few-layer, and thin-film MoS_2 from 190 to 1700 nm and their application in photonic device design. *Advanced Photonics Research*, *2*(5), Article#2000180.

Javaid, M., Drumm, D. W., Russo, S. P., & Greentree, A. D. (2017). A study of size-dependent properties of MoS_2 monolayer nanoflakes using density-functional theory. *Scientific Reports*, *7*(1), 1-11.

Jawaid, A., Nepal, D., Park, K., Jespersen, M., Qualley, A., Mirau, P., . . . Vaia, R. A. (2016). Mechanism for liquid phase exfoliation of MoS_2. *Chemistry of Materials*, *28*(1), 337-348.

Jensen, D. S., Kanyal, S. S., Madaan, N., Vail, M. A., Dadson, A. E., Engelhard, M. H., & Linford, M. R. (2013). Silicon (100)/SiO_2 by XPS. *Surface Science Spectra*, *20*(1), 36-42.

Jeon, J., Lee, J., & Lee, J. H. (2015). Numerical study on the minimum modulation depth of a saturable absorber for stable fiber laser mode locking. *JOSA B*, *32*(1), 31-37.

Jeong, H., Choi, S. Y., Jeong, E. I., Cha, S. J., Rotermund, F., & Yeom, D.-I. (2013). Ultrafast mode-locked fiber laser using a waveguide-type saturable absorber based on single-walled carbon nanotubes. *Applied Physics Express*, *6*(5), Article#052705.

Jia, Y., & Chen, F. (2019). Compact solid-state waveguide lasers operating in the pulsed regime: a review [Invited]. *Chinese Optics Letters*, *17*(1), 012302. https://opg.optica.org/col/abstract.cfm?URI=col-17-1-012302

Johnson, K. L., Kendall, K., & Roberts, a. (1971). Surface energy and the contact of elastic solids. *Proceedings of the Royal Society of London. A. Mathematical Physical Sciences*, *324*(1558), 301-313.

Kang, M.-A., Kim, S. J., Song, W., Chang, S.-j., Park, C.-Y., Myung, S., . . . An, K.-S. (2017). Fabrication of flexible optoelectronic devices based on MoS_2/graphene hybrid patterns by a soft lithographic patterning method. *Carbon*, *116*, 167-173.

Kelly, A. G., Finn, D., Harvey, A., Hallam, T., & Coleman, J. N. (2016). All-printed capacitors from graphene-BN-graphene nanosheet heterostructures. *Applied Physics Letters*, *109*(2), Article#023107.

Khazaeizhad, R., Kassani, S. H., Jeong, H., Yeom, D.-I., & Oh, K. (2014). Mode-locking of Er-doped fiber laser using a multilayer MoS_2 thin film as a saturable absorber in both anomalous and normal dispersion regimes. *Optics Express*, *22*(19), 23732-23742.

Kim, I. S., Sangwan, V. K., Jariwala, D., Wood, J. D., Park, S., Chen, K.-S., . . . Jose-Yacaman, M. (2014). Influence of stoichiometry on the optical and electrical properties of chemical vapor deposition derived MoS_2. *ACS Nano*, *8*(10), 10551-10558.

Kim, J. T., & Choi, C.-G. (2012). Graphene-based polymer waveguide polarizer. *Optics Express*, *20*(4), 3556-3562.

Kim, J. W., Choi, S. Y., Yeom, D.-I., Aravazhi, S., Pollnau, M., Griebner, U., . . . Rotermund, F. (2013). Yb: KYW planar waveguide laser Q-switched by evanescent-field interaction with carbon nanotubes. *Optics Letters*, *38*(23), 5090-5093.

Kivistö, S., Hakulinen, T., Kaskela, A., Aitchison, B., Brown, D. P., Nasibulin, A. G., . . . Okhotnikov, O. G. (2009). Carbon nanotube films for ultrafast broadband technology. *Optics Express*, *17*(4), 2358-2363.

Klein, J., Sigl, L., Gyger, S., Barthelmi, K., Florian, M., Rey, S., . . . Kastl, C. (2021). Engineering the luminescence and generation of individual defect emitters in atomically thin MoS_2. *ACS Photonics*, *8*(2), 669-677.

Kondekar, N. P., Boebinger, M. G., Woods, E. V., & McDowell, M. T. (2017). In situ XPS investigation of transformations at crystallographically oriented MoS_2 interfaces. *ACS Applied Materials Interfaces*, *9*(37), 32394-32404.

Kravets, V. G., Wu, F., Auton, G. H., Yu, T., Imaizumi, S., & Grigorenko, A. N. (2019). Measurements of electrically tunable refractive index of MoS_2 monolayer and its usage in optical modulators. *npj 2D Materials Applications*, *3*(1), 1-10.

Kretinin, A., Cao, Y., Tu, J., Yu, G., Jalil, R., Novoselov, K., . . . Lozada, M. (2014). Electronic properties of graphene encapsulated with different two-dimensional atomic crystals. *Nano Letters*, *14*(6), 3270-3276.

Krishnan, U., Kaur, M., Singh, K., Kumar, M., & Kumar, A. (2019). A synoptic review of MoS_2: Synthesis to applications. *Superlattices Microstructures*, *128*, 274-297.

Kumar, N., Najmaei, S., Cui, Q., Ceballos, F., Ajayan, P. M., Lou, J., & Zhao, H. (2013). Second harmonic microscopy of monolayer MoS_2. *Physical Review B*, *87*(16), Article#161403.

Kumar, N., Tomar, R., Wadehra, N., Devi, M. M., Prakash, B., & Chakraverty, S. (2018). Growth of highly crystalline and large scale monolayer MoS_2 by CVD: the role of substrate position. *Crystal Research Technology*, *53*(6), Article#1800002.

Kunstmann, J., Wendumu, T. B., & Seifert, G. (2017). Localized defect states in MoS_2 monolayers: Electronic and optical properties. *Physica Status Solidi*, *254*(4), Article#1600645.

Kuo, A. C. (1999). Poly (dimethylsiloxane). In J. E. Mark (Ed.), *Polymer data handbook* (pp. 411-435). Oxford University Press, Inc.

Laskar, M. R., Ma, L., Kannappan, S., Sung Park, P., Krishnamoorthy, S., Nath, D. N., . . . Rajan, S. (2013). Large area single crystal (0001) oriented MoS_2. *Applied Physics Letters*, *102*(25), Article#252108.

Lee, C., Wei, X., Kysar, J. W., & Hone, J. (2008). Measurement of the elastic properties and intrinsic strength of monolayer graphene. *Science*, *321*(5887), 385-388.

Lee, C., Yan, H., Brus, L. E., Heinz, T. F., Hone, J., & Ryu, S. (2010). Anomalous lattice vibrations of single-and few-layer MoS_2. *ACS Nano*, *4*(5), 2695-2700.

Lee, Y. H., Zhang, X. Q., Zhang, W., Chang, M. T., Lin, C. T., Chang, K. D., . . . Li, L. J. (2012). Synthesis of large‐area MoS_2 atomic layers with chemical vapor deposition. *Advanced Materials*, *24*(17), 2320-2325.

Li, D., Song, X., Xu, J., Wang, Z., Zhang, R., Zhou, P., . . . Zheng, Y. (2017a). Optical properties of thickness-controlled MoS_2 thin films studied by spectroscopic ellipsometry. *Applied Surface Science*, *421*, 884-890.

Li, H., Lu, G., Yin, Z., He, Q., Li, H., Zhang, Q., & Zhang, H. (2012a). Optical identification of single‐and few‐layer MoS_2 sheets. *Small*, *8*(5), 682-686.

Li, H., Wu, J., Yin, Z., & Zhang, H. (2014a). Preparation and applications of mechanically exfoliated single-layer and multilayer MoS_2 and WSe_2 nanosheets. *Accounts of Chemical Research*, *47*(4), 1067-1075.

Li, H., Xia, H., Lan, C., Li, C., Zhang, X., Li, J., & Liu, Y. (2014b). Passively Q-switched erbium-doped fiber laser based on few-layer MoS_2 saturable absorber. *IEEE Photonics Technology Letters*, *27*(1), 69-72.

Li, H., Zhang, Q., Yap, C. C. R., Tay, B. K., Edwin, T. H. T., Olivier, A., & Baillargeat, D. (2012b). From bulk to monolayer MoS_2: evolution of Raman scattering. *Advanced Functional Materials*, *22*(7), 1385-1390.

Li, S.-L., Miyazaki, H., Song, H., Kuramochi, H., Nakaharai, S., & Tsukagoshi, K. (2012c). Quantitative Raman spectrum and reliable thickness identification for atomic layers on insulating substrates. *ACS Nano*, *6*(8), 7381-7388.

Li, T., & Galli, G. (2007). Electronic properties of MoS_2 nanoparticles. *The Journal of Physical Chemistry C*, *111*(44), 16192-16196.

Li, X., Cai, W., An, J., Kim, S., Nah, J., Yang, D., . . . Tutuc, E. (2009a). Large-area synthesis of high-quality and uniform graphene films on copper foils. *Science*, *324*(5932), 1312-1314.

Li, X., Hu, K., Lyu, B., Zhang, J., Wang, Y., Wang, P., . . . He, J. (2016a). Enhanced nonlinear optical response of rectangular MoS_2 and MoS_2/TiO_2 in dispersion and film. *The Journal of Physical Chemistry C*, *120*(32), 18243-18248.

Li, X., & Zhu, H. (2015). Two-dimensional MoS_2: Properties, preparation, and applications. *Journal of Materiomics*, *1*(1), 33-44.

Li, X., Zhu, Y., Cai, W., Borysiak, M., Han, B., Chen, D., . . . Ruoff, R. S. (2009b). Transfer of large-area graphene films for high-performance transparent conductive electrodes. *Nano Letters*, *9*(12), 4359-4363.

Li, X., Zou, W., & Chen, J. (2014c). 41.9 fs hybridly mode-locked Er-doped fiber laser at 212 MHz repetition rate. *Optics Letters*, *39*(6), 1553-1556.

Li, X. L., Han, W. P., Wu, J. B., Qiao, X. F., Zhang, J., & Tan, P. H. (2017b). Layer-number dependent optical properties of 2D materials and their application for thickness determination. *Advanced Functional Materials*, *27*(19), Article#1604468.

Li, Y., Chernikov, A., Zhang, X., Rigosi, A., Hill, H. M., Van Der Zande, A. M., . . . Heinz, T. F. (2014d). Measurement of the optical dielectric function of monolayer transition-metal dichalcogenides: MoS_2, $MoSe_2$, WS_2, and WSe_2. *Physical Review B*, *90*(20), 205422.

Li, Y., Dong, N., Zhang, S., Wang, K., Zhang, L., & Wang, J. (2016b). Optical identification of layered MoS_2 via the characteristic matrix method. *Nanoscale*, *8*(2), 1210-1215.

Li, Y., Rao, Y., Mak, K. F., You, Y., Wang, S., Dean, C. R., & Heinz, T. F. (2013). Probing symmetry properties of few-layer MoS_2 and h-BN by optical second-harmonic generation. *Nano Letters*, *13*(7), 3329-3333.

Li, Z., Pang, C., Li, R., & Chen, F. (2020). Low-dimensional materials as saturable absorbers for pulsed waveguide lasers. *Journal of Physics: Photonics*, *2*(3), Article#031001.

Li, Z., Zhang, Y., Cheng, C., Yu, H., & Chen, F. (2018). 6.5 GHz Q-switched mode-locked waveguide lasers based on two-dimensional materials as saturable absorbers. *Optics Express*, *26*(9), 11321-11330.

Liang, X., Sperling, B. A., Calizo, I., Cheng, G., Hacker, C. A., Zhang, Q., . . . Li, Q. (2011). Toward clean and crackless transfer of graphene. *ACS Nano*, *5*(11), 9144-9153.

Lin, J.-H., Chen, Y.-J., Lin, H.-Y., & Hsieh, W.-F. (2005). Two-photon resonance assisted huge nonlinear refraction and absorption in ZnO thin films. *Journal of Applied Physics*, *97*(3), Article#033526.

Lin, Q., Yan, L., Song, Y., Jia, X., Feng, X., Hou, L., & Bai, J. (2021). Switchable single- and dual-wavelength femtosecond mode-locked Er-doped fiber laser based on carboxyl-functionalized graphene oxide saturable absorber. *Chinese Optics Letters*, *19*(11), Article#111405.

Lin, Y.-C., Zhang, W., Huang, J.-K., Liu, K.-K., Lee, Y.-H., Liang, C.-T., . . . Li, L.-J. (2012). Wafer-scale MoS_2 thin layers prepared by MoO_3 sulfurization. *Nanoscale*, *4*(20), 6637-6641.

Lin, Z., Zhao, Y., Zhou, C., Zhong, R., Wang, X., Tsang, Y. H., & Chai, Y. (2015). Controllable growth of large–size crystalline MoS_2 and resist-free transfer assisted with a Cu thin film. *Scientific Reports*, *5*(1), 1-10.

Liu, H.-B., & Gong, H.-Q. (2009). Templateless prototyping of polydimethylsiloxane microfluidic structures using a pulsed CO_2 laser. *Journal of Micromechanics Microengineering*, *19*(3), Article#037002.

Liu, H.-L., Shen, C.-C., Su, S.-H., Hsu, C.-L., Li, M.-Y., & Li, L.-J. (2014a). Optical properties of monolayer transition metal dichalcogenides probed by spectroscopic ellipsometry. *Applied Physics Letters*, *105*(20), Article#201905.

Liu, H., Luo, A.-P., Wang, F.-Z., Tang, R., Liu, M., Luo, Z.-C., . . . Zhang, H. (2014b). Femtosecond pulse erbium-doped fiber laser by a few-layer MoS_2 saturable absorber. *Optics Letters*, *39*(15), 4591-4594.

Liu, H., Wong, S. L., & Chi, D. (2015a). CVD growth of MoS_2-based two-dimensional materials. *Chemical Vapor Deposition*, *21*(10-11-12), 241-259.

Liu, H., Zheng, X.-W., Liu, M., Zhao, N., Luo, A.-P., Luo, Z.-C., . . . Wen, S.-C. (2014c). Femtosecond pulse generation from a topological insulator mode-locked fiber laser. *Optics Express*, *22*(6), 6868-6873.

Liu, K.-K., Zhang, W., Lee, Y.-H., Lin, Y.-C., Chang, M.-T., Su, C.-Y., . . . Zhang, H. (2012). Growth of large-area and highly crystalline MoS_2 thin layers on insulating substrates. *Nano Letters*, *12*(3), 1538-1544.

Liu, K., Yan, Q., Chen, M., Fan, W., Sun, Y., Suh, J., . . . Tongay, S. (2014d). Elastic properties of chemical-vapor-deposited monolayer MoS_2, WS_2, and their bilayer heterostructures. *Nano Letters*, *14*(9), 5097-5103.

Liu, L., Xu, K., Wan, X., Xu, J., Wong, C. Y., & Tsang, H. K. (2015b). Enhanced optical Kerr nonlinearity of MoS_2 on silicon waveguides. *Photonics Research*, *3*(5), 206-209.

Liu, X., Huang, K., Zhao, M., Li, F., & Liu, H. (2019). A modified wrinkle-free MoS_2 film transfer method for large area high mobility field-effect transistor. *Nanotechnology*, *31*(5), Article#055707.

Long, M., Wang, P., Fang, H., & Hu, W. (2019). Progress, challenges, and opportunities for 2D material based photodetectors. *Advanced Functional Materials*, *29*(19), Article#1803807.

Louette, P., Bodino, F., & Pireaux, J.-J. (2005). Poly (dimethyl siloxane) (PDMS) XPS reference core level and energy loss spectra. *Surface Science Spectra*, *12*(1), 38-43.

Luo, S., Cullen, C. P., Guo, G., Zhong, J., & Duesberg, G. S. (2020). Investigation of growth-induced strain in monolayer MoS_2 grown by chemical vapor deposition. *Applied Surface Science*, *508*, Article#145126.

Luo, Z., Huang, Y., Zhong, M., Li, Y., Wu, J., Xu, B., . . . Weng, J. (2014). 1-, 1.5-, and 2-μm fiber lasers Q-switched by a broadband few-layer MoS_2 saturable absorber. *Journal of Lightwave Technology*, *32*(24), 4077-4084.

Lv, R., Chen, Z., Liu, S., Wang, J., Li, Y., Wang, Y., & Wang, Y. (2019). Optical properties and applications of molybdenum disulfide/SiO_2 saturable absorber fabricated by sol-gel technique. *Optics Express*, *27*(5), 6348-6356.

Ma, X., Liu, Q., Xu, D., Zhu, Y., Kim, S., Cui, Y., . . . Liu, M. (2017). Capillary-force-assisted clean-stamp transfer of two-dimensional materials. *Nano Letters*, *17*(11), 6961-6967.

Magda, G. Z., Pető, J., Dobrik, G., Hwang, C., Biró, L. P., & Tapasztó, L. (2015). Exfoliation of large-area transition metal chalcogenide single layers. *Scientific Reports*, *5*(1), 1-5.

Major, G. H., Fairley, N., Sherwood, P. M., Linford, M. R., Terry, J., Fernandez, V., & Artyushkova, K. (2020). Practical guide for curve fitting in x-ray photoelectron spectroscopy. *Journal of Vacuum Science Technology A: Vacuum, Surfaces, Films*, *38*(6), Article#061203.

Mak, K. F., He, K., Shan, J., & Heinz, T. F. (2012). Control of valley polarization in monolayer MoS_2 by optical helicity. *Nature Nanotechnology*, *7*(8), 494-498.

Mak, K. F., Lee, C., Hone, J., Shan, J., & Heinz, T. F. (2010). Atomically thin MoS_2: a new direct-gap semiconductor. *Physical Review Letters*, *105*(13), Article#136805.

Manzeli, S., Ovchinnikov, D., Pasquier, D., Yazyev, O. V., & Kis, A. (2017). 2D transition metal dichalcogenides. *Nature Reviews Materials*, *2*(8), Article#17033.

Mao, D., Du, B., Yang, D., Zhang, S., Wang, Y., Zhang, W., . . . Zhao, J. (2016a). Nonlinear saturable absorption of liquid - exfoliated molybdenum/tungsten ditelluride nanosheets. *Small*, *12*(11), 1489-1497.

Mao, D., She, X., Du, B., Yang, D., Zhang, W., Song, K., . . . Zhao, J. (2016b). Erbium-doped fiber laser passively mode locked with few-layer $WSe_2/MoSe_2$ nanosheets. *Scientific Reports*, *6*(1), 1-9.

McCreary, K. M., Hanbicki, A. T., Robinson, J. T., Cobas, E., Culbertson, J. C., Friedman, A. L., . . . Jonker, B. T. (2014). Large - Area Synthesis of Continuous and Uniform MoS_2 Monolayer Films on Graphene. *Advanced Functional Materials*, *24*(41), 6449-6454.

McManus, D., Vranic, S., Withers, F., Sanchez-Romaguera, V., Macucci, M., Yang, H., . . . Iannaccone, G. (2017). Water-based and biocompatible 2D crystal inks for all-inkjet-printed heterostructures. *Nature Nanotechnology*, *12*(4), 343-350.

Meitl, M. A., Zhu, Z.-T., Kumar, V., Lee, K. J., Feng, X., Huang, Y. Y., . . . Rogers, J. A. (2006). Transfer printing by kinetic control of adhesion to an elastomeric stamp. *Nature Materials*, *5*(1), 33-38.

Menzel, R. (2007). Lasers. In *Photonics: linear and nonlinear interactions of laser light and matter* (2nd ed., pp. 359-474). Springer Science & Business Media.

Mohapatra, P., Deb, S., Singh, B., Vasa, P., & Dhar, S. (2016). Strictly monolayer large continuous MoS_2 films on diverse substrates and their luminescence properties. *Applied Physics Letters*, *108*(4), Article#042101.

Mushtaq, R. T., Wang, Y., Rehman, M., Khan, A. M., & Mia, M. (2020). State-of-the-art and trends in CO_2 laser cutting of polymeric materials—a review. *Materials*, *13*(17), Article#3839.

Nair, R. R., Blake, P., Grigorenko, A. N., Novoselov, K. S., Booth, T. J., Stauber, T., . . . Geim, A. K. (2008). Fine structure constant defines visual transparency of graphene. *Science*, *320*(5881), 1308-1308.

Neupane, T., Rice, Q., Jung, S., Tabibi, B., & Seo, F. J. (2020). Cubic Nonlinearity of Molybdenum Disulfide Nanoflakes. *Journal of Nanoscience Nanotechnology*, *20*(7), 4373-4375.

Ng, K. B., Chew, J. W., Chong, W. Y., Lim, C. S., & Ahmad, H. B. (2020). Surface ablation of poly allyl diglycol carbonate polymer using high-repetition-rate femtosecond laser. *Optical Engineering*, *59*(5), Article#057102.

Novoselov, K. S., Geim, A. K., Morozov, S. V., Jiang, D., Zhang, Y., Dubonos, S. V., . . . Firsov, A. A. (2004). Electric field effect in atomically thin carbon films. *Science*, *306*(5696), 666-669.

O'Neill, A., Khan, U., & Coleman, J. N. (2012). Preparation of high concentration dispersions of exfoliated MoS_2 with increased flake size. *Chemistry of Materials*, *24*(12), 2414-2421.

Ortiz, R., Basnett, P., Roy, I., & Quintana, I. (2020). Picosecond laser ablation of polyhydroxyalkanoates (PHAs): Comparative study of neat and blended material response. *Polymers*, *12*(1), Article#127.

Ouyang, Q., Zhang, K., Chen, W., Zhou, F., & Ji, W. (2016). Nonlinear absorption and nonlinear refraction in a chemical vapor deposition-grown, ultrathin hexagonal boron nitride film. *Optics Letters*, *41*(7), 1368-1371.

Pan, H., Chu, H., Pan, Z., Zhao, S., Yang, M., Chai, J., . . . Li, D. (2020). Large-scale monolayer molybdenum disulfide (MoS_2) for mid-infrared photonics. *Nanophotonics*, *9*(16), 4703-4710.

Pandey, M., Rasmussen, F. A., Kuhar, K., Olsen, T., Jacobsen, K. W., & Thygesen, K. S. (2016). Defect-tolerant monolayer transition metal dichalcogenides. *Nano Letters*, *16*(4), 2234-2239.

Paradisanos, I., Shree, S., George, A., Leisgang, N., Robert, C., Watanabe, K., . . . Marie, X. (2020). Controlling interlayer excitons in MoS_2 layers grown by chemical vapor deposition. *Nature Communications*, *11*(1), 1-7.

Park, J. W., So, H. S., Kim, S., Choi, S.-H., Lee, H., Lee, J., . . . Kim, Y. (2014a). Optical properties of large-area ultrathin MoS_2 films: Evolution from a single layer to multilayers. *Journal of Applied Physics*, *116*(18), Article#183509.

Park, W., Baik, J., Kim, T.-Y., Cho, K., Hong, W.-K., Shin, H.-J., & Lee, T. J. (2014b). Photoelectron spectroscopic imaging and device applications of large-area patternable single-layer MoS_2 synthesized by chemical vapor deposition. *ACS Nano*, *8*(5), 4961-4968.

Patil, C., Dalir, H., Kang, J. H., Davydov, A., Wong, C. W., & Sorger, V. J. (2022). Highly accurate, reliable, and non-contaminating two-dimensional material transfer system. *Applied Physics Reviews*, *9*(1), Article#011419.

Paton, K. R., Varrla, E., Backes, C., Smith, R. J., Khan, U., O'Neill, A., . . . King, P. (2014). Scalable production of large quantities of defect-free few-layer graphene by shear exfoliation in liquids. *Nature Materials*, *13*(6), 624-630.

Phare, C. T., Daniel Lee, Y.-H., Cardenas, J., & Lipson, M. (2015). Graphene electro-optic modulator with 30 GHz bandwidth. *Nature Photonics*, *9*(8), 511-514.

Pondick, J. V., Woods, J. M., Xing, J., Zhou, Y., & Cha, J. J. (2018). Stepwise sulfurization from MoO_3 to MoS_2 via chemical vapor deposition. *ACS Applied Nano Materials*, *1*(10), 5655-5661.

Quintero, F., Riveiro, A., Lusquiños, F., Comesaña, R., & Pou, J. (2011). Feasibility study on laser cutting of phenolic resin boards. *Physics Procedia*, *12*, 578-583.

Radisavljevic, B., Radenovic, A., Brivio, J., Giacometti, V., & Kis, A. (2011). Single-layer MoS_2 transistors. *Nature Nanotechnology*, *6*(3), 147-150.

Rollings, E., Gweon, G.-H., Zhou, S., Mun, B., McChesney, J., Hussain, B., . . . Lanzara, A. (2006). Synthesis and characterization of atomically thin graphite films on a silicon carbide substrate. *Journal of Physics Chemistry of Solids*, *67*(9-10), 2172-2177.

Roy, A., Movva, H. C., Satpati, B., Kim, K., Dey, R., Rai, A., . . . Banerjee, S. K. (2016). Structural and electrical properties of $MoTe_2$ and $MoSe_2$ grown by molecular beam epitaxy. *ACS Applied Materials Interfaces*, *8*(11), 7396-7402.

Rüdiger, P. (2004). *Q Switching*. Retrieved September 1, 2022 from https://www.rp-photonics.com/q_switching.html

Rusdi, M., Latiff, A., Hanafi, E., Mahyuddin, M., Shamsudin, H., Dimyati, K., & Harun, S. (2016). Molybdenum disulphide tape saturable absorber for mode-locked

double-clad ytterbium-doped all-fiber laser generation. *Chinese Physics Letters*, *33*(11), Article#114201.

Saha, A. K., & Yoshiya, M. (2018). Native point defects in MoS_2 and their influences on optical properties by first principles calculations. *Physica B: Condensed Matter*, *532*, 184-194.

Samad, L., Bladow, S. M., Ding, Q., Zhuo, J., Jacobberger, R. M., Arnold, M. S., & Jin, S. (2016). Layer-controlled chemical vapor deposition growth of MoS_2 vertical heterostructures via van der Waals epitaxy. *ACS Nano*, *10*(7), 7039-7046.

Samy, O., Zeng, S., Birowosuto, M. D., & El Moutaouakil, A. (2021). A Review on MoS_2 properties, synthesis, sensing applications and challenges. *Crystals*, *11*(4), Article#355.

Säynätjoki, A., Karvonen, L., Rostami, H., Autere, A., Mehravar, S., Lombardo, A., . . . Lipsanen, H. (2017). Ultra-strong nonlinear optical processes and trigonal warping in MoS_2 layers. *Nature Communications*, *8*(1), 1-8.

Sheik-Bahae, M., Said, A. A., & Van Stryland, E. W. (1989). High-sensitivity, single-beam n_2 measurements. *Optics Letters*, *14*(17), 955-957.

Sheik-Bahae, M., Said, A. A., Wei, T.-H., Hagan, D. J., & Van Stryland, E. W. (1990). Sensitive measurement of optical nonlinearities using a single beam. *IEEE Journal of Quantum Electronics*, *26*(4), 760-769.

Sheldon, S., Knight, L., & Thorne, J. (1982). Laser-induced thermal lens effect: a new theoretical model. *Applied Optics*, *21*(9), 1663-1669.

Shen, C.-C., Hsu, Y.-T., Li, L.-J., & Liu, H.-L. (2013). Charge dynamics and electronic structures of monolayer MoS_2 films grown by chemical vapor deposition. *Applied Physics Express*, *6*(12), Article#125801.

Sheng, P., & Cai, L.-H. (1996). Model-based path planning for laser cutting of curved trajectories. *International Journal of Machine Tools Manufacture*, *36*(6), 739-754.

Shi, J., Yang, Y., Zhang, Y., Ma, D., Wei, W., Ji, Q., . . . Li, C. (2015). Monolayer MoS_2 growth on Au foils and on-site domain boundary imaging. *Advanced Functional Materials*, *25*(6), 842-849.

Shi, Y., Zhou, W., Lu, A.-Y., Fang, W., Lee, Y.-H., Hsu, A. L., . . . Li, L.-J. (2012). van der Waals epitaxy of MoS_2 layers using graphene as growth templates. *Nano Letters*, *12*(6), 2784-2791.

Siddiq, N. A., Chong, W. Y., Pramono, Y. H., Muntini, M. S., & Ahmad, H. (2019). C-band tunable performance of passively Q-switched erbium-doped fiber laser using Tin (IV) oxide as a saturable absorber. *Optics Communications*, *442*, 1-7.

Song, Y.-W., Jang, S.-Y., Han, W.-S., & Bae, M.-K. (2010). Graphene mode-lockers for fiber lasers functioned with evanescent field interaction. *Applied Physics Letters*, *96*(5).

SPI Supplies Molybdenum Disulfide (MoS_2) Crystal. (2022). Retrieved August 22, 2022 from https://www.2spi.com/item/z429ml/

Spiess, W., & Strack, H. (1989). Structuring of polyimide by ArF excimer laser ablation. *Semiconductor Science Technology*, *4*(6), Article#486.

Splendiani, A., Sun, L., Zhang, Y., Li, T., Kim, J., Chim, C.-Y., . . . Wang, F. (2010). Emerging photoluminescence in monolayer MoS_2. *Nano Letters*, *10*(4), 1271-1275.

Stavrou, M., Chazapis, N., Nikoli, E., Arenal, R., Tagmatarchis, N., & Couris, S. (2022). Crystalline phase effects on the nonlinear optical response of MoS_2 and WS_2 nanosheets: Implications for photonic and optoelectronic applications. *ACS Applied Nano Materials*, *5*(11), 16674-16686.

Stavrou, M., Dalamaras, I., Karampitsos, N., & Couris, S. (2020). Determination of the nonlinear optical properties of single-and few-layered graphene dispersions under femtosecond laser excitation: electronic and thermal origin contributions. *The Journal of Physical Chemistry C*, *124*(49), 27241-27249.

Suhara, T., & Fujimura, M. (2003). Introduction. In *Waveguide nonlinear-optic devices* (Vol. 11, pp. 1-7). Springer Science & Business Media.

Sun, J., Li, X., Guo, W., Zhao, M., Fan, X., Dong, Y., . . . Fu, Y. (2017). Synthesis methods of two-dimensional MoS_2: a brief review. *Crystals*, *7*(7), Article#198.

Sun, Z., Hasan, T., Torrisi, F., Popa, D., Privitera, G., Wang, F., . . . Ferrari, A. C. (2010). Graphene mode-locked ultrafast laser. *ACS Nano*, *4*(2), 803-810.

Supradeepa, V., & Weiner, A. M. (2012). Bandwidth scaling and spectral flatness enhancement of optical frequency combs from phase-modulated continuous-wave lasers using cascaded four-wave mixing. *Optics Letters*, *37*(15), 3066-3068.

Syari'ati, A., Kumar, S., Zahid, A., El Yumin, A. A., Ye, J., & Rudolf, P. (2019). Photoemission spectroscopy study of structural defects in molybdenum disulfide

(MoS_2) grown by chemical vapor deposition (CVD). *Chemical Communications*, *55*(70), 10384-10387.

Tamulewicz-Szwajkowska, M., Zelewski, S. J., Serafińczuk, J., & Kudrawiec, R. (2022). Geometric progress in the thickness of exfoliated van der Waals crystals on the example of MoS_2. *AIP Advances*, *12*(2), Article#025328.

Tanaka, K., Matsuzaki, S., & Toyoshima, I. (1993). Photodecomposition of adsorbed methoxy species by UV light and formaldehyde adsorption on silicon (111) studied by XPS and UPS. *The Journal of Physical Chemistry*, *97*(21), 5673-5677.

Tang, H., Neupane, B., Neupane, S., Ruan, S., Nepal, N. K., & Ruzsinszky, A. (2022). Tunable band gaps and optical absorption properties of bent MoS_2 nanoribbons. *Scientific Reports*, *12*(1), Article#3008.

Tsang, H. K., Wong, C. S., Liang, T. K., Day, I., Roberts, S., Harpin, A., . . . Asghari, M. (2002). Optical dispersion, two-photon absorption and self-phase modulation in silicon waveguides at 1.5 μm wavelength. *Applied Physics Letters*, *80*(3), 416-418.

Udin, H. (1951). Grain boundary effect in surface tension measurement. *Journal of Metals*, *3*(1), 63-63.

Van Der Zande, A. M., Huang, P. Y., Chenet, D. A., Berkelbach, T. C., You, Y., Lee, G.-H., . . . Hone, J. C. (2013). Grains and grain boundaries in highly crystalline monolayer molybdenum disulphide. *Nature Materials*, *12*(6), 554-561.

Varrla, E., Backes, C., Paton, K. R., Harvey, A., Gholamvand, Z., McCauley, J., & Coleman, J. N. (2015). Large-scale production of size-controlled MoS_2 nanosheets by shear exfoliation. *Chemistry of Materials*, *27*(3), 1129-1139.

Vudayagiri, S., Junker, M. D., & Skov, A. L. (2013). Factors affecting the surface and release properties of thin polydimethylsiloxane films. *Polymer Journal*, *45*(8), 871-878.

Wang, J., Zhang, L., Chen, Y., Geng, Y., Hong, X., Li, X., & Cheng, Z. (2019a). Saturable absorption in graphene-on-waveguide devices. *Applied Physics Express*, *12*(3), Article#032003.

Wang, K., Feng, Y., Chang, C., Zhan, J., Wang, C., Zhao, Q., . . . Wang, J. (2014a). Broadband ultrafast nonlinear absorption and nonlinear refraction of layered molybdenum dichalcogenide semiconductors. *Nanoscale*, *6*(18), 10530-10535.

Wang, K., Wang, J., Fan, J., Lotya, M., O'Neill, A., Fox, D., . . . Zhao, Q. (2013). Ultrafast saturable absorption of two-dimensional MoS_2 nanosheets. *ACS Nano*, *7*(10), 9260-9267.

Wang, Q. H., Kalantar-Zadeh, K., Kis, A., Coleman, J. N., & Strano, M. S. (2012). Electronics and optoelectronics of two-dimensional transition metal dichalcogenides. *Nature Nanotechnology*, *7*(11), 699-712.

Wang, R., Chien, H.-C., Kumar, J., Kumar, N., Chiu, H.-Y., & Zhao, H. (2014b). Third-harmonic generation in ultrathin films of MoS_2. *ACS Applied Materials Interfaces*, *6*(1), 314-318.

Wang, R., Zhou, X., Xu, X., Hu, J., & Pan, J. (2017). The indirect–direct band gap tuning in armchair MoS_2 nanoribbon by edge passivation. *Journal of Physics D: Applied Physics*, *50*(9), Article#095102.

Wang, X., Kang, K., Godin, K., Fu, S., Chen, S., & Yang, E.-H. (2019b). Effects of solvents and polymer on photoluminescence of transferred WS_2 monolayers. *Journal of Vacuum Science Technology B, Nanotechnology Microelectronics: Materials, Processing, Measurement, Phenomena*, *37*(5), Article#052902.

Wang, Y., Guo, Z., You, J., Zhang, Z., Zheng, X., & Cheng, X. (2019c). Ultrafast nonlinear optical excitation behaviors of mono-and few-layer two dimensional MoS_2. *Photonic Sensors*, *9*(1), 1-10.

Watson, A. J., Lu, W., Guimarães, M. H., & Stöhr, M. (2021). Transfer of large-scale two-dimensional semiconductors: challenges and developments. *2D Materials*, *8*(3), Article#032001.

Weber, M. J. (2018). Introduction. In *Handbook of Laser Wavelengths* (pp. 1-19). CRC press.

Wei, R., Zhang, H., He, X., Hu, Z., Tian, X., Xiao, Q., . . . Qiu, J. (2015). Versatile preparation of ultrathin MoS_2 nanosheets with reverse saturable absorption response. *Optical Materials Express*, *5*(8), 1807-1814.

Wei, R., Zhang, H., Hu, Z., Qiao, T., He, X., Guo, Q., . . . Qiu, J. (2016). Ultra-broadband nonlinear saturable absorption of high-yield MoS_2 nanosheets. *Nanotechnology*, *27*(30), Article#305203.

Wiegand, B. C., Friend, C., & Roberts, J. T. (1989). Adsorbate thermodynamics as a determinant of reaction mechanism: pentamethylene sulfide on molybdenum (110). *Langmuir*, *5*(6), 1292-1298.

Woodward, R., Howe, R., Hu, G., Torrisi, F., Zhang, M., Hasan, T., & Kelleher, E. (2015). Few-layer MoS_2 saturable absorbers for short-pulse laser technology: current status and future perspectives. *Photonics Research*, *3*(2), A30-A42.

Woodward, R., Kelleher, E., Howe, R., Hu, G., Torrisi, F., Hasan, T., . . . Taylor, J. (2014). Tunable Q-switched fiber laser based on saturable edge-state absorption in few-layer molybdenum disulfide (MoS_2). *Optics express*, *22*(25), 31113-31122.

Woodward, R., Murray, R., Phelan, C., De Oliveira, R., Runcorn, T., Kelleher, E., . . . Eda, G. (2016). Characterization of the second-and third-order nonlinear optical susceptibilities of monolayer MoS_2 using multiphoton microscopy. *2D Materials*, *4*(1), Article#011006.

Woodward, R. I., & Kelleher, E. J. (2015). 2D saturable absorbers for fibre lasers. *Applied Sciences*, *5*(4), 1440-1456.

Wu, C., Xu, J., Zhang, T., Xin, G., Li, M., Rong, Y., . . . Huang, Y. (2022). Precision cutting of PDMS film with UV-nanosecond laser based on heat generation-diffusion regulation. *Optics Laser Technology*, *145*, Article#107462.

Wu, K., Li, Z., Tang, J., Lv, X., Wang, H., Luo, R., . . . Yuan, S. (2018). Controllable defects implantation in MoS_2 grown by chemical vapor deposition for photoluminescence enhancement. *Nano Research*, *11*(8), 4123-4132.

Wu, Y., Yao, B., Feng, Q., Cao, X., Zhou, X., Rao, Y., . . . Chen, Y. (2015). Generation of cascaded four-wave-mixing with graphene-coated microfiber. *Photonics Research*, *3*(2), A64-A68.

Xia, F., Wang, H., Xiao, D., Dubey, M., & Ramasubramaniam, A. (2014a). Two-dimensional material nanophotonics. *Nature Photonics*, *8*(12), Article#899.

Xia, H., Li, H., Lan, C., Li, C., Du, J., Zhang, S., & Liu, Y. (2015). Few-layer MoS_2 grown by chemical vapor deposition as a passive Q-switcher for tunable erbium-doped fiber lasers. *Photonics Research*, *3*(3), A92-A96.

Xia, H., Li, H., Lan, C., Li, C., Zhang, X., Zhang, S., & Liu, Y. (2014b). Ultrafast erbium-doped fiber laser mode-locked by a CVD-grown molybdenum disulfide (MoS_2) saturable absorber. *Optics Express*, *22*(14), 17341-17348.

Xiong, Z., Zhong, L., Wang, H., & Li, X. (2021). Structural defects, mechanical behaviors, and properties of two-dimensional materials. *Materials*, *14*(5), Article#1192.

Xu, Z.-Q., Zhang, Y., Lin, S., Zheng, C., Zhong, Y. L., Xia, X., . . . Cheng, Y.-B. (2015). Synthesis and transfer of large-area monolayer WS_2 crystals: moving toward the recyclable use of sapphire substrates. *ACS Nano*, *9*(6), 6178-6187.

Yamaguchi, H., Eda, G., Mattevi, C., Kim, H., & Chhowalla, M. (2010). Highly uniform 300 mm wafer-scale deposition of single and multilayered chemically derived graphene thin films. *ACS Nano*, *4*(1), 524-528.

Yan, W., Txoperena, O., Llopis, R., Dery, H., Hueso, L. E., & Casanova, F. (2016). A two-dimensional spin field-effect switch. *Nature Communications*, *7*(1), 1-6.

Ye, C., Yan, P., Gong, M., & Lei, M. (2005). Pulsed pumped Yb-doped fiber amplifier at low repetition rate. *Chinese Optics Letters*, *3*(5), 249-250.

Yin, X., Ye, Z., Chenet, D. A., Ye, Y., O'Brien, K., Hone, J. C., & Zhang, X. (2014). Edge nonlinear optics on a MoS_2 atomic monolayer. *Science*, *344*(6183), 488-490.

You, J., Bongu, S., Bao, Q., & Panoiu, N. (2019). Nonlinear optical properties and applications of 2D materials: theoretical and experimental aspects. *Nanophotonics*, *8*(1), 63-97.

Yu, H., Liao, M., Zhao, W., Liu, G., Zhou, X., Wei, Z., . . . Deng, K. (2017a). Wafer-scale growth and transfer of highly-oriented monolayer MoS_2 continuous films. *ACS Nano*, *11*(12), 12001-12007.

Yu, S., Wu, X., Wang, Y., Guo, X., & Tong, L. (2017b). 2D materials for optical modulation: challenges and opportunities. *Advanced Materials*, *29*(14), Article#1606128.

Yun, S. J., Chae, S. H., Kim, H., Park, J. C., Park, J.-H., Han, G. H., . . . Seok, J. (2015). Synthesis of centimeter-scale monolayer tungsten disulfide film on gold foils. *ACS Nano*, *9*(5), 5510-5519.

Zeng, Z., Yin, Z., Huang, X., Li, H., He, Q., Lu, G., . . . Zhang, H. (2011). Single-layer semiconducting nanosheets: high-yield preparation and device fabrication. *Angewandte Chemie*, *123*(47), 11289-11293.

Zhan, Y., Liu, Z., Najmaei, S., Ajayan, P. M., & Lou, J. (2012). Large-area vapor-phase growth and characterization of MoS_2 atomic layers on a SiO_2 substrate. *Small*, *8*(7), 966-971.

Zhang, G., Tang, X., Fu, X., Chen, W., Shabbir, B., Zhang, H., . . . Gong, M. (2019). 2D group-VA fluorinated antimonene: synthesis and saturable absorption. *Nanoscale*, *11*(4), 1762-1769.

Zhang, H., Healy, N., Runge, A. F., Huang, C. C., Hewak, D. W., & Peacock, A. C. (2018). Optical-resonance-enhanced nonlinearities in a MoS_2-coated single-mode fiber. *Optics Letters*, *43*(13), 3100-3103.

Zhang, H., Lu, S., Zheng, J., Du, J., Wen, S., Tang, D., & Loh, K. (2014a). Molybdenum disulfide (MoS_2) as a broadband saturable absorber for ultra-fast photonics. *Optics Express*, *22*(6), 7249-7260.

Zhang, H., Virally, S., Bao, Q., Ping, L. K., Massar, S., Godbout, N., & Kockaert, P. (2012). Z-scan measurement of the nonlinear refractive index of graphene. *Optics Letters*, *37*(11), 1856-1858.

Zhang, L., Agarwal, A. M., Kimerling, L. C., & Michel, J. (2014b). Nonlinear Group IV photonics based on silicon and germanium: from near-infrared to mid-infrared. *Nanophotonics*, *3*(4-5), 247-268.

Zhang, X., Qiao, X.-F., Shi, W., Wu, J.-B., Jiang, D.-S., & Tan, P.-H. (2015). Phonon and Raman scattering of two-dimensional transition metal dichalcogenides from monolayer, multilayer to bulk material. *Chemical Society Reviews*, *44*(9), 2757-2785.

Zhang, Y., Tao, L., Yi, D., Xu, J.-B., & Tsang, H. K. (2020). Enhanced four-wave mixing with MoS_2 on a silicon waveguide. *Journal of Optics*, *22*(2), Article#025503.

Zhang, Z., Ji, X., Shi, J., Zhou, X., Zhang, S., Hou, Y., . . . Zhang, Y. (2017). Direct chemical vapor deposition growth and band-gap characterization of MoS_2/h-BN van der Waals heterostructures on Au foils. *ACS Nano*, *11*(4), 4328-4336.

Zheng, X., Zhang, Y., Chen, R., Xu, Z., & Jiang, T. (2015). Z-scan measurement of the nonlinear refractive index of monolayer WS_2. *Optics Express*, *23*(12), 15616-15623.

Zhou, S., Tang, Q., Tian, H., Zhao, X., Tong, Y., Barlow, S., . . . Liu, Y. (2018). Direct effect of dielectric surface energy on carrier transport in organic field-effect transistors. *ACS Applied Materials Interfaces*, *10*(18), 15943-15951.

Zhou, W., Zou, X., Najmaei, S., Liu, Z., Shi, Y., Kong, J., . . . Idrobo, J.-C. (2013). Intrinsic structural defects in monolayer molybdenum disulfide. *Nano Letters*, *13*(6), 2615-2622.

Zhu, D., Shu, H., Jiang, F., Lv, D., Asokan, V., Omar, O., . . . Jin, C. (2017). Capture the growth kinetics of CVD growth of two-dimensional MoS_2. *npj 2D Materials Applications*, *1*(1), Article#8.

Zhu, P.-F., Lin, Z.-B., Ning, Q.-Y., Cai, Z.-R., Xing, X.-B., Liu, J., . . . Xu, W.-C. (2013). Passive harmonic mode-locking in a fiber laser by using a microfiber-based graphene saturable absorber. *Laser Physics Letters*, *10*(10), Article#105107.